

UNIVERSIDADE FEDERAL DE MINAS GERAIS  
Escola de Engenharia  
Colegiado do Curso de Graduação em Engenharia ...

Nome da pessoa autora

**TÍTULO DO TRABALHO**

Belo Horizonte  
2023

Nome da pessoa autora

## **TÍTULO DO TRABALHO**

Trabalho de Conclusão de Curso apresentado ao  
Curso de Engenharia de Sistemas da Universi-  
dade Federal Minas Gerais, como requisito par-  
cial para o grau de bacharel (a) em Engenharia  
de Sistemas.

Orientadora: Profa. Dra. Fulana Beltrano

Coorientador: Prof. Dr. Ciclano da Silva

Belo Horizonte  
2024

Troque pelo arquivo PDF da ficha  
catalográfica após obtê-la da biblioteca  
da sua unidade.

Troque pelo arquivo PDF da folha de aprovação ou ata de defesa após obtê-la do seu programa de pós-graduação (após a defesa).

*Esse trabalho é dedicado a aquela pessoa.*

# Agradecimentos

Você pode escrever aqui os agradecimentos a pessoas que contribuíram para a realização do trabalho.

“Aqui vai uma bela e inspiradora frase.”

# Resumo

Escreva aqui o resumo do seu trabalho.

**Palavras-chave:** palavra-chave 1; palavra-chave 2; palavra-chave 3.

# **Abstract**

Translate here the abstract of your work.

**Keywords:** keyword 1; keyword 2; keyword 3.

# **Lista de Siglas e Símbolos**

## **Siglas**

ACO	Ant Colony Optimization
BIM	Born Iterative Method
CNN	Convolutional Neural Networks
DE	Differential Evolution
EA	Evolutionary Algorithm
GA	Genetic Algorithm
GAN	Generative Adversarial Network
PSO	Particle Swarm Optimization
TMz	Modo Magnético Transversal em $z$

## **Símbolos**

$\epsilon$	Permissividade complexa [F/m + $j\Omega/m$ ]
$\epsilon_r$	Permissividade relativa
$\theta$	Ângulo da coordenada polar [rad]
$\lambda_b$	Comprimento de onda de fundo [m]
$\sigma$	Condutividade [ $\Omega/m$ ]
$\phi$	Ângulo de incidência [rad]
<b>E</b>	Vetor de intensidade elétrica [V/m]
$E_z$	Componente $z$ do vetor de intensidade elétrica [V/m]
$k$	Número de onda [1/m]
$\mathbb{R}$	Conjunto dos números reais
<b>r</b>	Vetor posição no espaço 3D [m]
$x, y, z$	Coordenadas cartesianas [m]
$V$	Espaço tridimensional

# Sumário

<b>1</b>	<b>Introdução</b>	<b>13</b>
1.1	Objetivos Gerais e Específicos . . . . .	13
1.2	Organização do Trabalho . . . . .	13
<b>2</b>	<b>Problem Statement</b>	<b>14</b>
2.1	Electromagnetic Theory . . . . .	14
2.2	Integral Equations . . . . .	16
2.3	Basic Theory of Inverse Ill-Posed Problems . . . . .	18
2.4	The Eletromagnetic Inverse Scattering Problem . . . . .	19
2.4.1	Formulations . . . . .	19
2.4.2	The Two-Dimensional Problem . . . . .	22
2.4.3	Vector spaces and operator properties . . . . .	23
2.4.4	Uniqueness, Stability and Nonlinearity . . . . .	24
2.4.5	Degrees of Freedom . . . . .	25
2.5	Conclusion . . . . .	27
<b>3</b>	<b>Methods Overview</b>	<b>29</b>
3.1	Domain Definition . . . . .	29
3.2	Discretization . . . . .	31
3.2.1	The Subdomain Method . . . . .	35
3.2.2	The Collocation Method . . . . .	35
3.2.3	The Galerkin Method . . . . .	40
3.2.4	Some Aspects on Discretization . . . . .	41
3.3	The Linear Case . . . . .	43
3.3.1	Approximated Solutions for Weak Scatterers . . . . .	43
3.3.2	The Back-Propagation Method . . . . .	44
3.3.3	Dominant Current Scheme . . . . .	45
3.4	Regularization Methods . . . . .	47
3.4.1	The Tikhonov Regularization . . . . .	47
3.4.2	The Landweber Regularization . . . . .	52
3.4.3	The Conjugate Gradient Method . . . . .	53

3.4.4	Spectral Cut-Off . . . . .	54
3.5	Qualitative Methods . . . . .	55
3.5.1	Linear Sampling Method . . . . .	55
3.5.2	Orthogonality Sampling Method . . . . .	56
3.6	Deterministic Quantitative Methods . . . . .	57
3.6.1	The Born Iterative Method . . . . .	57
3.6.2	The Distorted Born Iterative Method . . . . .	59
3.6.3	The Variational Born Iterative Method . . . . .	61
3.6.4	The Conjugated-Gradient Method . . . . .	62
3.6.5	The Level-Set Method . . . . .	63
3.6.6	The Contrast Source Inversion . . . . .	64
3.6.7	Compressive Sensing . . . . .	65
3.6.8	The Subspace-Based Optimization Method . . . . .	67
3.6.9	Regularization on $L^p$ Banach Spaces . . . . .	72
3.6.10	Virtual Experiments . . . . .	74
3.7	Stochastic Quantitative Methods . . . . .	76
3.7.1	Representation of Solutions . . . . .	77
3.7.2	Objective Function Formulation . . . . .	79
3.7.3	Mechanisms and Evolutionary Operators . . . . .	82
3.7.4	Population Initialization . . . . .	84
3.8	Deep-Learning Methods . . . . .	84
3.9	Conclusion . . . . .	88
<b>4</b>	<b>Proposed Methodology</b>	<b>90</b>
4.1	Literature Criticism and Opportunities . . . . .	90
4.2	Proposal . . . . .	94
4.3	Surrogate model-Assisted Algorithms for EISPs . . . . .	94
4.3.1	The Optimization Model . . . . .	95
4.3.2	Surrogate Models . . . . .	98
4.3.3	Kriging Model . . . . .	98
4.3.4	Surrogate model-Assisted Algorithms . . . . .	100
4.4	EISPY2D: A Platform for Developing and Testing Algorithms for EISPs . . . . .	108
4.4.1	Structure Description . . . . .	109
4.4.2	Performance Metrics Proposal . . . . .	111
4.4.3	Randomization of the Test Set . . . . .	113
4.4.4	Comparison Structure . . . . .	114
4.5	Conclusion . . . . .	118
<b>5</b>	<b>Results</b>	<b>119</b>
5.1	Case Studies . . . . .	119

5.1.1	Austria Profile . . . . .	121
5.1.2	Multiple Scatterers . . . . .	127
5.1.3	Non-Homogeneous Scatterer . . . . .	133
5.1.4	Strong Scatterer . . . . .	137
5.2	Benchmarking . . . . .	145
5.2.1	Test Sets and Algorithms Parameters Considerations . . . . .	145
5.2.2	Discussion . . . . .	147
<b>6</b>	<b>Conclusion</b>	<b>157</b>
6.1	Recapitulation . . . . .	157
6.2	Self-Criticism . . . . .	160
6.3	Continuity Proposals . . . . .	160
6.4	Bibliographic Production . . . . .	161
<b>Referências Bibliográficas</b>		<b>163</b>
<b>A</b>	<b>Como fazer citações</b>	<b>190</b>
<b>B</b>	<b>Dyadic Green's Function</b>	<b>191</b>
B.1	Dyadic Green's Function for Homogeneous Medium . . . . .	191
B.2	The Singularity of the Dyadic Green's Function . . . . .	193
B.3	Dyadic Green's Function for Inhomogeneous Medium . . . . .	195
<b>C</b>	<b>Integral Equation Formulation</b>	<b>197</b>
<b>D</b>	<b>Functional Analysis</b>	<b>200</b>
D.1	Normed and Hilbert Spaces . . . . .	200
D.2	Linear Bounded and Compact Operators . . . . .	203
<b>E</b>	<b>Shape metrics</b>	<b>206</b>

# **Capítulo 1**

## **Introdução**

Parte inicial do texto na qual se apresenta a delimitação do assunto tratado, os objetivos da pesquisa e outros elementos necessários para apresentar o tema do trabalho. O texto tem o objetivo de introduzir o leitor ao trabalho e apresentar as informações para uma compreensão geral da proposta desenvolvida.

### **1.1 Objetivos Gerais e Específicos**

Descrever os objetivos gerais e específicos do trabalho. Os objetivos gerais devem ser claros e concisos, indicando o propósito do trabalho. Os objetivos específicos devem ser apresentados de forma a indicar os passos necessários para atingir o objetivo geral.

### **1.2 Organização do Trabalho**

Descrever a organização do trabalho, indicando o conteúdo de cada capítulo e a relação entre eles. A organização do trabalho deve ser clara e coerente, de forma a facilitar a compreensão do leitor.

# Capítulo 2

## Problem Statement

Microwave Imaging is an Electromagnetic Inverse Scattering Problem (EISP). Because of its nature, its magnitudes are defined in terms of Maxwell's equations which describe the electromagnetic phenomenon. In particular, the problem can be written in the form of an integral equation, which is very common for problems involving radiation from a current, whether impressed or induced. Rather than determining the effect from a cause, the problem is defined inversely. Thus, there are several characteristics peculiar to this kind of problem which is considered an ill-posed one in the literature.

This chapter aims to describe in a general way the mathematical model which represents the problem and to discuss its most important aspects. In Section 2.1, the electromagnetic model will be presented. Then, in Section 2.2, the equation which relates all the required quantities will be developed. Subsequently, some fundamentals about inverse problems are presented in Section 2.3. Afterward, several important aspects of the problem are discussed in Section 2.4. Finally, a conclusion is presented highlighting the main topics of the chapter. Appendices B, C and D were also written as supporting material for several concepts and deductions that will be used in this chapter.

### 2.1 Electromagnetic Theory

Maxwell's equations mathematically describe the electromagnetic phenomena. The four equations relate fields and sources in space and time. They are expressed as follows (Harrington, 2001):

$$\nabla \times \mathcal{E}(\mathbf{r}, t) = -\frac{\partial \mathcal{B}}{\partial t}(\mathbf{r}, t) \quad (2.1)$$

$$\nabla \times \mathcal{H}(\mathbf{r}, t) = \frac{\partial \mathcal{D}}{\partial t}(\mathbf{r}, t) + \mathcal{J}(\mathbf{r}, t) \quad (2.2)$$

$$\nabla \cdot \mathcal{D}(\mathbf{r}, t) = \rho(\mathbf{r}, t) \quad (2.3)$$

$$\nabla \cdot \mathcal{B}(\mathbf{r}, t) = 0 \quad (2.4)$$

The vector  $\mathbf{r} = x\mathbf{x} + y\mathbf{y} + z\mathbf{z} = \langle x, y, z \rangle$  denotes the space coordinates (in meters [m]) and  $t$  is the time (in seconds [s]). The vectors  $\mathcal{E}$ ,  $\mathcal{H}$ ,  $\mathcal{D}$ , and  $\mathcal{B}$  represent electric field intensity (in volts per meter [V/m]), magnetic field intensity (in amperes per meter [A/m]), electric flux density (in coulombs per square meter [C/m<sup>2</sup>]), and magnetic flux density (in tesla [T]). The sources are the electric current density  $\mathcal{J}$  (in amperes per square meter [A/m<sup>2</sup>]) and the volume electric charge density  $\rho$  (in coulombs per cubic meter [C/m<sup>3</sup>]).

Maxwell's equations can also be written in harmonic form, i.e., when time dependence is expressed in sinusoidal form. In this case, the fields and sources can be written as quantities of a complex nature based on the following relationship:

$$\mathcal{F}(\mathbf{r}, t) = \Re\{\mathbf{F}(\mathbf{r})e^{j\omega t}\} \quad (2.5)$$

In this way, the real vector field  $\mathcal{F}$  is completely described by the complex field  $\mathbf{F}$  and the known angular frequency  $\omega = 2\pi f$  (in radians per second [rad/s]). In (2.5),  $j = \sqrt{-1}$  is the imaginary unit. Thus, Maxwell's equations in harmonic regime are defined as:

$$\nabla \times \mathbf{E}(\mathbf{r}) = -j\omega \mathbf{B}(\mathbf{r}) \quad (2.6)$$

$$\nabla \times \mathbf{H}(\mathbf{r}) = j\omega \mathbf{D}(\mathbf{r}) + \mathbf{J}(\mathbf{r}) \quad (2.7)$$

$$\nabla \cdot \mathbf{D}(\mathbf{r}) = \rho(\mathbf{r}) \quad (2.8)$$

$$\nabla \cdot \mathbf{B}(\mathbf{r}) = 0 \quad (2.9)$$

In addition to Maxwell's equations, constitutive relationships are important for describing the relationship between fields and the environments in which they exist. In general, the relationships between field intensity and flux density vectors are expressed as:

$$\mathbf{D}(\mathbf{r}) = F_1(\mathbf{E}, \mathbf{H})(\mathbf{r}) \quad (2.10)$$

$$\mathbf{B}(\mathbf{r}) = F_2(\mathbf{E}, \mathbf{H})(\mathbf{r}) \quad (2.11)$$

The operators  $F_1$  and  $F_2$  represent the relationships between these two types of vector quantities. They are defined according to the medium in which these fields are present. Depending on the properties of each medium, these operators can be: linear or nonlinear; dependent on  $\mathbf{E}$  and  $\mathbf{H}$  or just one of these two vectors; defined as tensors or even scalars. Considering only linear, isotropic, and non-dispersive media, the constitutive relationships can be simplified to:

$$\mathbf{D}(\mathbf{r}) = \epsilon_0 \epsilon_r(\mathbf{r}) \mathbf{E}(\mathbf{r}) \quad (2.12)$$

$$\mathbf{B}(\mathbf{r}) = \mu_0 \mu_r(\mathbf{r}) \mathbf{H}(\mathbf{r}) \quad (2.13)$$

The constants  $\epsilon_0$  and  $\mu_0$  represent vacuum dielectric permittivity (in farads per meter

$[F/m]$ ) and vacuum magnetic permeability (in henries per meter  $[H/m]$ ), respectively. These constants are already known and are equivalent to  $\epsilon_0 \approx 8.854 \times 10^{-12} [F/m]$  and  $\mu_0 = 4\pi \times 10^{-7} [H/m]$ . The dimensionless quantities  $\epsilon_r$  and  $\mu_r$  represent the relative dielectric permittivity and magnetic permeability, i.e., they define the electromagnetic properties of a medium in proportion to the vacuum ones. They can be defined as functions which map their scalar value in space, either to delimit objects or to represent heterogeneities. In addition to these properties, if conductive objects are considered, the source  $\mathbf{J}$  in (2.7) must be rewritten as the sum of an impressed current  $\mathbf{J}_i$  and an induced one  $\sigma\mathbf{E}$  defined by Ohm's law, i.e.,  $\mathbf{J}(\mathbf{r}) = \mathbf{J}_i(\mathbf{r}) + \sigma(\mathbf{r})\mathbf{E}(\mathbf{r})$ . The electrical conductivity  $\sigma$  (in siemens per meter  $[S/m]$ ) is the property that describes the ability of the medium to induce current in the presence of an electric field. From this definition, (2.7) can be rewritten as:

$$\nabla \times \mathbf{H}(\mathbf{r}) = j\omega\epsilon_0\epsilon_r\mathbf{E}(\mathbf{r}) + \sigma(\mathbf{r})\mathbf{E}(\mathbf{r}) + \mathbf{J}_i(\mathbf{r}) \quad (2.14)$$

$$= j\omega\epsilon_0 \left( \epsilon_r(\mathbf{r}) - j\frac{\sigma(\mathbf{r})}{\omega\epsilon_0} \right) \mathbf{E}(\mathbf{r}) + \mathbf{J}_i(\mathbf{r}) \quad (2.15)$$

$$= j\omega\epsilon(\mathbf{r})\mathbf{E}(\mathbf{r}) + \mathbf{J}_i(\mathbf{r}) \quad (2.16)$$

The quantity  $\epsilon = \epsilon_0\epsilon_r - j\sigma/\omega$  is called effective dielectric permittivity and is a complex scalar.

## 2.2 Integral Equations

The scattering problem consists of a source  $\mathbf{J}_i(\mathbf{r})$  which propagates a wave through a medium with electromagnetic properties  $\epsilon_b$  and  $\mu_b$  and in the presence of a non-homogeneous scatter with properties  $\epsilon(\mathbf{r})$  and  $\mu(\mathbf{r})$  (Figure 2.1) (Chew, 1995). In this scenario, the equations (2.6)-(2.9) are valid for any point  $\mathbf{r}$  of space. With the aid of (2.13), the equation (2.6) can be rewritten as:

$$\nabla \times \mathbf{E}(\mathbf{r}) = -j\omega\mu(\mathbf{r})\mathbf{H}(\mathbf{r}) \quad (2.17)$$

$$\mu^{-1}(\mathbf{r})\nabla \times \mathbf{E}(\mathbf{r}) = -j\omega\mathbf{H}(\mathbf{r}) \quad (2.18)$$

If we take the curl of (2.18), we can use (2.16) to obtain an equation with only the electric field:

$$\nabla \times \mu^{-1}(\mathbf{r})\nabla \times \mathbf{E}(\mathbf{r}) = -j\omega\nabla \times \mathbf{H}(\mathbf{r}) \quad (2.19)$$

$$\nabla \times \mu^{-1}(\mathbf{r})\nabla \times \mathbf{E}(\mathbf{r}) = -j\omega(j\omega\epsilon(\mathbf{r})\mathbf{E}(\mathbf{r}) + \mathbf{J}_i(\mathbf{r})) \quad (2.20)$$

Through this, we obtain the vector wave equation:

$$\nabla \times \mu^{-1}(\mathbf{r})\nabla \times \mathbf{E}(\mathbf{r}) - \omega^2\epsilon(\mathbf{r})\mathbf{E}(\mathbf{r}) = -j\omega\mathbf{J}_i(\mathbf{r}) \quad (2.21)$$

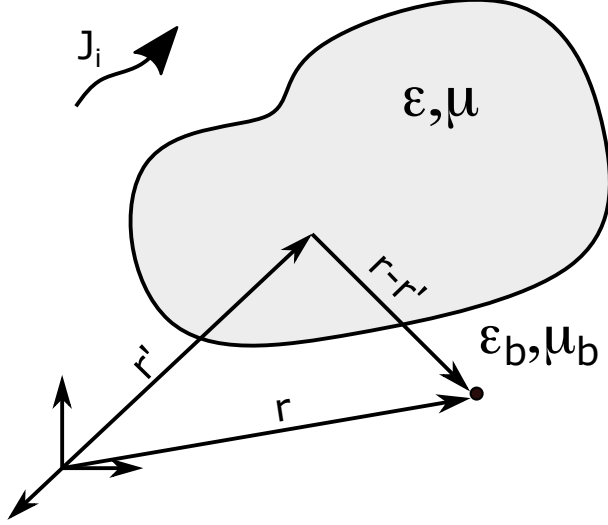


Figura 2.1: General scattering problem.

Subtracting both sides of (2.21) by  $\nabla \times \mu_b^{-1} \nabla \times \mathbf{E}(\mathbf{r}) - \omega^2 \epsilon_b \mathbf{E}(\mathbf{r})$ , one can obtain:

$$\begin{aligned} \nabla \times (\mu^{-1}(\mathbf{r}) - \mu_b^{-1}) \nabla \times \mathbf{E}(\mathbf{r}) - \omega^2 (\epsilon(\mathbf{r}) - \epsilon_b) \mathbf{E}(\mathbf{r}) \\ = -j\omega \mathbf{J}_i(\mathbf{r}) - \nabla \times \mu_b^{-1} \nabla \times \mathbf{E}(\mathbf{r}) + \omega^2 \epsilon_b \mathbf{E}(\mathbf{r}) \end{aligned} \quad (2.22)$$

$$\begin{aligned} \nabla \times \mu_b^{-1} \nabla \times \mathbf{E}(\mathbf{r}) - \omega^2 \epsilon_b \mathbf{E}(\mathbf{r}) \\ = -j\omega \mathbf{J}_i(\mathbf{r}) + \omega^2 (\epsilon(\mathbf{r}) - \epsilon_b) \mathbf{E}(\mathbf{r}) - \nabla \times (\mu^{-1}(\mathbf{r}) - \mu_b^{-1}) \nabla \times \mathbf{E}(\mathbf{r}) \end{aligned} \quad (2.23)$$

The right side of (2.23) represents the effective current source  $\mathbf{J}$ . This equation is analogous to the problem described in Apêndice C. Therefore, similarly to (C.15), the solution of (2.23) is:

$$\begin{aligned} \mathbf{E}(\mathbf{r}) = j\omega \int_V d\mathbf{r}' \bar{\mathbf{G}}(\mathbf{r}, \mathbf{r}') \cdot \mu_b \mathbf{J}(\mathbf{r}) + \omega^2 \int_V d\mathbf{r}' \bar{\mathbf{G}}(\mathbf{r}, \mathbf{r}') \cdot \mu_b (\epsilon(\mathbf{r}') - \epsilon_b) \mathbf{E}(\mathbf{r}') \\ - \int_V d\mathbf{r}' \bar{\mathbf{G}}(\mathbf{r}, \mathbf{r}') \cdot \mu_b \nabla' \times (\mu^{-1}(\mathbf{r}') - \mu_b^{-1}) \nabla' \times \mathbf{E}(\mathbf{r}') \end{aligned} \quad (2.24)$$

The first term on the right side of (2.24) is the field produced by the impressed source of the problem, which is also called the incident field  $\mathbf{E}_i(\mathbf{r})$ . The function  $\bar{\mathbf{G}}(\mathbf{r}, \mathbf{r}')$  is the Dyadic Green's Function for homogeneous medium (B.17) and it is the impulse response, i.e., the solution of the equations for a point source (see Appendix B for further information). The second term represents the field due to the displacement or conduction electric currents, while the third term represents the field due to the magnetic polarization charges. If we suppose that there are only non-magnetic materials, i.e.,  $\mu = \mu_b = \mu_0$ , then we can rewrite (2.24) as:

$$\mathbf{E}(\mathbf{r}) = \mathbf{E}_i(\mathbf{r}) + k_b^2 \int_V d\mathbf{r}' \bar{\mathbf{G}}(\mathbf{r}, \mathbf{r}') \cdot \chi(\mathbf{r}') \mathbf{E}(\mathbf{r}') \quad (2.25)$$

in which:

$$\chi(\mathbf{r}) = \frac{\epsilon_r(\mathbf{r})}{\epsilon_{rb}} - 1 - j \frac{\sigma(\mathbf{r}) - \sigma_b}{\omega \epsilon_b} \quad (2.26)$$

is called the contrast function and  $k_b = \omega \sqrt{\mu_0 \epsilon_b}$  is the background wavenumber (in meters [m]).

## 2.3 Basic Theory of Inverse Ill-Posed Problems

There is no rigorous mathematical definition of inverse problems. In fact, when someone defines a problem as the inverse counterpart of some other, this is usually arbitrary. A very known definition was written by Keller (1976) in which two problems are inverse to each other if the formulation of each involves the complete solution of the other. Also, as stated by Bertero and Boccacci (2020), the direct problem used to be the one that had been extensively studied while the inverse counterpart used to be one that was still poorly understood. From a physical perspective, for a given phenomenon, if the cause is known and we attempt to know the effect, then we are dealing with a direct or forward problem. On the other hand, if the effect is known and the cause is sought, then we are dealing with an inverse problem.

One of the reasons for inverse problems being the least attractive one is that they are often ill-posed. Hadamard (1923) defined that a mathematical model for a physical problem would be well-posed or properly posed if three conditions were guaranteed. Mathematically, let  $X$  and  $Y$  be normed spaces and  $\mathcal{K}$  a linear or nonlinear operator in which  $\mathcal{K} : X \rightarrow Y$ , the equation  $\mathcal{K}\{x\} = y$  is well-posed if (Kirsch, 2011):

1. **Existence:** for each  $y \in Y$  there is at least one  $x \in X$  in which  $\mathcal{K}\{x\} = y$ ;
2. **Uniqueness:** for each  $y \in Y$  there is at most one  $x \in X$  in which  $\mathcal{K}\{x\} = y$ ;
3. **Stability:** solution  $x$  has continuous dependence on  $y$ , i.e., for each sequence  $(x_n) \subset X$  in which  $\mathcal{K}\{x_n\} \rightarrow \mathcal{K}\{x\}$  when  $n \rightarrow \infty$ , follows  $x_n \rightarrow x$  when  $n \rightarrow \infty$ .

When a problem does not satisfy at least one of these conditions, then it is called ill-posed or improperly posed. However, when any of them is violated, it is possible to adopt some strategies so that the posedness conditions are fulfilled. For example, when there is no solution, the space of solutions can be enlarged so that the respective criterion is satisfied. When there are many solutions, then there may be a lack of information which could reduce space and ensures uniqueness. However, when the problem is not stable, then it is practically impossible to find a solution unless a new information about its form is added. As stated by Lanczos (1961), when information is lacking, there is no mathematical trickery that can fix it.

Besides, the conditions of existence and uniqueness depend only on the nature of the spaces and the operators. The stability condition also depends on whether the operator  $\mathcal{K} : X \rightarrow Y$  is surjective. Continuity of the inverse operator  $\mathcal{K}^{-1} : Y \rightarrow X$  is also relevant information. For example, an inverse operator  $\mathcal{K}^{-1}$  is automatically continuous if  $\mathcal{K}$  is linear and continuous and  $X$  and  $Y$  are Banach spaces (Teorema 9). Furthermore, if  $\mathcal{K}$  is a continuous and compact operator, the inverse problem is ill-posed unless  $X$  is of finite dimension (Colton and Kress,

2019).

The addition of information to solve ill-posed problems can be achieved through regularization strategies. In problems where  $X$  and  $Y$  are Hilbert spaces,  $\mathcal{K}$  is an operator that is linear, compact<sup>1</sup>, and one-to-one; and  $y \in Y$  is not known except for an error  $\delta > 0$  such that:

$$\|y - y^\delta\| \leq \delta \quad (2.27)$$

where  $y^\delta \in Y$ .

The equation  $\mathcal{K}\{x^\delta\} = y^\delta$  usually has no solution since  $y^\delta$  is not in the range  $\mathcal{K}(X)$  of  $X$ . So, the goal would be to determine a solution  $x^\delta \in X$  that approximates  $x \in X$ . In addition,  $x^\delta$  must depend continuously on the data  $y^\delta$ . Therefore, the objective is to construct a linear and bounded operator  $\mathcal{R}_\alpha : Y \rightarrow X$  that is an approximation of  $\mathcal{K}^{-1}$ , i.e.:

$$\lim_{\alpha \rightarrow 0} \mathcal{R}_\alpha\{y\} = x, \forall x \in X \quad (2.28)$$

In other words, the  $\mathcal{R}_\alpha\{\mathcal{K}\{\cdot\}\}$  operation is such that it converges pointwise to an identity operator. Through this definition,  $x^{\alpha,\delta} = \mathcal{R}_\alpha\{y^\delta\}$  is an approximation to the solution  $x$  of  $\mathcal{K}\{x\} = y$ . A more in-depth discussion can be found in books on functional analysis and regularization strategies (Kirsch, 2011; Lebedev et al., 1996).

## 2.4 The Eletromagnetic Inverse Scattering Problem

So far, the fundamentals for EISP have been introduced. This section presents the problem by describing several possible formulations, both in the general three-dimensional representation and in a particular two-dimensional case (Transverse Magnetic mode). In addition, discussions about important aspects of the problem are elaborated, such as the vector spaces of functions, uniqueness, stability, non-linearity, and degrees of freedom.

### 2.4.1 Formulations

The equation (2.25) describes the total electric field through the sum of an incident component and another one caused by induced currents. This latter component is called the scattered field  $\mathbf{E}_s$ . Particularly, (2.25) can be rewritten as:

$$\mathbf{E}(\mathbf{r}) = \mathbf{E}_i(\mathbf{r}) + \mathbf{E}_s(\mathbf{r}) \quad (2.29)$$

where:

$$\mathbf{E}_s(\mathbf{r}) = k_b^2 \int_V d\mathbf{r}' \bar{\mathbf{G}}(\mathbf{r}, \mathbf{r}') \cdot \chi(\mathbf{r}') \mathbf{E}(\mathbf{r}') \quad (2.30)$$

---

<sup>1</sup>In few words, the compactness of an operator means that its has infinitely small singular values accumulating at zero. A more precise definition is available at Teorema 16.

When the contrast function  $\chi$  and the incident field  $\mathbf{E}_i$  are known within a region  $V$ , the total field  $\mathbf{E}$  can be determined using equation (2.25). This problem is called the forward or direct problem and the equation (2.25) is an example of a Fredholm Integral Equation of Second Kind (Polyanin and Manzhirov, 2008). On the other hand, if the scattered field  $\mathbf{E}_s$  is known at one or a set of points  $\mathbf{r}$ , usually outside  $V$ , equation (2.30) can be used to determine  $\chi$ . We call this problem the Electromagnetic Inverse Scattering Problem (EISP). However, it is necessary to note that the total field in  $V$  is also unknown and depends on  $\chi$ . Thus, EISP is a non-linear problem.

In EISPs, equation (2.30) is called data equation, since it relates the problem data ( $\mathbf{E}_s$ ) with the unknown variables ( $\chi$  and  $\mathbf{E}$ ). This equation belongs to a class called Lippmann-Schwinger integral equations (Lippmann and Schwinger, 1950). It can be written in the form of a non-linear operator:

$$\mathbf{E}_s(\mathbf{r}) = \mathcal{L}^D \{ \chi(\mathbf{r}'), \mathbf{E}(\mathbf{r}') \}, \mathbf{r} \notin V, \mathbf{r}' \in V \quad (2.31)$$

The equation (2.25) is also used in EISPs and is known as the state equation. It is a relationship between unknown variables ( $\chi$  and  $\mathbf{E}$ ) with a known one which is a general entry for the problem ( $\mathbf{E}_i$ ). It is also possible to write (2.25) in terms of an operator:

$$\mathbf{E}_i(\mathbf{r}) = \mathbf{E}(\mathbf{r}) - \mathcal{L}^S \{ \chi(\mathbf{r}), \mathbf{E}(\mathbf{r}) \}, \mathbf{r} \in V \quad (2.32)$$

Frequently, this equation is used in situations where  $\mathbf{r} \in V$ , i.e., the  $\mathcal{L}^S$  operator can involve singularities. However, there are approaches to address singularities in this equation (see Apêndice B section B.2).

Alternatively, the EISP formulation in terms of the contrast source  $\mathbf{J}_{eq}(\mathbf{r}) = \chi(\mathbf{r})\mathbf{E}(\mathbf{r})$  is also widely found in the literature van den Berg and Kleinman (1997):

$$\mathbf{E}_s(\mathbf{r}) = k_b^2 \int_V d\mathbf{r}' \bar{\mathbf{G}}(\mathbf{r}, \mathbf{r}') \cdot \mathbf{J}_{eq}(\mathbf{r}') \quad (2.33)$$

$$\chi(\mathbf{r})\mathbf{E}_i(\mathbf{r}) = \mathbf{J}_{eq}(\mathbf{r}) - k_b^2 \chi(\mathbf{r}) \int_V d\mathbf{r}' \bar{\mathbf{G}}(\mathbf{r}, \mathbf{r}') \cdot \mathbf{J}_{eq}(\mathbf{r}') \quad (2.34)$$

The advantage of this type of formulation is that the  $\mathcal{L}^D$  and  $\mathcal{L}^S$  operators are linear. However, there are still two unknown variables in the problem ( $\chi$  and  $\mathbf{J}_{eq}$ ) that are related in a non-linear fashion in (2.34).

There are alternative forms of writing the integrals in (2.25) and (2.30) through manipulating the derivative operators of dyadic Green's function. These kinds of manipulations can be convenient to facilitate the computational implementation of integral equations. A very common manipulator is to move one of the  $\nabla$  operators within Green's function to the integral. The advantage of this technique is that it reduces the numerical quadrature error. As stated in section 4.4.1 of Chew (2009), if we consider equation (B.12), which represents the integrals in (2.25)

and (2.30), the integral can be rewritten as:

$$\begin{aligned} \int_V d\mathbf{r}' g(\mathbf{r}' - \mathbf{r}) \left[ \bar{\mathbf{I}} + \frac{\nabla' \nabla'}{k_b^2} \right] \cdot \chi(\mathbf{r}') \mathbf{E}(\mathbf{r}') &= \int_V d\mathbf{r}' g(\mathbf{r}' - \mathbf{r}) \chi(\mathbf{r}') \mathbf{E}(\mathbf{r}') \\ &+ \frac{\nabla}{k_b^2} \int_V d\mathbf{r}' g(\mathbf{r}' - \mathbf{r}) \nabla' \cdot \chi(\mathbf{r}') \mathbf{E}(\mathbf{r}') \end{aligned} \quad (2.35)$$

Alternatively, instead of the equation being written in terms of a tensor product of the  $\nabla$  operator, it can also be written in terms of a vector product. This formulation can be interesting for certain forms of discretization of the equation. As described by Chew (2009), the integral equation can be written as:

$$\boldsymbol{\epsilon}(\mathbf{r}) \mathbf{E}(\mathbf{r}) = \mathbf{E}_i(\mathbf{r}) - \nabla \times \int_V d\mathbf{r}' g(\mathbf{r}' - \mathbf{r}) \nabla' \times \chi(\mathbf{r}') \mathbf{E}(\mathbf{r}') \quad (2.36)$$

$$\mathbf{J}_{eq}(\mathbf{r}) = p(\mathbf{r}) \mathbf{E}_i(\mathbf{r}) + p(\mathbf{r}) \left( k_b^2 \int_V d\mathbf{r}' \bar{\mathbf{G}}(\mathbf{r}, \mathbf{r}') \cdot \mathbf{J}_{eq}(\mathbf{r}') - \mathbf{f}_d(\mathbf{r}) \cdot \bar{\mathbf{I}} \right) \quad (2.37)$$

Recently, a new formulation has received the attention of the literature. Taking into account (2.34), Zhong et al. (2016) proposed to multiply both sides by a function  $\beta(\mathbf{r}) [\beta(\mathbf{r}) \chi(\mathbf{r}) + 1]^{-1}$  to obtain:

$$\beta(\mathbf{r}) \mathbf{J}_{eq}(\mathbf{r}) = R(\mathbf{r}) \beta(\mathbf{r}) \mathbf{J}_{eq}(\mathbf{r}) + R(\mathbf{r}) \left[ \mathbf{E}_i(\mathbf{r}) + k_b^2 \int_V d\mathbf{r}' \bar{\mathbf{G}}(\mathbf{r}, \mathbf{r}') \cdot \mathbf{J}_{eq}(\mathbf{r}') \right] \quad (2.38)$$

where  $R(\mathbf{r}) = \beta(\mathbf{r}) \chi(\mathbf{r}) [\beta(\mathbf{r}) \chi(\mathbf{r}) + 1]^{-1}$  is a modified contrast function which must respect the condition  $\beta(\mathbf{r}) \chi(\mathbf{r}) + 1 \neq 0$ . This formulation is based on the Contracted Integral Equation (Hursán and Zhdanov, 2002; Pankratov et al., 1995) which is generally used to solve the forward problem. The  $\beta$  function is chosen arbitrarily so that (2.38) represents a family of integral equations, which aggregates other formulations in the literature such as the Contrast Source-Extended Born integral equation (Catapano et al., 2007a; D'Urso et al., 2010; Isernia et al., 2004). The main differences between (2.38) and (2.34) are (i) the term  $R(\mathbf{r}) \beta(\mathbf{r}) \mathbf{J}_{eq}(\mathbf{r})$  is a term of local effect while  $\mathbf{J}_{eq}$  is of global one; (ii) through an appropriate choice of  $\beta(\mathbf{r})$  it is possible to make local wave effects dominate over global ones, which is very important for problems with strong scatterers<sup>2</sup> which increase the non-linearity of the problem through multi-scattering effects. However, the optimal choice of  $\beta(\mathbf{r})$  is still an open problem, as stated by the authors. They defined  $\beta(\mathbf{r})$  as a constant function and, in addition, other studies followed the same strategy, such as (Zhong et al., 2020).

---

<sup>2</sup>Strong scatterers are objects whose contrast-size ratio is such that the non-linear condition of the problem becomes more intense. For example, high-contrast objects can be addressed with some efficiency if their size, proportional to the wavelength, is small enough. After a certain size, the inverse problem becomes harder to be solved. This subject will also be discussed in the following sections and chapters.

### 2.4.2 The Two-Dimensional Problem

If it is possible to assume that the object to be reconstructed can be approximated by an infinite cylinder on the  $z$  axis, then (2.25) can be rewritten as a two-dimensional problem, i.e., where the quantities vary only in the  $x$  and  $y$  coordinates of the Cartesian space (Figure 2.2). In addition, if we assume a magnetic transverse problem in  $z$  (TM $_z$ ), the electric field vectors will be reduced to just their  $z$  component. Thus, if we define  $\rho = xx + yy$  and denote  $S$  a cross section area in  $V$ , then equation (2.30) can be rewritten as:

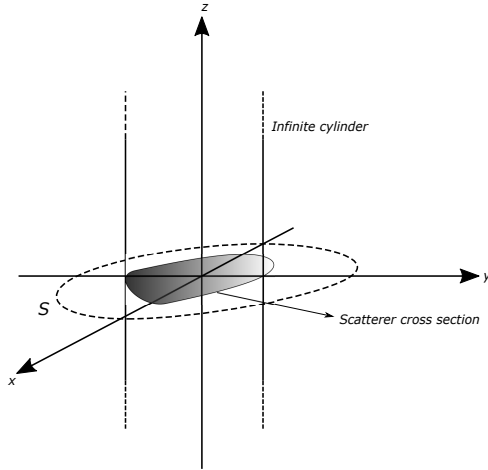


Figura 2.2: Infinite cylinder with inhomogeneous cross section.

$$E_{s_z}(\rho)\mathbf{z} = k_b^2 \int_S \int_{-\infty}^{\infty} dz' d\rho' \bar{\mathbf{G}}(\mathbf{r}, \mathbf{r}') \cdot \chi(\rho') E_z(\rho') \mathbf{z} \quad (2.39)$$

$$= k_b^2 \int_S d\rho' \left[ \int_{-\infty}^{\infty} dz' \left( \bar{\mathbf{I}} + \frac{\nabla \nabla}{k_b^2} \right) \frac{e^{jk_b |\mathbf{r} - \mathbf{r}'|}}{4\pi |\mathbf{r} - \mathbf{r}'|} \right] \cdot \chi(\rho') E_z(\rho') \mathbf{z} \quad (2.40)$$

The integral over  $z$  on the right side of equation (2.40) is known (Balanis, 2012):

$$\int_{-\infty}^{\infty} dz' \left( \bar{\mathbf{I}} + \frac{\nabla \nabla}{k_b^2} \right) \frac{e^{jk_b |\mathbf{r} - \mathbf{r}'|}}{4\pi |\mathbf{r} - \mathbf{r}'|} = \frac{j}{4} H_0^{(2)}(k_b |\rho - \rho'|) \quad (2.41)$$

where  $H_0^{(2)}$  is the Hankel function of the second kind. Thus, (2.40) can be rewritten as:

$$E_{s_z}(\rho) = -\frac{jk_b^2}{4} \int_S dS' H_0^{(2)}(k_b |\rho - \rho'|) \chi(\rho') E_z(\rho') \quad (2.42)$$

Similarly, equations (2.25), (2.33), (2.34), and (2.38) can be rewritten as:

$$E_z(\boldsymbol{\rho}) = E_{zi}(\boldsymbol{\rho}) - \frac{jk_b^2}{4} \int_S dS' H_0^{(2)}(k_b |\boldsymbol{\rho} - \boldsymbol{\rho}'|) \chi(\boldsymbol{\rho}') E_z(\boldsymbol{\rho}') \quad (2.43)$$

$$E_{sz}(\boldsymbol{\rho}) = -\frac{jk_b^2}{4} \int_S dS' H_0^{(2)}(k_b |\boldsymbol{\rho} - \boldsymbol{\rho}'|) J_{zeq}(\boldsymbol{\rho}') \quad (2.44)$$

$$\chi(\boldsymbol{\rho}) E_{zi}(\boldsymbol{\rho}) = J_{zeq}(\boldsymbol{\rho}) + \frac{jk_b^2}{4} \chi(\boldsymbol{\rho}) \int_S dS' H_0^{(2)}(k_b |\boldsymbol{\rho} - \boldsymbol{\rho}'|) J_{zeq}(\boldsymbol{\rho}') \quad (2.45)$$

$$\begin{aligned} \beta(\boldsymbol{\rho}) J_{zeq}(\boldsymbol{\rho}) &= R(\boldsymbol{\rho}) \beta(\boldsymbol{\rho}) J_{zeq}(\boldsymbol{\rho}) \\ &\quad + R(\boldsymbol{\rho}) \left[ E_{zi}(\boldsymbol{\rho}) - \frac{jk_b^2}{4} \int_S dS' H_0^{(2)}(k_b |\boldsymbol{\rho} - \boldsymbol{\rho}'|) J_{zeq}(\boldsymbol{\rho}') \right] \end{aligned} \quad (2.46)$$

Recently, Bevacqua and Isernia (2021a) proposed to decompose the Hankel function in two terms using the known identity  $H_0^{(2)}(x) = J_0(x) + Y_0$ , where the  $Y_0$  is the zero order Bessel function of second kind. Then, (2.35) might be rewritten as:

$$\begin{aligned} \chi(\boldsymbol{\rho}) E_{zi}(\boldsymbol{\rho}) &= J_{zeq}(\boldsymbol{\rho}) + \frac{jk_b^2}{4} \chi(\boldsymbol{\rho}) \int_S dS' J_0(k_b |\boldsymbol{\rho} - \boldsymbol{\rho}'|) J_{zeq}(\boldsymbol{\rho}') \\ &\quad + \frac{jk_b^2}{4} \chi(\boldsymbol{\rho}) \int_S dS' Y_0(k_b |\boldsymbol{\rho} - \boldsymbol{\rho}'|) J_{zeq}(\boldsymbol{\rho}') \end{aligned} \quad (2.47)$$

The first advantage in (2.47) is that the first integral, which does not exhibit singularity, can be easily computed from the available scattered field data. Its meaning is the contribution of main spectral component of the radiating currents to the total field in  $S$ . The second advantage is the potential to mitigate the nonlinearity condition of the problem (see Subsection 2.4.4 for more information). The authors also provides a straightforward procedure to compute the first integral and a discretization formula to address the second integral.

### 2.4.3 Vector spaces and operator properties

The  $\chi(\mathbf{r})$  function is continuous by parts since it represents the dielectric properties of the media. Therefore,  $\chi$  is an integrable and differentiable function except at the interface between media. The function which represents the total electric field, in three-dimensional problems, may have discontinuities in its components due to interface conditions. However, this does not happen in two-dimensional problems, since the  $E_z$  component is always perpendicular to the normal defined on the interface between the media. Either way, the field is always integrable and differentiable. This is also true for the scattered field. However, it is generally measured in a homogeneous media, i.e., it does not usually involve discontinuities.

Taking into account (2.33), the set of all scattered fields can be defined in terms of a linear space of analytical functions with exponential growth at infinity and regular within a subdomain of the measurement region  $D$ , which is external to the scatterer domain (Bucci and Franceschetti, 1989). These functions are uniformly bounded in this subdomain since the equi-

valent current  $\mathbf{J}_{eq}$  is uniformly bounded. In other words, since the kernel of (2.33) is analytical (except at singularities), this operator is compact, and therefore, the image of any bounded set is pre-compact (Bucci and Franceschetti, 1989). It is also possible to reach the same conclusions if we assume that the total field within the scatterer is uniformly bounded, provided we equip the defined  $\chi$  space with the  $L^\infty$  norm and the  $\mathbf{E}$  space with the  $L^2$  norm. This is consistent since the contrast and the incident field are limited. Consequently, the equivalent current also belongs to a bounded set and the scattered field belongs to a pre-compact one. Furthermore, since the inverse operator of a compact one cannot be continuous, then the inverse problem is ill-posed.

#### 2.4.4 Uniqueness, Stability and Nonlinearity

As discussed in Section 2.3, three criteria need to be satisfied for a problem to be considered well-posed. EISP is ill-posed because it does not meet the stability criterion. The condition of uniqueness is considered only in some theoretical analyzes, i.e., in practical situations, the problem does not usually have a single solution. In addition, the problem is non-linear, which provides other aspects to the problem.

As demonstrated by Colton and Päiväranta (1992), the uniqueness of the relative permittivity for a given distant field pattern is guaranteed under certain conditions, among them: a fixed number of wavenumber, all directions of incidence, and all polarizations of the field incident. Therefore, the existence condition is also fulfilled. However, in practical situations, all of this information is not always available. It is also worth noting that there are situations for which uniqueness is not guaranteed from an analytical point of view, such as, problems in which permittivity and permeability can be zero or infinite.

Even if a sufficient amount of information is available for uniqueness, the relationship between known and unknown variables is not continuous (Chen, 2017). As already demonstrated in the literature (Caro, 2010; Stefanov, 1990), for a problem involving dielectric scatterers, if the error in the known data is at most  $\delta$ , then the worst scenario of the error in the solution is in the order of  $\ln|\delta|^{-s}$ , where  $0 < s < 1$ . This is known as a problem stability estimate and, when  $\delta \rightarrow 0$ , by the L'Hôpital rule, the error order increases dramatically. This type of situation is known in the literature as an exponential or severely ill-posed problem. This type of condition cannot change if we have infinite field measurements. However, stability can increase with some strategies, such as, for example, increasing operating frequencies (Bao et al., 2015; Isakov et al., 2016; Nagayasu et al., 2013).

As stated earlier, the relationship between contrast and scattered field is not linear since there are mutual interactions between induced currents. Therefore, we cannot interpret the field as a linear superposition of individual responses. Besides, the nonlinearity of the problem is not of the convex kind, i.e., from the optimization point of view, there may be multiple local minima which can cause algorithms to get trapped in false solutions (Bucci and Isernia, 1997; Chen, 2017). Therefore, finding the exact solution becomes more complex.

A deeper explanation on non-linearity is found in Bucci et al. (2001). The authors developed the Degree of Nonlinearity (DNL) which is indicator to how difficult is solving the correspond EISP. Considering the state equation in the operator (2.32), the total field  $E_z$  may be rewritten as:

$$\mathbf{E}_z(\mathbf{r}) = \left( \mathcal{I} - \mathcal{L}^S \{\chi(\mathbf{r})\} \right)^{-1} \mathbf{E}_i(\mathbf{r}) \quad (2.48)$$

where  $\mathcal{I}$  is the identity operator and

$$\mathcal{L}^S \{\chi(\mathbf{r})\} = -k_b^2 \int_V d\mathbf{r}' \bar{\mathbf{G}}(\mathbf{r}, \mathbf{r}') \cdot \chi(\mathbf{r}').$$

When the  $L^2$ -norm over  $\mathcal{L}^S \{\chi(\mathbf{r})\}$  is lower than 1, the inverse operator is approximated by Neumann series, i.e.:

$$\left( \mathcal{I} - \mathcal{L}^S \{\chi(\mathbf{r})\} \right)^{-1} = \mathcal{I} + \mathcal{L}^S \{\chi(\mathbf{r})\} + \left( \mathcal{L}^S \{\chi(\mathbf{r})\} \right)^2 + \cdots + \left( \mathcal{L}^S \{\chi(\mathbf{r})\} \right)^n + \cdots \quad (2.49)$$

Then, Bucci et al. (2001) defined DNL indicator as  $\|\mathcal{L}^S \{\chi(\mathbf{r})\}\|_{L^2}$ . They observed that, the smaller than 1 DNL is, the stronger linear approximation is. As DNL tends to 1, a polynomial relation holds true between data and unknowns. The larger the order of polynomial is, the larger the number of local minima. When DNL is greater than 1, then a non-polynomial relation holds true. Therefore, the larger the DNL, the larger overall difficulty of the problem due its nonlinearity. In these cases, the possible number of local minima in respect to some cost functional can be higher, which increases the difficulty of finding the global minimum that defines the solution of the inverse problem. Moreover, the indicator is also applied to the two-dimensional case (2.43), the Contrast Source Integral Equation (2.45), its Extended-Born version (2.46), and when the Green's function is decomposed (Bevacqua and Isernia, 2021a; D'Urso et al., 2010). In D'Urso et al. (2010), the authors provide criteria for choosing between (2.45) and (2.46). In Bevacqua and Isernia (2021a), the authors show that the Green's Function Decomposition formulation has a much lower growth of DNL than the traditional Contrast Source Integral (2.45) when the scatterer size increases. Bevacqua and Isernia (2021c) showed that, for certain configurations of scatterers and values of  $\beta$  in (2.38), the DNL can be drastically reduced (mainly when  $\beta \geq 2$ ). The authors also showed significant reductions in the degree of non-linearity when the YO (2.47) and NIE (2.38) formulations are combined (Bevacqua and Isernia, 2021b). For  $\beta = 6$ , the results showed less DNL growth as the scatterer grew when compared to the other formulations.

## 2.4.5 Degrees of Freedom

From an analytical point of view, two fields are distinguishable when their definitions are distinct from each other. However, when these physical quantities differ very little from each other, they can be indistinguishable in practice. Many factors can contribute to the impossibility

of distinguishing fields, such as, for example, noise, dynamics of measurement mechanisms, precision, and numerical errors. Based on the definition of the concept of distinction, it is possible to define different states of the system, and with that, the notion of a minimum number of independent parameters that can describe the system to a certain precision. This issue plays an important role in EISPs since scattered fields that are considered indistinguishable will have identical reconstructions which will not always represent the investigated media well.

In the first work on the subject, Bucci and Franceschetti (1989) showed that the number of Degrees of Freedom (DoF) in a scattered field is essentially equal to the Nyquist number defined in proportion to the dimensions of the source and observation regions. In particular, the Nyquist  $N_0$  number was defined as:

$$N_0 = \frac{2SW_0}{\pi} \approx \frac{2Ska}{\pi} \quad (2.50)$$

where  $S$  is half the length of the observation domain,  $W_0$  is the signal bandwidth,  $k$  is the source wavenumber and  $a$  is the maximum radius of the domain that the scatterers occupy. This, then, would be the minimum number of parameters (information) necessary to represent the spread field with a certain precision. The authors also concluded that a sample interpolation at equidistant points would be a practically optimal reconstruction of the scattered field.

Subsequently, Bucci and Isernia (1997) evaluated the dimension of the data space which is consistent with a certain contrast space configuration. Their analysis is based on the fact that only a finite-dimensional representation of the contrast can be reconstructed. This assessment was made for both single and multiple cases. In the case of simple incidence, the authors realized that the relationship between amount and value of kernel eigenvalues in (2.33) behaves similarly to the step function, i.e., as the number of eigenvalues grows, their values fall sharply from a certain threshold. Also, the larger the scatterer, the more sudden the fall. This behavior is also observed when we consider the approximation error, which allows us to identify the number of degrees of freedom by the number of eigenvalues for which the approximation error exceeds a certain established threshold. For spherical sources and spherical (concentric) observation surfaces, if  $k_b a \gg 1$ , then DoF is approximated by:

$$DoF \approx (ka)^2 \quad (2.51)$$

In a two-dimensional case of concentric circles for circular sources:

$$DoF \approx 2ka \quad (2.52)$$

Considering multiple incidences, the authors stated that the number of independent parameters must not be greater than  $DoF^2/2$ , where  $DoF$  is the number of degrees of freedom for simple incidence. In their experiments, the authors did not observe a significant difference between a  $32 \times 32$  and a  $36 \times 36$  scattered matrices, considering a low contrast circular object

with a diameter of  $5\lambda_b$  ( $DoF \approx 32$ ).

Chew et al. (1994) also discussed this issue. Firstly, they demonstrated why solving (2.33) for  $\mathbf{J}_{eq}$  and evaluating  $\mathbf{E}$  and  $\chi$  through (2.25) and  $\mathbf{J}_{eq}/\mathbf{E}$ , respectively, is not an adequate approach. Although it seems attractive since there is no iteration process, the solution in practical situations is not unique, as discussed in Subsection 2.4.4. One of the solutions is due to non-radiating sources which are also inverse solutions to the Green's function. The non-radiating solution is due to the non-trivial null space in (2.33), i.e., there is a non-trivial solution for  $\mathbf{E}_s = \mathbf{0}$ . Consequently, if a unique solution to (2.33) is obtained (e.g., minimum norm solution through pseudo-inverse method (Ney et al., 1984)), the null space solution is eliminated. Even though, it does not contribute to the scattered field, it does contribute to the total field within the scatterer. Therefore, without the null space solution, the total field obtained by the application of  $\chi\mathbf{E} = \mathbf{J}_{eq}$  in (2.25) and the following contrast function estimation by  $\mathbf{J}_{eq}/\mathbf{E}$  will not be correct.

Second, the authors stated that a very large number of measurements will not make the null space smaller, which agrees with Bucci and Franceschetti (1989) and Bucci and Isernia (1997). In addition, the difference in the dimensionality between the measurement and image domains is also a practical obstacle for raising the number of measurements. The authors called the growth of linear dependency as the number of measurements increases as the *law of diminishing return*. Their explanation is based on the high-spatial-components of the induced current which generates evanescent waves that decay fast away from the scatterer and are very small at the measurement space. The decay is also related to the nature of the Green's function which can be compared to a low-pass filter. These components also contributes to the null space. Through the Fourier analysis of the scattered field, the authors came to the same conclusion as Bucci and Franceschetti (1989) about the Nyquist number as upper bound of sampling rate.

Finally, some efforts have been made towards a numerical approach for computing DoF. Lin et al. (2021) proposed to modify the Green function taking into account the maximum contrast value and evaluate DoF based on the singular values of the Green function. When the maximum contrast is not available, then it is assumed that the contrast tends to infinity and a new modification for the Green function is formulated.

## 2.5 Conclusion

This chapter presented a brief discussion of the theoretical aspects of EISP. Section 2.1 introduced the physical quantities and their most basic relations taking into account a model with linear, isotropic, non-dispersive, and non-magnetic materials. Section 2.2 presented the development of the integral equation (2.25) that is the basis for the problem.

Based on the definition proposed by Hadamard (1923), Section 2.3 discussed what is an ill-posed inverse problem through the criteria of existence, uniqueness, and stability of the solution. The section also presented the general formulation of regularization operators using

equation (2.28).

Section 2.4 defined the electromagnetic inverse scattering problem by presenting three-dimensional formulations through equations (2.30), (2.33)-(2.38); and the two-dimensional formulations based on the TM<sub>z</sub> mode described through equations (2.42)-(2.46). Besides, the properties of the vector spaces and operators were discussed. It has also been shown that the problem can have a unique solution in some situations which are hardly possible in practice. Nevertheless, even when there is a unique solution, the problem is still ill-posed for reasons of instability whose explanation can be demonstrated through the theory of inverse operators of compact ones. Furthermore, instability can be quantified through the worst-case estimate which is exponential for the problem. In addition to these factors that contribute to the complexity of the problem, non-convex non-linearity is an important feature that can cause optimization algorithms to be trapped in local minima which may represent spurious images. Finally, the degrees of freedom of the problem were defined using (2.52), which is an important measure for determining the necessary amount of observations of the scattered field considering a given configuration of the problem.

# Capítulo 3

## Methods Overview

Since the inverse problem is ill-posed and nonlinear, analytical approaches are usually not considered. Due to such complexity numerical approaches are necessary to obtain a solution. This chapter aims to provide a comprehensive review of the various methods and techniques used to address the inverse problem.

Section 3.1 presents a general overview of the problem domain, followed by a discussion on the different approaches to discretization of the equations for the two-dimensional problem in Section 3.2. In Section 3.3, methodologies for a linear approach to the problem are presented. Regularization methods, which are used after linearization of the integral equation, are discussed in Section 3.4.

Section 3.5 focuses on qualitative methods, which are used when only the shape of the scatterers needs to be recovered. The two classes of quantitative methods are presented in the subsequent sections, i.e., deterministic methods in Section 3.6 and stochastic methods in Section 3.7. These sections provide a bibliographic review of the main methods, strategies, and ideas proposed in the literature.

The chapter also emphasizes the application of Deep-Learning methods, which has recently gained significant attention in the literature, as discussed in Section 3.8. Lastly, a brief conclusion is presented in Section 3.9 to summarize the main points covered in the chapter.

### 3.1 Domain Definition

All the research conducted in this work will presuppose a two-dimensional TMz problem with linear, isotropic, non-dispersive and non-magnetic materials. Therefore, (2.42)-(2.46) will be the equations that will describe the relationships between fields, source and medium. However, before entering the methodologies, it is necessary to adequately define the problem domain, i.e., the geometry of the spaces where all variables and constants are defined. These definitions will be the foundation for all the methodologies described in this work.

Figura 3.1 describes the geometry of the problem. The scattered field  $E_{z_s}$  is defined over

a circle centred on the origin of the Cartesian axes whose radius is denoted by  $R_O$ , and the angle, by  $\theta$ . This circle is immersed in a homogeneous medium characterized by the electromagnetic properties  $\varepsilon_b$ ,  $\sigma_b$ , and  $\mu_b$ . The vector  $\boldsymbol{\rho}$  in (2.42)-(2.46) can be written as:

$$\boldsymbol{\rho} = R_O \cos \theta \mathbf{x} + R_O \sin \theta \mathbf{y} \quad (3.1)$$

The state-space  $S$  is the rectangular region centred at the origin on the axis of coordinate whose lengths are equal to  $L_X$  and  $L_Y$ . This region represents the image to be reconstructed. Therefore, the variables  $E_z$ ,  $\varepsilon_r$ , and  $\sigma$  are defined within them. The last two are related to the contrast function  $\chi$  through (2.26).

Finally, the incident field  $E_{i_z}$  will be represented by a plane wave known throughout the problem space. The amplitude of this wave will be denoted by  $E_0$ , while its incidence angle concerning the Cartesian axis will be denoted by  $\phi$ . Therefore, the incident field can be written as:

$$E_{i_z}(\boldsymbol{\rho}) = E_0 e^{-j\mathbf{k}_b \cdot \boldsymbol{\rho}} \quad (3.2)$$

where  $\mathbf{k}_b = |k_b| \cos \phi \mathbf{x} + |k_b| \sin \phi \mathbf{y}$  is the wavenumber vector. Other forms of incident waves are possible and compatible with the methodology described throughout this chapter.

Data-space  $D$  will be defined as a two-dimensional domain as follows:

$$D := \{(\theta, \phi) : \theta, \phi \in [0, 2\pi]\} \quad (3.3)$$

Therefore,  $D$  is a region that relates the angles in which the scattered field is defined and those of incidence. The scattered field varies according to  $\theta$  and according to the angle of

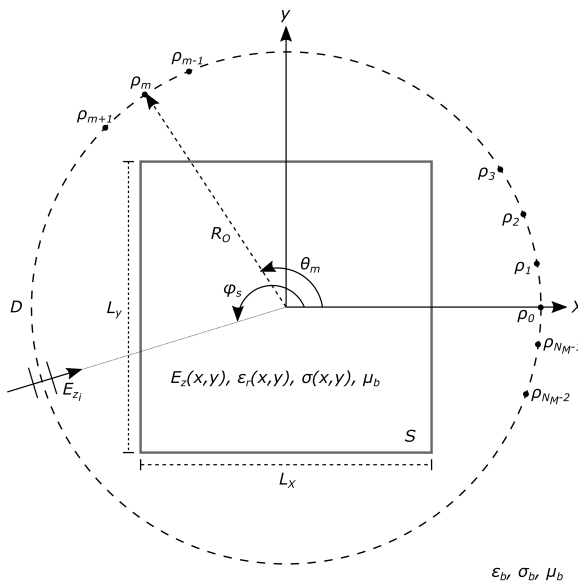


Figura 3.1: Problem geometry.

incidence ( $\phi$ ) since the field scattered is the result of the interaction of the incident field with the scattering object. So, from now on, we will say that  $E_{z_s}$  is a function defined in the  $D$  domain, i.e.,  $E_{z_s}(\theta, \phi)$ . This definition would also be possible with incident waves due to infinitesimal impressed sources in a circular arrangement.

From those definitions, (2.42)-(2.46) will be rewritten as:

$$E_{s_z}(\theta, \phi) = -\frac{jk_b^2}{4} \int_S dx dy G_{2D}^D(\theta, x, y) \chi(x, y) E_z(\phi, x, y) \quad (3.4)$$

$$\begin{aligned} E_z(\phi, x, y) &= E_{z_i}(\phi, x, y) \\ &\quad - \frac{jk_b^2}{4} \int_S dx' dy' G_{2D}^S(x, y, x', y') \chi(x', y') E_z(\phi, x', y') \end{aligned} \quad (3.5)$$

$$E_{s_z}(\theta, \phi) = -\frac{jk_b^2}{4} \int_S dx dy G_{2D}^D(\theta, x, y) J_{z_{eq}}(\phi, x, y) \quad (3.6)$$

$$\begin{aligned} \chi(x, y) E_{z_i}(\phi, x, y) &= J_{z_{eq}}(\phi, x, y) \\ &\quad + \frac{jk_b^2}{4} \chi(x, y) \int_S dx' dy' G_{2D}^S(x, y, x', y') J_{z_{eq}}(\phi, x', y') \end{aligned} \quad (3.7)$$

$$\begin{aligned} \beta(x, y) J_{z_{eq}}(\phi, x, y) &= R(x, y) \beta(x, y) J_{z_{eq}}(\phi, x, y) + R(x, y) \left[ E_{z_i}(\phi, x, y) \right. \\ &\quad \left. - \frac{jk_b^2}{4} \int_S dx' dy' G_{2D}^S(x, y, x', y') J_{z_{eq}}(\phi, x', y') \right] \end{aligned} \quad (3.8)$$

where<sup>1</sup>

$$G_{2D}^D(\theta, x, y) = H_0^{(2)}(k_b \sqrt{(R_O \cos \theta - x)^2 + (R_O \sin \theta - y)^2}) \quad (3.9)$$

$$G_{2D}^S(x, y, x', y') = H_0^{(2)}(k_b \sqrt{(x - x')^2 + (y - y')^2}) \quad (3.10)$$

The choice for such geometry is to be as simple as possible since the intention is to avoid any influence that any specific characteristic can perform. The advantage is that it is simpler for the definition of classical discretization formulas. On the other hand, it may not represent most of the real problems. However, this is not the goal of the thesis.

## 3.2 Discretization

In practical situations, the scattered field  $E_{z_s}$  is known only at a set of points in  $D$ . Furthermore, it is necessary to adopt some discretization to solve (3.4)-(3.8) numerically. In the context of numerical methods for differential equations, the discretization is made either from

---

<sup>1</sup>The reader should have noticed that, unlike other works in the literature (Chen, 2017), we will use the letter  $D$  for the region of the scattered field and the letter  $S$  for the image region. It is a choice made so that the  $G_{2D}$  superscript indicates whether the equation is data or state.

the weak or from the strong forms of the equations (Liu, 2009). An example of a methodology based on the strong form is the Finite Difference Method, where the derivatives are approximated by differences between finite nodal values (Taflove and Hagness, 2005; Yee, 1966). Regarding the weak one, there is a class of methods based on weighting the residuals of the equations. It is called the Method of Weighted Residuals (MWR) (Fletcher, 1984). In these methods, for a given differential equation:

$$\mathcal{K}\{u\} = 0 \quad (3.11)$$

the approximate solution  $u_a$  is written as follows:

$$u_a(\mathbf{r}) = u_0(\mathbf{r}) + \sum_{j=1}^N a_j \psi_j(\mathbf{r}) \quad (3.12)$$

where  $u_0$  is a function that satisfies the boundary conditions,  $a_j$  is an unknown constant, and  $\psi$  are analytical functions usually called trial functions. The residual function  $R_{u_a}$  is defined in terms of the application of this approximate solution in (3.11), i.e.:

$$\mathcal{K}\{u_a\} = R_{u_a} \quad (3.13)$$

Hence, MWR is based on determining the coefficients  $a_j$ 's by solving the set of equations:

$$\langle R_{u_a}, w_k(\mathbf{r}) \rangle = 0, k = 1, \dots, N \quad (3.14)$$

where  $w_k$ 's are analytical functions known as weight functions or test functions. These functions must be independent of each other. Furthermore, if they are part of a base, when  $N$  tends to infinity, this is equivalent to saying that  $R_{u_a}$  must be orthogonal for each member of the base functions. However, this also implies that  $R_{u_a}$  converges to zero on average.

Similarly, we can apply MWR to integral equations such as (3.4). Considering a nonlinear problem, where  $E_z$  and  $\chi$  are unknown, the following approximations will be made:

$$\chi(x, y) \approx \sum_{i=1}^{N_I} \sum_{j=1}^{N_J} a_{ij} f_i^{(x)}(x) f_j^{(y)}(y) \quad (3.15)$$

$$E_z(\phi, x, y) \approx \sum_{p=1}^{N_P} \sum_{q=1}^{N_Q} \sum_{r=1}^{N_R} b_{pqr} g_p^{(x)}(x) g_q^{(y)}(y) g_r^{(\phi)}(\phi) \quad (3.16)$$

The functions  $f^{(x)}$ ,  $f^{(y)}$ ,  $g^{(x)}$ ,  $g^{(y)}$  and  $g^{(\phi)}$  are the trial functions while the coefficients  $a$  and  $b$  are unknown. They can be defined everywhere in  $S$  or even locally, i.e., some portions of the state space. It should be noted that we are choosing the trial function formulation  $f(x, y) = f^{(x)}(x) f^{(y)}(y)$ , but other formulations are possible. Our choice is due our previous experience with this kind of formulation. From these definitions, we can write the following set

of equations:

$$\begin{aligned} \iint_D E_{z_s}(\theta, \phi) w_u^{(\theta)}(\theta) w_v^{(\phi)}(\phi) d\theta d\phi = \\ -\frac{jk_b^2}{4} \sum_{i=1}^{N_I} \sum_{j=1}^{N_J} \sum_{p=1}^{N_P} \sum_{q=1}^{N_Q} \sum_{r=1}^{N_R} a_{ij} b_{pqr} \iint_D \iint_S d\theta d\phi dx dy \left[ G_{2D}^D(\theta, x, y) \right. \\ \left. f_i^{(x)}(x) f_j^{(y)}(y) g_p^{(x)}(x) g_q^{(y)}(y) g_r^{(\phi)}(\phi) w_u^{(\theta)}(\theta) w_v^{(\phi)}(\phi) \right], \\ u = 1, \dots, N_U, v = 1, \dots, N_V \quad (3.17) \end{aligned}$$

where  $w^{(\theta)}$  and  $w^{(\phi)}$  are the chosen weight functions. These integrals can be rearranged as follows:

$$\begin{aligned} \int_0^{2\pi} \int_0^{2\pi} E_{z_s}(\theta, \phi) w_u^{(\theta)}(\theta) w_v^{(\phi)}(\phi) d\theta d\phi = -\frac{jk_b^2}{4} \sum_{i=1}^{N_I} \sum_{j=1}^{N_J} \sum_{p=1}^{N_P} \sum_{q=1}^{N_Q} \sum_{r=1}^{N_R} a_{ij} b_{pqr} \int_0^{2\pi} d\phi \left[ g_r^{(\phi)}(\phi) w_v^{(\phi)}(\phi) \right. \\ \left. \cdot \int_{-L_X/2}^{L_X/2} dx f_i^{(x)}(x) g_p^{(x)}(x) \left[ \int_{-L_Y/2}^{L_Y/2} dy f_j^{(y)}(y) g_q^{(y)}(y) \left[ \int_0^{2\pi} d\theta G_{2D}^D(\theta, x, y) w_u^{(\theta)}(\theta) \right] \right] \right], \\ u = 1, \dots, N_U, v = 1, \dots, N_V \quad (3.18) \end{aligned}$$

As is evident, the integral on  $\phi$  on the right-hand side of (3.18) can be separated from the others. Each integral results in a scalar. Therefore, each equation in (3.18) can be rewritten as a sum of coefficients:

$$\Lambda_{uv} = \sum_{i=1}^{N_I} \sum_{j=1}^{N_J} \sum_{p=1}^{N_P} \sum_{q=1}^{N_Q} \sum_{r=1}^{N_R} a_{ij} b_{pqr} \Phi_{vr} \Omega_{uijpq} \quad (3.19)$$

in which:

$$\Lambda_{uv} = \int_0^{2\pi} \int_0^{2\pi} E_{z_s}(\theta, \phi) w_u^{(\theta)}(\theta) w_v^{(\phi)}(\phi) d\theta d\phi \quad (3.20)$$

$$\Phi_{rv} = \int_0^{2\pi} d\phi g_r^{(\phi)}(\phi) w_v^{(\phi)}(\phi) \quad (3.21)$$

$$\begin{aligned} \Omega_{uijpq} = -\frac{jk_b^2}{4} \int_{-L_X/2}^{L_X/2} dx f_i^{(x)}(x) g_p^{(x)}(x) \left[ \int_{-L_Y/2}^{L_Y/2} dy f_j^{(y)}(y) g_q^{(y)}(y) \left[ \int_0^{2\pi} d\theta G_{2D}^D(\theta, x, y) w_u^{(\theta)}(\theta) \right] \right] \quad (3.22) \end{aligned}$$

It is also possible to write (3.19) in a matrix form:

$$\bar{\Lambda} = \bar{\Omega} \bar{\Psi} \bar{\Phi} \quad (3.23)$$

where:

$$\bar{\Lambda} = \begin{bmatrix} \Lambda_{11} & \Lambda_{12} & \cdots & \Lambda_{1N_V} \\ \Lambda_{21} & \Lambda_{22} & \cdots & \Lambda_{2N_V} \\ \vdots & \vdots & \vdots & \vdots \\ \Lambda_{u1} & \Lambda_{u2} & \cdots & \Lambda_{uN_V} \\ \vdots & \vdots & \vdots & \vdots \\ \Lambda_{N_U 1} & \Lambda_{N_U 2} & \cdots & \Lambda_{N_U N_V} \end{bmatrix} \quad (3.24)$$

$$\bar{\Omega} = \begin{bmatrix} \Omega_{11111} & \Omega_{11112} & \cdots & \Omega_{1N_I N_J N_P N_Q} \\ \Omega_{21111} & \Omega_{21112} & \cdots & \Omega_{2N_I N_J N_P N_Q} \\ \vdots & \vdots & \vdots & \vdots \\ \Omega_{u1111} & \Omega_{u1112} & \cdots & \Omega_{uN_I N_J N_P N_Q} \\ \vdots & \vdots & \vdots & \vdots \\ \Omega_{N_U 1111} & \Omega_{N_U 1112} & \cdots & \Omega_{N_U N_I N_J N_P N_Q} \end{bmatrix} \quad (3.25)$$

$$\bar{\Psi} = \begin{bmatrix} a_{11} b_{111} & a_{11} b_{112} & \cdots & a_{11} b_{11N_R} \\ a_{11} b_{121} & a_{11} b_{122} & \cdots & a_{11} b_{12N_R} \\ \vdots & \vdots & \vdots & \vdots \\ a_{ij} b_{pq1} & a_{ij} b_{pq2} & \cdots & a_{ij} b_{pqN_R} \\ \vdots & \vdots & \vdots & \vdots \\ a_{N_I N_J} b_{N_P N_Q 1} & a_{N_I N_J} b_{N_P N_Q 2} & \cdots & a_{N_I N_J} b_{N_P N_Q N_R} \end{bmatrix} \quad (3.26)$$

$$\bar{\Phi} = \begin{bmatrix} \Phi_{11} & \Phi_{12} & \cdots & \Phi_{1N_V} \\ \Phi_{21} & \Phi_{22} & \cdots & \Phi_{2N_V} \\ \vdots & \vdots & \vdots & \vdots \\ \Phi_{r1} & \Phi_{r2} & \cdots & \Phi_{rN_V} \\ \vdots & \vdots & \vdots & \vdots \\ \Phi_{N_R 1} & \Phi_{N_R 2} & \cdots & \Phi_{N_R N_V} \end{bmatrix} \quad (3.27)$$

This is the general form for the discretization of (3.4). The other equations also can be similarly discretized. It is worth noting that, depending on the discretization, these matrices can be computationally expensive. They also can be sparse if the functions were defined locally only. Consequently, the computational cost to calculate the matrices and to solve the system might become prohibitive. It is also necessary to note that (3.23) is a nonlinear system since the unknown constants  $a$  and  $b$  ( $N_I N_J + N_P N_Q N_R$ ) multiply in  $N_U N_V$  equations.

The difference between the MWR class methods is based on the choice of weight func-

tions  $w$ . The most common ones will be discussed in the following subsections.

### 3.2.1 The Subdomain Method

In the Subdomain Method, domain  $D$  is divided into a finite number of  $D_{uv}$  subdomains that might overlap. Mathematically:

$$w_{uv} = \begin{cases} 1, & \text{in } D_{uv}, \\ 0, & \text{outside, } D_{uv} \end{cases} \quad (3.28)$$

Thus, the integrals over  $\theta$  and  $\phi$  in (3.17) are calculated only in pieces of  $D$ . The practical effect of this kind of method is to eliminate the contribution of some terms in  $\bar{\Psi}$  in which  $r \neq v$ . Consequently, the sum in  $r$  in (3.19) would not be necessary because only  $b_{pqv}$  would be different from zero for the  $uv$  equation.

This kind of formulation is more suitable for differential equation problems since the domains for weight and trial functions are the same. Therefore, the solution in a subdomain involves only a few elements of the unknown function and not all of them, as in the case of EISP. However, the Subdomain method has also been applied to integral equations (Deputat et al., 2005; Gabbasov and Zamaliev, 2014). This approach is also known in the literature as the Finite Volume Method, usually obtained by energy conservation principles.

### 3.2.2 The Collocation Method

The Collocation Method is based on the following choice of the weight function:

$$w_i(x) = \delta(x - x_k) \quad (3.29)$$

where  $\delta$  is the Dirac Delta function. If we apply this definition in (3.17), the integrals in  $D$  will be eliminated. Thus, the matrix  $\bar{\Phi}$  becomes the identity matrix and does not need to be considered in (3.23).

This type of method is widely used in EISP since the scattered field is only available at a set of sampled points in  $D$  in practical situations. One of its forms widely used in the literature is proposed by Richmond (1965), at which the trial functions are defined as rectangular pulse functions. This choice is equivalent to dividing the  $S$  domain into subdomains where the trial function corresponding to a subdomain is 1 in its region and 0 otherwise. In other words, this means that we are assuming that  $E_z$  and  $\chi$  are constant within the subdomain. In this case, the integral in (3.22) can be solved by approximating the subdomain  $S_{ij}$  by a circular region. In this

case, the integral over the Hankel's function has an analytical solution:

$$\frac{jk_b^2}{4} \int_0^{2\pi} \int_0^{r_a} H_0^{(2)}(k_b \rho) \rho' d\rho' d\psi' = \begin{cases} \frac{j}{2} [\pi k_b r_a H_1^{(2)}(k_b r_a) - 2j], & \rho \in S_{ij}, \\ \frac{j\pi k_b r_a}{2} J_1(k_b r_a) H_0^{(2)}(k_b \rho), & \rho \notin S_{ij} \end{cases} \quad (3.30)$$

where  $r_a$  is the radius of the circular region and might be approximated by  $\sqrt{\Delta x \Delta y / \pi}$  in which  $\Delta x$  and  $\Delta y$  are the dimensions of the subdomain of  $S_{ij}$ . Note that (3.30) can also be used for situations involving singularities, which applies to the state equation (3.5), for example. Another advantage is that this representation is very suitable for homogeneous scatterers.

Therefore, considering a case where the input data are scattered field samples obtained through  $N_M$  measurements for each one of  $N_S$  incidences and the image to be recovered is divided into  $N_I \times N_J$  elements (pixels), then this is equivalent to the model (3.17) with  $N_U = N_M$ ,  $N_V = N_R = N_S$ ,  $N_P = N_I$  and  $N_Q = N_J$ . Therefore, the problem has  $N_I N_J (1 + N_S)$  unknowns and  $N_M N_S$  equations. In addition,  $f_i^{(x)}(x) g_p^{(x)}(x) = 1$  and  $f_j^{(y)}(y) g_q^{(y)}(y) = 1$  only when  $i = p$  and  $j = q$ , respectively. Hence, (3.17) can be rewritten like:

$$E_{zs}(\theta_m, \phi_s) = -\frac{j\pi k_b r_a}{2} J_1(k_b r_a) \sum_{i=1}^{N_I} \sum_{j=1}^{N_J} H_0^{(2)}(k_b \sqrt{(R_O \cos \theta_m - x_i)^2 + (R_O \sin \theta_m - y_j)^2}) \chi(x_i, y_j) E_z(\phi_s, x_i, y_j) \quad (3.31)$$

Instead of choosing the general notation present in (3.19), we will use a more particular one that is common in the literature. For this notation, we will use  $E_{ms}^s = E_{zs}(\theta_m, \phi_s)$ ,  $E_{ijs}^i = E_{zi}(\psi_s, x_i, y_j)$ ,  $\chi_{ij} = \chi(x_i, y_j)$ ,  $J_{ijs}^{eq} = J_{zeq}(\phi_s, x_i, y_j)$ ,  $\beta_{ij} = \beta(x_i, y_j)$ ,  $R_{ij} = R(x_i, y_j)$  and  $E_{ijs} = E_z(\phi_s, x_i, y_j)$ . Thus, both (3.31) and the application of Collocation Method for (3.5)-(3.8) can be written as:

$$E_{ms}^s = - \sum_{i=1}^{N_I} \sum_{j=1}^{N_J} G_{mij}^D \chi_{ij} E_{ijs} \quad (3.32)$$

$$E_{ijs} = E_{ijs}^i - \sum_{p=1}^{N_I} \sum_{q=1}^{N_J} G_{ijpq}^S \chi_{pq} E_{pqs} \quad (3.33)$$

$$E_{ms}^s = - \sum_{i=1}^{N_I} \sum_{j=1}^{N_J} G_{mij}^D J_{ijs}^{eq} \quad (3.34)$$

$$\chi_{ij} E_{ijs}^i = J_{ijs}^{eq} + \chi_{ij} \sum_{p=1}^{N_I} \sum_{q=1}^{N_J} G_{ijpq}^S J_{pqs}^{eq} \quad (3.35)$$

$$\beta_{ij} J_{ijs}^{eq} = R_{ij} \beta_{ij} J_{ijs}^{eq} + R_{ij} \left[ E_{ijs}^i - \sum_{p=1}^{N_I} \sum_{q=1}^{N_J} G_{ijpq}^S J_{pqs}^{eq} \right] \quad (3.36)$$

where:

$$G_{mi}^D = \frac{j\pi k_b r_a}{2} J_1(k_b r_a) H_0^{(2)}(k_b \sqrt{(R_O \cos \theta_m - x_i)^2 + (R_O \sin \theta_m - y_j)^2}) \quad (3.37)$$

$$G_{ijpq}^S = \begin{cases} \frac{j}{2} [\pi k_b r_a H_1^{(2)}(k_b r_a) - 2j], & i = p \text{ and } j = q \\ \frac{j\pi k_b r_a}{2} J_1(k_b r_a) H_0^{(2)}(k_b \sqrt{(x_i - x_p)^2 + (y_j - y_q)^2}), & \text{otherwise.} \end{cases} \quad (3.38)$$

These equations can also be written in matrix form:

$$\bar{\mathbf{E}}^s = -\bar{\mathbf{G}}^D \bar{\chi} \bar{\mathbf{E}} \quad (3.39)$$

$$\bar{\mathbf{E}} = \bar{\mathbf{E}}^i - \bar{\mathbf{G}}^S \bar{\chi} \bar{\mathbf{E}} \quad (3.40)$$

$$\bar{\mathbf{E}}^s = -\bar{\mathbf{G}}^D \bar{\mathbf{J}}^{eq} \quad (3.41)$$

$$\bar{\chi} \bar{\mathbf{E}}^i = \bar{\mathbf{J}}^{eq} + \bar{\chi} \bar{\mathbf{G}}^S \bar{\mathbf{J}}^{eq} \quad (3.42)$$

$$\bar{\beta} \bar{\mathbf{J}}^{eq} = \bar{\mathbf{R}} \bar{\beta} \bar{\mathbf{J}}^{eq} + \bar{\mathbf{R}} [\bar{\mathbf{E}}^i - \bar{\mathbf{G}}^S \bar{\mathbf{J}}^{eq}] \quad (3.43)$$

in which the matrices have the following patterns:

$$\bar{\mathbf{E}}^s = \begin{bmatrix} E_{11}^s & E_{12}^s & \cdots & E_{1N_S}^s \\ E_{21}^s & E_{22}^s & \cdots & E_{1N_S}^s \\ \vdots & \vdots & \ddots & \vdots \\ E_{N_M 1}^s & E_{N_M 2}^s & \cdots & E_{N_M N_S}^s \end{bmatrix} \quad \bar{\mathbf{E}}^i = \begin{bmatrix} E_{111}^i & E_{112}^i & \cdots & E_{11N_S}^i \\ E_{121}^i & E_{122}^i & \cdots & E_{11N_S}^i \\ \vdots & \vdots & \ddots & \vdots \\ E_{ij1}^i & E_{ij2}^i & \cdots & E_{ijN_S}^i \\ \vdots & \vdots & \ddots & \vdots \\ E_{N_I N_J 1}^i & E_{N_I N_J 2}^i & \cdots & E_{N_I N_J N_S}^i \end{bmatrix} \quad (3.44)$$

$$\bar{\mathbf{E}} = \begin{bmatrix} E_{111} & E_{112} & \cdots & E_{11N_S} \\ E_{121} & E_{122} & \cdots & E_{11N_S} \\ \vdots & \vdots & \ddots & \vdots \\ E_{ij1} & E_{ij2} & \cdots & E_{ijN_S} \\ \vdots & \vdots & \ddots & \vdots \\ E_{N_I N_J 1} & E_{N_I N_J 2} & \cdots & E_{N_I N_J N_S} \end{bmatrix} \quad \bar{\mathbf{J}}^{eq} = \begin{bmatrix} J_{111}^{eq} & J_{112}^{eq} & \cdots & J_{11N_S}^{eq} \\ J_{121}^{eq} & J_{122}^{eq} & \cdots & J_{11N_S}^{eq} \\ \vdots & \vdots & \ddots & \vdots \\ J_{ij1}^{eq} & J_{ij2}^{eq} & \cdots & J_{ijN_S}^{eq} \\ \vdots & \vdots & \ddots & \vdots \\ J_{N_I N_J 1}^{eq} & J_{N_I N_J 2}^{eq} & \cdots & J_{N_I N_J N_S}^{eq} \end{bmatrix} \quad (3.45)$$

$$\bar{\mathbf{G}}^D = \begin{bmatrix} G_{111}^D & G_{112}^D & \cdots & G_{1N_I N_J}^D \\ G_{211}^D & G_{212}^D & \cdots & G_{2N_I N_J}^D \\ \vdots & \vdots & \ddots & \vdots \\ G_{m11}^D & G_{m12}^D & \cdots & G_{mN_I N_J}^D \\ \vdots & \vdots & \ddots & \vdots \\ G_{N_M 11}^D & G_{N_I N_J 2}^D & \cdots & G_{N_M N_I N_J}^D \end{bmatrix} \quad \bar{\mathbf{G}}^S = \begin{bmatrix} G_{1111}^S & G_{1112}^S & \cdots & G_{11N_I N_J}^S \\ G_{1211}^S & G_{1212}^S & \cdots & G_{12N_I N_J}^S \\ \vdots & \vdots & \ddots & \vdots \\ G_{ij11}^S & G_{ij12}^S & \cdots & G_{ijN_I N_J}^S \\ \vdots & \vdots & \ddots & \vdots \\ G_{N_I N_J 11}^S & G_{N_I N_J 12}^S & \cdots & G_{N_I N_J N_I N_J}^S \end{bmatrix} \quad (3.46)$$

$$\bar{\boldsymbol{\chi}} = \begin{bmatrix} \chi_{11} & 0 & \cdots & 0 \\ 0 & \chi_{12} & \cdots & 0 \\ \vdots & \vdots & \ddots & \vdots \\ 0 & 0 & \cdots & \chi_{N_I N_J} \end{bmatrix} \quad \bar{\boldsymbol{\beta}} = \begin{bmatrix} \beta_{11} & 0 & \cdots & 0 \\ 0 & \beta_{12} & \cdots & 0 \\ \vdots & \vdots & \ddots & \vdots \\ 0 & 0 & \cdots & \beta_{N_I N_J} \end{bmatrix} \quad \bar{\mathbf{R}} = \begin{bmatrix} R_{11} & 0 & \cdots & 0 \\ 0 & R_{12} & \cdots & 0 \\ \vdots & \vdots & \ddots & \vdots \\ 0 & 0 & \cdots & R_{N_I N_J} \end{bmatrix} \quad (3.47)$$

Note that  $\bar{\boldsymbol{\chi}}$ ,  $\bar{\boldsymbol{\beta}}$  and  $\bar{\mathbf{R}}$  are diagonal matrices, i.e., their elements are different from zero only on the main diagonal. In addition, specifically in  $\bar{\boldsymbol{\chi}}$ , the diagonal elements are nonzero only at the points where the contrast is different from zero, i.e., where there is a scatterer. Therefore, the most efficient approach to store this data is a sparse matrix. The same might be valid for  $\bar{\mathbf{J}}^{\text{eq}}$ , in which the lines corresponding to points where there is no contrast contains only zeros.

It is also worth noting that  $\bar{\mathbf{G}}^S$  is a symmetric matrix whose structure is known as Blocked Symmetric Toeplitz (Böttcher and Grudsky, 2000). All the diagonal elements are the same, and there are several equal terms for which the root in (3.38) has the same value, i.e., equidistant points assuming a uniform discretization. This kind of structure is crucial because it allows applying the Fast Fourier Transform (FFT) technique for matrix multiplication. Then, the computational cost is reduced from  $O(n^2)$  to  $O(n \log n)$ <sup>2</sup>.

This discretization will be assumed both in the methods that will be mentioned soon and in the investigations conducted. Worth it to point out that other ways of implementing the trial functions of the Collocation Method are also possible. One of them is the discretization of space by rectangular or triangular elements in which the trial functions take polynomial forms in some areas of space and zero in the rest. This kind of discretization is similar to the Finite Element Method, which addresses differential equations. An example is a bilinear function (Figura 3.2)

---

<sup>2</sup>To see how this technique applies to (3.40), (3.42), and (3.43), we suggest reading Appendix D of (Chen, 2017)

whose definition of  $f_i^{(x)}(x)$  and  $f_j^{(y)}(y)$  are expressed by:

$$f_i^{(x)}(x) = \begin{cases} \frac{x-x_{i-1}}{x_i-x_{i-1}}, & x_{i-1} < x \leq x_i \\ \frac{x-x_{i+1}}{x_i-x_{i+1}}, & x_i < x < x_{i+1} \\ 0, & \text{otherwise.} \end{cases} \quad (3.48)$$

$$f_j^{(y)}(y) = \begin{cases} \frac{y-y_{j-1}}{y_j-y_{j-1}}, & y_{j-1} < y \leq y_j \\ \frac{y-y_{j+1}}{y_j-y_{j+1}}, & y_j < y < y_{j+1} \\ 0, & \text{otherwise.} \end{cases} \quad (3.49)$$

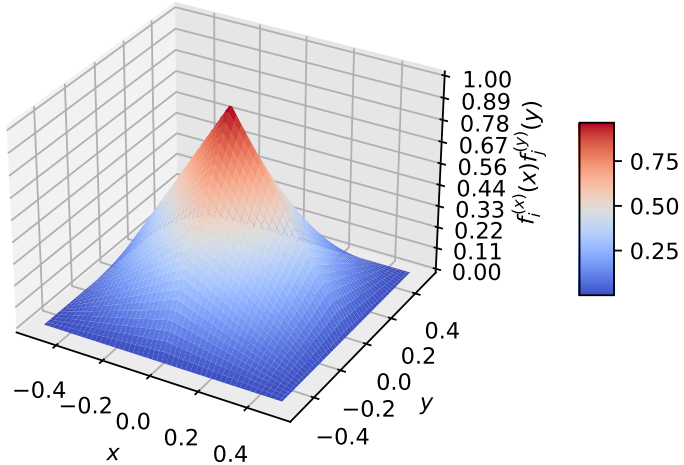


Figura 3.2: Bilinear shape function on a rectangular grid.

This function can better represent heterogeneities in the scatterers as well as the electric field. However, unlike pulse discretization, more elements will contribute to the value of the function at a given point. This can make the computational cost of calculating the integral (3.22) more expensive while improving integration accuracy.

Alternatively to the trial functions defined in only pieces of the domain, the Spectral Methods define them everywhere in the domain. The efficiency of this sort of methodology depends on a careful choice of the functions, i.e., they need to be a good representation of the unknown functions. For this reason, applying such a strategy to contrast function discretization may not be a good choice, especially in the case of traditional geometries. However, this may be compatible with the representation of the electric field essentially because, in analytical problems that involve only a single scatterer, the solution is written in terms of complex exponentials or Bessel's functions. For example, the functions  $g_p^{(x)}(x)$  and  $g_q^{(y)}(y)$  could be chosen

in such a way so that:

$$g_p^{(x)}(x)g_q^{(y)}(x) = H_0^{(2)}(k_b \sqrt{(x_p - x)^2 + (y_q - y)^2}) \quad (3.50)$$

This choice example refers to the Minimum Norm Collocation. Theoretically, supposing a linear inverse problem whose operator  $\mathcal{K} : X \rightarrow C[a,b]$  is linear, bounded, and injective of a space of Hilbert  $X$  in a space  $C[a,b]$  of continuous functions in  $[a,b]$ ; then the trial function can be defined as the one whose norm  $L^2(a,b)$  is minimum. This solution, in the case of an integral equation as in (D.5), is the kernel  $k_i(s) = k(t_i, s)$ , which belongs to  $L^2(a,b)$  (Kirsch, 2011).

Nevertheless, exceptional attention to possible singularities needs to be taken. For this reason, the analytical description and implementation of this kind of method might be more complex.

### 3.2.3 The Galerkin Method

Another possibility is to choose the weight function from the same family as the trial ones, i.e.:

$$w_k(x) = f_i(x) \quad (3.51)$$

This strategy is known in the literature as the Galerkin or Bubnov-Galerkin Method. For problems modeled from differential equations, the choice of these functions need to meet the following criteria (Fletcher, 1984):

1. The weight and trial functions are chosen from the same family;
2. Weight and trial functions must be linearly independent;
3. The weight and trial functions must be the first N members of a dense set of functions;
4. The weight and trial functions must satisfy the essential homogeneous boundary conditions exactly.

While the first condition defines the method, the second concerns the relationship between linearly independent equations and unknown variables.

However, it is necessary to note that, in EISP, the domains of the weight and trial functions are different, i.e., their arguments in (3.51) are unrelated. In addition, it is necessary to integrate  $E_{zs}$  across the  $D$  domain (3.20). This requirement can make the practical application of the method unfeasible since the scattered field is known only at a finite set of points. An alternative for this problem is to use an interpolation method. However, this strategy can induce the inversion to solutions far from the real one.

Finally, we can mention some of the few papers in the literature that used methodologies based on this type of discretization. Rather than discretizing the integral equation, Zakaria et al. (2010) applied it to the wave equation (2.25). The differential equation was written in terms of the scattered field and the source. In addition, the Sommerfeld radiation boundary condition was imposed, modeled with second-order absorption conditions. The authors used

a non-uniform triangular elements discretization and developed a methodology based on the Contrast Source Inversion (which will be explained later in the text). Alternatively, Brown et al. (2019) proposed a hybrid and discontinuous approach to the Galerkin Method to solve the problem within the scope of the Contrast Source Inversion, which requires fewer degrees of freedom.

### 3.2.4 Some Aspects on Discretization

Before concluding the section, two aspects also deserve to be highlighted when discussing discretization. First, it is necessary to underline that discretization methodologies are also regularization strategies, as defined in Section 2.3 (Kirsch, 2011). Discretization is an issue within the scope of projection. Mathematically, a projection operator is defined as follows:

#### **Definição 1. Projection Operator**

*Let  $X$  be a normed space over the field  $\mathbb{K} = \mathbb{R}$  or  $\mathbb{K} = \mathbb{C}$ . Let  $U \subset X$  be a closed subspace. A linear bounded operator  $\mathcal{P} : X \rightarrow X$  is called a projection operator on  $U$  if*

- $\mathcal{P}\{x\} \in U, \forall x \in X$  and
- $\mathcal{P}\{x\} = x, \forall x \in U$ .

Within this context, the weight and trial functions are members of finite-dimension subspaces  $X_n \subset X$  and  $Y_n \subset Y$ , respectively. Then, for a given  $y \in Y$  in which  $\mathcal{K}\{x\} = y$  is linear and one-to-one, discretization is a projection operator  $\mathcal{Q}_n : Y \rightarrow Y_n$  that solves the equation:

$$\mathcal{Q}_n\{K\{x_n\}\} = \mathcal{Q}_n\{y\} \quad (3.52)$$

for  $x_n \in X_n$ . So, let  $\{\hat{x}_1, \dots, \hat{x}_n\}$  and  $\{\hat{y}_1, \dots, \hat{y}_n\}$  be bases of  $X_n$  and  $Y_n$ , respectively. The terms  $\mathcal{Q}_n\{y\}$  and  $\mathcal{Q}_n\{K\{x_n\}\}$  can be represented as follows:

$$\mathcal{Q}_n\{y\} = \sum_{i=1}^n b_i \hat{y}_i, \quad j = 1, \dots, n \quad (3.53)$$

$$\mathcal{Q}_n\{K\{x_n\}\} = \sum_{i=1}^n A_{ij} \hat{y}_i, \quad j = 1, \dots, n \quad (3.54)$$

in which  $b_i, A_{ij} \in \mathbb{K}$ . The linear combination  $x_n = \sum_{j=1}^n a_j \hat{x}_j$  is a solution of (3.52) if and only if  $\{a_1, \dots, a_n\} \in \mathbb{K}^n$  is a solution of the finite system of linear equations:

$$\sum_{i=1}^n A_{ij} a_j = b_i, \quad i = 1, \dots, n \quad (3.55)$$

In this context, the Collocation Method is an example of a projection method whose operator is called an interpolation one. The Galerkin Method is known as an orthogonal projection operator. This implies that the error is orthogonal to the approximation space and the

solution is the best one (minimum error) in that approximation space.

Second, the choice of trial functions, i.e., its shape and size, needs to consider not only the aspects discussed about degrees of freedom in Subsection 2.4.5 but also a concept in the literature known as Inverse Crime. As highlighted by Colton and Kress (2019), it is necessary that, when the experimentation involves synthetic data generated by direct solvers, the latter must not have connections with the inverse solver. In other words, in an inverse problem of finite dimension, trivial solutions should be avoided.

The concept can be illustrated through a generic problem where its objective is to recover a family  $G_m$  of contour surfaces with  $m$  parameters. For this problem, if we use data synthesized by a direct resolver  $\mathbf{M}$  to obtain  $n$  input data, such as distant field samples, this is equivalent to a function  $g : \mathbb{R}^m \rightarrow \mathbb{C}^n$ . Therefore, if a given surface  $\partial D \in G_m$  is generated from the set of parameters  $p_0$ , an inversion method that incorporates the same direct solver  $\mathbf{M}$  is doing nothing more than solving the finite dimension problem  $g(p) = g(p_0)$ . Therefore, the  $\partial D$  surface will inevitably be well reconstructed, assuming that  $m$  and  $n$  are not too big.

Wirgin (2004) brought more contributions to the subject by analyzing three examples that, although not universal, deepened the understanding of the concept introduced by Colton and Kress (2019). The conclusions made by Wirgin can be summarized in:

- Regarding the meaning of the lack of connection between a direct solver and an inverse one, he proposed that its practical meaning is the difference in the number of terms of the power series representing the forward and inverse solver. That is, if that number of terms are different, then there would be no connection.
- Wirgin concluded that the more significant difference between both solvers in terms of their functionals, the larger relative inversion error. That means recovering the parameters very accurately is possible when the two resolvers are connected.
- Committing the inverse crime also has the practical sense of at least revealing whether the inverse problem has a unique solution or not.
- When the inverse crime is committed, the solution may not only be the “trivial” one, but others can also be observed through a robust numerical method system, which would not necessarily be observed in a situation where the crime is not committed.

Wirgin also criticizes the use of the term “trivial solution” since the objective is, in fact, to recover the parameters as accurately as possible. In addition, even if his mathematical analysis is based on the reconstruction of a single parameter for a single data, mathematical analysis for larger problems, including two parameters and two data, becomes much more complicated. However, he claims that it would be difficult to expect contradictions between their conclusions for a simple case and those that might be obtained for more complex ones. Finally, in experiments with real data, it does not make sense to worry about inverse crime since, in fact, the “direct resolver” is unknown. Even that a direct solver represents the physical phenomenon well, this does not prevent the observation of disturbances in the solution, representing something false.

### 3.3 The Linear Case

Although EISP is non-linear, the study of the linear case is significant because many methods use strategies based on problem linearization. These strategies can be essential when defining search directions and initial solutions. In addition, it is possible to use approximations for the total field in problems where we assume weak scatterers. In this case, the problem may be approximated to a linear one. The discretization of (3.32) and (3.21) will be used to discuss them. However, all of these methodologies can be easily adapted to other equations and discretizations.

#### 3.3.1 Approximated Solutions for Weak Scatterers

When the dielectric properties of a scatterer differ very little from the background, and its size is not too large, it is considered a weak one ( $DNL \ll 1$ ). Under these conditions, it is possible to approximate the electric field and turn the problem into a linear one. Two classic techniques address this situation: the Born Approximation (BA) and the Rytov Approximation (RA). The first is best suited for low frequencies, while the second is more suitable for high ones.

Born's series is a methodology that writes the electric field as a series in terms of Green's function, contrast, and incident field. Recapitulating the formulas from Subsection 2.4.4, if the  $L^2(S)$ -norm

$$\left\| \int_S d\mathbf{r}' \bar{\mathbf{G}}(\mathbf{r}, \mathbf{r}') \chi(\mathbf{r}') \right\| < 1,$$

then:

$$\mathbf{E}(\mathbf{r}) = \sum_{n=0}^{\infty} \left( \int_S d\mathbf{r}' \bar{\mathbf{G}}(\mathbf{r}, \mathbf{r}') \chi(\mathbf{r}') \right)^n \mathbf{E}_i(\mathbf{r}) \quad (3.56)$$

Following the matrix form (3.40), (3.56) can be written in a discretized fashion as:

$$\bar{\mathbf{E}} = \sum_{n=0}^{\infty} (\bar{\mathbf{G}}^S \bar{\chi})^n \bar{\mathbf{E}}^i \quad (3.57)$$

The First-Order Born Approximation is a single-scattering approximation obtained from the truncation of the Born series (3.56) in its first term  $n = 0$ , i.e.:

$$\mathbf{E}(\mathbf{r}) \approx \mathbf{E}_i(\mathbf{r}) \quad (3.58)$$

Although it even violates the energy conservation principle, the reciprocity is still valid because of the symmetry of dyadic Green's function (Chew, 1995). In addition, if the size of the scatterer is of the order  $L$  in which  $k_b L \ll 1$ , then dyadic Green's function (B.17), contrast

and volumetric integral can be approximated by (Chew, 1995):

$$\bar{\mathbf{G}}(\mathbf{r}, \mathbf{r}') \approx \left(1 + \frac{1}{k_b^2 L^2}\right) \frac{1}{L} \quad (3.59)$$

$$k^2(\mathbf{r}) - k_b^2 \approx k_b^2 \Delta \epsilon_r \quad (3.60)$$

$$\int_D d\mathbf{r}' \approx L^3 \quad (3.61)$$

where  $\Delta \epsilon_r = \epsilon_r / \epsilon_{rb} - 1$ . Thus, (2.30) is approximated by:

$$\mathbf{E}_s(\mathbf{r}) \approx [(k_b L)^2 + 1] \Delta \epsilon_r \mathbf{E}_i(\mathbf{r}) \quad (3.62)$$

However, in situations where the frequency is higher, the field variation inside the object is dominant. In these cases, the operator  $\nabla \nabla$  is approximated by  $k_b^2$  and the field phase within the scatterer needs to be taken into account. Assuming that the field inside the scatterer is a superposition of plane waves, the approximation in (3.58) needs to be fixed to:

$$\mathbf{E}(\mathbf{r}) \approx \mathbf{E}_i(\mathbf{r}) e^{j(\mathbf{k} - \mathbf{k}_b) \cdot \mathbf{r}} \quad (3.63)$$

This approximation depends on  $(k - k_b)L \ll 1$ , which is a stronger constraint than the previous one.

Rytov's First-Order Approximation is based on a reduction in the vector equation by a scalar equation. This reduction consists of replacing the total field by a complex exponential whose phase is a function, i.e.:

$$E_z(\mathbf{r}) \approx E_{i_z}(\mathbf{r})^{\psi(\mathbf{r})} \quad (3.64)$$

in which the first-order phase  $\psi(\mathbf{r})$  is based on the scattered field of (2.30) calculated by the Born Approximation (3.58), i.e.:

$$\psi(\mathbf{r}) = \frac{1}{E_i(\mathbf{r})} \int_S d\mathbf{r}' g(\mathbf{r}, \mathbf{r}') E_{i_z}(\mathbf{r}') \chi(\mathbf{r}') \quad (3.65)$$

When we apply an analysis similar to (3.59)-(3.61), it is possible to demonstrate that  $\psi(\mathbf{r}) \approx k_b^2 L^2 \Delta \epsilon_r$  when  $k_b L \rightarrow 0$  (Chew, 1995). This condition is equivalent to  $(k_b L)^2 \Delta \epsilon_r \ll 1$ . On the other hand, if the frequency tends to infinity, then  $\psi(\mathbf{r}) \approx k_b L \Delta \epsilon_r$ . The condition for this approximation is  $\Delta \epsilon_r \ll 1$ , which is much weaker than the previous one. Therefore, this approach is more suitable for high frequencies.

### 3.3.2 The Back-Propagation Method

The Back-Propagation (BP) Method is noniterative algorithm which is able to provide a solution for the contrast image. Such solution is often used as initial guess in many methods. The method is suitable for arbitrary incident fields, near and far fields measurements. BP is

based on three steps: (i) estimate the induced current; (ii) compute total field in  $S$  through the state equation; and (iii) determine the contrast image by relation between total field and induced current. If the induced current is assumed to be proportional to the back-propagation field, then the induced current is evaluated according to:

$$\bar{\mathbf{J}}^{\text{eq}} = \gamma \bar{\mathbf{G}}^{\mathbf{D}^*} \bar{\mathbf{E}}^s \quad (3.66)$$

where the superscript \* is the operator's adjoint and numerically given by the conjugated-transposed. The parameter  $\gamma$  is a complex value that is chosen to minimize the cost function defined as the quadratic error in the scattered field:

$$F(\gamma) = \|\bar{\mathbf{E}}^s - \bar{\mathbf{G}}^{\mathbf{D}}(\gamma \bar{\mathbf{G}}^{\mathbf{D}^*} \bar{\mathbf{E}}^s)\|^2 \quad (3.67)$$

The minimum of (3.67) might be obtained analytically and is given as follows:

$$\gamma = \frac{\langle \bar{\mathbf{E}}^s, \bar{\mathbf{G}}^{\mathbf{D}} \bar{\mathbf{G}}^{\mathbf{D}^*} \bar{\mathbf{E}}^s \rangle}{\|\bar{\mathbf{G}}^{\mathbf{D}} \bar{\mathbf{G}}^{\mathbf{D}^*} \bar{\mathbf{E}}^s\|} \quad (3.68)$$

where  $\langle \cdot, \cdot \rangle$  is the inner product, which is numerically computed as the product between the transpose of the first argument and the complex conjugate of the second one.

Once the induced current is obtained, then the total electric field might be evaluated according to (3.40) replacing  $\bar{\chi} \bar{\mathbf{E}}$  by  $\bar{\mathbf{J}}^{\text{eq}}$ . Finally, the contrast might be evaluated according to:

$$\chi_{ij} = \frac{\sum_{s=1}^{N_S} J_{ijs}^{\text{eq}} E_{ijs}^*}{\sum_{s=1}^{N_S} |E_{ijs}^*|^2} \quad (3.69)$$

If it is known that only lossless scatterers are present, then the imaginary part of  $\bar{\chi}$  can be neglected.

### 3.3.3 Dominant Current Scheme

In nonlinear problems with large number of variables, there may be some unknowns which are more relevant. Since recovering the induced current might be a hard task when a limited number of measurements are available, the dominant part of the induced current might be prioritized. Such strategy is based on the fact that the dominant current contains the most important features of the unknown scatterers and it is more robust against noise. This is the core idea behind the Dominant Current Scheme (DCS) (Wei and Chen, 2019a).

When the Singular Value Decomposition is applied to  $\bar{\mathbf{G}}^{\mathbf{D}}$ , the dominant current might

be evaluated according to:

$$\bar{\mathbf{J}}_+^{\text{eq}} = \sum_{n=1}^L \frac{\bar{u}_n^* \cdot \bar{\mathbf{E}}^s}{\xi_n} \bar{v}_j \quad (3.70)$$

where  $\bar{u}$ ,  $\bar{v}$ , and  $\xi$  are the left, right, and singular value vectors from the decomposition; and  $L$  is an index that limits the singular values in descending order, i.e., the dominant current is computed taking into account the first  $L$  largest singular values. Therefore, the  $N_I N_J - L$  smallest singular values are neglected and unstable components corrupted by noise are avoided. However, a compensation for the missing information is also provided, i.e.:

$$\bar{\mathbf{J}}_-^{\text{eq}} = \bar{\mathbf{F}} \cdot \boldsymbol{\alpha} \quad (3.71)$$

where  $\bar{\mathbf{F}}$  and  $\boldsymbol{\alpha}$  are the low-frequency matrices composed by the first  $m$  low-frequency Fourier bases and their corresponding coefficients, respectively. Since  $\boldsymbol{\alpha}$  is an unknown, some approximation has to be made to complete the scheme. Wei and Chen (2019a) proposed the following objective-function:

$$F(\boldsymbol{\alpha}) = \left[ \frac{\|\bar{\mathbf{G}}^F \cdot \boldsymbol{\alpha} + \bar{\mathbf{G}}^E\|^2}{\|\bar{\mathbf{E}}^s\|^2} + \frac{\|\bar{\mathbf{A}} \cdot \boldsymbol{\alpha} + \bar{\mathbf{B}}\|^2}{\|\bar{\mathbf{J}}_+^{\text{eq}}\|^2} \right] \quad (3.72)$$

where  $\bar{\mathbf{G}}^F = \bar{\mathbf{G}}^D \cdot \bar{\mathbf{F}}$ ,  $\bar{\mathbf{G}}^E = \bar{\mathbf{G}}^D \cdot \bar{\mathbf{J}}_+^{\text{eq}} - \bar{\mathbf{E}}^s$ ,  $\bar{\mathbf{A}} = \bar{\mathbf{F}} - \bar{\boldsymbol{\chi}} \cdot \bar{\mathbf{G}}^s \cdot \bar{\mathbf{F}}$ , and  $\bar{\mathbf{B}} = \bar{\boldsymbol{\chi}} (\bar{\mathbf{E}}^i + \bar{\mathbf{G}}^S \bar{\mathbf{J}}_+^{\text{eq}}) - \bar{\mathbf{J}}_-^{\text{eq}}$ .

Based on (3.72), the authors proposed an iterative process to update  $\bar{\boldsymbol{\chi}}$  and  $\boldsymbol{\alpha}$ , starting by  $\bar{\boldsymbol{\chi}} = \mathbf{0}$ . The variable  $\boldsymbol{\alpha}$  is approximated according to  $\boldsymbol{\alpha} = \beta \boldsymbol{\gamma}$  where:

$$\boldsymbol{\gamma} = \left( \frac{\bar{\mathbf{G}}^{F*} \cdot \bar{\mathbf{G}}^E}{\|\bar{\mathbf{E}}^s\|^2} - \frac{\bar{\mathbf{A}}^* \cdot \bar{\mathbf{B}}}{\|\bar{\mathbf{J}}_+^{\text{eq}}\|^2} \right) \quad (3.73)$$

$$\beta = \frac{\text{Num}}{\text{Den}} \quad (3.74)$$

$$\text{Num} = -\frac{\bar{\mathbf{G}}^{F*} \cdot \boldsymbol{\gamma} \cdot \bar{\mathbf{G}}^E}{\|\bar{\mathbf{E}}^s\|^2} + \frac{(\bar{\mathbf{A}} \cdot \boldsymbol{\gamma})^* \cdot \bar{\mathbf{B}}}{\|\bar{\mathbf{J}}_+^{\text{eq}}\|^2} \quad (3.75)$$

$$\text{Den} = \frac{\|\bar{\mathbf{G}}^F \cdot \boldsymbol{\gamma}\|^2}{\|\bar{\mathbf{E}}^s\|^2} + \frac{\|\bar{\mathbf{A}} \cdot \boldsymbol{\gamma}\|^2}{\|\bar{\mathbf{J}}_+^{\text{eq}}\|^2} \quad (3.76)$$

Then, after using  $\boldsymbol{\alpha}$  to compute the low-frequency compensation through (3.71), the following steps are required:

$$\bar{\mathbf{J}}^{\text{eq}} = \bar{\mathbf{J}}_+^{\text{eq}} + \bar{\mathbf{J}}_-^{\text{eq}} \quad (3.77)$$

$$\bar{\mathbf{E}} = \bar{\mathbf{E}}^i + \bar{\mathbf{G}}^S \bar{\mathbf{J}}^{\text{eq}} \quad (3.78)$$

$$\chi_{ijs} = \frac{J_{ijs}^{\text{eq}} E_{ijs}^*}{\|E_{ijs}\|^2} \quad (3.79)$$

In (3.79), it is computed one contrast image for each incidence. The authors had decided for this based in its application to Convolution Neural Networks. However, a computation similar to (3.69) might also be used.

## 3.4 Regularization Methods

Whenever the total electric field in the state space is known, the inverse problem turns into a linear one. This may happen when approximating the total field by the incident one (subsection 3.3.1) or when a forward solver is employed to determine it for a given outdated contrast image. For a linear problem, regularization methods might be applied to solve an inverse problem which usually has more unknowns than equations. In the next subsections, traditional regularization methods will be covered.

### 3.4.1 The Tikhonov Regularization

Perhaps the most traditional technique for regularizing inverse problems with linear and limited operators is the Tikhonov Regularization (Kirsch, 2011; Tikhonov, 1963). Not only in this case but also in underdetermined systems of equations, i.e., where the number of equations is less than that of variables. In general, the principle of this method is to determine the solution  $x \in X$  that minimizes  $\|\mathcal{K}\{x\} - y\|$  for some norm in  $Y$ . If  $X$  has a finite dimension and  $\mathcal{K}$  is compact, then the minimization problem is also ill-posed.

The Tikhonov Regularization proposes to determine a solution  $x^{\alpha_T} \in X$  which minimizes the Tikhonov's functional  $J_{\alpha_T}$ <sup>3</sup>:

$$J_{\alpha_T}(x) := \|\mathcal{K}\{x\} - y\|^2 + \alpha_T \|x\|^2 \quad (3.80)$$

in which  $\alpha_T > 0$  is a constant and  $X$  and  $Y$  are Hilbert spaces. In this case,  $x^{\alpha_T}$  is the solution of:

$$\alpha_T x^{\alpha_T} + \mathcal{K}^* \{\mathcal{K}\{x^{\alpha_T}\}\} = \mathcal{K}^* \{y\} \quad (3.81)$$

where  $\mathcal{K}^*$  is the adjoint operator of  $\mathcal{K}$ . Therefore, the solution  $x^{\alpha_T}$  can be written in the form in (2.28) through

$$\mathcal{R}_{\alpha_T} := (\alpha_T \mathcal{I} + \mathcal{K}^* \mathcal{K})^{-1} \mathcal{K}^* : Y \rightarrow X \quad (3.82)$$

where  $\mathcal{I}$  is the identity operator. The linear system (3.81) can also be written as:

$$(\alpha_T \mathcal{I} + \mathcal{K}^* \mathcal{K}) x^{\alpha_T} = \mathcal{K}^* \{y\} \quad (3.83)$$

The upper limit of the error for this approximation is known and expressed in terms of the norm of error in  $y$ , i.e.,  $\|y - y^\delta\| \leq \delta$ ; and in terms of a constant  $\Delta$  such that  $\|z\| \leq \Delta$ ,  $x = \mathcal{K}^* \{z\} \in \mathcal{K}^* \{Y\}$ , and  $z \in Y$ . In this case, if  $\alpha_T(\delta) = c\delta/\Delta$  for a  $c > 0$ , then the error of

---

<sup>3</sup>Another possible interpretation for the Tikhonov Regularization was recently proposed by Gerth (2021). The author has observed that the exact solution is estimated from the range of the adjoint operator and the properties are derived through the concept of approximate source conditions.

the solution  $x^{\alpha_T(\delta), \delta}$ , which is based on these assumptions, follows below (Kirsch, 2011):

$$\|x^{\alpha_T(\delta), \delta} - x\| \leq \frac{1}{2} (1/\sqrt{c} + \sqrt{c}) \sqrt{\delta E} \quad (3.84)$$

On the other hand, if the auxiliary function  $z$  is defined as  $x = \mathcal{K}\{\mathcal{K}^*\{z\}\} \in \mathcal{K}\{\mathcal{K}^*\{X\}\}$  and choosing  $\alpha_T(\delta) = c(\delta/\Delta)^{2/3}$  for a  $c > 0$ , then the upper limit of the error it will be (Kirsch, 2011):

$$\|x^{\alpha_T(\delta), \delta} - x\| \leq \left( \frac{1}{2\sqrt{c}} + c \right) \Delta^{1/3} \delta^{2/3} \quad (3.85)$$

In other words, (3.84) and (3.85) establish that Tikhonov regularization is optimum given information  $\|(\mathcal{K}^*)^{-1}\{x\}\| \leq \Delta$  or  $\|(\mathcal{K}^*\mathcal{K})^{-1}\{x\}\| \leq \Delta$ , provided that  $\mathcal{K}^*$  is an one-to-one operator.

It is worth noting that the regularization method is also a correction to the eigenvalues of the system. In other words, if the eigenvalues of  $\mathcal{K}$  tend to zero due to their ill-posedness, those of  $\alpha_T \mathcal{I} + \mathcal{K}^* \mathcal{K}$  are established above zero by  $\alpha_T > 0$ . Also highlighted is the relationship between the choice of  $\alpha_T$  and  $\delta$ . This relationship is such that  $\alpha_T$  tends to zero when  $\delta \rightarrow 0$ . Also, the smoother  $x$  is, the slower  $\alpha_T$  will tend to zero. Therefore, in situations where it is already known that smoothness is a predominant aspect of solution  $x$ , the Tikhonov regularization method is not optimal. In these cases, the Landweber and Gradient-Conjugate methods, which will be discussed soon, perform better.

The method can be applied to the matrix equation (3.39). This is achieved if we define the column vector  $\boldsymbol{\chi}$ , which represents the main diagonal of  $\bar{\mathbf{E}}$  and the column vector  $\bar{\mathbf{E}}^{SF}$  which is the rearrangement of the matrix  $\bar{\mathbf{E}}^s$  in the following form<sup>4</sup>:

$$\bar{\mathbf{E}}^{SF} = \begin{bmatrix} E_{11}^s \\ E_{12}^s \\ \vdots \\ E_{N_M N_S}^s \end{bmatrix} \quad (3.86)$$

In addition, we will define the  $\bar{\mathbf{K}}$  matrix as:

$$\bar{\mathbf{K}} = \begin{bmatrix} G_{111}^D E_{111} & G_{112}^D E_{121} & \cdots & G_{1ij}^D E_{ij1} & \cdots & G_{1N_I N_J}^D E_{N_I N_J 1} \\ G_{111}^D E_{112} & G_{112}^D E_{122} & \cdots & G_{1ij}^D E_{ij2} & \cdots & G_{1N_I N_J}^D E_{N_I N_J 2} \\ \vdots & \vdots & \ddots & \vdots & \ddots & \vdots \\ G_{m11}^D E_{11s} & G_{m12}^D E_{12s} & \cdots & G_{mij}^D E_{ijs} & \cdots & G_{mN_I N_J}^D E_{N_I N_J s} \\ \vdots & \vdots & \ddots & \vdots & \ddots & \vdots \\ G_{N_M 11}^D E_{11N_S} & G_{N_M 12}^D E_{12N_S} & \cdots & G_{N_M ij}^D E_{ijN_S} & \cdots & G_{N_M N_I N_J}^D E_{N_I N_J N_S} \end{bmatrix} \quad (3.87)$$

---

<sup>4</sup>The “F” operator will always mean transforming a matrix into a column vector throughout this thesis. The order will be standardized in column first and row after. The letter F was chosen in order to refer to the word flatten.

Through these definitions, (3.39) can be resolved by:

$$\mathbf{x} = (\bar{\mathbf{K}}^* \bar{\mathbf{K}} + \alpha_T \bar{\mathbf{I}})^{-1} \bar{\mathbf{K}}^* \bar{\mathbf{E}}^{sF} \quad (3.88)$$

where  $\bar{\mathbf{K}}^*$  is the conjugate-transposed of  $\bar{\mathbf{K}}$ , which is equivalent to the operator's adjoint in this case. It is not necessary to apply a matrix inversion algorithm on  $(\bar{\mathbf{K}}^* \bar{\mathbf{K}} + \alpha_T \bar{\mathbf{I}})$ . Instead, a linear systems solution algorithm can be used where the matrix of coefficients is  $(\bar{\mathbf{K}}^* \bar{\mathbf{K}} + \alpha_T \bar{\mathbf{I}})$  and the column vector on the right side of the equation is  $\bar{\mathbf{K}}^* \bar{\mathbf{E}}^{sF}$ . This type of approach is computationally more efficient. In a way similar to (3.88), the method can also be applied in (3.40)-(3.41) provided that arrays are adequately rearranged.

An important question is how to choose the  $\alpha_T$  value. Since choosing this value based on the strategies of (3.84) and (3.85) to (3.88) is hardly possible, an alternative capable of calculating a suitable value for this parameter is needed. In the following subsubsections, some methods of determining  $\alpha_T$  will be discussed.

### The Discrepancy Principle of Morozov

A possible strategy is to choose the parameter  $\alpha_T$  that satisfies the following equation:

$$\|\mathcal{K}\{x^{\alpha_T, \delta}\} - y^\delta\| = \delta \quad (3.89)$$

This strategy is known in the literature as the Discrepancy Principle of Morozov (Kirsch, 2011; Morozov, 1984). It is based on the fact that  $\|x^{\alpha_T}\|$  is monotonically non-increasing and tends to zero when  $\alpha_T \rightarrow \infty$ ; and also on the fact that  $\|\mathcal{K}\{x_T^\alpha\} - y\|$  is monotonically decreasing and tends to zero when  $\alpha_T \rightarrow 0$ . Under these conditions, the problem is equivalent to finding the minimum of the function:

$$f_{\alpha_T}(\alpha_T) := \|\mathcal{K}\{x^{\alpha, \delta}\} - y^\delta\|^2 - \delta^2 \quad (3.90)$$

The minimum of (3.90) can be approximated by classical methodologies such as Newton's method (Rao, 2019), where the derivative is the solution to the equation:

$$(\alpha_T \mathcal{I} + \mathcal{K}^* \mathcal{K}) \frac{d}{d\alpha_T} x^{\alpha, \delta} = -x^{\alpha, \delta} \quad (3.91)$$

in which the best order of convergence is  $O(\sqrt{\delta})$ . In addition, a suggestion for initial value in this algorithm is (Kirsch, 2011):

$$\alpha_{T,0} = \frac{\delta \|\mathcal{K}\|^2}{\|y^\delta\| - \delta} \quad (3.92)$$

Applying the method in (3.88) requires resolving the system several times up to the stop criterion for the functional (3.90) to be achieved. Hence, this is classified as *a posteriori* strategy because the parameter is defined during the execution. In addition, it is necessary to have an

estimate of the error between the data obtained and the exact field, i.e.,  $\|E_{zs} - E_{zs}^\delta\| \leq \delta$ .

## Generalized Cross Validation

A strategy that does not depend on prior knowledge of the noise level present in the data is the Generalized Cross-Validation (GCV) method (Chen, 2017). In this type of method, the parameter  $\alpha_T$  is the minimum of the functional defined by:

$$f_{GCV}(\alpha_T) = \frac{\left\| \left( \bar{\mathbf{I}} - \bar{\mathbf{K}} [\bar{\mathbf{K}}^* \bar{\mathbf{K}} + \alpha_T \bar{\mathbf{I}}]^{-1} \bar{\mathbf{K}}^* \right) \bar{\mathbf{E}}^{sF} \right\|^2 / (N_M N_S)}{\left[ \text{Trace} \left( \bar{\mathbf{I}} - [\bar{\mathbf{K}}^* \bar{\mathbf{K}} + \alpha_T \bar{\mathbf{I}}]^{-1} \bar{\mathbf{K}}^* \right) / (N_M N_S) \right]^2} \quad (3.93)$$

Therefore, this is also an *a posteriori* strategy because  $\alpha_T$  is calculated while the problem is addressed. In this case, one may use a one-dimensional kind of optimizer like the Golden Section Method (Rao, 2019). However, in some cases, the region where the optimum solution is located can be very close to a flat one (Varah, 1983), turning it into a challenging task for traditional one-dimensional optimization methods. In addition, the strategy depends on the normality assumption of noise distribution (Gilmore et al., 2009). A more in-depth discussion regarding the theoretical aspects of this method can be found in (Golub et al., 1979).

## L-Curve Method

Another *a posteriori* strategy is to choose a value that represents a balance between the two terms of the functional (3.80), i.e., the residual norm and the solution norm. When the value of these two terms is plotted on a graph, it is common to observe an L-shaped curve (Figura 3.3). The strategy is to choose the value of  $\alpha_T$  corresponding to the inflection point on the L-curve from that graph. There are numerical methods to determine this point (Calvetti et al., 2000; Hansen and O’Leary, 1993). A simple method is to choose the value of  $\alpha_T$  from a finite set of options that has the shortest normalized distance from the origin of the L-curve graph. That is, given a set of parameters  $\langle \alpha_T^1, \dots, \alpha_T^N \rangle$  with their respective pairs  $(\|\mathcal{K}x - y\|, \|x\|)$ , the one whose distance:

$$d(\alpha_T^n) = \sqrt{\left( \frac{\|\mathcal{K}\{x^{\alpha_i}\} - y\| - \min(\|\mathcal{K}\{x^\alpha\} - y\|)}{\max(\|\mathcal{K}\{x^\alpha\} - y\|) - \min(\|\mathcal{K}\{x^\alpha\} - y\|)} \right)^2 + \left( \frac{\|x^{\alpha_i}\| - \min(\|x^\alpha\|)}{\max(\|x^\alpha\|) - \min(\|x^\alpha\|)} \right)^2} \quad (3.94)$$

is minimal. This kind of strategy is similar to the Compromise Programming technique within the subject of Multiobjective Optimization and Decision Theory (Chankong and Haimes, 2008).

As stated by Hansen and O’Leary (1993), this method is similar to GCV and Morozov’s Discrepancy Principle. In addition, the authors observed in their experiments that whenever the GCV found a good value, the corresponding point on the L-curve was located at the inflection.

However, the advantages of this approach are its easy numerical implementation and the rare influence of errors correlated in the performance of the methodology. A disadvantage is to estimate a reasonable interval in which the inflection is present. The Lanczos' Bidiagonalization Method might be used to estimate the interval (Calvetti et al., 2002). Its computational cost  $O(N_M N_S N_I N_J)$  is less than a formulation of Decomposition by Singular Value (SVD) whose cost is  $O(N_M N_S (N_I N_J)^2)$  (Gilmore et al., 2009).

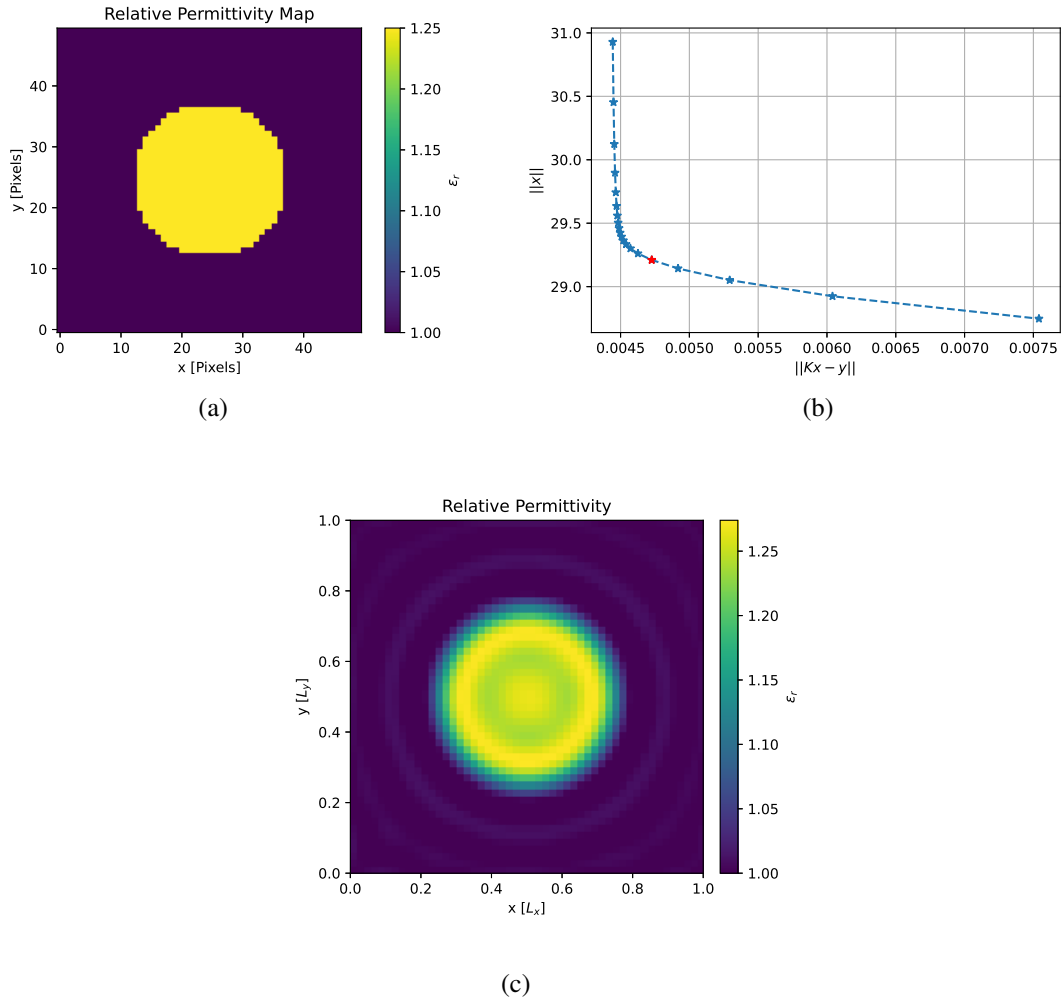


Figura 3.3: Example of applying the L-curve Method to a linear problem where it presupposes knowledge of the total field. (a) A simple instance of a contrast dielectric circle  $\chi = 0.25$  and radius  $0.8\lambda_b$ . Respecting the degrees of freedom, the scattered field was sampled in 45 positions for 45 incidence angles at a distance of  $10\lambda_b$  from the center of the image. (b) L-curve considering 20 values of  $\alpha_T$  in a range of  $10^{-5}$  a  $10^{-2}$ . The red dot represents the solution with the shortest normalized distance to the origin. Its  $\alpha_T$  value is approximately  $2.3357 \times 10^{-3}$ . (c) Reconstruction of the image using the  $\alpha_T$  value from the red dot. No inverse crime was committed since the data were obtained from the analytical solution.

## Trial and Error

Finally, the trial-and-error approach is another popular strategy. A set of  $\alpha_T$  values are tested for a canonical problem. The most reasonable result value is chosen according to some criterion, and this value is used for other experiments. In many practical situations, no effort is required to obtain the best value but only identifying a range in which any chosen value produces reasonable results. Therefore, this is *a priori* strategy, in which the value is defined at the input of the algorithm.

### 3.4.2 The Landweber Regularization

It is possible to solve the system  $\mathcal{K}\{x\} = y$  iteratively if we write the solution  $x$  in the form  $x = (\mathcal{I} - \alpha_L \mathcal{K}^* \mathcal{K})x + \alpha_L \mathcal{K}^*\{y\}$  for an  $\alpha_L > 0$ . That is, the solution is computed iteratively by:

$$x^m = (\mathcal{I} - \alpha_L \mathcal{K}^* \mathcal{K})x^{m-1} + \alpha_L \mathcal{K}^*\{y\} \quad (3.95)$$

where the initial guess can be defined as  $x^0 := 0$ . This scheme is similar to a descent step algorithm in which the quadratic functional  $\|\mathcal{K}\{x\} - y\|^2$  is minimized. The regularization operator equivalent to the definition (2.28) can be expressed in this case as:

$$\mathcal{R}_L := \alpha_T \sum_{k=0}^{m-1} (\mathcal{I} - \alpha_L \mathcal{K}^* \mathcal{K})^k \mathcal{K}^*, \quad m = 1, 2, \dots \quad (3.96)$$

However, it is necessary to define a stopping criterion for the method. If  $\mathcal{K} : X \rightarrow Y$  is a linear, compact, and one-to-one operator with a dense interval, then the sequence  $x^{m,\delta}$  of (3.95),  $m = m = 0, 1, 2, \dots$ , can be rearranged to:

$$x^{m+1,\delta} = x^{m,\delta} + \alpha_L \mathcal{K}^*\{y - \mathcal{K}\{x^{m,\delta}\}\}, \quad m = 0, 1, 2, \dots \quad (3.97)$$

Within this definition, it is assumed that  $\|y - y^\delta\| \leq \delta$ ,  $\|y^\delta\| \geq r\delta$  for an  $r > 1$ ,  $\delta \in (0, \delta_0)$  and  $0 \leq \alpha_L \leq 1/\|\mathcal{K}\|^2$ . Under these conditions, the stop criterion  $\|\mathcal{K}\{x^{m,\delta}\} - y^\delta\| \leq r\delta$  is well defined, i.e., there is a  $m = m(\delta) \in \mathbb{N}_0$  for which  $\|\mathcal{K}\{x^{m,\delta}\} - y^\delta\| \leq r\delta$ . In addition, it is possible to demonstrate that this sequence converges to  $x$  and that, if  $x = \mathcal{K}^*\{z\} \in \mathcal{K}^*(Y)$  or  $x = \mathcal{K}^*\{\mathcal{K}\{z\}\} \in \mathcal{K}^*\mathcal{K}(X)$  for a  $z$  such that  $\|z\| \leq \Delta$ , then the convergence order is expressed by (Kirsch, 2011):

$$\|x^{m(\delta),\delta} - x\| \leq c\sqrt{\Delta\delta} \quad (3.98)$$

$$\|x^{m(\delta),\delta} - x\| \leq c\Delta^{1/3}\delta^{2/3} \quad (3.99)$$

respectively, for a  $c > 0$ . In other words, this means that the choice  $m(\delta)$  is optimal.

The method can be applied in  $\bar{\mathbf{E}}^{s,F} = \bar{\mathbf{K}}\chi$  as illustrated in algorithm 1.

---

**Algorithm 1:** Landweber Method.

---

**Input:**  $\bar{\mathbf{E}}^{s,F}, \bar{\mathbf{K}}, \alpha_L, \delta$

**Output:**  $\boldsymbol{x}^m$

```

1  $\boldsymbol{x}^0 \leftarrow \mathbf{0}$ 
2  $m \leftarrow 0$ 
3 while  $\|\bar{\mathbf{K}}\boldsymbol{x}^m - \bar{\mathbf{E}}^{s,F}\| \leq \delta$  do
4    $\boldsymbol{x}^{m+1} = \boldsymbol{x}^m + \alpha_T \bar{\mathbf{K}}^* (\bar{\mathbf{E}}^{s,F} - \bar{\mathbf{K}}\boldsymbol{x}^m)$ 
5    $m \leftarrow m + 1$ 
6 end

```

---

### 3.4.3 The Conjugate Gradient Method

The Conjugated Gradient Method (CG) is very popular and applied to several situations. This section will focus on its formulation for the inverse problem with integral equations considering bounded, linear, and injective operators between Hilbert spaces. Particularly, given equation  $\mathcal{K}\{x\} = y$  in which  $\mathcal{K} : X \rightarrow Y$  has the previous properties commented and the adjoint  $\mathcal{K}^* : Y \rightarrow X$ , we define the functional:

$$f(x) := \|\mathcal{K}\{x\} - y\|^2 = \langle \mathcal{K}\{x\} - y, \mathcal{K}\{x\} - y \rangle \quad (3.100)$$

The gradient of (3.100) is calculated by the Riesz representation of the Frechét derivative, which is expressed by:

$$\nabla f(x) := 2\mathcal{K}^*\{\mathcal{K}\{x\} - y\} \in X \quad (3.101)$$

Auxiliary, we will call two elements  $p, q \in X$  as  $\mathcal{K}$ -conjugated if  $\langle \mathcal{K}\{p\}, \mathcal{K}\{q\} \rangle = 0$ . If  $\mathcal{K}$  is one-to-one, this definition has the same properties as an inner product in  $X$ .

From these definitions, we can define the sequence  $x^m$  established for CG as:

$$x^{m+1} = x^m - t_m p^m \quad (3.102)$$

where:

$$t_m = \langle \mathcal{K}\{x^m\} - y, \mathcal{K}\{p^m\} \rangle \quad (3.103)$$

$$p^{m+1} := \mathcal{K}^*\{\mathcal{K}\{x^{m+1}\} - y\} + \gamma_m p^m \quad (3.104)$$

$$\gamma_m := \frac{\|\mathcal{K}^*\{\mathcal{K}\{x^{m+1}\} - y\}\|^2}{\|\mathcal{K}^*\{\mathcal{K}\{x^m\} - y\}\|^2} \quad (3.105)$$

In this method, the gradients of the  $x$  sequences are orthogonal. Furthermore, the sequences of directions  $p$  are  $\mathcal{K}$ -conjugated. Under certain conditions, this algorithm converge to a solution in which  $\mathcal{K}^*\{\mathcal{K}\{x^{m+1}\} - y\} = 0$ . However, when only a  $y^\delta \in I$  is known such that  $\|y^\delta - y\| \leq \delta$ , then a stopping criterion is the threshold  $\|\mathcal{K}\{x^{m,\delta}\} - y^\delta\| \leq \delta$ .

The application of this method on  $\bar{\mathbf{E}}^{s,F} = \bar{\mathbf{K}}\boldsymbol{\chi}$  can be seen in algorithm 2. One of the advantages is that it does not depend on a regularization parameter as Tikhonov and Landweber methods. However, the method depends on more operations.

---

**Algorithm 2:** Conjugated Gradient Method.

---

**Input:**  $\bar{\mathbf{E}}^{s,F}, \bar{\mathbf{K}}, \delta$   
**Output:**  $\boldsymbol{\chi}^m$

- 1  $\mathbf{p}^0 \leftarrow -\bar{\mathbf{K}}^* \bar{\mathbf{E}}^{s,F}$
- 2  $\boldsymbol{\chi}^0 \leftarrow \mathbf{0}$
- 3  $m \leftarrow 0$
- 4 **while**  $\|\bar{\mathbf{K}}^*(\bar{\mathbf{K}}\boldsymbol{\chi}^m - \bar{\mathbf{E}}^{s,F})\| < \delta$  **do**
- 5      $t_m = \frac{[\bar{\mathbf{K}}\boldsymbol{\chi}^m - \bar{\mathbf{E}}^{s,F}]^T \bar{\mathbf{K}}\mathbf{p}^m}{\|\bar{\mathbf{K}}\mathbf{p}^m\|^2}$
- 6      $\boldsymbol{\chi}^{m+1} \leftarrow \boldsymbol{\chi}^m - t_m \mathbf{p}^m$
- 7      $\gamma_m = \frac{\|\bar{\mathbf{K}}^*(\bar{\mathbf{K}}\boldsymbol{\chi}^{m+1} - \bar{\mathbf{E}}^{s,F})\|^2}{\|\bar{\mathbf{K}}^*(\bar{\mathbf{K}}\boldsymbol{\chi}^m - \bar{\mathbf{E}}^{s,F})\|^2}$
- 8      $\mathbf{p}^{m+1} = \bar{\mathbf{K}}^*(\bar{\mathbf{K}}\boldsymbol{\chi}^{m+1} - \bar{\mathbf{E}}^{s,F}) + \gamma_m \mathbf{p}^m$
- 9      $m \leftarrow m + 1$
- 10 **end**

---

### 3.4.4 Spectral Cut-Off

Since the problem is ill-posed,  $\bar{\mathbf{K}}$  is a matrix whose eigenvalues approach zero. When the Single Value Decomposition (SVD) is applied in  $\bar{\mathbf{K}}$ , the following product is obtained:

$$\bar{\mathbf{K}} = \bar{\mathbf{U}} \bar{\boldsymbol{\xi}} \bar{\mathbf{V}}^* \quad (3.106)$$

in which  $\bar{\mathbf{U}}$  is a matrix  $N_M N_S \times N_M N_S$  composed of singular vectors  $\mathbf{u}_m$ 's which are orthogonal and unitary;  $\bar{\mathbf{V}}$  is an  $N_I N_J \times N_I N_J$  matrix composed of singular vectors  $\mathbf{v}_m$ 's which are also orthogonal and unitary; and  $\bar{\boldsymbol{\xi}}$  is the diagonal matrix composed of the singular values  $\xi_i$ 's which are real and place in nonincreasing order  $\xi_1 \geq \xi_2 \geq \dots \geq 0$ . Mathematically, the solution  $\boldsymbol{\chi}$  can be written as:

$$\boldsymbol{\chi} = \bar{\mathbf{K}}^{-1} \bar{\mathbf{E}}^{s,F} = \sum_{\xi_i \neq 0} \frac{1}{\xi_i} (\mathbf{u}_i^* \cdot \bar{\mathbf{E}}^{s,F}) \mathbf{v}_i \quad (3.107)$$

Once  $\bar{\boldsymbol{\xi}}$  contains eigenvalues close or equal to zero, the operation (3.107) is not feasible since it can lead to substantial numerical errors. This is equivalent to saying that the inverse of  $\bar{\mathbf{K}}$  is unbounded. Therefore, an alternative is to exclude eigenvalues smaller than a threshold, i.e.,  $\xi_i < \alpha_S$ . Then, (3.107) can be written as an operator regularization  $\mathcal{R}_{SC}$  as:

$$\boldsymbol{\chi} = \mathcal{R}_{SC}\{\bar{\mathbf{E}}^{s,F}\} = \sum_{\xi_i > \alpha_S} \frac{1}{\xi_i} (\mathbf{u}_i^* \cdot \bar{\mathbf{E}}^{s,F}) \mathbf{v}_i \quad (3.108)$$

This regularization method is called the Spectral Cut-Off and depends on setting a cutting parameter  $\alpha_S$ . This solution is also known as Minimum Norm. This method is suitable when the size of the matrices is not too large since the computational cost for evaluating eigenvectors and eigenvalues may be high. However, the method is convenient for classifying ill-posed problems. The reason is: problems whose eigenvalues drop to zero smoothly are called mildly ill-posed; problems whose eigenvalues rapidly decay to zero are called severely ill-posed problems.

## 3.5 Qualitative Methods

When the contrast estimation is not a required information, qualitative methods are more efficient as they retrieve information about shape and position of scatterers with less computational effort. Even though applications that do not require electric property retrieval seem to be rare, qualitative methods might provide initial solutions for quantitative ones. In the next subsections, some of the qualitative methods are discussed. For a survey of them, readers are referred to (Potthast, 2006).

### 3.5.1 Linear Sampling Method

The Linear Sampling Method (LSM) is a fast and traditional qualitative method (Colton and Kirsch, 1996; Colton and Kress, 2019). If plane waves propagate through the space and the scattered field is sampled in far field conditions, then the scattered field admits the asymptotic behavior given by:

$$E_{s_z}(\rho, \theta, \phi) = \frac{e^{-jk_b\rho}}{\sqrt{\rho}} E_{s_\infty}(\theta, \phi) \quad (3.109)$$

where  $E_{s_\infty}(\theta, \phi)$  is the far-field pattern of the scattered field. For any point  $\boldsymbol{\rho}$  in  $S$ , the following far-field integral holds:

$$\int_D d\phi E_{s_\infty}(\theta, \phi) g(\boldsymbol{\rho}, \phi) = \Phi_\infty(\theta, \boldsymbol{\rho}) \quad (3.110)$$

where  $\Phi_\infty(\theta, \boldsymbol{\rho})$  is the far-field pattern of the Green's function  $-(jk_b^2/4)G_{2D}^D(\theta, \boldsymbol{\rho})$  when the source point is at  $\boldsymbol{\rho}$  and the observation point is in the direction  $\theta$ .  $\Phi_\infty(\theta, \boldsymbol{\rho})$  is a function that might be approximated by:

$$\Phi_\infty(\theta, \boldsymbol{\rho}) \approx \frac{-j}{4} \sqrt{\frac{2}{\pi k_b}} e^{j\pi/4} e^{jk_b \cos(\theta - \psi)} \quad (3.111)$$

where  $\boldsymbol{\rho} = \langle x, y \rangle = \langle \rho \cos(\psi), \rho \sin(\psi) \rangle$ .

The idea behind LSM is to choose an indicator function defined in  $S$  which determines if a spatial point belongs or not to a scatterer. The integral equation (3.110) is solved for  $g(\boldsymbol{\rho}, \phi)$  for each  $\boldsymbol{\rho}$  in  $S$  and each  $\phi$  in  $D$ . The integral equation might be solved through a regularization

method (Section 3.4) after computing the kernel in (3.110) by (3.109) based on the scattered field data and the right-hand-side (3.111). The indicator function  $I(\boldsymbol{\rho})$  is defined as:

$$I(\boldsymbol{\rho}) = \|g(\boldsymbol{\rho})\| = \sqrt{\int_D d\theta |g(\boldsymbol{\rho})|^2} \quad (3.112)$$

The value indicator function becomes unbound if  $\boldsymbol{\rho}$  is not within a scatterer region (Colton and Kirsch, 1996). Therefore, after computing  $I(\boldsymbol{\rho})$  for many points in  $S$ , we are able to recover the scatterer image by verifying if  $I(\boldsymbol{\rho})$  tends to infinite or not. Due to discretization of  $D$  and  $S$  and noise presence in the scattered field data,  $I(\boldsymbol{\rho})$  cannot be infinite. Therefore is necessary to set a threshold heuristically for which the background will be set apart from the scatterer.

The LSM is not limited to far-field data. For near-field data, the integral equation (3.110) is replaced by (Cakoni and Colton, 2016):

$$\int_D d\phi E_{s_z}(\theta, \phi) g(\boldsymbol{\rho}, \phi) = -\frac{jk_b^2}{4} G_{2D}^D(\theta, \boldsymbol{\rho}) \quad (3.113)$$

The LSM cannot estimate the dielectric properties of the media. However, it might help the performance of other inversion methods (Bao et al., 2007; Catapano et al., 2007b) and some approximations might be done to turn it into a quantitative method (Crocco et al., 2012). Further discussion may be found in (see Chen, 2017, chap. 5), (Cakoni and Colton, 2016) and (see Pastorino, 2010a, chap. 5).

### 3.5.2 Orthogonality Sampling Method

The Orthogonality Sampling Method (OSM) is another approach to define an indicator function which detects the presence of scatterers (Potthast, 2010). Instead of writing it in terms of the solution of the integral equation (3.110), the orthogonality between far-field data and an exponential function is tested. Another interpretation is the superposition of plane waves back into the region of the scatterer, which is a very known idea. Mathematically, the orthogonality is tested according to (Akıncı et al., 2016; Potthast, 2010):

$$E_{s_z}^{red}(\boldsymbol{\rho}, \theta) = \int_D d\phi E_{s_\infty}(\theta, \phi) e^{-jk_b \rho \cos(\theta - \psi)} = \int_D d\phi \frac{e^{-jk_b/4}}{\sqrt{8\pi k_b}} E_{s_z}(\theta, \phi) e^{-jk_b \rho \cos(\theta - \psi)} \quad (3.114)$$

where  $E_{s_z}^{red}$  is know as the reduced scattered field. The indicator function is defined as:

$$I(\boldsymbol{\rho}) = \int_D d\theta |E_{s_z}^{red}(\boldsymbol{\rho}, \theta)|^2 \quad (3.115)$$

Therefore, the indicator function computation does not require solving an integral equation. Rather it depends on integrating reduced scattered field. The maxima of the function is

used to identify the scatterers. Near-field data is also compatible with the method. However, the reduced scattered field definition needs to be adapted (Akıncı et al., 2016):

$$E_{s_z}^{red}(\boldsymbol{\rho}, \theta) == \int_D d\phi E_{s_z}(\theta, \phi) K^{TM}(\theta, \boldsymbol{\rho}) \quad (3.116)$$

where:

$$K^{TM}(\theta, \boldsymbol{\rho}) = \frac{-2j}{\pi R_O} \sum_{n=-\infty}^{\infty} \frac{J_n(k_b \rho)}{H_n^{(2)}(k_b R_O)} e^{-jn(\theta - \psi)} \quad (3.117)$$

Akıncı et al. (2016) stated that the reduced scattered field is directly related to the electrical properties of the scatterers. Bevacqua et al. (2020) went further and concluded that the reduced scattered field can be related to the radiating component of the induced currents. As a consequence, OSM is able to image discontinuities within unknown scatterers and identify regions with different electromagnetic properties, differently than other qualitative methods.

## 3.6 Deterministic Quantitative Methods

Now considering the nonlinear and quantitative problem, there is a class of methods that solve the equations in a deterministic fashion, i.e., without the use of random operations. This class is the most popular in the problem literature, which has a large number of methods. This section will discuss both traditional methods relevant to the history of literature and those that are considered state-of-the-art.

### 3.6.1 The Born Iterative Method

One of the first methods to become popular was proposed by Wang and Chew (1989). Assuming a homogeneous background medium, the authors proposed an iterative approach where each iteration was equivalent to the solution by Neumann series. From an initial estimate of the contrast function, the iterative process is based on obtaining a solution for the total field through a direct solver and solving the inverse linear problem to update the estimate of the contrast function based on the current estimate of the total field (algorithm 3). Therefore, the method is based on a linearization strategy, i.e., dividing the problem into two linear subproblems.

Initially, the authors used the Method of Moments defined by Richmond (1965) as the forward solver and Tikhonov's Regularization with a parameter chosen by trial-and-error as an inverse solver. However, other solvers can be used in such a way that the method has become a generic structure where many strategies can be defined, for example, the other regularizers defined in the previous section, the use of Level Set functions (Shah and Moghaddam, 2018) and Quadratic Programming (Batista et al., 2021). This latter technique may be suitable for coupling different forms of regularization through the objective function definition.

In the original article, the authors called the Modified Newton Method algorithm since

---

**Algorithm 3:** Born Iterative Method.

---

**Input:**  $\bar{\mathbf{E}}^s, \bar{\mathbf{E}}^i, \bar{\mathbf{G}}^D, \bar{\mathbf{G}}^S$

**Output:**  $\bar{\chi}, \bar{\mathbf{E}}$

- 1 Compute an initial guess  $\bar{\chi}^0$  based on available information
  - 2  $m \leftarrow 0$
  - 3 **while** some criterion is not reached **do**
  - 4   | Update  $\bar{\mathbf{E}}^m$  based on the current  $\bar{\chi}^m$  estimation
  - 5   | Update  $\bar{\chi}^m$  based on the current  $\bar{\mathbf{E}}^m$  estimation
  - 6 **end**
- 

the iterative process can be compared with the definition of a search direction for a current solution. However, the algorithm was known in the literature as the Born Iterative Method (BIM) since the objective was to propose a solution for cases where the Born Approximation was not valid. Although this was the intention, the algorithm also has limits concerning the application in cases of high contrast. Generally, the initial solution is determined by the Born Approximation, and therefore, the convergence of the algorithm can be compromised when strong scatterers are considered. Moghaddam and Chew (1993) went deeper into this issue showing good reconstructions for objects with a diameter of  $8.5\lambda_b$  in relation to the central frequency of operation<sup>5</sup> and contrast  $\chi = 1$ . However, there is no robust measurement in the literature on the relationship between contrast and size that BIM can support. Also noteworthy is the comparison between BIM and the Tarantola Method carried out by Moghaddam et al. (1991). Although Tarantola's Method has a lower computational cost than BIM, the latter can converge faster and be more robust with objects that have edges.

It is also necessary to highlight that BIM implementations that use parameter-based regularizers need strategies to choose their value. As in the original article, many other works in the literature that use this kind of regularizer choose a fixed value for all iterations based on trial-and-error strategy (Batista et al., 2021; Chew and Lin, 1995; Chew and Liu, 1994; Li et al., 2004; Yao et al., 1997). In fact, the choice is not trivial, and there is no simple rule for the optimal choice in the nonlinear problem (Engl and Neubauer, 1988).

However, there are strategies for a dynamic definition of  $\alpha_T$  throughout the iterative process. In the original work, the authors state that high  $\alpha_T$  values are essential to avoid high-spatial-frequency components in the contrast function associated with noise in the image. However, these components can also be necessary for the object's vertex reconstructions. As advocated by Moghaddam and Chew (1992), the small eigenvalues in  $\bar{\mathbf{K}}$  can better reconstruct the contours when the contrast function is already sufficiently smooth during the reconstruction process. For this reason, they propose that, in the first BIM iterations, high values of  $\alpha_T$  should be used to filter out sudden variations in the contrast function; after that,  $\alpha_T$  would be decreased to improve the contours of the image. As they explain, this strategy is equivalent to start looking

---

<sup>5</sup>In this work, the authors formulated the problem in the time domain. This type of formulation has the advantage of considering more frequencies in the inversion process.

for solutions in a smaller subspace and expanding over iterations. Rules for this adaptation of  $\alpha_T$  have also been proposed in the literature (Franchois and Pichot, 1997; Joachimowicz et al., 1991; Lavarello and Oelze, 2008; Zaiping et al., 2000). Similarly, methodologies that consider scattered field data with multiple frequencies suggest a similar dynamic use, i.e., starting with the lowest frequencies and ending with the highest ones (Batista et al., 2021; Chew and Lin, 1995).

### 3.6.2 The Distorted Born Iterative Method

The same BIM authors also published an alternative methodology the following year (Chew and Wang, 1990). In this new approach, the inverse subproblem equations are not solved for  $\chi$  but a variation  $\Delta\chi$ . Consequently, the contrast function is updated at each iteration  $t$  by the form  $\chi^t = \chi^{t-1} + \Delta\chi$ . However, to solve the inverse subproblem as a function of  $\Delta\chi$ , it is necessary to solve the integral equation considering a inhomogeneous background medium according to (B.28). Therefore, at each iteration, Green's function for the inhomogeneous medium (B.29) needs to be calculated, taking the contrast estimate at the end of the previous iteration as the background medium.

The following equation must be considered for calculating the inhomogeneous Green function in a two-dimensional problem for a pair of points  $\boldsymbol{\rho}_m$  e  $\boldsymbol{\rho}_n$ :

$$G_{in}(\boldsymbol{\rho}_m, \boldsymbol{\rho}_n) = G_{2D}(\boldsymbol{\rho}_m, \boldsymbol{\rho}_n) - \frac{jk_0^2}{4} \int_S dS' G_{2D}(\boldsymbol{\rho}_m, \boldsymbol{\rho}') \chi(\boldsymbol{\rho}') G_{in}(\boldsymbol{\rho}', \boldsymbol{\rho}_n) \quad (3.118)$$

where  $G_{2D}(\boldsymbol{\rho}_m, \boldsymbol{\rho}_n) = H_0^{(2)}(k_0 |\boldsymbol{\rho}_m - \boldsymbol{\rho}_n|)$ . By the reciprocity theorem, we can rewrite (3.118) as:

$$G_{in}(\boldsymbol{\rho}_n, \boldsymbol{\rho}_m) = G_{2D}(\boldsymbol{\rho}_n, \boldsymbol{\rho}_m) - \frac{jk_0^2}{4} \int_S dS' G_{2D}(\boldsymbol{\rho}_n, \boldsymbol{\rho}') \chi(\boldsymbol{\rho}') G_{in}(\boldsymbol{\rho}', \boldsymbol{\rho}_m) \quad (3.119)$$

Following the same discretization of (3.32)-(3.36), the  $S$  region will be divided into  $N_I N_J$  elements, and the value of  $G_{in}$  will be sampled at these points:

$$G_{in}(\boldsymbol{\rho}_n, \boldsymbol{\rho}_m) = G_{2D}(\boldsymbol{\rho}_n, \boldsymbol{\rho}_m) - \sum_{p=1}^{N_I} \sum_{q=1}^{N_J} \chi(\boldsymbol{\rho}_{pq}) G_{in}(\boldsymbol{\rho}_{pq}, \boldsymbol{\rho}_m) \left( \frac{jk_0^2}{4} \int_{S_k} dS' G_{2D}(\boldsymbol{\rho}_n, \boldsymbol{\rho}') \right) \quad (3.120)$$

Note that the integral in parentheses is equivalent to (3.30). So it can be replaced as was done in (3.38). Therefore, (3.120) can be written as a system of linear equations:

$$G_{nm}^{in} = G_{nm}^{2D} - \sum_{p=1}^{N_I} \sum_{q=1}^{N_J} \chi_{pq} G_{pqm}^{in} G_{npq}^{2D} \quad (3.121)$$

in which  $G_{nm}^{in} = G_{in}(\boldsymbol{\rho}_n, \boldsymbol{\rho}_m)$ ,  $G_{nm}^{2D} = G_{2D}(\boldsymbol{\rho}_n, \boldsymbol{\rho}_m)$ ,  $\chi_{pq} = \chi(\boldsymbol{\rho}_{pq})$ ,  $G_{pqm}^{in} = G_{in}(\boldsymbol{\rho}_{pq}, \boldsymbol{\rho}_m)$  and  $G_{npq}^{2D}$  is equivalent to (3.30).

The objective is to determine the inhomogeneous Green function  $G^{in}$  so that this replaces

$G_{2D}^D$  in (3.4). Therefore,  $\rho_m$  is a measurement point of the field in  $D$ . Now  $\rho_n$  is a point of discretization in  $S$ . Therefore, (3.121) should be rewritten as:

$$G_{mi,j}^{in} = G_{mi,j}^{2D} - \sum_{p=1}^{N_I} \sum_{q=1}^{N_J} \chi_{pq} G_{mpq}^{in} G_{ijpq}^S \quad (3.122)$$

where  $G_{mi,j}^{in} = G_{in}(\theta_m, x_i, y_j)$ ,  $G_{mi,j}^{2D}$  is the same of (3.9) for  $\theta_m, x_i, y_j$ ;  $\chi_{pq} = \chi(x_p, y_q)$  and  $G_{npq}^S$  is equivalent to (3.38). Consequently, (3.122) might be rewrite in a matrix fashion:

$$(\bar{\mathbf{I}} - \bar{\mathbf{G}}^S \bar{\boldsymbol{\chi}}) \bar{\mathbf{G}}^{in} = \bar{\mathbf{G}}^{2D} \quad (3.123)$$

in which the matrices  $\bar{\mathbf{G}}^{in}$  and  $\bar{\mathbf{G}}^{2D}$  are defined similarly to  $\bar{\mathbf{G}}^D$ . (3.123) can be solved using techniques for solving linear systems if we transform  $\bar{\mathbf{G}}^{in}$  e  $\bar{\mathbf{G}}^{2D}$  in column-vectors.

Therefore, the method proposed by Chew and Wang (1990) needs to solve (3.123) at each iteration, replacing the  $\bar{\boldsymbol{\chi}}$  matrix with the solution of the contrast function obtained at the end of the previous iteration. It should be noted that many forward solvers already use the matrix  $(\bar{\mathbf{I}} - \bar{\mathbf{G}}^S \bar{\boldsymbol{\chi}})$  in their formulations, such as the Method of Moments (Richmond, 1965). In addition, it is necessary to take into account the scattered field data in each iteration. Since the integral equation must be solved for  $\Delta\chi$ , the scattered field at the left-hand side of (3.39) must be subtracted from the current estimate done by the forward solver. That is, the forward solver calculates the total field  $\bar{\mathbf{E}}^t$  and the corresponding scattered field  $\bar{\mathbf{E}}^{s,t}$ . Thus, the inverse solver determines  $\Delta\chi$  from  $\bar{\mathbf{E}}^t$ ,  $\bar{\mathbf{G}}^{in,t}$ , and  $\Delta\bar{\mathbf{E}}^s = \bar{\mathbf{E}}^s - \bar{\mathbf{E}}^{s,t}$ .

This methodology is known as the Distorted Born Iterative Method (DBIM) since it is based on the Distorted-Wave Born Approximation (DWBA), similar to BA. However, the difference is that instead of approximating the total field by the incident one in a homogeneous medium, DWBA considers the total field due to an inhomogeneous medium. The basic operation of DBIM can be shown in algorithm 4.

---

**Algorithm 4:** Distorted Born Iterative Method.

---

**Input:**  $\bar{\mathbf{E}}^s, \bar{\mathbf{G}}^{2D}, \bar{\mathbf{G}}^S$

**Output:**  $\bar{\boldsymbol{\chi}}, \bar{\mathbf{E}}$

- 1 Compute an initial guess  $\bar{\boldsymbol{\chi}}^0$  based on available information
  - 2  $t \leftarrow 0$
  - 3 **while** some criterion is not reached **do**
  - 4     Solve  $(\bar{\mathbf{I}} - \bar{\mathbf{G}}^S \bar{\boldsymbol{\chi}}^t) \bar{\mathbf{G}}^{in,t} = \bar{\mathbf{G}}^{2D}$  for  $\bar{\mathbf{G}}^{in,t}$
  - 5     Solve the direct problem for  $\bar{\mathbf{E}}^t$  and  $\bar{\mathbf{E}}^{s,t}$
  - 6      $\Delta\bar{\mathbf{E}}^s = \bar{\mathbf{E}}^s - \bar{\mathbf{E}}^{s,t}$
  - 7     Solve the inverse linear problem  $\Delta\bar{\mathbf{E}}^s = \bar{\mathbf{G}}^{in,t} \Delta\bar{\boldsymbol{\chi}} \bar{\mathbf{E}}^t$  for  $\Delta\bar{\boldsymbol{\chi}}$
  - 8      $\bar{\boldsymbol{\chi}}^t \leftarrow \bar{\boldsymbol{\chi}}^{t-1} + \Delta\bar{\boldsymbol{\chi}}^t$
  - 9      $t \leftarrow t + 1$
  - 10 **end**
-

Once the method solves the inverse subproblem taking into account the error in approaching the scattered field, the algorithm may diverge from when the error  $\Delta\bar{\mathbf{E}}^s$  starts to be close to the noise level in the data. Therefore, a reasonable stopping criterion is ending the algorithm when the residual starts to grow from one iteration to another. Due to this condition, the authors demonstrated that DBIM is less robust than BIM in noisy data situations. However, the experiments showed a significant difference in the convergence speed, i.e., DBIM converges earlier than BIM.

Finally, it is worth noting that DBIM is a methodology equivalent to Newton-Kantorovich (NK) method (Remis and van den Berg, 2000). NK is an extension of Newton's method for solving nonlinear equations in functional spaces. Its main difference is that, in addition to determining  $\Delta\chi$  such that it satisfies  $\Delta\bar{\mathbf{E}}^s = \bar{\mathbf{G}}^{\text{in},t} \Delta\bar{\chi}\bar{\mathbf{E}}^t$ , the method also requires that  $\Delta\chi$  simultaneously satisfy  $\Delta\bar{\mathbf{E}}^s = \bar{\mathbf{G}}^s(\bar{\mathbf{I}} - \bar{\mathbf{G}}^s\bar{\chi}^t)^{-1}\Delta\bar{\chi}\bar{\mathbf{E}}^t$ . However, this is equivalent to calculating Green's function in (3.123). As stated by Chen (2017), these methodologies are equivalent to determining a gradient for the contrast function based on the Frechét derivative of the  $\bar{\mathbf{E}}^s + \bar{\mathbf{G}}^D\bar{\chi}(\bar{\mathbf{I}} + \bar{\mathbf{G}}^s\bar{\chi})^{-1}\bar{\mathbf{E}}^i$ . This residue can be obtained by replacing  $\bar{\mathbf{E}}$  in (3.39) with the solution of (3.40) as a forward problem. Since the problem is nonlinear and has many local minima (Chen, 2017), both DBIM and NK do not guarantee the convergence to a global optimum represented by the minimum residue of equations.

### 3.6.3 The Variational Born Iterative Method

Zaiping and Yerong (1998) carried out experiments considering the coupling between BIM and DBIM. Specifically, DBIM was used in the first iterations, while BIM, in the latter. The goal was to bring together the best features of each method, i.e., the rapid convergence of DBIM and BIM stability. However, the authors found that this hybrid version, called Hybrid Born Iterative Method (HBIM), took too many operations for coupling these two methodologies.

Later, Zaiping et al. (2000) proposed replacing DBIM with a method called Variational Born Iterative Method (VBIM). Its difference was that Green's function was not updated in each iteration. That is, the algorithm used Green's function for the homogeneous medium throughout the process. This reduces the number of operations dramatically. Experiments with conductive objects indicated a 20% difference in computational efficiency<sup>6</sup> between VBIM and DBIM, whereas the images reconstructed by the two were similar. He also found that the hybridization between VBIM and BIM, called NHBIM, allowed recovering good images at a lower computational cost than HBIM.

---

<sup>6</sup>In their work, only three instances were used to compare BIM, DBIM, and VBIM. The number of instances is too low to consider an unbiased comparison, i.e., to exclude the impact on the choice of the instances in the results. In addition, there was no plot or table that could give a clear explanation about the meaning of the computational efficiency stated.

### 3.6.4 The Conjugated-Gradient Method

The Conjugate Gradient Method has a dual utility as both a regularizer for linear ill-posed problems and as a quantitative inversion method. This means that its structure can be tailored to tackle non-linear problems and reconstruct contrast images in scenarios where linear approximations prove to be insufficient. Lobel et al. (1996) suggested minimizing the following functional:

$$F(\bar{\chi}) = \sum_{s=1}^{N_S} \|\kappa_s\|^2 \quad (3.124)$$

where:

$$\kappa_s = \bar{E}_s^s + \bar{G}^D \bar{\chi} \bar{L} \bar{E}_s^i \quad (3.125)$$

and  $\bar{L} = (\bar{I} - \bar{G}^S \bar{\chi})^{-1}$ , which is the kernel for the total field equation based on (3.22). Eq. (3.125) represents the mismatch between scattered field and the computed one for each incidence angle. The method updates the contrast image in the iteration  $k + 1$  by:

$$\bar{\chi}^{k+1} = \bar{\chi}^{k+1} + \alpha^k \bar{D}^k \quad (3.126)$$

where  $\bar{D}^k$  is the update direction and  $\alpha^k$  is the optimum step. The latter is a complex parameter computed by:

$$\alpha^k = \frac{\sum_{s=1}^{N_S} \langle \kappa_s, \bar{V}_s \rangle}{\sum_{s=1}^{N_S} \|\bar{V}_s\|^2} \quad (3.127)$$

where:

$$\bar{V}_s = \bar{G}^D \bar{L}^T \bar{D}^k \bar{L} \bar{E}_s^i \quad (3.128)$$

The update direction might be written according to Polak-Ribière formulation. The diagonal terms of  $\bar{D}^k$ , denoted as  $\mathbf{d}^k$ , are computed by:

$$\mathbf{d}^k = \mathbf{g}^k + \frac{\langle \mathbf{g}^k, \mathbf{g}^k - \mathbf{g}^{k-1} \rangle}{\|\mathbf{g}^k\|^2} \mathbf{d}^{k+1} \quad (3.129)$$

where:

$$\mathbf{g}^k = 2 \sum_{s=1}^{N_S} \left[ \text{diag}(\bar{L} \bar{E}_s^i) \bar{L} \right]^* \bar{G}^D \kappa_s \quad (3.130)$$

The method requires an initial guess to  $\bar{\chi}$  which may be obtained by linear methods, such as Back-Propagation or Dominant Current. The performance might improve if an edge-preserving regularization term is added in the functional (3.124) (Lobel et al., 1997).

The most computationally expensive step is the matrix inversion required in  $\bar{L}$ , which may render the method impractical for high-resolution problems. However, this computational burden can be alleviated by replacing the term  $\bar{L} \bar{E}_s^i$  with the actual total field computation, which

can be computed using algorithms like the Method of Moments. Faster computational might be attained if implemented according to the Conjugate Gradient Fast Fourier Transform procedure. Vargas et al. (2021) demonstrated that this modification results in a significant reduction in complexity. Further improvements can be achieved by adding a portion of the variational-induced current to the total field, as demonstrated by Vargas and Adriano (2022).

### 3.6.5 The Level-Set Method

When the possible dielectric properties are known, the problem is reduced to detecting, locating, and determining the shapes of these materials. In this case, a popular methodology for segmentation and image registration is the Level Set Method (Dorn and Lesselier, 2006; Osher and Fedkiw, 2003). This type of method assumes the estimation of the total field to solve the inverse linear problem by identifying the contours of the objects. Therefore, it is usually used within a framework such as BIM, for example.

In general, the contrast is represented by a function called level set function  $\psi(\mathbf{r})$ . For example, if we assume that there is only a single material somewhere in the space characterized by a homogeneous medium, the contrast function can be determined by:

$$\chi(\mathbf{r}) = \chi_o U(\psi(\mathbf{r}) - l_0) \quad (3.131)$$

where  $\chi_o$  is the object contrast,  $U(x)$  is a unit step function, and  $l_0$  is a threshold that defines the boundaries between object and background, i.e., their contours. That is, if  $\psi(\mathbf{r}) > l_0$ , then that point is an object and vice versa. Therefore, the method determines the function  $\psi(\mathbf{r})$  by minimizing residues, either from the data equation or from the state one.

Regarding minimizing the residuals of the data equation, the optimization of the level set function is obtained by solving the following differential equation:

$$\frac{\partial \psi}{\partial t} + \frac{\partial f}{\partial \psi} = 0 \quad (3.132)$$

subject to  $\nabla \psi = 0 \in \partial S$ . In (3.132),  $t$  has the meaning of artificial time related to the movement of  $\psi$  (and not about the electromagnetic phenomenon);  $f$  is the function defined as  $f = \|\mathcal{F}\| = \|\mathbf{E}_s - \mathcal{L}\{\chi, \mathbf{E}\}\|$  and  $\partial S$  is the outline of the image. This equation defines that, if the variation of the error as a function of  $\psi$  is null, so  $\psi$  does not vary, i.e., its shape does not change.

Solving (3.132) requires the calculation of the derivative  $\partial \mathcal{F} / \partial \psi$ . The Gâteaux derivative can be obtained through the first-order approximation of the Taylor series (Shah and Moghaddam, 2018):

$$\frac{\partial \mathcal{F}}{\partial \psi} = \Re \left\{ [\mathcal{F}'(\chi)]^* \mathcal{F}(\chi) \right\} \chi_o \delta(\psi) \quad (3.133)$$

where ‘\*’ is the adjoint operator (15). A major bottleneck for this methodology is calculating the adjoint of  $\mathcal{F}$ . In practice, the operation means running the forward solver once again, i.e.,

to estimate  $\mathbf{E}$  and for  $\mathcal{F}^*$  (El-Shenawee et al., 2009; Woten et al., 2010). However, when  $\mathbf{E}$  is fixed, then the problem is linear, and the adjoint of  $\mathcal{F}$  equals  $\bar{\mathbf{K}}^*$  (3.87) in the corresponding discretization (Colgan et al., 2015; Shah and Moghaddam, 2015). Therefore, being  $\boldsymbol{\psi}$  a column-vector which represents the value of the level set function at each point of discretization and considering the approximation of  $\partial\psi/\partial t$  as  $(\psi^t - \psi^{t-1})/\Delta t$ , then:

$$\boldsymbol{\psi}^t = \boldsymbol{\psi}^{t-1} + \Re e \left\{ \bar{\mathbf{K}}^* (\bar{\mathbf{E}}^{s,F} - \bar{\mathbf{K}} \boldsymbol{\chi}) \right\} \Delta t \quad (3.134)$$

In addition to the right-hand side of (3.134), regularization terms can be added. Shah and Moghaddam (2018) implemented the total variation functional in terms of level set function, i.e.:

$$f_R(\psi) = \int_S dS' p(|\nabla \psi|) \quad (3.135)$$

where  $p$  is an analytical function defined as (Li et al., 2010):

$$p(x) = \begin{cases} \frac{1}{4\pi^2} (1 - \cos(2\pi x)), & x < 1 \\ \frac{1}{2} (x - 1)^2, & x \geq 1 \end{cases} \quad (3.136)$$

In addition, Shah and Moghaddam (2018) reformulated the problem to a finite number of possible materials. There are two options for implementing this strategy: increasing the number of levels or the number of level set functions. In the first case, this can be useful for representing objects that have layers with different properties. At the second, many level functions may be important to represent disconnected objects with different dielectric properties. Subsequently, Shah et al. (2019) reformulated the method for the three-dimensional case and included a step for contrast estimation after detecting the shape of the scatterers in each iteration. This estimate was formulated in terms of a constraint optimization problem where the Split Bregman Method is applied, which is a suitable method for problems with regularizers (Xiong et al., 2019).

### 3.6.6 The Contrast Source Inversion

To avoid incorporating forward solvers within a methodology for EISP, Kleinman and den Berg (1992) proposed an algorithm based on a formulation of a modified gradient that iteratively solves field and contrast through an over-relaxation technique. After successive refinements in the methodology (Kleinman and van den Berg, 1993, 1994; van den Berg and Kleinman, 1995), van den Berg and Kleinman (1997) proposed adapting the approach to the contrast source equation (2.33)-(2.34) that became very well known in the literature. This method, called Contrast Source Inversion (CSI), is based on the weighted minimization of the residual norm in (2.33) and (2.34). Once the objective function was defined, the authors determined the descent direction and step size considering the Conjugate Gradient method based on the Polak-Ribière formulation. It should be noted that, at each iteration, the algorithm first determines a new

estimate of the contrast source  $\mathbf{J}_{\text{eq}}$  and then updates the contrast function  $\chi$ .

Later, van den Berg et al. (1999) modified the gradient of the contrast function and added a regularization strategy known as Total Variation (TV). The regularizer is based on the integration of the contrast function gradient, i.e.:

$$f_{TV}(\chi) = \int_S d\mathbf{r} \left( \sqrt{|\nabla \chi(\mathbf{r})|^2 + \delta^2} \right)^p \quad (3.137)$$

where  $\delta^2$  is the norm of the data equation residual considering the contrast source formulation. Moreover,  $p$  is an exponent usually choose as  $-1$ .

As an advantage, TV contributes to a better reconstruction of both soft and sharp objects. However, if this functional is summed to the objective function, it is necessary to choose a weighting parameter. In this case, the weight is empirically determined after successive experiments only. However, an alternative is to multiply the TV functional by the residual norm. The authors verified that this methodology was robust, even with noisy data, besides improving objects recovering in the considered synthetic experiments. Later, other works considered different applications and minor modifications (Abubakar et al., 2008, 2002; van den Berg et al., 2003). A modification that became common in the following works is the use of the contrast function obtained from the previous iteration as a weight in (3.137), i.e.:

$$f_{TV}(\chi) = \frac{1}{V} \int_S d\mathbf{r} \frac{|\nabla \chi(\mathbf{r})|^2 + \delta^2}{|\nabla \chi_{t-1}(\mathbf{r})|^2 + \delta^2} \quad (3.138)$$

where  $V$  is the volume or area of  $S$ . This method became known as Multiplicative-Regularized Contrast Source Inversion (MR-CSI).

Gilmore et al. (2009) compared MR-CSI against DBIM. The authors considered the Tikhonov Regularization as the inverse solver. For a fairer comparison, a dynamic choice of the regularization parameter was employed. The L-Curve strategy was implemented, aided by the Lanczos' bidiagonalization. In addition, an a posteriori regularization was considered by TV functional multiplication. The authors considered synthetic and five real data cases, which were reconstructed at different frequencies. The authors noted that the reconstructed images were very similar to each other. Regarding the execution time of the algorithms, the MR-CSI spent less time. However, this is also dependent on the implementation of the algorithms.

### 3.6.7 Compressive Sensing

In the field of signal processing, Compressive Sensing (CS) is a methodology for signal reconstruction based on an underdetermined system of linear equations (Donoho, 2006). This methodology assumes that the signal to be reconstructed is sparse, i.e., it can be represented with few elements of a domain. In addition to sparseness, the input and output of the system must

be incoherent<sup>7</sup> (Candès and Romberg, 2007). Incoherence is an application of the Restricted Isometry Property (RIP) (Shah et al., 2016).

This technique has also been applied to several situations in electromagnetics (Massa et al., 2015). When it comes to Microwave Imaging, CS has some difficulties: (i) the problem is non-linear while CS is an approach to linear problems; (ii) the unknown variables are not usually intrinsically sparse; and (iii) the problem's ill-posedness can turn its application impracticable. However, there are efforts for linearization, sparse representation of unknown variables, and system regularization.

Table 1, available at (Oliveri et al., 2017), lists references in the literature that presented alternatives to adapt the methodology to the problem. Some considered either Born or Rytov Approximations as linearization strategies, which constraints the algorithm to weak scatterers only. Regarding discretization, many studies have considered the traditional approach described in (3.32)-(3.36). As a result, the application is limited to unique or very small scatterers compared to the image size, which is necessary to meet the sparsity criterion. Much of the work also considered the Bayesian Compressive Sensing (Ji et al., 2008) or Multitask Bayesian Compressive Sensing (Ji et al., 2009) solvers since they are efficient and robust in these situations.

Shah et al. (2016) proposed a relevant approach in this field. To satisfy RIP, the authors used the BIM structure and implemented a regularizer based on  $L^2$  and  $L^1$  norms. The regularizers based on the  $L^2$  norm, such as those in section 3.3, tend to significantly smooth the object's edges. On the other hand, the coupling of the  $L^1$  norm within the regularizer formulation can better reconstruct edges. For this reason, the authors redefined the Tikhonov regularizer by changing the norm of contrast function for an  $L^1$  one and maintaining the  $L^2$  norm for the integral equation residual. The formulation met the RIP condition and the sparsity condition when the parameters were chosen correctly. The implementation was divided into five steps necessary to solve the inverse subproblem without disrespecting the CS conditions.

Rather than sparse discrete scatterers, the Bayesian approach to CS is also applicable to continuous random media. Fouda and Teixeira (2014a) proposed to reconstruct this kind of scatterer incorporating ultrawideband multistatic measurements and confidence level estimation of the inversion. The method is based on linear regression model where the contrast function is solved indirectly through the solution of a covariance matrix using the Relevance Vector Machine technique. The linearization is accomplished by BA. However, the authors had also applied the method within a nonlinear framework (DBIM). Instead of a general representation, the contrast function is represented through its spatial harmonics since it conforms better with the sparsity requirement of the model as well as a better regularization. The authors also proposed an adaptive approach to measurement location and another one to reduce the image.

---

<sup>7</sup>Coherence is a statistical measure that relates two signals and that, in some instances, can estimate the causality between input and output. The coherence of a linear system might be understood as the fractional part of the output signal power produced by the input at that frequency.

The last is achieved through a time-reverse scheme to localize the most important areas. These two approaches were important to quality of the scattered field information and to reduce computational cost. The methodology has also been applied to breast cancer detection (Fouda and Teixeira, 2014b).

Finally, we highlight one of the last CS formulations developed by Oliveri et al. (2019). In this study, the authors proposed an approach similar to BIM. Unlike other methodologies that shared the same inspiration, the methodology did not depend on full-wave simulations. In this case, the algorithm estimates the contrast function first. Then, it determines the field by solving an optimization problem with an iterative algorithm based on the Distorted-Wave Born Approximation (Caorsi et al., 1996). The contrast is recovered from a Bayesian approach based on probability distribution maximization. The optimization is achieved through a local search technique based on the Relevance Vector Machine (Oliveri et al., 2017).

### 3.6.8 The Subspace-Based Optimization Method

When the problem involves discrete point scatterers, Green's function operator in the data equation maps the source space into the scattered field space. Furthermore, it is injective. This property gives birth to some methods that decompose the Green's function operator into subspaces (Chen and Zhong, 2008; Kirsch, 2002). When the source is a distribution, the properties of the operator are very different. However, this does not prevent obtaining a subspace of the induced current source.

Taking into account  $\bar{\mathbf{G}}^D$  (3.46), its decomposition into singular values is represented by:

$$\bar{\mathbf{G}}^D = \bar{\mathbf{U}} \bar{\boldsymbol{\xi}} \bar{\mathbf{V}}^* \quad (3.139)$$

where  $\bar{\mathbf{U}}$  is an  $N_M \times N_M$  matrix composed of the orthonormal left singular vectors  $\mathbf{u}_m$ ;  $\bar{\mathbf{V}}$  is an  $N_I N_J \times N_I N_J$  matrix composed of the orthonormal right singular vectors  $\mathbf{v}_{ij}$ ; and  $\bar{\boldsymbol{\xi}}$  is an  $N_M \times N_I N_J$  diagonal matrix composed by the set of  $N_I N_J$  singular values  $\boldsymbol{\xi}$  arranged in non-increasing order. Thus, (3.139) can be rewritten as:

$$\bar{\mathbf{G}}^D \mathbf{v}_{ij} = \xi_{ij} \mathbf{u}_m \quad (3.140)$$

Through (3.140), it is possible to observe that the set of vectors  $\mathbf{u}_m$  forms an orthonormal base in the scattered field space for a given source  $s$ . Similarly, vectors  $\mathbf{v}_{ij}$  form the orthonormal basis of  $\bar{\mathbf{J}}_s^{\text{eq}}$  space. Thus, the  $s^{\text{th}}$  column of  $\bar{\mathbf{J}}_s^{\text{eq}}$  can be written as a linear combination of the vectors in  $\bar{\mathbf{V}}$ :

$$\bar{\mathbf{J}}_s^{\text{eq}} = \bar{\mathbf{V}} \mathbf{v} \quad (3.141)$$

where  $\mathbf{v}$  is a  $N_I N_J$ -dimensional vector and can be determined analytically in absence of noise

by:

$$v_{ij} = \frac{\mathbf{u}_{ij}^* \bar{\mathbf{E}}_s^s}{\xi_{ij}}, \quad ij \leq N_M \quad (3.142)$$

Due to noise, some singular values in (3.142) are very small and lead to very large errors in  $v_{ij}$ . However, an alternative is to separate the vector  $\mathbf{v}$  into two parts in which there will be one with the values whose error is within an established threshold and the remainder in the other. This strategy will lead us to write the vector  $\bar{\mathbf{J}}_s^{\text{eq}}$  as the sum of two parts, i.e.,  $\bar{\mathbf{J}}_s^{\text{eq}} = \bar{\mathbf{J}}_{s,+}^{\text{eq}} + \bar{\mathbf{J}}_{s,-}^{\text{eq}}$ . Thus:

$$\bar{\mathbf{J}}_s^{\text{eq}} = \bar{\mathbf{J}}_{s,+}^{\text{eq}} + \bar{\mathbf{J}}_{s,-}^{\text{eq}} = \bar{\mathbf{V}}_s^+ \mathbf{v}_s^+ + \bar{\mathbf{V}}_s^- \mathbf{v}_s^- \quad (3.143)$$

where  $\mathbf{v}_s^+$  is the set of values  $v$  whose error is less than the established criterion and  $\mathbf{v}_s^-$  the opposite. Correspondingly,  $\bar{\mathbf{V}}_s^+$  is a matrix composed of the column-vectors of  $\bar{\mathbf{V}}_s$  corresponding to  $\mathbf{v}_s^+$ , and  $\bar{\mathbf{V}}_s^-$ , to  $\mathbf{v}_s^-$ . In this way, we can use  $\mathbf{v}_s^+$  and rewrite the norm of the data equation residual (3.41):

$$\left\| \bar{\mathbf{G}}^D \bar{\mathbf{V}}_s^- \mathbf{v}_s^- + \bar{\mathbf{G}}^D \bar{\mathbf{J}}_{s,+}^{\text{eq}} + \bar{\mathbf{E}}_s^s \right\|^2 \quad (3.144)$$

However, the same idea can be applied to the state equation (3.42):

$$\left\| \left[ \bar{\mathbf{V}}_s^- - \bar{\chi} \bar{\mathbf{G}}^S \bar{\mathbf{V}}_s^- \right] \mathbf{v}_s^- + \bar{\mathbf{J}}_{s,+}^{\text{eq}} + \bar{\chi} \left[ \bar{\mathbf{G}}^S \bar{\mathbf{J}}_{s,+}^{\text{eq}} - \bar{\mathbf{E}}^i \right] \right\|^2 \quad (3.145)$$

In general, we can formulate an optimization problem to determine  $\bar{\chi}$  and  $\mathbf{v}_s^-$ , which minimizes the following functional:

$$f_{SOM}(\bar{\chi}, \mathbf{v}_s^-) = \frac{1}{2} \sum_{s=1}^{N_S} \left( \frac{\left\| \bar{\mathbf{G}}^D \bar{\mathbf{V}}_s^- \mathbf{v}_s^- + \bar{\mathbf{G}}^D \bar{\mathbf{J}}_{s,+}^{\text{eq}} + \bar{\mathbf{E}}_s^s \right\|^2}{\|\bar{\mathbf{E}}_s^s\|^2} + \frac{\left\| \left[ \bar{\mathbf{V}}_s^- - \bar{\chi} \bar{\mathbf{G}}^S \bar{\mathbf{V}}_s^- \right] \mathbf{v}_s^- + \bar{\mathbf{J}}_{s,+}^{\text{eq}} + \bar{\chi} \left[ \bar{\mathbf{G}}^S \bar{\mathbf{J}}_{s,+}^{\text{eq}} - \bar{\mathbf{E}}^i \right] \right\|^2}{\|\bar{\mathbf{J}}_{s,+}^{\text{eq}}\|^2} \right)^2 \quad (3.146)$$

The first methodology to solve (3.146) was proposed by Chen (2009). The author proposed to solve  $\mathbf{v}_s^-$  and  $\bar{\chi}$  separately. The variables  $\mathbf{v}_s^-$  were determined through the following linear system:

$$(\bar{\mathbf{A}}^* \bar{\mathbf{A}}) \mathbf{v}_s^- = (\bar{\mathbf{A}}^* \bar{\mathbf{B}}) \quad (3.147)$$

where  $\bar{\mathbf{A}} = \bar{\mathbf{V}}_s^- - \bar{\chi} \bar{\mathbf{G}}^S \bar{\mathbf{V}}_s^-$  and  $\bar{\mathbf{B}} = \bar{\mathbf{J}}_{s,+}^{\text{eq}} + \bar{\chi} \left[ \bar{\mathbf{G}}^S \bar{\mathbf{J}}_{s,+}^{\text{eq}} - \bar{\mathbf{E}}^i \right]$ . This solution is equivalent to the least-squares solution of (3.145). After that, (3.146) was solved through Levenberg-Marquardt Method (Franchois and Pichot, 1997). Note that determining  $\bar{\chi}$  requires  $\mathbf{v}_s^-$  and vice-versa. Therefore, it is required to iterate the two solutions until a convergence criterion is reached. This methodology was initially known as the Subspace-based Optimization Method (SOM). Thereafter, this formulation and the next one that will be introduced in the next paragraph were called  $G^D$ -SOM<sup>8</sup>, since they are based on the decomposition of the matrix  $\bar{\mathbf{G}}^D$ .

---

<sup>8</sup>In the literature, the acronym  $G^S$ -SOM is more popular because, as previously stated, meanings of the  $\bar{\mathbf{G}}^D$  and

Later, Chen (2010) proposed three modifications to the approach: (i) the fraction 1/2 and the summation square have been removed from the objective function (3.146); (ii)  $\bar{\chi}$  and  $\mathbf{v}_s^-$  are resolved simultaneously; and (iii) the Levenberg-Marquardt method was replaced by a formulation adapted from CG to determine descent directions for  $\bar{\chi}$  and  $\mathbf{v}_s^-$ . Through these modifications, the problem has become equivalent to a Quadratic-Constraint Quadratic Programming (QCQP) formulation in which the objective function is (3.144) and constraints are expressed by (3.145) (Chen, 2017). This problem is known in the literature as NP-hard, i.e., for which deterministic algorithms with polynomial complexity do not yet exist.

Chen (2010) also made comparisons of SOM against CSI both from a theoretical point of view as well as an experimental one. Although the algorithms share many properties, some differences between them are relevant: (i) the amount of unknown variables in SOM is smaller, since only  $\mathbf{v}_s^-$  is resolved; (ii) the search direction for unknown variables is determined separately in the CSI, whereas in this SOM approach, the calculations for determining the search direction are performed only once per iteration; and (iii) because of the need of calculating the SVD of the  $\bar{\mathbf{G}}^D$  matrix, the computational cost of SOM is higher. Once, generally,  $N_I N_J \gg N_M N_S$ , then the cost of SOM is equivalent to SVD one, i.e.,  $O((N_I N_J)^2)$ ; while the cost of the CSI is the equivalent to the operations in each iteration, i.e.,  $O(N_I N_J \log(N_I N_J))$ .

Another important aspect is the cut in the set of eigenvalues, i.e., where the separation between  $\mathbf{v}_s^+$  and  $\mathbf{v}_s^-$  will be made given that these are non-increasingly ordered. The author pointed out that, although the convergence of the method depends on this choice, it does not depend on any other parameter in the algorithm. In addition, the higher the noise level in the  $\bar{\mathbf{E}}^S$  data, the greater the set  $\mathbf{v}_s^-$ , and vice versa. The author defined a criterion for defining the cut in  $\mathbf{v}_s$  based on when the eigenvalues  $\xi$  start to fall. As shown in Figure 2 of the article, the eigenvalue curve looks approximately constant at the beginning and, after a certain point, it starts to fall. Therefore, the eigenvalue index from which the decay starts to be noticeable is the criterion of the division of  $\mathbf{v}_s$ . All coefficients  $\mathbf{v}_s$  before this index are maintained, and all later are determined by the method. A conservative choice that can avoid error amplification is the low cut-off index, i.e., dividing after the first eigenvalues (first or second, in extreme cases). Although this can increase the number of variables, the choice is feasible since there is no need to determine an optimal cut, assuming that the limit is the index for which eigenvalues start to decay.

Pan et al. (2010) made more comparisons between the two implementations announced so far. Six images were used whose maximum contrast of the objects was 2. The data from the scattered fields were synthetically generated and considered different noise levels. As noted, although the first version converges faster, the second has better reconstructions. Secondly, the computational cost of the first version is higher due to the way  $\bar{\mathbf{v}}_s^-$  is calculated. Finally, the authors understood that the second version had more chances to converge to the global optimum.

An alternative to reduce the computational cost of the  $G^D$ -SOM was proposed by Zhong  


---

 $\bar{\mathbf{G}}^S$  matrices tend to be inverse to the meaning adopted in this work.

et al. (2010). Based on the identity  $\bar{\mathbf{I}} = \bar{\mathbf{V}}\bar{\mathbf{V}}^* = \bar{\mathbf{V}}^+\bar{\mathbf{V}}^{+*} + \bar{\mathbf{V}}^-\bar{\mathbf{V}}^{-*}$ ,  $\bar{\mathbf{J}}_{s,-}^{\text{eq}}$  can be rewritten as:

$$\begin{aligned}\bar{\mathbf{J}}_{s,-}^{\text{eq}} &= \bar{\mathbf{V}}_s^- \mathbf{v}_s^- \\ &= \bar{\mathbf{V}}_s^- \bar{\mathbf{V}}_s^{-*} \boldsymbol{\tau} \\ &= (\bar{\mathbf{I}} - \bar{\mathbf{V}}_s^+ \bar{\mathbf{V}}_s^{+*}) \boldsymbol{\tau} \\ &= \boldsymbol{\tau} - \bar{\mathbf{V}}_s^+ \bar{\mathbf{V}}_s^{+*} \boldsymbol{\tau}\end{aligned}\quad (3.148)$$

The advantage of (3.148) is that, first of all, instead of calculating all  $\bar{\mathbf{V}}$  columns, only  $\bar{\mathbf{V}}^+$  is required. That is, only eigenvalues that will not be determined by the optimization method need to be calculated. Consequently, the objective function (3.146) needs to be rewritten replacing the term  $\bar{\mathbf{V}}_s^- \mathbf{v}_s^-$  by  $\boldsymbol{\tau} - \bar{\mathbf{V}}_s^+ \bar{\mathbf{V}}_s^{+*} \boldsymbol{\tau}$ .

As well as decomposing  $\bar{\mathbf{G}}^D$ , it is also possible to decompose  $\bar{\mathbf{G}}^S$ . We will hereinafter call  $\bar{\mathbf{V}}^{D+}$  and  $\bar{\mathbf{V}}^{D-}$  the sets of right singular vectors from the decomposition of  $\bar{\mathbf{G}}^D$ ; and  $\bar{\mathbf{V}}^{S+}$  and  $\bar{\mathbf{V}}^{S-}$  as the corresponding ones from decomposition of  $\bar{\mathbf{G}}^S$ . As proposed by Zhong and Chen (2009), the space of  $\bar{\mathbf{J}}^{\text{eq}}$  can then be described by the composition of three orthogonal subspaces: the corresponding space of  $\bar{\mathbf{V}}^{D+}$  ( $S_{D+}$ ); the space corresponding to the intersection between  $\bar{\mathbf{V}}^{D-}$  and  $\bar{\mathbf{V}}^{S+}$  ( $S_{D-S+}$ ); and the intersection between  $\bar{\mathbf{V}}^{D-}$  and  $\bar{\mathbf{V}}^{S+}$  ( $S_{D-S-}$ ). The authors then assumed that the part of  $\bar{\mathbf{J}}^{\text{eq}}$  found in  $S_{D-S-}$  has a negligible contribution to the equation of states, and consequently, little contribution to the data equation. Therefore, it can be neglected, so  $\bar{\mathbf{J}}_s^{\text{eq}}$  can be written as:

$$\bar{\mathbf{J}}_s^{\text{eq}} = \bar{\mathbf{V}}_s^{D+} \mathbf{v}^+ + \bar{\mathbf{B}}_s^{D-S+} \boldsymbol{\tau}^{D-S+} \quad (3.149)$$

where  $\bar{\mathbf{B}}_s^{D-S+}$  is the matrix with the bases from the intersection between  $\bar{\mathbf{V}}^{D-}$  and  $\bar{\mathbf{V}}^{S+}$ . Now, in addition to  $\bar{\chi}$  and  $\mathbf{v}^+$ ,  $\boldsymbol{\tau}^{D-S+}$  is also an unknown variable. Its size is generally less than  $\mathbf{v}^+$  and depends only on  $N_I N_J$  and the cut that is made in  $\bar{\mathbf{V}}^S$ .

This version of the algorithm became known as Twofold-SOM (TSOM). Although it has a larger number of unknown variables, its performance tends to be better than  $G^D$ -SOM (Chen, 2017). However, the price for a better performance is the computational cost of the algorithm. First, the calculation of  $\bar{\mathbf{B}}_s^{D-S+}$ , although not so complex, it is computationally expensive (Zhong, 2010). Consequently, an approximation was proposed (Zhong and Chen, 2009):

$$\bar{\mathbf{B}}_s^{D-S+} \boldsymbol{\tau}^{D-S+} \approx \bar{\mathbf{V}}_s^{D-} \bar{\mathbf{V}}_s^{D-*} \bar{\mathbf{V}}_s^{S+} \boldsymbol{\tau} \quad (3.150)$$

The approach in (3.150) is equivalent to making a projection of  $\bar{\mathbf{V}}^{S+}$  on  $\bar{\mathbf{V}}^{D-}$  instead of an intersection as in the exact formulation. The more orthogonal  $\bar{\mathbf{V}}^{S+}$  is in relation to  $\bar{\mathbf{V}}^{D-}$ , the closer to exact the approximation is.

Second, the strategy for choosing the eigenvalue cut-off index for  $\bar{\mathbf{G}}^S$  is not quite the same. In this case, the index cannot be very low. On the other hand, it does not need to be chosen to satisfy the state equation. The choice proposed by Zhong and Chen (2009) resumes

to: in the first iteration, solving the problem for a low cut index and increase over the iterations up to a value that represents 0.5-1.0% of the largest eigenvalue. Unlike the eigenvalue curve of  $\bar{\mathbf{G}}^D$ , eigenvalues of  $\bar{\mathbf{G}}^S$  decay much more slowly because of the singularity present in their formulation.

Finally, the SVD calculation of  $\bar{\mathbf{G}}^S$  and the  $\bar{\mathbf{V}}^{S+} \boldsymbol{\tau}$  multiplication are also expensive. However, these costs can be reduced as proposed by Zhong and Chen (2011). The authors proposed to approximate  $\bar{\mathbf{V}}^{S+}$  using discrete Fourier bases, which allows to reduce the computational cost of the multiplication  $\bar{\mathbf{V}}^{S+} \boldsymbol{\tau}$  for a Fast Fourier Transform (FFT) operation and eliminates the need to calculate the SVD of  $\bar{\mathbf{G}}^S$ . This methodology became known as FFT-SOM.

Alternatively to look for solutions for  $\bar{\mathbf{J}}_{s,-}^{\text{eq}}$  through the space of  $\bar{\mathbf{V}}^{D-}$  concerning the  $G^D$ -SOM methodology, it is possible to use all the space  $\bar{\mathbf{V}}^D$ . One motivation for this is that, since the cutting index in this case tends to be small, the dimension of  $\bar{\mathbf{V}}^{D-}$  is very close to  $\bar{\mathbf{V}}^D$ . In addition, the number of removed dimensions is much less than  $N_I N_J$ . Therefore, a proposal is to reconstruct  $\bar{\mathbf{J}}_{s,-}^{\text{eq}}$  across the entire space  $\bar{\mathbf{V}}^D$  using bases Fourier. In this case, the equivalent current is defined as:

$$\bar{\mathbf{J}}_s^{\text{eq}} = \bar{\mathbf{J}}_{s,+}^{\text{eq}} + \bar{\mathbf{F}} \mathbf{v} \quad (3.151)$$

where  $\bar{\mathbf{F}}$  is a  $N_I N_J \times N_I N_J$  matrix containing the Fourier bases in which a  $F_{ijpq}$  element is determined by:

$$F_{ijpq} = e^{-j2\pi(i-1)(j-1)(p-1)(q-1)/(N_I N_J)} \quad (3.152)$$

The second term of (3.151) can be interpreted as a residual current that can compensate for errors in  $\bar{\mathbf{J}}_{s,+}^{\text{eq}}$ , especially in cases of high noise levels. The objective function, in this case, might be the same as  $G^D$ -SOM, i.e., (3.146). Although the computational cost of  $G^D$ -SOM and NFFT-SOM are the same, (Chen, 2017) compared the two methods and noticed some differences. Although  $G^D$ -SOM converges faster in the beginning, NFFT-SOM has a smaller error after a certain number of iterations. Furthermore, NFFT-SOM has a relatively simpler implementation as well as presenting a longer range for a robust choice of cut index.

Finally, there are other works in the literature which either use SOM or join new strategies or explore the principle of decomposing spaces into different algorithms, formulations, and situations: three-dimensional problems (Zhong and Chen, 2011); modified integral equation (3.43) (Xu et al., 2020, 2018b,c; Zhong et al., 2016); multiplicative regularization (Xu et al., 2016); multi-image resolutions (Oliveri et al., 2011; Zhong et al., 2020); subspace decomposition for DBIM (Ye and Chen, 2017) and VBIM (Liu and Nie, 2019); Convolutional Neural Networks (Wei and Chen, 2019b); Wavelet Transform (Zhang et al., 2020a); non-iterative methods (Yin et al., 2020); phaseless data (Zhang et al., 2020c); biomedical imaging (Xu et al., 2018a); iterative domain decomposition approach suitable for strong scatterers Zhang et al. (2022).

### 3.6.9 Regularization on $L^p$ Banach Spaces

The presented regularization approaches are based on  $L^2$  Hilbert spaces. When we assume that the known and unknown functions belong to Hilbert spaces, many mathematical tools are provided which simplifies the analysis and possible applications. The linear regularization strategies in Section 3.3 and the SVD strategy in SOM are examples. However, a drawback is the smoothness (over-smoothness) of solutions. This property is an obstacle to retrieve clear contours in the image domain.

Hilbert space is a specific case of  $L^p$  Banach spaces (see Appendix D for further information) in which  $p = 2$ . However, other choices may be explored. In fact, the regularization based on Banach spaces has been explored in different contexts (Bach et al., 2011; Elad, 2010). These studies have shown advantages for  $1 < p < 2$ , which are lower over-smoothness and sparsity, i.e., the solution can be represented with less components.

The application to EISP was firstly proposed in Estatico et al. (2012a) and further explained in Estatico et al. (2012b). The formulation was based on the combination of data and state equations, which is very common for gradient methods. Specifically, if we rewrite the electric field in (2.42) in terms of (2.43), we obtain:

$$\begin{aligned} E_{zs}(\boldsymbol{\rho}) = & -\frac{jk_b^2}{4} \int_S dS' H_0^{(2)}(k_b|\boldsymbol{\rho} - \boldsymbol{\rho}'|) \chi(\boldsymbol{\rho}') \left( E_{zi}(\boldsymbol{\rho}') \right. \\ & \left. + \frac{jk_b^2}{4} \int_S dS'' H_0^{(2)}(k_b|\boldsymbol{\rho}' - \boldsymbol{\rho}''|) \chi(\boldsymbol{\rho}'') E_{zi}(\boldsymbol{\rho}'') \right)^{-1} \end{aligned} \quad (3.153)$$

which can be rewritten as a nonlinear operator equation as:

$$E_{zs} = \mathcal{K}\{\chi\} \quad (3.154)$$

where  $\mathcal{K} : X \rightarrow Y$  is a nonlinear and ill-posed map between  $X$  and  $Y$ , which will be defined as Banach spaces  $L^p(S)$  and  $L^p(D)$ , respectively. We will assume as well that only a noisy version of the scattered field is known ( $E_{zs}^\delta$ ), i.e.,  $\|E_{zs} - E_{zs}^\delta\| \leq \delta$ .

Formulations of Gauss-Newton methods, based on the gradient information, have the general iterative structure as follows:

$$\chi^{i+1} = \chi^i - \tau^i \mathcal{L}^N \{\chi^i, E_{zs}^\delta\} \quad (3.155)$$

where  $\tau^i > 0$  is the step length and  $\mathcal{L}^N : X \times Y \rightarrow X$  is an operator which is used to minimizes the following functional:

$$f_N(\chi) = \frac{1}{p} \|\mathcal{K}\{\chi\} - E_{zs}^\delta\|_Y^p \quad (3.156)$$

Therefore, this is the generalization of Gauss-Newton method for regularization in Banach spaces where  $\chi \in L^p(S)$  and  $E_{zs} \in L^p(D)$  are  $p^{\text{th}}$  power Lebesgue integrable functions

(Appendix D).

In Hilbert spaces, where  $p = 2$ , the derivative of the quadratic operator is a linear one. However, the same is not true in Banach space, generally. In fact, the derivative of (3.156) is nonlinear for many  $p$  choices. The Tikhonov and Landweber regularization can also be extended to address these cases, even though they are more complexes. Estatico et al. (2012b) proposed a formulation of Gauss-Newton method where, in each step, the descent direction is evaluated by an adequate formulation of Landweber methods.

Given an initial solution  $\chi^0$ , the linearization of (3.154) is given by:

$$\mathcal{K}'\{\chi^i\}\tilde{\chi}^i = E_{z_s}^\delta - \mathcal{K}\{\chi^i\} \quad (3.157)$$

where  $\mathcal{K}'$  is the Frechét derivative of  $\mathcal{K}$  and  $\tilde{\chi}^i$  is the unknown function that must be solved to determine the step, i.e.:

$$\chi^{i+1} = \chi^i + \tilde{\chi}^i \quad (3.158)$$

The authors proposed a formulation of Landweber method to solve (3.157). Starting with  $\tilde{\chi}_0^i = 0$ , the solution  $\tilde{\chi}^i$  is determined through successive iterations. In each iteration  $l$ , the next  $\tilde{\chi}_{l+1}^i$  value is computed by:

$$\tilde{\chi}_{l+1}^i = \mathcal{J}_{r^*}^{X^*} \left\{ \tilde{\chi}_l^i - \tau \mathcal{K}^*\{\chi^i\} \mathcal{J}_r^Y \left\{ \mathcal{K}\{\chi^i\} \tilde{\chi}_l^i - E_{z_s}^\delta + \mathcal{K}\{\chi^i\} \right\} \right\} \quad (3.159)$$

where the function within  $\mathcal{J}_{r^*}^{X^*}\{\cdot\}$  belongs to the dual space<sup>9</sup>  $X^*$  of  $X$ ;  $\mathcal{K}^*$  is the dual operator<sup>10</sup> of  $\mathcal{K}$ ;  $\tau > 0$  is the step length; and  $\mathcal{J}_r^Y$  and  $\mathcal{J}_{r^*}^{X^*}$  are duality maps of  $Y$  and  $X^*$  (Schöpfer et al., 2006) defined as:

$$\mathcal{J}_{p^*}^{X^*}\{\cdot\} = \|\cdot\|_{L^p}^{r^*-p^*} |\cdot|^{p^*-1} sign(\cdot) \quad (3.160)$$

$$\mathcal{J}_r^Y\{\cdot\} = \|\cdot\|_{L^p}^{r-p} |\cdot|^{p-1} sign(\cdot) \quad (3.161)$$

where  $r^*$  and  $p^*$  are the Holder conjugate of  $r$  and  $p$ , respectively, i.e.,  $r^* = r/(r-1)$  and  $p^* = p/(p-1)$ ;  $r > 1$  acts merely as a scaling factor which impacts the step size and it is not very significative; and the sign function is given by:

$$sign(x) = \begin{cases} e^{\angle x}, & x \neq 0 \\ 0, & x = 0 \end{cases} \quad (3.162)$$

The process described by (3.159) is repeated until a stopping rule is satisfied. Then (3.158) is computed. If a stopping rule for the Gauss-Newton process has not been satisfied, then the known terms in (3.157) are computed and the Landweber method is executed once

---

<sup>9</sup>Given a vector space  $V$ , its dual space is the vector space of all linear functionals on  $V$ .

<sup>10</sup>Given an operator  $\mathcal{T} : V \rightarrow W$ , its dual one  $\mathcal{T}^*$  is a linear map from  $W^*$  to  $V^*$  defined by  $\mathcal{T}^*\{\psi\} = \psi \cdot \mathcal{T}$  for  $\psi \in W^*$ .

again.

Besides  $p$ , the number of Landweber iterations is also a regularization parameter. A high number of iterations means low regularization, less Gauss-Newton iterations and greater noise sensitivity. In Estatico et al. (2014), the authors carried out more experiments to analyze the choice of these regularization parameters plus the stopping rule for the Gauss-Newton iterations. They had concluded that a reasonable trade-off between different aspects in the results were represented by 5 Landweber iterations and 0.01 residual norm threshold as the stopping criterion of Gauss-Newton process. In respect to  $p$ , they had concluded that low values ( $p < 2$ ) are responsible for less oscillations specially in background area (clearer background) and over-estimations of contrast value in object area. On the other hand, high  $p$  values had the opposite behavior and the algorithms had diverged sometimes. They also have noticed that, for  $p < 1.2$ , the solution was more affected by noise. In addition, Fedeli et al. (2015a) have assessed the impact of the following factors on the algorithm: number of sources, noise level, initial guess, contrast level, and scatterer size.

Instead of using a fixed choice for  $p$ , an automatic and adaptive strategy is also possible. Estatico et al. (2018a) proposed to define the parameter based on the current contrast estimation. Given a predefined range,  $p$  is evaluated proportionally to the contrast function in each point of the image, i.e., the authors rearranged the formulation to support a local definition of  $p$ . The results from cases studies show that the automatic and adaptive strategy had outperformed the regularization in Hilbert space ( $p = 2$ ) and was equivalent to the fixed choices considered. Therefore, the advantage is a practical one, i.e., to free from choosing a suitable fixed value.

The method has been tested in diverse situations: buried objects and GPR imaging (Estatico et al., 2013; Fedeli et al., 2015b, 2021); multi-frequency data (Estatico et al., 2015a,b); biomedical imaging (Bisio et al., 2018, 2020, 2017; Dachena et al., 2021; Estatico et al., 2017; Fedeli et al., 2017a; Randazzo et al., 2021b); three-dimensional reconstructions (Estatico et al., 2018b, 2016, 2018c); through-the-wall imaging (Fedeli et al., 2017b); phaseless data (Estatico et al., 2020); multiscaling approach (Randazzo et al., 2021a).

### 3.6.10 Virtual Experiments

Since incident and scattered fields are variables linearly related in state equation, *a posteriori* recombination of sampled values can be explored in order to enforce particular and convenient conditions. The result is therefore a *virtual* problem which must have the same solution. In other words, a superposition of the sampled incident, scattered, and induced current

fields data ( $E_{ijs}^i$ ,  $E_{ms}^s$ , and  $J_{ijs}^{eq}$ , respectively) might be performed as (Di Donato et al., 2015):

$$\mathcal{E}_{ij}^i = \sum_{s=1}^{N_S} \alpha_s E_{ijs}^i \quad (3.163)$$

$$\mathcal{E}_m^s = \sum_{s=1}^{N_S} \alpha_s E_{ms}^s \quad (3.164)$$

$$\mathcal{J}_{ij}^{eq} = \sum_{s=1}^{N_S} \alpha_s J_{ijs}^{eq} \quad (3.165)$$

Then, the following system of equations must be solved:

$$\mathcal{E}_m^s = - \sum_{i=1}^{N_I} \sum_{j=1}^{N_J} G_{mij}^D \mathcal{J}_{ij}^{eq} \quad (3.166)$$

$$\chi_{ij} \mathcal{E}_{ij}^i = \mathcal{J}_{ij}^{eq} + \chi_{ij} \sum_{p=1}^{N_I} \sum_{q=1}^{N_J} G_{ijpq}^S \mathcal{J}_{pq}^{eq} \quad (3.167)$$

Eq. (3.166) and (3.167) are similar to (3.32) and (3.35), respectively. Different choices of parameters  $\alpha_1, \dots, \alpha_s$  will give different re-arrangements of the original experiment without requirement new measurements. Such virtual experiment is also a re-weight of the collected information. The choice might enforce convenient conditions that might allow new approximations. Di Donato et al. (2015) have proposed to enforce circular symmetry of the contrast source around pivots points. The strategy is accomplished by solving the following linear system:

$$\sum_{s=1}^{N_S} \alpha_s E_{ms}^s = \sqrt{\frac{2}{\pi k_b |\boldsymbol{\rho}_m - \boldsymbol{\rho}_p|}} e^{-jk_b |\boldsymbol{\rho}_m - \boldsymbol{\rho}_p|} \quad (3.168)$$

where  $\boldsymbol{\rho}_p$  is the considered pivot point. Eq. (3.168) is similar to (3.110), i.e., the integral equation that defines LSM for far-field conditions, with  $\boldsymbol{\rho}_p$  acting as the sampling point. The linear system (3.168) is ill-posed and, therefore, must be solved by some regularization method (Subsection 3.4).

Di Donato et al. (2015) proposed to solve (3.168) for a set of pivot points. The pivot points are chosen within the scatterer region, after an analysis of an indicator function based on the norm of vector containing the  $\alpha$  values for each point in the grid. The CSI method is then adapted to solve the set of equations based on (3.166) and (3.167).

Different approaches based on Virtual Experiments are also possible: Di Donato et al. (2016) have proposed to adapt DWBA to address the linear system noniteratively; similarly, Palmeri et al. (2017) proposed to adapt DBIM; Bevacqua et al. (2015) proposed to express the induced current in terms of a superposition of Bessel functions and they obtain an algebraic solution for the problem based on truncating the series; Bevacqua et al. (2021) have proposed a general procedure to define the virtual experiment based on the adjoint solution of an auxiliary

problem without having to use explicit inversion and regularization processes.

## 3.7 Stochastic Quantitative Methods

When methodologies employ operations with random variables, they are called stochastics. Stochastic operations in optimization algorithms are widespread in problems where deterministic search direction techniques are computationally expensive. In addition, they are very used in problems with multiple local minima since these operations can contribute to the method escaping from a local minimum, unlike deterministic algorithms based on the gradient of the objective function.

A fundamental class within stochastic algorithms is Evolutionary Computation (EC) (Eiben and Smith, 2015). The name suggests computational operations inspired by the natural evolution of species. However, this class encompasses a wide range of methodologies based on other biological or even social processes, such as ant colony, particle swarms, antibodies, bird migration, anarchist societies, FIFA World Cup, among many others (Campelo and Aranha, 2018). In general, any method in this class is also called in the literature an Evolutionary Algorithm (EA). Initially, inspiration in biological processes for problem-solving came even before the development of computers. As Fogel (1998) argued, Alan Turing in 1948 was already proposing a genetic or evolutionary search. The popularization of this type of methodology started in the 1960s with methodologies that gained attention: Fogel et al. (1966) proposed Evolutionary Programming (EP); Holland (1973) proposed the Genetic Algorithm (GA); Vent (1975) proposed the Evolutionary Strategies (ES). Since then, such subject has become deeply studied, which is evidenced by relevant journals such as *IEEE Transactions on Evolutionary Computation* and important conferences such as *Genetic and Evolutionary Computation Conference*.

In general, these methods address the problem through a population of candidate solutions, commonly referred to as individuals. Iteratively, individuals are chosen to undergo operations that cross information to generate new individuals and update the population. This process is driven either by random selection of individuals or random crossing of information. Throughout iterations, also called generations, the population may converge to a solution that has characteristics that have been preserved throughout the generations for giving a good evaluation. There is no guarantee that the algorithm converges to a global optimum, but this technique can simultaneously exploit multiple search space regions.

Concerning using this kind of methodology in EISP, the advantage is to enable a broader search in the solutions space. This characteristic is very relevant considering the non-linear aspect of the problem and the existence of multiple local minima, as already mentioned in Subseção 2.4.5. Furthermore, most of the time in which this sort of strategy is employed, both contrast and field are considered simultaneously. This means that the problem is solved without employing techniques as forward solvers, matrix decomposition, or Green's function estimation. This aspect is very relevant for application in three-dimensional problems. Another

advantage is that this structure also offers opportunities to facilitate the implementation of prior information and different types of regularizers. On the other hand, the main difficulty is the high number of variables usually present in this approach. In these cases, the disadvantage is that the convergence of this class of methodology can be very slow. Another disadvantage is that it is not possible to guarantee that the algorithm always converge to the same solution given the same input. Therefore, the measurement of performance of these algorithms should take account its average performance for a given number of execution. This information is related to the method's reliability and it is crucial for its application in real situations. Specific review articles about EAs in EISP have already been published in the literature (Pastorino, 2007; Rocca et al., 2009).

In this section, there will be discussions about the main aspects of implementing EAs, i.e., representing solutions, defining the objective function, searching mechanisms with their evolutionary operators, and starting the solutions. These issues will be addressed based on the works available in the literature that propose EAs formulations to solve EISPs, i.e., reviewing and differentiating the works from these four aspects<sup>11</sup>.

### 3.7.1 Representation of Solutions

The first works that used EAs to solve EISPs considered previous knowledge about the shape or position of the object so that the problem could be represented with few decision variables. In addition, in these cases, it may also be possible to derive expressions for the electric field to avoid including it in the unknown variables of the problem.

A straightforward approach is to reconstruct a circle where the variables are the position on a bidimensional space, the contrast and the radius (Michalski, 2000). Similar to this case, when the object is an ellipse, two variables are needed to represent the shape instead of one (Michalski, 2001). However, there are cases where cylinders with multiple layers were considered (Caorsi et al., 2003b; Kent and Günel, 1997; Michalski, 2000; Pastorino, 2007). In such cases, the decision variables are simply the position of the cylinder within a two-dimensional space, the radius and the dielectric property of each layer. In problems like this, the number of variables does not usually pass ten. Besides, these quantities can be represented in a binary fashion instead of a real one (Kent and Günel, 1997).

However, it is possible to represent objects with a slightly more complex contour. Chiu and Liu (1996) proposed representing the contour of a cylinder through a series of sines and

---

<sup>11</sup>For further discussions on the general formulation of evolutionary methods, we recommend the following references: a general and broad discussion on CE (Eiben and Smith, 2015); a work in Portuguese dedicated to the theme (Gaspar-Cunha et al., 2013); a chapter with a general presentation of the methods and their application in EISPs (Pastorino, 2010b).

cosines. That is, the outline of an object was represented by a function  $S(\theta)$ :

$$S(\theta) = \sum_{n=0}^{N/2} B_n \cos(n\theta) + \sum_{n=1}^{N/2} C_n \sin(n\theta) \quad (3.169)$$

In this case, the unknown variables are, in addition to the contrast, the constant of each term in (3.169). This modelling can also be expanded to more than an object, as was done in (Qing, 2006; Qing et al., 2001). Instead of a sum of sines and cosines, it is possible to substitute for cubic splines, i.e., third-degree polynomials, as proposed by Huang et al. (2008). Furthermore, Salucci et al. (2022b) have proposed to use quadratic Bézier spline functions.

Another specific case in the literature is identifying multiple cracks in structures (Benedetti et al., 2007). In this case, the contrast function was defined in terms of a finite number of possible cracks represented by position, length, width, angle of inclination, and contrast. The electric field was discretized as in (3.45) and considered an unknown addressed by the algorithm.

However, another form of representation is also very used in the literature. Considering the discretization (3.39)-(3.42), decision variables can be simply the matrices  $\bar{\mathbf{E}}$  and  $\bar{\chi}$ . This type of representation has been widely used since the early 2000s (Caorsi and Pastorino, 2000; Donelli et al., 2006; Donelli and Massa, 2005; Etminan and Moghaddam, 2018; Salucci et al., 2017; Yang et al., 2021a). When there is information about the possible materials in the image (e.g., human tissues), it is possible to represent these quantities as discrete variables (Modiri and Kiasaleh, 2012).

The critical issue in this kind of representation is the number of variables of the electric field. Following the most used discretization in this chapter, it would be necessary to optimize  $N_I N_J N_S$  variables and those of the contrast function. Although this type of approach has already been used in some studies (Caorsi et al., 2004a; Donelli and Massa, 2005), it is not efficient since the generic formulations of EAs have difficulty with a high number of variables. In these cases, only image reconstructions with low resolution are feasible. Therefore, several strategies have already been used in the literature to get around this issue: (i) BA (Caorsi et al., 1991; Yang et al., 2021a); (ii) prior execution of deterministic algorithms (Brignone et al., 2008; Liu et al., 2020); (iii) parallelization (Massa et al., 2005); (iv) the estimation of the field by a direct resolver of all individuals (Huang et al., 2008; Huang and Sanagavarapu Mohan, 2007) or only those considered acceptable by a neural network (Ashtari et al., 2010; Noghalian et al., 2014); (v) the use of Markov Random Fields to correct the Born Approximation (Caorsi et al., 1994, 2004c).

A methodology that deserves particular attention is the Iterative Multi-Scaling Approach (IMSA), which aims to reduce the number of variables. Initially, Caorsi et al. (2002) proposed to reduce the image area by calculating the “center of contrast”<sup>12</sup> of the image. In other words,

---

<sup>12</sup>This calculation is similar to the concept of center of mass in gravitational theory. However, this calculation is not named in the literature. It is just a way used in this text to describe the calculation.

the EA is executed for the first time considering the entire image in a low resolution; then background regions in the image are excluded; after the exclusion, the EA receives the new region and optimize the model for a new resolution; the process of exclusion and running the EA is repeated until a specific stopping criterion is reached. This process is similar to a zoom strategy over the most significant areas within the figure. Its idea was based on previous work (Miller and Willsky, 1996a,b). The same idea was repeated (Caorsi et al., 2003a), and after, a clustering strategy was added, consisting of three steps: thresholding, noise filtering and object detection (Caorsi et al., 2004b).

This strategy is relevant since it eliminates regions where the background medium can be assumed (in these regions, the total field does not need to be considered since, as the contrast is zero, the contribution to the integral is null). However, the proposed clustering operations may be unclear and ineffective for some patterns in the images. That same strategy was considered in many works in the literature without any further consideration (Benedetti et al., 2010; Donelli et al., 2009, 2006; Oliveri et al., 2012, 2011; Salucci et al., 2017; Zhong et al., 2020). A modification was proposed recently by Hajebi and Hoofar (2022). The authors have proposed to use the Diffraction Tomography to obtain an initial image. Such technique allows to identify scatterers before the evolutionary process and without significant computational cost. After obtaining a first impression of the image, more advanced image segmentation algorithms were applied to crop scatterer areas and, then, the IMSA approach is conducted.

### 3.7.2 Objective Function Formulation

The definition of the objective function has a fundamental role in the development of EAs. Through it, individuals will be qualified and compared in the process of updating the population. In works that considered known shapes of objects, the objective function was defined in terms of the residual norm of the data equation. The state equation was not considered since, in these cases, there were analytical approximations for the electric field (Caorsi et al., 2003b; Chiu and Liu, 1996; Kent and Günel, 1997; Michalski, 2001; Qing et al., 2001). Similarly, the state equation does not need to be taken into account either when the Born Approximation (Caorsi and Pastorino, 2000; Yang et al., 2021a) or when the total field of each individual is evaluated by some forward solver (Huang et al., 2008; Noghanian et al., 2014). It is also worth mentioning the function proposed by Caorsi et al. (1991) defined as the probability in which a given contrast candidate solution is the true one given the known scattered field. In other words, the problem resumes to maximizing the conditional probability  $P(\bar{\mathbf{x}}|\bar{\mathbf{E}}^s)$ :

$$P(\bar{\mathbf{x}}|\bar{\mathbf{E}}^s) = \frac{P(\bar{\mathbf{E}}^s|\bar{\mathbf{x}})P(\bar{\mathbf{x}})}{P(\bar{\mathbf{E}}^s)} \quad (3.170)$$

It is worth mentioning that the probabilities involved in this formulation are estimated by an analytical expression which presupposes the Born Approximation.

Similar to what was introduced in SOM, a vast amount of EAs formulations for EISP considered a weighting between the residuals of data and state equations (Pastorino, 2010a). Many works consider the discretization formula (3.32) and (3.33). Therefore, the weighting of the residuals is given by:

$$f_{EA}(\bar{\mathbf{E}}, \bar{\boldsymbol{\chi}}) = \alpha_1^{EA} \sum_{m=1}^{N_M} \sum_{s=1}^{N_S} \left| E_{ms}^s + \sum_{i=1}^{N_I} \sum_{j=1}^{N_J} G_{mij}^D \chi_{ij} E_{ijs} \right|^2 + \alpha_2^{EA} \sum_{i=1}^{N_I} \sum_{j=1}^{N_J} \sum_{s=1}^{N_S} \left| E_{ijs}^i - E_{ijs} + \sum_{p=1}^{N_I} \sum_{q=1}^{N_J} G_{ijpq}^S \chi_{pq} E_{pq} \right|^2 \quad (3.171)$$

There are many possible ways in which  $\alpha_1^{EA}$  and  $\alpha_2^{EA}$  are defined. However, the most implemented way in the literature is (Benedetti et al., 2007; Caorsi et al., 2002, 2004b; Donelli and Massa, 2005; Salucci et al., 2017):

$$\alpha_1^{EA} = \left( \sum_{m=1}^{N_M} \sum_{s=1}^{N_S} |E_{ms}^s|^2 \right)^{-1} \quad (3.172)$$

$$\alpha_2^{EA} = \left( \sum_{i=1}^{N_I} \sum_{j=1}^{N_J} \sum_{s=1}^{N_S} |E_{ijs}^i|^2 \right)^{-1} \quad (3.173)$$

Therefore, the objective function (3.171) can be rewritten as follows:

$$f_{EA}(\bar{\mathbf{E}}, \bar{\boldsymbol{\chi}}) = \frac{\sum_{m=1}^{N_M} \sum_{s=1}^{N_S} \left| E_{ms}^s + \sum_{i=1}^{N_I} \sum_{j=1}^{N_J} G_{mij}^D \chi_{ij} E_{ijs} \right|^2}{\sum_{m=1}^{N_M} \sum_{s=1}^{N_S} |E_{ms}^s|^2} + \frac{\sum_{i=1}^{N_I} \sum_{j=1}^{N_J} \sum_{s=1}^{N_S} \left| E_{ijs}^i - E_{ijs} + \sum_{p=1}^{N_I} \sum_{q=1}^{N_J} G_{ijpq}^S \chi_{pq} E_{pq} \right|^2}{\sum_{i=1}^{N_I} \sum_{j=1}^{N_J} \sum_{s=1}^{N_S} |E_{ijs}^i|^2} \quad (3.174)$$

In cases where the contrast and field variables are optimized simultaneously, it is very important to also consider the state equation in the objective function. The main reason is that its inclusion represents a penalty in solutions where the electric field is not consistent with the contrast. In other words, there may be solutions that minimize the data equation residual, but the relationship between the two unknown quantities is very distant from that established by Maxwell's equations. Therefore, the insertion of this residue contributes to the rejection of solutions with no physical meaning.

The meaning of including the state equation into the formulation might also be understood through the concept of constraint optimization. Following this concept, the actual problem

which has been addressed is:

$$\min_{\bar{\mathbf{E}}, \bar{\chi}} \sum_{m=1}^{N_M} \sum_{s=1}^{N_S} \left| E_{ms}^s + \sum_{i=1}^{N_I} \sum_{j=1}^{N_J} G_{mij}^D \chi_{ij} E_{ijs} \right|^2 \quad (3.175)$$

$$\text{subject to : } E_{ijs} - \sum_{p=1}^{N_I} \sum_{q=1}^{N_J} G_{ijpq}^S \chi_{pq} E_{pqs} = E_{ijs}^i \quad \forall \begin{cases} i = 1, \dots, N_I \\ j = 1, \dots, N_J \\ s = 1, \dots, N_S \end{cases} \quad (3.176)$$

Thus, methods that use forward solvers to estimate  $\bar{\mathbf{E}}$  guarantee (3.176) in their structure while the ones that address (3.174) are using an external penalty methodology (Rao, 2019). While determining the total field by forward solvers might eliminate variables from problem, the disadvantage is the computational cost that is added to the algorithm. An alternative to overcome such drawback is the use of surrogate models (He et al., 2023). Surrogate models (also called meta-models) are, in other words, interpolation techniques that can predict the evaluation of an expensive objective function based on samples collected from it. Such strategy, when applied to optimization algorithms, may reduce the computational cost by reducing the number of times in which the expensive objective function is called. In Surrogate-Assisted Evolutionary Algorithms (SAEAs), the surrogate model is build in the beginning by randomly sampling the search space and the model is updated according some rules throughout the evolutionary process. The first application of SAEAs in EISP was accomplished by Salucci et al. (2022b).

Another way of interpreting (3.174) is as an application of weighting objectives in a multi-objective approach (Chankong and Haimes, 2008). Multi-objective problems are those in which there are more than one objective functions to be optimized which conflict with each other. Regarding the question about the conflict between the data and the state equation, it is reasonable that the exact solution of the problem minimizes both equations. However, while any solution to Maxwell's equations minimizes the state equation error, it may not minimize the data one since it might be the scattering of another object. In addition, due to ill-posedness, there might be solutions that minimize the data equation residual while representing significant errors in the state equation since they have no physical meaning. As far as this author knows, there is no work in the literature discussing possible conflicts between data and space equations as well as the application of other multi-objective methodologies (eg.,  $\varepsilon$ -constraint, Multi-Objective Evolutionary Algorithms, etc). Therefore, it is an open problem the application of multi-objective techniques into the problem.

Finally, it is worth noting that regularization terms might be added to the objective function. Qing (2006) added a penalty term to solutions that contained intersections between the cylinders; Chiu and Liu (1996) added the square of the absolute value of the derivative of (3.169); Pastorino et al. (2000) and Caorsi et al. (2001) added the mean of the absolute difference between all pairs of contrast elements inspired by the Markov chains (Caorsi et al., 1994). As far as this author knows, no implementation of EA in the literature has added regulariza-

tion terms such as Tikhonov (3.80) or TV (3.138). Possibly, the difficulty of determining a weight for this type of objective has inhibited its application. In any case, it is worth noting that this kind of functionals conflicts with the data and state equations since its optimal solution is either the zero function (Tikhonov) or a constant function (Total Variational). The L-Curve in Figura 3.3 is an example of such conflict.

### 3.7.3 Mechanisms and Evolutionary Operators

Each EA has its search engine which is made up of operators who can take inspiration from biological, physical or social processes. GA has a mechanism based on crossing and mutation operations. EP is near to GA; its main differences are that only the mutation operation is considered and each parent generates only one offspring. Particle Swarm Optimization (PSO) bases its operators on the particle path. Differential Evolution (DE) is also inspired by evolutionary behavior but its mutation operator is based on the difference vector between the solutions. Ant Colony Optimization (ACO) works based on the path of ants through communication by pheromone trails. Simulated Annealing (SA) is based on thermodynamic processes. These are the main EAs and those that have been implemented in the literature to address EISPs<sup>13</sup>.

Until mid-2005, GA was the most popular among works on EA applied to EISP, mainly among those where the electric field had an analytical solution or approximation (Caorsi and Pastorino, 2000; Kent and Günel, 1997; Qing et al., 2001). However, it was also applied sometimes in situations where the field was also resolved (Pastorino et al., 2000), either when the number of contrast variables was decreased (Benedetti et al., 2007) or in the form of a memetic<sup>14</sup> algorithm (Caorsi et al., 2003b,c; Massa et al., 2005; Pastorino et al., 2004), in which some deterministic algorithm (eg, CG) was coupled as a local search operator. Concerning evolutionary operators, classical operators were used for binary or real variables. If we consider the last works: (Massa et al., 2005) chose the convex recombination and non-uniform mutation; Benedetti et al. (2007) implemented the binary and uniform mutation crossing; and Noghanian et al. (2014) used convex recombination and boundary mutation. Although these operators are very common, they do not exploit characteristics of the problem, which is its main disadvantage.

In the same period, another methodology that had a reasonable number of publications was DE. Rocca et al. (2011) made a review dedicated to the application of this methodology both in inverse problems and in optimization of antennas and other situations. In table 2 of the article, the authors listed eleven works of DE applications to the inverse problem, being that: (i) six works considered problems with perfect conductors; (ii) eight studies made assumptions about the shape of the scatterers so that the number of variables was smaller; (iii) six studies implemented the classic evolutionary operators such as “*DE/best/1/bin*” or “*DE/rand/1/bin*”, in

---

<sup>13</sup>An implementation of the Bat Algorithm was also found (Yang et al., 2021b). But since this algorithm is not so relevant within the context of EAs, it will not be included in the discussion.

<sup>14</sup>Memetic algorithms combine evolutionary and deterministic approaches. Usually, after some generations, an arbitrary deterministic algorithm is applied to the best solution as a local search operation.

which the mutation is performed through the difference vector formed from the best solution (or a random one) and the combination of the two other random solutions; in addition, the binary crossover is used. They are classic operators that do not use information about the structure of the problem; (iv) two studies implemented a strategy of partitioning the population into groups and added a competition operator between them (Breard et al., 2008; Qing, 2003). It is worth noting that, in these two cases, the shape of the scatterer was parameterized. For purposes of illustration, Pastorino (2010a) made a comparison between DE and GA. However, the comparison is quite limited since, in addition to considering only one instance, there was no discussion about how many times the algorithms were run to obtain the residual convergence and mean contrast error curves in Figures 7.14 and 7.15 of the cited reference. Finally, it is worth highlighting the integration of the IMSA strategy with DE available in (Donelli et al., 2010).

As of 2005, the most applied EA in the literature was PSO. As far this author knows, the first implementation was proposed by Caorsi et al. (2004a). The authors justified their choice based on the popularization of the method in EC, the simplicity of its implementation (its structure has only one variation operator and no selection one), and less complexity about the calibration of its parameters. Traditionally, the inertia and acceleration parameters are adjusted to 0.4 and 2.0, respectively (Rocca et al., 2009). For this algorithm, there are implementations considering: (i) the three-dimensional case (Donelli et al., 2009); (ii) coupling with the IMSA strategy (Donelli et al., 2006); (iii) variations in the formulation (Huang and Sanagavarapu Mohan, 2007; Yang et al., 2021c); and (iv) the representation of the object by series of sines and cosines (3.169) (Huang et al., 2008). The most advanced formulation for the algorithm was proposed by Salucci et al. (2017). The authors considered the Ground-Penetration-Radar case. Therefore, the technique was adapted to solve the equations considering multiple frequencies simultaneously. The operation of updating the particles followed the traditional formulation of the algorithm, which does not take into account the problem's structure. To contribute to the search process, the IMSA strategy was used. It is worth highlighting the experimental studies carried out to justify the choice of parameters of inertia, acceleration, and population size, and the real experiments carried out.

The SA and ACO algorithms have been applied in a few studies in the literature. In addition to the traditional applications available in (Caorsi et al., 1991; Garnero et al., 1991), we highlight: (i) Brignone et al. (2008) proposed a hybrid algorithm where the ACO was integrated with the Linear Sampling technique; (ii) Etminan and Moghaddam (2018) proposed adapting SA for a multiple directions search strategy; (iii) Hajebi and Hoofar (2022) have proposed the application of the Covariance Matrix Adaptation Evolution Strategy (CMA-ES) which shows a better performance in large scale problems; and (iv) Pastorino (2010a) compared traditional formulations of GA and ACO and found a faster convergence of ACO in an experiment with synthetic data. However, only one instance was used and there is no information on how many times the algorithms were run.

### 3.7.4 Population Initialization

One aspect that is also relevant to the performance of EAs is how individuals are initialized. Population-based algorithms rely on good diversity at startup for proper convergence. If the initial population does not have this characteristic, in addition to premature convergence, promising regions of the search space will not be explored.

In EAs, the range of allowed values for contrast and field unknowns is a common *a priori* information used for population initialization and evolutionary operators (Donelli and Massa, 2005; Pastorino et al., 2000; Salucci et al., 2017). Although this is important for convergence, it can be a condition that limits the application of the algorithms.

Many initialization strategies are possible using the range information. Population individuals might be initialized with random values taken within the allowed range, considering a uniform distribution (Donelli and Massa, 2005; Pastorino et al., 2000; Salucci et al., 2022b). But it is also possible to initialize the population as disturbances in the free space solution (Donelli et al., 2009, 2006). Another way to initialize the solutions is to use a random strategy for the contrast variables and define the field from (3.40) using the Born Approximation to perform the integral (Salucci et al., 2017). All of these forms are BA-based. Therefore, these initialization strategies may be inefficient for strong scatterers situations.

## 3.8 Deep-Learning Methods

Deep Learning (DL) is a technique within the context of Machine Learning that has become increasingly popular given the numerous variety of possible applications (LeCun et al., 2015). Its potential to predict effects and to classify data has also attracted attention and impacted many studies in computational electromagnetics (Campbell et al., 2021; Li et al., 2021; Massa et al., 2018; Seretis and Sarris, 2022a). Considering its application into Microwave Imaging, in most of the cases, the technique will consist of training Deep Neural Networks (DNN) to predict the result of new entries or even to group them. Although the first works that use DNNs to solve some formulation of EISP are from the 90s (Azimi-Sadjadi et al., 1992; Low and Chao, 1992), the development of DLs for EISP started to become popular in the last five years (Figure 3.4). One of the main attractions is the possibility of real-time imaging from a well-trained network.

Recently, Chen et al. (2020b) and Salucci et al. (2022a) reviewed the DL methodologies applied to EISP. They highlighted three main classes of methods: Fully Data-Driven Learning, Learning-Assisted Objective-Function (LAOF), and Physics-Assisted Learning (PAL). The difference between them was established through the division of the scattering problem into three phases: (i) the propagation of the incident wave; (ii) the interaction between the incident wave and the scatterer which induces a current; and (iii) the radiation of the induced current that propagates the scattered field. Interpreting these phases in the light of the contrast source equations

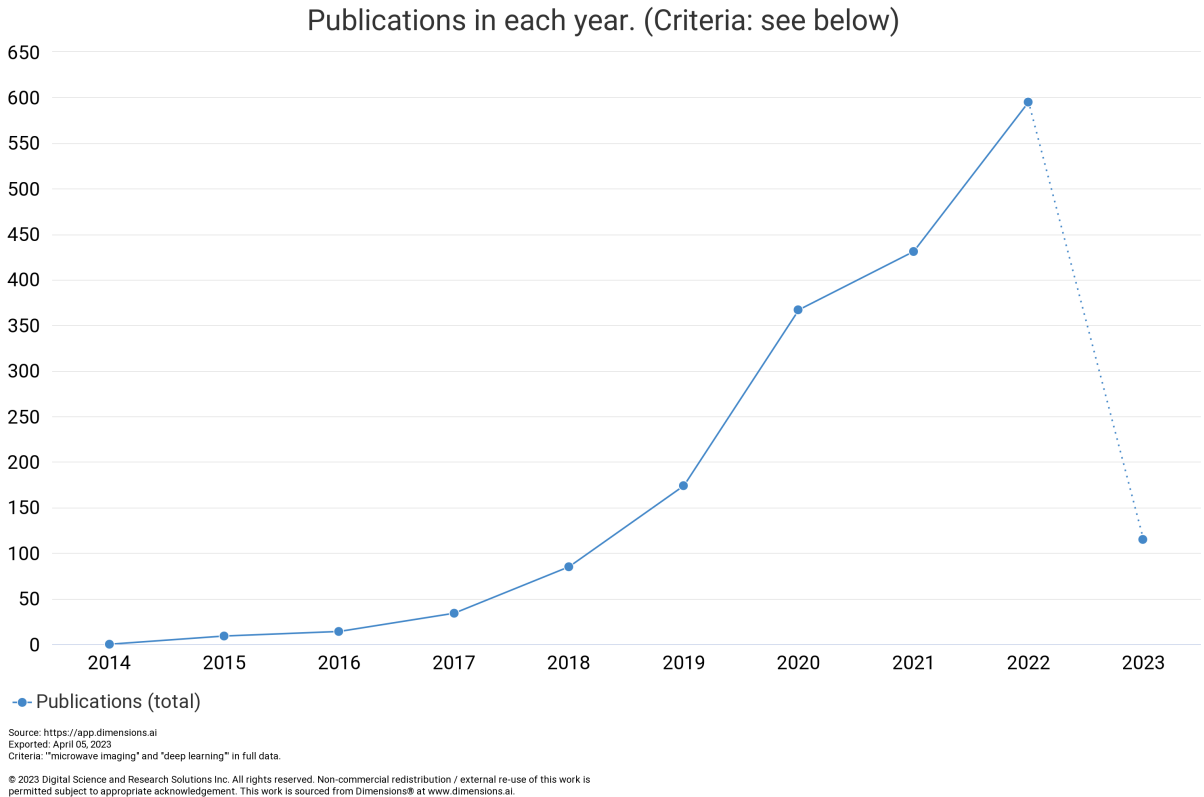


Figura 3.4: Emerging trends: the intersection of Microwave Imaging and Deep Neural Networks garnering increasing attention among researchers, as reflected by the growth of published papers. Source: <http://app.dimensions.ai>

(2.33)-(2.34), only the second phase depends on the contrast function, i.e., in the first and third phases, the incident field and the induced current source are predominant, respectively.

The Fully Data-Drive Learning class is composed of methods whose input to the network is the scattered field data and the output is the contrast function, i.e., the methods make a direct mapping between scattered fields and contrast (Direct Learning Scheme). Therefore, the networks are trained to learn the three phases of the scattering process. Although this is the easiest implementation, it is not the most efficient one since the network is forced to learn processes for which they have an analytical form, such as the incident field propagation. The computational cost for the training phase is very high, especially when the solution is represented by linear elements. In addition, performance can be unsatisfactory for multiple or strong scatterers (Chen et al., 2020b). This methodology can be efficient in simple cases where there is a priori information about the shapes of the scatterers (Fajardo et al., 2019; Ran et al., 2019) or the media is assumed to be inhomogeneous (Zhang et al., 2023b). If a refinement network is added after the initial one, that is used to invert the scattered field data, it has the potential to further enhance the performance and achieve better results (Chen et al., 2022; Song et al., 2021; Yao et al., 2019). Furthermore, there are additional techniques that can aid in enhancing the initial contrast estimation, such as inverting the Contract Integral Equation (2.38) using Fourier bases (Xu et al., 2022) or adding acoustic data in the input (Qin et al., 2022). Another approach

involves predicting multi-frequency scattered fields based on a single-frequency one, which can alleviate the complexity of the direct inversion (Zhang et al., 2023a).

The LAOF Class is based on using deep-learning to accelerate the convergence of an iterative method. In other words, a trained network can be inserted into the methods of sections 3.6 and 3.7 to provide better search directions to accelerate convergence. An example of this type of approach was proposed in (Guo et al., 2019). The authors formulated a gradient learning method, i.e., instead of calculating the gradient to determine the direction of error minimization, they use one provided by a previously trained network to determine the average descent direction. For this reason, it was called the Supervised Descent Method. But other types of strategies are possible:

1. Chen et al. (2020a) proposed to train a network to receive magnetic resonance images and estimate the contrast of the images. The results of this initial step were coupled to the BIM to refine the solution;
2. Similarly, Sanghvi et al. (2020) proposed to train a network to receive the  $\bar{\mathbf{J}}_{s,+}^{\text{eq}}$  vector of the decomposition performed by SOM and obtain an estimate of the total induced source. This step combined with SOM contributes to the solution of problems with strong scatterers.
3. Yao et al. (2022) proposed a descent method where the forward problem in each iteration is solved by a complex-valued deep CNN.

The PAL class principle is to incorporate the physical aspects of the problem into the mathematical formulation of the network architecture. Although adapting the internal structure to combine the electromagnetism laws is not a trivial task, Chen et al. (2020b) also consider that this principle can be used in the configuration of the network input. An example is to train the network to operate only in the space of contrast solutions, i.e., a mapper of the contrast solutions space for itself. In practice, this means training a network to receive an initial reconstruction done by some method and return a high-resolution image with more precise contours of the true contrast. In other words, this also means predicting the high-spatial-frequency components that are missing from an image with the low ones. Examples of this approach in the literature are:

1. Different network structures developed to receive the image reconstructed by linear methods such as Born Approximation, Back-Propagation, and Dominant Current (Guo et al., 2021; Li et al., 2019a; Sun et al., 2018; Wei and Chen, 2019a; Xiao et al., 2020; Zong et al., 2022). Specifically, Wei (2022) suggested using each contrast image obtained by each incident angle in the Back-Propagation method as the input of the network.
2. The refinement of images recovered Near-Field Scanning Microwave Microscopy (Zhou et al., 2023);
3. The network trained from reconstructions made by the CSI (Khoshdel et al., 2019);
4. The threefold hybrid method that recovers the shape through LSM, refine it through CNN, and estimate the dielectric properties by BIM (Chen et al., 2021);
5. (Zhang et al., 2020b) proposed the combination of a qualitative and quantitative approach

as an input to a CNN.

6. In (Chen et al., 2020a), the authors proposed an approach that utilized Convolutional Neural Networks (CNN) to estimate dielectric properties from Magnetic Resonance images. This estimated property was then used as an initial guess for a qualitative inversion method.

In an effort to integrate physical principles into neural network structures, researchers have utilized the iterative nature of quantitative inversion methods. This approach is also known as unrolled method and has been investigated in the most recent research papers. They have consistently demonstrated improved network performance. Notable examples of such papers include:

1. Li et al. (2019b) proposed a cascade of CNN stages that represents the recursive solution derived from the regularization of the inverse problem.
2. Liu et al. (2022a) introduced a comparable architecture, but with a distinct feature. In this structure, each stage consists of four layers dedicated to predicting four different variables: induced current, total field, contrast image, and an auxiliary variable.
3. In the method proposed by Liu et al. (2022b), the induced current and contrast map from the previous stage are combined to generate a novel prediction of the induced current. This approach was compared to SOM.
4. Shan et al. (2023) put forward a novel approach to enhance BIM framework by utilizing two CNNs in place of the conventional forward and inverse solvers. Consequently, each stage of the updated framework was characterized as an iteration of BIM.
5. Zhang et al. (2023c) has proposed a novel approach in which each stage comprises of two Contrast Source Inversion (CSI) iterations and two Convolutional Neural Networks (CNNs). In the first CSI iteration, the contrast image is updated, following which the two CNNs predict the residual between the correct image and the present one. This information is then fed into another CSI iteration that fine-tunes the current contrast image for further improvement.
6. Zhou et al. (2022) has presented a Generative Adversarial Network (GAN) where each stage of the generative network implements an iteration of CSI in which each variable is a layer, similarly to Liu et al. (2022a). In addition, they incorporated a refinement layer after predicting the contrast image to further enhance the reconstruction.

DL techniques have found applications beyond the inverse two-dimensional problem. Researchers have explored the use of these techniques for solving three-dimensional problems (Chen et al., 2023; Han et al., 2022; Khoshdel et al., 2021; Xiao et al., 2022; Zhao et al., 2022; Zhou et al., 2021) and for estimating fields in the forward problem (Guo et al., 2022; Hu et al., 2022; Ma et al., 2021; Seretis and Sarris, 2022b; Yao et al., 2023; Yin et al., 2022). Additionally, peripheral issues have been addressed in the literature: learning regularization parameters (Afkham et al., 2021); independence of measurement configuration (Li et al., 2023); phase information (Pan et al., 2021) and prediction (Luo et al., 2022); scatterer and background clas-

sification for qualitative methods (Yago Ruiz et al., 2022); dielectric breast phantoms generated by GAN (Shao and Zhou, 2022); and the inversion of dielectric and perfect electric conductor scatterers (Song et al., 2022).

### 3.9 Conclusion

This chapter has reviewed the EISP solution methodologies. To facilitate the translation of ideas into numerical implementation, an effort was made to define the problem discretization in Section 3.2 based on a usual problem configuration defined in 3.1. We highlight the discretization of (3.32)-(3.36) which is the most popular form in the literature, as well as the matrix form in (3.39)-(3.43). Then, linear approaches such as the Born and Rytov approximations and the Back-Propagation and Dominant Current methods were presented. The classic regularization methodologies, often required for solving linear ill-posed inverse problems, were also presented. We mention the Tikhonov Regularization (Subsection 3.4.1) with its several parameter choice methods, where the L-Curve is one of the main ones (Subsection 3.4.1).

Nonlinear methods are classified as either qualitative or quantitative. The former is suitable for when only the shape of the scatterers are necessary to recover. On the other hand, the latter is the class for when shape and dielectric information need to be estimated. The quantitative methods are divided into deterministic (Section 3.6) or stochastic (Section 3.7) methods. The main advantage of deterministic methods is the reconstruction by operations that are fully based on the physical properties while the advantage of stochastic algorithms is their compatibility with nonlinear problems with multiple minimums. Among the deterministic ones, the most traditional ones are BIM (Subsection 3.6.1), DBIM (Subsection 3.6.2), and CSI (Subsection 3.6.6) while the ones that have been most used in recent works are CS (Subsection 3.6.7), Level-Set (Subsection 3.6.5) and SOM (Subsection 3.6.8). Considering the stochastic methods, we highlight the evolutionary algorithms that can be adapted for different types of representations (Subsection 3.7.1), objective functions (Subsection 3.7.2), search engines and operations (Subsection 3.7.3); and initializations (Subsection 3.7.4). The latest formulations usually consider a representation of the solution by the discretization elements, the PSO mechanism, the weighted residuals of data and state equations. One of the most successful strategies to reduce the problem is IMSA and the replacement of the objective function by surrogate models. Table 3.1 summarizes the various methods according to their properties.

Finally, a brief discussion was made on the use of DLs (Section 3.8), usually coupled with linear or non-linear deterministic strategies for the refinement and resolution increase of the contrast image. This subject has received a lot of attention from the literature recently and it represents one of the main research opportunities for the development of methodologies that address EISP.

Tabela 3.1: Classification of methods by their properties.

Classes	Methods		
Qualitative	Linear Sampling Method Orthogonality Sampling Method		
	Linear	Born Approximation Rytov Approximation Back-Propagation Method Dominant Current Scheme	
Deterministic		Forward and inverse subproblems	Born Iterative Method Distorted Born Iterative Method Variational Born Iterative Method Level-Set Method
	Nonlinear	Gradient-based	Conjugated-Gradient Method Contrast Source Inversion Subspace-based Optimization Method
Quantitative		Other	Compressive Sensing Regularization on $L_p$ Banach Spaces Virtual Experiments Deep learning methods
Components	Types		
Representation	Known geometries Contours Pixel-based		
Stochastic	Objective function	Data equation residual Data and state equation residual	
	Mechanism	GA DE PSO	
	Population	Random	
	Initialization	Born Approximation	

# Capítulo 4

## Proposed Methodology

This thesis aims to enhance the current state-of-the-art algorithms for microwave imaging by proposing novel approaches based on surrogate models. Additionally, a comprehensive framework for the development and testing of algorithms specific to this problem is presented. In Section 4.1, a critical review of the literature is presented, highlighting the gaps and areas for improvement in the current state of the art. Building on this analysis, Section 4.2 proposes a novel approach to address some of the limitations, specifically, the use of surrogate models and the framework for development and comparison of algorithms designed for EISPs. Section 4.3 provides a detailed discussion of surrogate-model assisted algorithms for microwave imaging, including a description of the transformation of the inversion problem into a bidimensional optimization one, the Kriging model, and the proposed algorithms. Section 4.4 outlines a framework for developing and testing algorithms for microwave imaging, including the proposed metrics to assess their performance. Finally, Section 4.5 presents the concluding remarks.

### 4.1 Literature Criticism and Opportunities

In the early stages of developing algorithms for microwave imaging, several challenges were encountered (Bertero and Boccacci, 2020; Kirsch, 2011; Pastorino et al., 2000). In the early context, the available data was significantly limited and noisy, which represented a serious challenge for a problem with non-unique solution. When more data was available, the limited computing power was other challenge. The understanding of the physics involved in microwave imaging also evolved throughout the years, which was also important for the development of the subject.

Currently, two significant challenges are faced by researchers in the literature: real-time imaging and the retrieval of strong scatterers. Real-time imaging requires fast and efficient algorithms that can produce accurate images in real-time or nearly, which is essential for many applications such as medical imaging (Li et al., 2021) and security screening (Asok et al., 2022). To address this challenge, researchers have turned to deep-learning techniques that

can efficiently process large amounts of data and provide accurate results in real-time (Salucci et al., 2022a).

The other challenge is the imaging of strong scatterers, which refers to objects with high contrast levels or large dimensions when comparing to the wavelength. Such objects result in high nonlinearity and can create significant artifacts in the resulting image, making it difficult to accurately reconstruct the underlying structure. This is particularly challenging when imaging complex structures, such as biological tissues or composite materials (Lazebnik et al., 2007). This type of scenario has been addressed in three main ways:

1. The first approach is to reduce the degree of non-linearity by changing the integrals solved by the algorithms (Section 2.4);
2. The second approach is based on domain decomposition (Zhang et al., 2022). This approach divides the scatterer region into dominant and subordinate subdomains based on the information of the induced current. The dominant subdomain is then reconstructed iteratively, narrowing the inversion domain and reducing the nonlinearity of the problem.
3. The third approach is the use of surrogate models (Koziel and Leifsson, 2008). Salucci et al. (2022b) proposed a surrogate model to predict the data equation error considering curve-based representations of scatterers. By using this approach, the computational cost of stochastic algorithms that do not solve the contrast and the total field simultaneously can be significantly reduced. This is because such algorithms rely on forward problem simulations to estimate the error. The authors demonstrated the effectiveness of their approach in high-contrast scenarios, showing promising results.

Some ideas in the field have yet to receive the attention they deserve, and one of them is the use of qualitative methods to define initial solutions for quantitative algorithms. Even though this approach has been explored in some papers (Bevacqua et al., 2015; Han et al., 2022; Zhang et al., 2020b), it has yet to be fully utilized to improve the performance of stochastic algorithms for the problem. The use of qualitative methods can help to improve the robustness of images reconstructed by these algorithms to noise and high contrasts, as well as guide the convergence of population-based algorithms towards more promising regions of the search space.

Another aspect that draws attention in the literature is experiment design and quality evaluation of algorithms. A highly relevant aspect of experimentation is using more realistic scatterer models or data obtained from real measurements. This has become popular in the literature through laboratories that make the data available. Two widespread examples are the *UWCEM Numerical Breast Phantom Repository* (Burfeindt et al., 2012) and the measurements made by the *Institut Fresnel* (Geffrin et al., 2005).

In addition, Kurrant et al. (2021b) have recently proposed a methodology to evaluate the performance of the algorithms applied to breast cancer detection. Given a reference image and the recovered one, the authors proposed to segment the tissues in the images by an unsupervised machine learning approach. After decomposing the images and mapping the tissues, five metrics were proposed to evaluate shape fidelity, malignant tissue reconstruction in tumor

regions, among others. Therefore, the novelty is a technique to measure the quality of breast reconstruction with suitable tools. Their methodology is also available as a MATLAB toolbox (Kurrant et al., 2021a).

However, in many publications addressing general applications, traditional instances have been chosen with particular characteristics to demonstrate the reconstruction ability of the proposed method in the corresponding situation. Performance is measured through some quality indicator, and the result is compared to other algorithms and formulations (Zhang et al., 2020a; Zhong et al., 2020; Zhou et al., 2021). Although this approach is interesting to illustrate the algorithm's suitability, it has little methodological rigor to offer robust answers to questions such as: (i) what is the impact of the choice of the instance on the performance quantifier's value? (ii) How does the indicator vary if the object's geometry changes? (iii) How does the difference in performance observed between the two methods vary if the geometries vary? (iv) What is the average or worst-case performance of the method for a given configuration? Among others.

Even though these questions may fall outside the scope of proposals based on case studies (e.g., physical experiments), general conclusions about suitability and performance can be very weak without an adequate experimental methodology that considers different effect factors in the configuration of the problem. Although the noise level factor is usually the most explored in this sense (Batista et al., 2021; Chen, 2010; Chew and Wang, 1990; Shah and Moghaddam, 2018), experiments with random instances for a more robust measurement performance are not usually performed. Even when the publication had the main objective of comparing algorithms (Gilmore et al., 2009; Moghaddam et al., 1991; Pan et al., 2010). This practice is essential to eliminate the observer's bias in algorithms analysis (Montgomery and Runger, 2010). Other examples are several works in the literature that propose stochastic methodologies and do not even inform how many times the algorithm was repeated when showing the result for a given instance. There is no information if the result shown represents the worst, average, or best case. This is problematic since these methodologies have no guarantee of returning the same solution in every execution (Ashtari et al., 2010; Massa et al., 2005; Salucci et al., 2017).

Therefore, another opportunity in the literature is to introduce more robust comparisons between algorithms, i.e., benchmarking. A reference on best practices for comparing optimization algorithms is the article written by Beiranvand et al. (2017). Among the many relevant notes made by the authors, we highlight the following:

- A test suite with few problems should be referred to as a case study or proof of concept, but not benchmarking.
- A test suite should avoid the following deficiencies: (i) few problems; (ii) slight or excessive variation in the complexity of the instances, making it impossible to extract helpful information; (iii) problems with no known solutions (which can be inevitable in real situations); (iv) bias at the starting point of the algorithms; (v) hidden structures.
- All algorithms must receive the same amount of input information and ensure that there

is an assumption that is only respected by one of the algorithms in order to verify the influence of that assumption.

These topics do not necessarily represent failures in the experiments described in the literature. However, these concepts already established in the optimization literature can bring maturity to the algorithms for EISP.

Finally, we also highlight the metrics used to assess the quality of the reconstructions. In the vast majority of works, the quality of the reconstructed images of the contrast function is quantified in one of the following ways (Chew and Wang, 1990; Oliveri et al., 2019, 2011; Salucci et al., 2017; Shah et al., 2019; Wang and Chew, 1989; Zhang et al., 2020b):

$$\zeta_{\epsilon} = \sqrt{\frac{1}{N_I N_J} \sum_{i=1}^I \sum_{j=1}^J \left| \frac{\epsilon_{r,ij}^* - \epsilon_{r,ij}}{\epsilon_{r,ij}^*} \right|^2} \quad (4.1)$$

$$\zeta_{\chi} = \sqrt{\frac{1}{N_I N_J} \sum_{i=1}^I \sum_{j=1}^J \left| \frac{\chi_{ij}^* - \chi_{ij}}{\chi_{ij}^* + 1} \right|^2} \quad (4.2)$$

where  $\epsilon_{r,ij}^*$  and  $\chi_{ij}^*$  are the actual values of relative permittivity and contrast, respectively. In general, (4.1) and (4.2) are formulas based on the root of the average percentage error. Slight variations can also be adopted, such as replacing  $N_I N_J$  with the image area or removing the root and square of the error.

In general, when it comes to identifying objects in the image, a good reconstruction is characterized by the correct identification of the scatterer's position, shape, and contrast. (4.1) and (4.2) are metrics that address these three characteristics at the same time. A reconstruction equal to the actual one will minimize these indicators. However, there are situations in which these indicators are not as efficient. When the area of a scatterer is much smaller than the figure, the error will be minimal. This might happen even if there are many deviations in the estimate of the contrast in the scatterer area (e.g.,  $\chi = 0$ ). This can also disguise significant errors in the position and shape of the rebuilt scatterers. It is worth noting that the residuals of the equations are not necessarily taken as quality meters, given that, due to ill-posedness, there may be solutions with low residues and images that are different from those expected.

As suggested by Beiranvand et al. (2017), other indicators can also evaluate interesting aspects of algorithms performance: (i) success rate, i.e., the number of times that an algorithm reaches a certain tolerance in a specific time limit; (ii) percentage of a class of solutions found in a given situation; (iii) accuracy profile, i.e., percentage of problems that an algorithm can solve for a given percentage of accuracy; (iii) performance profile, i.e., the probability that an algorithm will solve a problem given a time limit; among others. These indicators could provide information that would greatly enrich the comparison of the algorithms.

## 4.2 Proposal

In the previous section, the state-of-the-art and the gaps in the literature on the inverse electromagnetic scattering problem were discussed. Based on this discussion, two contributions are proposed by our research. First, algorithms assisted by surrogate models that use images generated by qualitative methods are aimed to be designed. Second, the design of specialized software for the development and testing of algorithms for this problem is proposed, with support for randomized testing and measurement of average performance through a set of indicators. These contributions aim to explore new possibilities of applying surrogate models and bring more robustness to the analysis of algorithms for the problem.

New applications of surrogate models in this problem are encouraged since their introduction is recent and has only been explored by Salucci et al. (2022b). Using curves to represent scatterers that define their contours allows a reconstruction compatible with complex geometries, but it requires several variables, which can still be very high for surrogate models (Wu et al., 2019). Furthermore, it is necessary to know beforehand how many scatterers exist in the image so that the compatible number of contours can be defined. If the image obtained by qualitative methods is used, the problem becomes one of estimating the contrast of the objects and adjusting the threshold that separates the background from the objects. In other words, this would turn the inversion process into a two-dimensional optimization problem, in which the performance of surrogate models is higher. The OSM can capture different levels of contrast in the images, making the application feasible in cases of multiple objects with different levels of contrast. However, the application is restricted to cases where the qualitative methods work properly.

As a second contribution, a framework for algorithms for the inverse electromagnetic scattering problem is proposed to facilitate their implementation and testing. Suitable experiments need to be designed to assess the impact of modifications on the performance of algorithms. Arbitrary situations can illustrate the ability of methods to make good reconstructions, and experiments with real data are relevant to attest to the application in practical situations. However, measuring the performance of methods and making comparisons need to follow principles such as control of effect factors and random instances, which are well-established in the specialized literature on Evolutionary Algorithms but little widespread in the literature on methods for Electromagnetic Inverse Scattering. A framework that addresses the insulation of effects factors and new indicators can better qualify the algorithm's reconstruction performance. This applies not only to stochastic methods but also to deterministic ones.

## 4.3 Surrogate model-Assisted Algorithms for EISPs

This section focuses on the proposed application of surrogate models to solve the electromagnetic inverse scattering problem. To address it, a bi-dimensional optimization approach

is employed, where the objective function represents the discrepancy between the estimation of the scattered field and the measured data. Surrogate models have proven to be effective tools in approximating complex objective functions in optimization problems. Therefore, the section also introduces the concept of surrogate models and their application in solving electromagnetic inverse scattering problems. The Kriging model, a popular surrogate modeling technique, is briefly explained, followed by a description of the proposed algorithms that employ the Kriging model to solve the inverse scattering problem.

### 4.3.1 The Optimization Model

Qualitative inversion methods are commonly employed when only the shape of objects needs to be retrieved. The method operates by classifying image points as either part of a scatterer or not, based on an indicator function that assigns a value to each point. However, these methods do not offer a quantitative estimate of the scatterer's contrast, meaning they do not estimate the dielectric properties of the objects. One possible solution is to transform the qualitative problem into a quantitative one by identifying the best classification threshold and estimating the contrast in the object region, based on the image obtained from the normalized indicator function. Furthermore, the Orthogonality Sampling Method (OSM), discussed in subsection 3.5.2, not only classifies the points but also identifies different levels of contrast in the image. This ability makes it possible to apply a qualitative method in scenarios with multiple scatterers of different contrasts, which is particularly useful in the field of electromagnetic scattering.

Mathematically, let  $\boldsymbol{\chi}^{norm}$  be the  $N_I \times N_J$  image obtained by OSM in which the pixel values are normalized between 0 and 1. Then, a quantitative inversion result could be obtained if (i) a threshold level  $T$  is applied to separate background and scatterers, i.e., set  $\chi_{ij}^{norm} = 0$  for pixels where  $\chi_{ij}^{norm} < T$ ; and (ii) multiply the remaining non-zero pixels by a factor  $\chi^F$ . In other words, a new quantitative image  $\boldsymbol{\chi}$  is obtained by:

$$\chi_{ij} = \begin{cases} \chi^F \chi_{ij}^{norm}, & \text{if } \chi_{ij}^{norm} \geq T, \\ 0, & \text{otherwise.} \end{cases} \quad (4.3)$$

Figure 4.1 illustrates each step of the proposed process. Note that the transformation does not assume homogeneity within the contrast area, which means that contrast variations are allowed. However, if homogeneity is assumed, the truncation by the average value can be performed.

The image  $\boldsymbol{\chi}$  represents the diagonal elements of the contrast matrix  $\bar{\boldsymbol{\chi}}$  mentioned in (3.47). Consequently, the data equation error (3.39) can be calculated only if the total electric field is evaluated. Hence, a two-dimensional optimization problem can be defined based on a

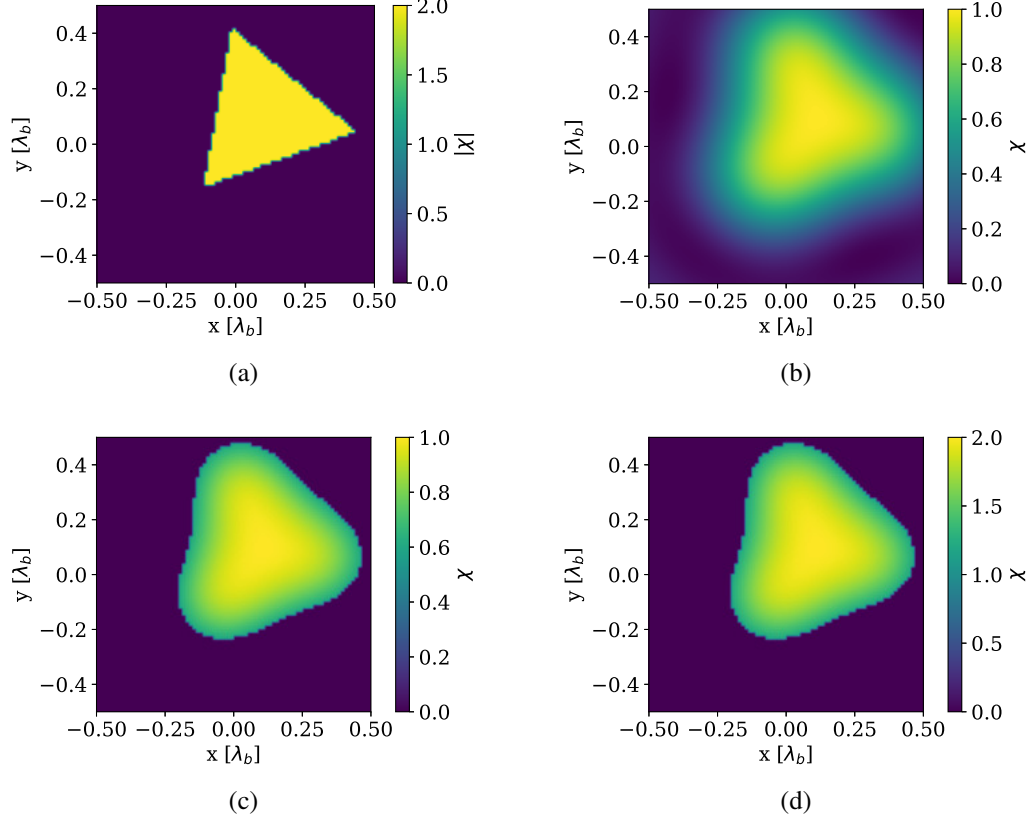


Figura 4.1: Example of the process of transforming a qualitative image into a quantitative one: (a) ground-truth image; (b) image obtained by OSM ( $\chi^{norm}$ ); (c) image obtained after the thresholding process; and (d) final image obtained after the multiplication step.

given scattered field data and its corresponding Green function matrix.

$$T^*, \chi^{F*} = \arg \min f(T, \chi^F) \quad (4.4)$$

$$T \in [0, 1], \chi^F \in [\chi_{min}^F, \chi_{max}^F] \quad (4.5)$$

where  $f(T, \chi^F)$  is the function that determines the data equation error based on the process of solving qualitatively the inverse problem through OSM and applying the transformation according (4.3). Evidently, the total field must be computed for each pair  $(T, \chi^F)$ .

Understanding the characteristics of the objective function is crucial for solving any optimization problem effectively. This is because the choice of the most appropriate algorithm depends on this information. Therefore, having knowledge of the objective function's properties is essential for selecting the best optimization method and achieving the desired outcome.

In the optimization problem defined by (4.4)-(4.5), varying the multiplication factor  $\chi^F$  leads to continuous variations in the error of the data equation. However, varying the threshold  $T$  does not produce a significant change on a small scale. This is due to the fact that the image is a discrete representation of the contrast function, and small variations in the thresholding operator may not cause any change in the resulting image. Hence, the value of the objective

function remains constant in this small interval.

Although this effect occurs on a small scale and the objective function appears smooth and convex from a macro perspective, when we visualize the surface of the function on a smaller scale, we will notice non-smoothness. This makes the function multi-scale and can create problems for optimization methods that depend on derivative information. When close to a roughness, the adjustment of the discrete value for perturbation of the solution might be complicated, making the gradient point in the wrong direction. Derivative-free methods or population-based methods may be more efficient in such cases.

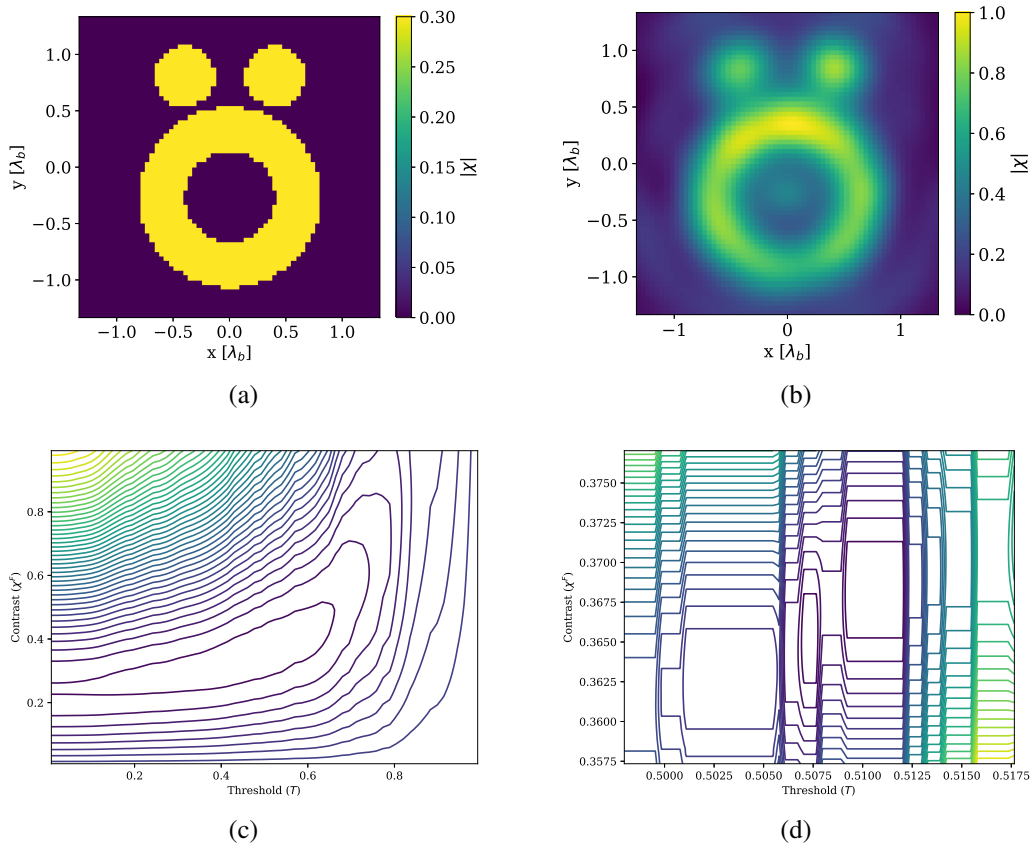


Figura 4.2: Example of an objective function resulting from the transformation of the inversion problem into a two-dimensional optimization one: (a) the ground-truth image; (b) the image obtained by OSM; (c) the surface obtained by the transformation of the inversion problem into a two-dimensional optimization problem. The surface appears smooth from a macro perspective, but when we zoom in on the image close to the optimum (Figure 4.2d), we see the roughness on the  $T$  variable axis.

Figure 4.2 illustrates this problem. Figure 4.2b shows the reconstruction from the qualitative method for a test represented by Figure 4.2a. In Figure 4.2c, we see the surface of the objective function resulting from the transformation of the inversion problem into a two-dimensional optimization problem. The surface appears smooth from a macro perspective, but when we zoom in on the image close to the optimum (Figure 4.2d), we see the roughness on the  $T$  variable axis.

Another issue is that the optimal value of the multiplication factor may not coincide with the exact value of the image contrast, mainly in cases of homogeneous scatterers. This is

because contrast variations within the object region make it difficult to accurately reconstruct the image. An alternative to mitigate this effect is to assume that the object is all homogeneous and truncate the values within the object's region by their average or maximum value.

Finally, it is worth emphasizing that the evaluation of the objective function is not cheap since it depends on the execution of the direct resolver to estimate the corresponding total field. Therefore, applying an optimization algorithm that depends on many evaluations can be prohibitive.

### 4.3.2 Surrogate Models

In many optimization problems, the objective function can be computationally expensive to evaluate, meaning that it takes a long time to compute the value of the function for a given set of input parameters. This can make it difficult to find good quality solutions, as it may take many iterations of the optimization algorithm to explore the search space thoroughly.

Surrogate Models are approximations of the expensive objective function that are designed to reduce the computational cost of evaluating the objective function (Mendes et al., 2013; Sacks et al., 1989; Schonlau, 1997). A surrogate model is typically trained on a set of input-output pairs, where the inputs are the parameters of the optimization problem and the outputs are the value of the objective function for those parameters. The surrogate model learns to approximate the objective function using this training data, allowing it to make predictions about the value of the objective function for new sets of input parameters without actually evaluating the expensive objective function.

Surrogate models can be used to speed up the convergence of optimization algorithms, as the surrogate model can be evaluated much more quickly than the expensive objective function. This means that the optimization algorithm can explore the search space more quickly, potentially finding good quality solutions in fewer iterations. Additionally, the use of surrogate models can reduce the number of evaluations of the expensive objective function, which can be a significant computational cost in some problems (Sobester et al., 2008).

There are many different types of surrogate models, including regression models, neural networks, and Gaussian processes, among others. In this thesis, the Kriging model is considered since it is widely used in optimization problems (Emmerich et al., 2006; Yang et al., 2019; Zhao et al., 2011) and it has shown slightly better performance in single-objective optimization problems (?).

### 4.3.3 Kriging Model

Let  $y : \mathbb{X} \subset \mathbb{R}^n \Rightarrow \mathbb{R}$  be an objective function for a given problem. A sample with  $N$  solutions and their respective evaluations are  $\mathbf{X} = [\mathbf{x}^1, \dots, \mathbf{x}^N]^T$  and  $\mathbf{y} = [y(\mathbf{x}^1), \dots, y(\mathbf{x}^N)]^T$ , respectively. The Kriging model is a regression model where each observation of the objective

function is treated as (Jones et al., 1998; Sacks et al., 1989; Schonlau, 1997):

$$y(\mathbf{x}^i) = f(\mathbf{x}^i) + e(\mathbf{x}^i), i = 1, \dots, N \quad (4.6)$$

where  $f(\mathbf{x}^i) = \mathbf{f}^T \boldsymbol{\alpha} = \sum_{k=0}^d \alpha_k f_k(\mathbf{x}^i)$ ,  $d \leq N - 1$ , is a linear combination of the regression functions  $f_k(\cdot)$  and  $\alpha_k$ ,  $k = 0, \dots, d$ , are the corresponding coefficients;  $e(\cdot)$  is a random normal variable with zero mean and variance  $\Sigma^2$ . Regression functions are similar to the trial functions presented in Section 3.2. In the scope of present subsection:

$$f_k(\mathbf{x}) = \prod_{r=1}^n x_r^{q_r}, q_r \in [0, Q], \sum_{r=1}^n q_r \leq Q \quad (4.7)$$

where  $Q$  is the highest integer that satisfies  $\frac{(n+Q)!}{Q!n!} < N - 1$  (Zhao et al., 2011). The covariance of  $e(\cdot)$  is assumed as:

$$\text{Cov}(e(\mathbf{x}^i), e(\mathbf{x}^j)) = \Sigma^2 R(\boldsymbol{\theta}, \mathbf{x}^i, \mathbf{x}^j) \quad (4.8)$$

where  $R(\cdot, \cdot, \cdot)$  is a Gaussian correlation function whose form is:

$$R(\boldsymbol{\theta}, \mathbf{x}^i, \mathbf{x}^j) = \prod_{r=1}^n e^{-\theta_r |x_r^i - x_r^j|^2} \quad (4.9)$$

with  $\boldsymbol{\theta} \in \mathbb{H}$ ,  $\mathbb{H} = \{[\theta_1, \dots, \theta_n] | \theta_r > 0 \forall r = 1, \dots, n\}$ . Other correlation functions are also possible (MacKay et al., 1998; Sacks et al., 1989). However, (4.9) is often used when the Kriging model is considered (Jin, 2005; Zhao et al., 2011). The parameters  $\boldsymbol{\theta}$  are estimated based on the available sample and they mean the importance of each variable and how correlated they are.

The optimal choice of  $\boldsymbol{\theta}$ , based on the sample data, is defined as the maximum likelihood estimator (MLE), where the likelihood function has the following form:

$$L(\boldsymbol{\theta}) = \frac{1}{\sqrt{(2\pi\Sigma^2)^N |\mathbf{R}|}} \exp\left(-\frac{1}{2\Sigma^2} (\mathbf{y} - \mathbf{F}\boldsymbol{\alpha})^T \mathbf{R}^{-1} (\mathbf{y} - \mathbf{F}\boldsymbol{\alpha})\right) \quad (4.10)$$

where  $\mathbf{F} = [f_k(\mathbf{x}^i)]_{N \times (d+1)}$  and  $\mathbf{R} = [R(\boldsymbol{\theta}, \mathbf{x}^i, \mathbf{x}^j)]_{N \times N}$  are the regression and correlation matrices, respectively, with  $i, j \in 1, \dots, N$  and  $k \in 0, \dots, d$ . For a given  $\boldsymbol{\theta}$ , the expressions:

$$\hat{\boldsymbol{\alpha}} = (\mathbf{F}^T \mathbf{R}^{-1} \mathbf{F})^{-1} \mathbf{F}^T \mathbf{R}^{-1} \mathbf{y} \quad (4.11)$$

$$\hat{\Sigma}^2 = \frac{1}{N} (\mathbf{y} - \mathbf{F}\hat{\boldsymbol{\alpha}})^T \mathbf{R}^{-1} (\mathbf{y} - \mathbf{F}\hat{\boldsymbol{\alpha}}) \quad (4.12)$$

provide the respective MLEs of  $\boldsymbol{\alpha}$  and  $\Sigma^2$ . If (4.11) and (4.12) are used in (4.10), then the optimal  $\boldsymbol{\theta}$  is obtained through:

$$\arg \max_{\boldsymbol{\theta} \in \mathbb{H}} \ln L(\boldsymbol{\theta}) \quad (4.13)$$

where:

$$\ln L(\boldsymbol{\theta}) = -\frac{N}{2} \ln(2\pi) - N \ln(\hat{\Sigma}) - \ln(|\mathbf{R}|) - \frac{1}{2} \quad (4.14)$$

By determining the optimal  $\boldsymbol{\theta}$  through (4.13), the correlation matrix  $\mathbf{R}$  is obtained and  $\hat{\alpha}$  and  $\hat{\Sigma}^2$  are computed according to (4.11) and (4.12), respectively. Then, for an untried input  $\mathbf{x}$ , the predicted evaluation and its mean squared error are, respectively:

$$\hat{y}(\mathbf{x}) = \mathbf{f}^T \hat{\alpha} + \mathbf{r}^T \mathbf{R}^{-1} (y - \mathbf{F} \hat{\alpha}) \quad (4.15)$$

$$\hat{s}^2(\mathbf{x}) = \hat{\Sigma}^2 \left[ 1 - (\mathbf{f}^T(\mathbf{x}) + \mathbf{r}^T(\mathbf{x})) \begin{pmatrix} \mathbf{0} & \mathbf{F}^T \\ \mathbf{F} & \mathbf{R} \end{pmatrix}^{-1} \begin{pmatrix} \mathbf{f}(\mathbf{x}) \\ \mathbf{r}(\mathbf{x}) \end{pmatrix} \right] \quad (4.16)$$

where  $\mathbf{r}^T(\mathbf{x}) = [R(\boldsymbol{\theta}, \mathbf{x}^1, \mathbf{x}), \dots, R(\boldsymbol{\theta}, \mathbf{x}^N, \mathbf{x})]$  is the vector of correlation;  $R(\boldsymbol{\theta}, \mathbf{x}^i, \mathbf{x})$  represents the correlation between  $e(\cdot)$  at the sampled point  $\mathbf{x}^i$  and  $e(\cdot)$  at an untried  $\mathbf{x}$ , for  $i = 1, \dots, N$ .

Finally, such Kriging model is an interpolation model. Interestingly, when (4.15) is evaluated at a point that belongs to the sample, then the prediction is the actual evaluation. This is due to the matching of  $\mathbf{r}^T$  for the considered point with a line of the matrix  $\mathbf{R}$ .

#### 4.3.4 Surrogate model-Assisted Algorithms

The chapter presented various aspects related to the proposed optimization problem and the use of surrogate models. Subsection 4.3.1 showed how the inversion problem was transformed into a two-dimensional optimization problem. However, the obtained objective function is non-smooth and computationally expensive due to the non-smoothness of the thresholding operator and the need to solve the problem directly to estimate the data equation error. To address these challenges, one alternative is to use a surrogate model, which can reconstruct the objective function by considering its macroscopic characteristics through a set of surface points that are not too close together. The surrogate model works as an interpolation operator and can overcome the microscale problem, resulting in a smooth function when smooth basis functions are used. Additionally, predicting the objective function evaluation is less costly than evaluating it, making it feasible to apply search direction and population-based algorithms.

In order to implement an algorithm assisted by surrogate models, the first step is to obtain a sample of points in the search space along with their respective evaluations. Based on this sample, the surrogate model of the objective function can be constructed. Once the surrogate model is obtained, the search process can begin, and the model can be updated with new solutions that are chosen to be evaluated by the objective function. Thus, in addition to the various methods for obtaining the initial set of points, it is also possible to explore different methodologies for searching and updating the surrogate model.

One way to obtain the initial sample of solutions is through uniform sampling of the search space. This involves sampling equidistant points on each axis within the range of decision variables. However, the more traditional approach is Latin Hypercube Sampling (LHS) Iman

et al. (1981), which is a statistical method that generates quasi-random sampling distributions. LHS is widely used in computer experiments due to its simplicity and projection properties in high-dimensional problems. To construct the LHS design, the space of each variable dimension is divided into  $n$  sections, where  $n$  is the number of sampling points. Only one point is then placed in each section.

To illustrate the differences between these two sampling methods, a high-contrast scatterer problem was simulated (Figure 4.3a), resulting in a multimodal objective function (Figure 4.3b). Sampling by the LHS method resulted in a surface with a barrier separating the original minimum region in two, in which there was no sample (Figure 4.3b). Since the LHS method is stochastic, each sampling can result in a different surface, and important regions can be left without any samples. Uniform sampling can also result in regions running out of samples, especially if the number of samples is low. However, with a reasonable number of samples, a surface with similar characteristics can be obtained, especially in two-dimensional problems, as it is shown in Figure 4.3d. Therefore, to avoid the stochastic aspect of sampling, a uniform methodology is adopted, and it is always necessary to choose an adequate number of samples.

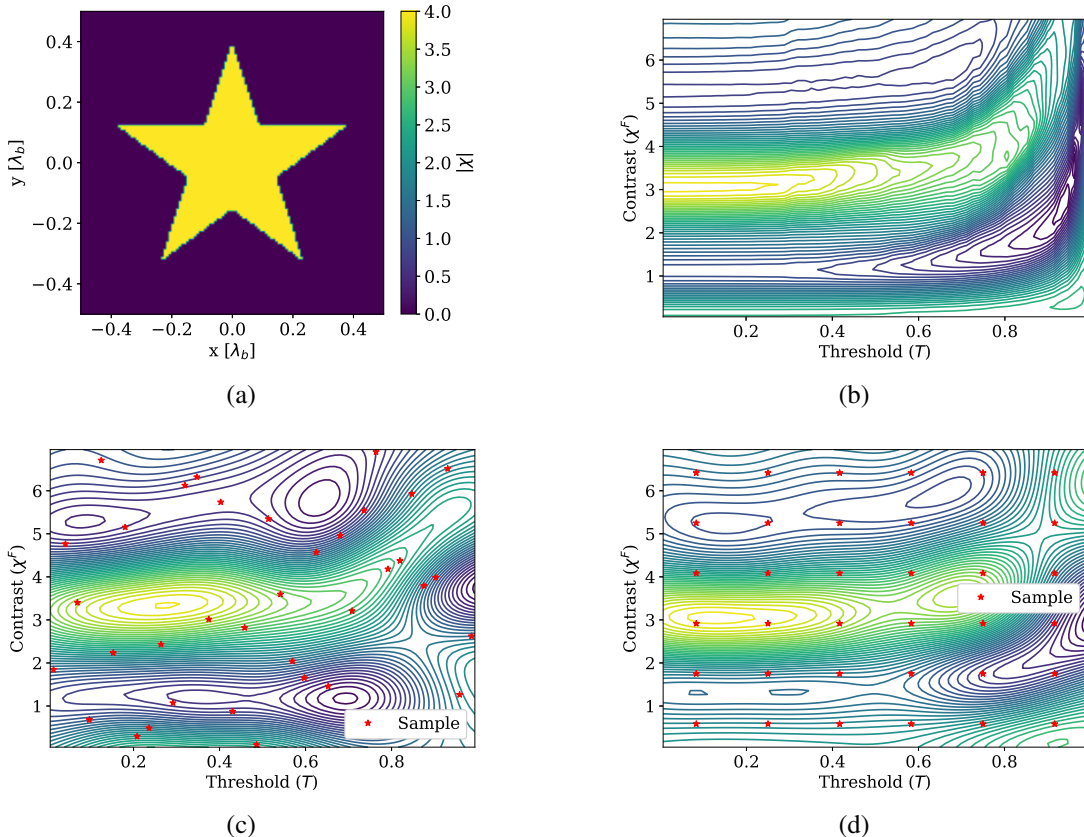


Figura 4.3: Comparison of Latin Hypercube Sampling and Uniform Sampling methods for strong scatterer instance: (a) the ground-truth image; (b) the surface of the corresponding objective-function; (c) the predicted surface obtained by LHS; (d) the predicted surface obtained by uniform sampling.

Surrogate Model-Assisted Evolutionary Algorithms (SAEAs) are a popular approach

(Emmerich et al., 2006; Liu et al., 2014). Despite the various possible formulations of SAEAs (Buche et al., 2005), they all share the same general structure (He et al., 2023). In Figure 4.4, the general flowchart is illustrated. The main cycle of the algorithm is initiated after the initial set of solutions is obtained and the surrogate model is built. In each generation of the cycle, the current surrogate-model is utilized to evaluate the fitness values of individuals instead of the real objective-function. An evolutionary algorithm is then employed to continually search for the optimal solution of the problem. Meanwhile, high-quality individuals are selected to update the sample and, therefore, are evaluated according the true objective function to update the surrogate-model (Liu et al., 2014; Sun et al., 2017; Zhou et al., 2007). These operations are repeated until the termination condition is met (Jin, 2005).

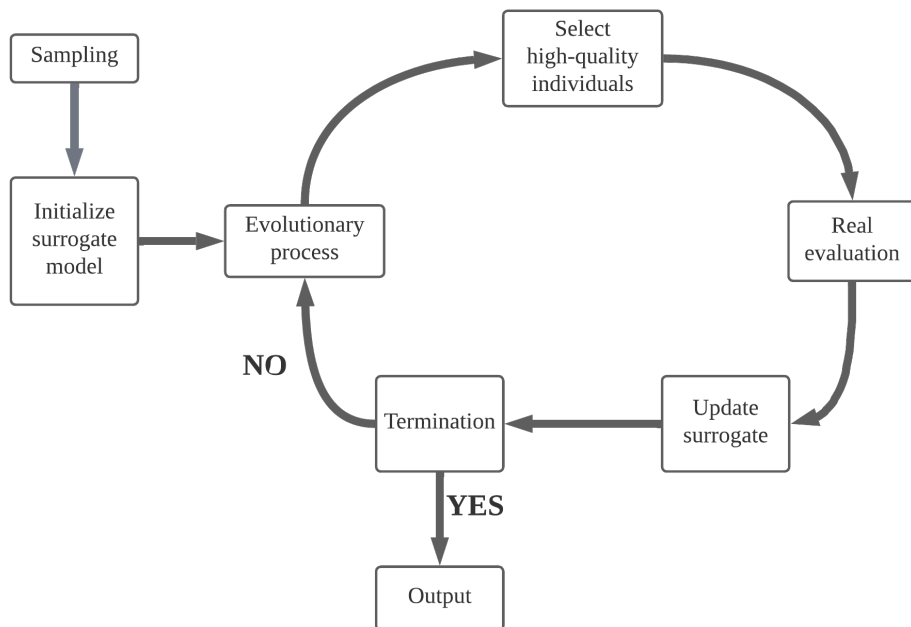


Figura 4.4: The basic flowchart of SAEAs.

In surrogate model-assisted optimization algorithms, it is not only population-based algorithms that can be used. Since the surrogate model is constructed from smooth basis functions, it is also possible to use search direction methods based on derivatives. Once the surrogate model is built, a local optimum of the predicted surface can be obtained by applying such methods to a given starting point. This local optimum is then evaluated based on the true objective function, and the surrogate model is updated with this new sample. This process is then repeated with the final solution from the previous iteration as the new starting point. Given that the objective function is reasonably sampled early on, such a method could converge to the optimum solution. A stopping criterion for this method could be consecutive iterations in which the optimal solution does not change. Different formulations can be explored for choosing the first starting point of the search direction method. This can be especially important in multimodal problems, such as the one addressed in this thesis.

In this thesis, three SAEAs approaches are considered. Their differences are the way in which the population is initialized and the way in which the high-quality individuals are selected for updating the model. In addition, two Surrogate model-Assisted Descent Methods (SADMs) are also proposed. Their main difference is the approach for obtaining an initial solution. The next subsubsections describe all of them.

## SAEA1

The first SAEA approach is inspired in (Salucci et al., 2022b). After initializing the surrogate model, the population is initialized by simply sampling random points in the search space following the uniform distribution. Their fitness are computed by the surrogate model prediction. Then, the algorithm executes a single iteration of the chosen evolutionary process. After the new population is selected<sup>1</sup>, the current best solution is compared against the sample. If it differs from all available solutions in the sample, its fitness is updated according to the real objective function and it is added to the sample. The model is trained again and all the individuals in the current population are re-evaluated according the updated surrogate model. The cycle repeats and this process continues until the stop criterion is met, at which point the algorithm returns the best solution in the sample. The pseudo-code presented in Algorithm 5 outlines this process.

Overall, the following observations are drawn for the considered algorithm:

- The sample contains the initial solution and the best individuals discovered throughout the generations.
- The total number of evaluations of the true objective function is not greater than the sum of the number of initial samples and the number of generations.
- The offspring population is created using the DE/best/1 operator, and the F factor is randomly selected from a predetermined range.
- In addition, a local search step based on a Descent Method is added and performed after a fixed number of generations, which distinguishes this process from the one proposed by Salucci et al. (2022b).

## SAEA2

The second approach is inspired in the one proposed by ?. The approach for selection and mutation in this algorithm differs from the typical prediction model-based population evaluation implemented in SAEA1. Instead, individual evaluation using the real function serves as the criterion for selection. The mutation strategy is also distinct, with mutation vectors calculated based on solutions stored in an archive. The archive is initially populated with the best solutions from the samples and is updated in each generation with the best  $N_A$  solutions from

---

<sup>1</sup>The elitism strategy is considered, i.e., the best solution among the parent and offspring populations is preserved for the next generation.

---

**Algorithm 5:** The SAEA1 algorithm.
 

---

**Input:** Scattered field data, discretization configuration, lower and upper bounds for  $\chi^F$  and  $T$ , number of initial sampled solutions, population size

**Output:** Contrast image.

- 1 Solve qualitatively the problem and obtain the normalized contrast image.
- 2 Sample solutions within the search space uniformly in the defined interval of  $\chi^F$  and  $T$ . Evaluate the sampled solutions.
- 3 Evaluations  $\leftarrow$  number of initial sampled solutions.
- 4 Build and train the surrogate model based on the sample.
- 5 Initialize a population of individuals by randomizing  $\chi^F$  and  $T$  values following the uniform distribution.
- 6 Set their fitness according to their corresponding prediction obtained by the surrogate model.
- 7 **while** stopping criteria is not met **do**
- 8   Generate a offspring population based on the DE/best/1 operator.
- 9   Evaluate the offspring based on the surrogate model.
- 10   Selected the new population considering the union of parents and offspring individuals by Binary Tournament and preserving the best solution among them (elitism).
- 11   **if** the local search has not been executed in the last  $N_{LS}$  generations **then**
- 12     Perform a local search using a Steepest Descent algorithm considering the current best solution as initial guess and the surrogate model as objective function.
- 13     **if** the returned solution by the local search is better **then**
- 14       Update the current best solution.
- 15     **end**
- 16   **end**
- 17   **if** the current best solution is not equal to any other in the sample **then**
- 18     Evaluate the current best solution according the objective function.
- 19     Evaluations  $\leftarrow$  evaluations + 1
- 20     Add the current best solution to the sample.
- 21     Train the surrogate model.
- 22     Re-evaluate the population using the updated surrogate model.
- 23   **end**
- 24 **end**

---

the updated sample. Each offspring-individual is generated from a sub-selection of solutions, generated and evaluated by the surrogate model. The sub-selection generates a set of solutions, and the one with the best value for the prediction of the objective function is selected as the offspring. Then, its fitness is updated according the real objective function. The pseudo-code presented in Algorithm 6 outlines this process.

In practice, the described algorithm leads to the following observations:

- The sample solutions are continuously updated with the best solutions found up to the current generation. This means that sampled solutions with the worst evaluations are removed to prioritize the reconstruction of the most promising region.
- The number of evaluations increases with each generation in proportion to the population

size, causing this algorithm to require more evaluations to converge.

- The current version of the algorithm applies the same mutation and local search operators in each iteration.

---

**Algorithm 6:** The SAEA2 algorithm.

---

**Input:** Scattered field data, discretization configuration, lower and upper bounds for  $\chi^F$  and  $T$ , number of initial sampled solutions, population size

**Output:** Contrast image.

```

1 Solve qualitatively the problem and obtain the normalized contrast image.
2 Sample solutions within the search space uniformly in the defined interval of  $\chi^F$  and  $T$ .
   Evaluate the sampled solutions.
3 Evaluations  $\leftarrow$  number of initial sampled solutions.
4 Build and train the surrogate model based on the sample.
5 Initialize a population of individuals by selecting the  $p$  best solutions from the sample.
6 Store in the archive the best  $N_A$  solutions.
7 while stopping criteria is not met do
8   Generate  $k$  solutions for each one in the population based on the DE/best/1 operator
      and evaluate them according to the surrogate model.
9   For each group of  $k$  solutions, selects the best, evaluate it according to the real function
      and set it as offspring individual.
10  Evaluations  $\leftarrow$  evaluations + population size.
11  Selected the new population considering the union of parents and offspring individuals
      by Binary Tournament and preserving the best solution among them (elitism).
12  if the local search has not been executed in the last  $N_{LS}$  generations then
13    Perform a local search using a Steepest Descent algorithm considering the current
      best solution as initial guess and the surrogate model as objective function.
14    if the returned solution by the local search is better then
15      | Update the current best solution.
16    end
17  end
18  if the current best solution is not equal to any other in the sample then
19    | Add the current best solution to the sample.
20    | Train the surrogate model.
21  end
22  | Update the archive with the  $N_A$  best solutions in the sample.
23 end

```

---

### SAEA3

SAEA1 has the main advantage of spending only one evaluation per generation, while SAEA2 has the advantage of considering an archive of best solutions as parents during mutation. The features of these two algorithms can be combined in a hybrid formulation, called SAEA3, where the population of parent and offspring individuals is evaluated by the surrogate model, and mutation vectors are generated based on a file with the best sample solutions. As a result, only the best solution of the generation is evaluated by the actual function. This approach

enables SAEA3 to have a high number of generations, similar to SAEA1, while the offspring individuals tend to inherit more characteristics of the best solutions (exploitation), similar to SAEA2. The same mutation and local search operators in each iteration. The pseudo-code presented in Algorithm 7 outlines this process.

---

**Algorithm 7:** Explanation of the functioning of the SAEA3 algorithm.

---

**Input:** Scattered field data, discretization configuration, lower and upper bounds for  $\chi^F$  and  $T$ , number of initial sampled solutions, population size

**Output:** Contrast image.

```

1 Solve qualitatively the problem and obtain the normalized contrast image.
2 Sample solutions within the search space uniformly in the defined interval of  $\chi^F$  and  $T$ .
   Evaluate the sampled solutions.
3 Evaluations  $\leftarrow$  number of initial sampled solutions.
4 Build and train the surrogate model based on the sample.
5 Initialize a population of individuals by selecting the  $p$  best solutions from the sample.
6 Store in the archive the best  $N_A$  solutions.
7 while stopping criteria is not met do
8   Generate  $k$  solutions for each one in the population based on the DE/best/1 operator
      and evaluate them according to the surrogate model.
9   For each group of  $k$  solutions, selects the best and set it as offspring individual.
10  Selected the new population considering the union of parents and offspring individuals
      by Binary Tournament and preserving the best solution among them (elitism).
11  if the local search has not been executed in the last  $N_{LS}$  generations then
12    Perform a local search using a Steepest Descent algorithm considering the current
      best solution as initial guess and the surrogate model as objective function.
13    if the returned solution by the local search is better then
14      | Update the current best solution.
15    end
16  end
17  if the current best solution is not equal to any other in the sample then
18    Evaluate the current best solution according the objective function.
19    Evaluations  $\leftarrow$  evaluations + 1
20    Add the current best solution to the sample.
21    Train the surrogate model.
22    Re-evaluate the population using the updated surrogate model.
23  end
24  Update the archive with the  $N_A$  best solutions in the sample.
25 end
```

---

## SADM1

Evolutionary algorithms are powerful optimization techniques based on a population of solutions. They are capable of exploring the entire search space (exploration), and when combined with local search operators, performance can improve significantly due to the exploitation of a potential solution. The initial surrogate model construction can be seen as a population

of solutions, which, if sampled broadly, can cover the most promising region of the search space. Different strategies can be applied to choose a starting point and apply a steepest descent algorithm on the surrogate model.

The best solution found may not necessarily be close to the global optimum, but it can be evaluated against the actual function and added to the sample set to update the model. By repeating this process iteratively, the algorithm will tend to converge to a location when the optimal solutions found in a set of iterations are identical or very close. However, the question of how to choose the initial solution that will start the iterative optimization process remains.

One possible strategy is to run an evolutionary algorithm considering the initial surrogate model and take the best solution found as the initial solution of the iterative process. This way, a global search is performed, and the iterative process tends to focus on the region of the best basin of attraction available in the first construction of the model. Such an approach will be denoted as SADM1 where the initials stand for Surrogate-model Assisted Descent Method. The pseudo-code presented in Algorithm 8 outlines this process.

Overall, the following observations are drawn for the considered algorithm:

- The evolutionary algorithm employed to determine an initial guess is the Differential Evolution with the following formulation: DE/best/1/bin (Rocca et al., 2011).
- The employed descent method is the L-BFGS-B algorithm which is a limited-memory version of Broyden-Fletcher-Goldfarb-Shanno (BFGS) algorithm for boundary constrained optimization (Byrd et al., 1995; Zhu et al., 1997).

## SADM2

Rather than determining the starting point for the SADM iterative process using an evolutionary algorithm, a simpler alternative is to choose the best sample as the starting point. That is, after sampling the search space, the iterative process starts assuming the best sample of the model as the current solution. In addition to being simpler, an advantage is to avoid the possibility of converging to another basin of attraction different from the global minimum when this is close to the best sample. In other words, considering the surface generated by the surrogate model, the evolutionary algorithm does not guarantee convergence to the global minimum, since it is stochastic. However, if by chance the global minimum is close to the best sample, which is quite possible, then the first iteration of SADM will certainly converge to that location. Of course, if the surface is not sampled well at the beginning, then the process may converge to a region other than the global optimum of the real function. And this can be more complicated in cases of strong scatterers, where the objective function tends to be multi-modal. But when the objective function is less complex then this strategy can be quite efficient. This approach will be denoted as SADM2 and its pseudo-code is shown in Algorithm 9. The L-BFGS-B algorithm will be used in a similar manner to SADM1.

---

**Algorithm 8:** The SADM1 algorithm.

---

**Input:** Scattered field data, discretization configuration, lower and upper bounds for  $\chi^F$  and  $T$ , number of initial sampled solutions, population size

**Output:** Contrast image.

- 1 Solve qualitatively the problem and obtain the normalized contrast image.
  - 2 Sample solutions within the search space uniformly in the defined interval of  $\chi^F$  and  $T$ . Evaluate the sampled solutions.
  - 3 Evaluations  $\leftarrow$  number of initial sampled solutions.
  - 4 Build and train the surrogate model based on the sample.
  - 5 Run an evolutionary algorithm considering the surrogate model as objective function and take the best solution as current solution.
  - 6 Evaluate the current solution according the true objective function, add it to the sample and retrain the model.
  - 7 **while** stopping criteria is not met **do**
  - 8     Run the descent method considering the current solution as initial guess and optimizing the predicted surface.
  - 9     Evaluate the returned solution according the true objective function.
  - 10    Evaluations  $\leftarrow$  evaluations + 1
  - 11    **if** the returned solution is not equal to any other in the sample **then**
  - 12      Add the current best solution to the sample.
  - 13      Train the surrogate model.
  - 14    **end**
  - 15    **if** the returned solution is better than the current one **then**
  - 16      Set the current solution as the returned by the last call of the descent optimization.
  - 17    **end**
  - 18 **end**
- 

## 4.4 EISPY2D: A Platform for Developing and Testing Algorithms for EISPs

This section presents the proposed framework for the development and testing of algorithms for the electromagnetic inverse scattering problem. The framework is a Python package with implemented classes that provide a structured environment for algorithm development and testing. The novelty of the proposed framework lies in three key aspects. Firstly, it includes the collection of indicators with the proposal of two specific metrics that allow for a comprehensive evaluation of the algorithms' performance. Secondly, the framework proposes an approach to test randomization, which ensures a fairer and more reliable comparison between algorithms. Finally, a statistical routine based on traditional statistical tests is proposed to compare the algorithms' performance. This section provides a brief description of the proposed framework and its features, highlighting the significance and contribution of each aspect.

---

**Algorithm 9:** The SADM2 algorithm.

---

**Input:** Scattered field data, discretization configuration, lower and upper bounds for  $\chi^F$  and  $T$ , number of initial sampled solutions, population size

**Output:** Contrast image.

- 1 Solve qualitatively the problem and obtain the normalized contrast image.
- 2 Sample solutions within the search space uniformly in the defined interval of  $\chi^F$  and  $T$ . Evaluate the sampled solutions.
- 3 Evaluations  $\leftarrow$  number of initial sampled solutions.
- 4 Build and train the surrogate model based on the sample.
- 5 Set the best sample as the current solution.
- 6 **while** stopping criteria is not met **do**
- 7     Run the descent method considering the current solution as initial guess and optimizing the predicted surface.
- 8     Evaluate the returned solution according the true objective function.
- 9     Evaluations  $\leftarrow$  evaluations + 1
- 10    **if** the returned solution is not equal to any other in the sample **then**
- 11      Add the current best solution to the sample.
- 12      Train the surrogate model.
- 13    **end**
- 14    **if** the returned solution is better than the current one **then**
- 15      Set the current solution as the returned by the last call of the descent optimization.
- 16    **end**
- 17 **end**

---

#### 4.4.1 Structure Description

In order to be able to compare algorithms, it was necessary to develop a common platform for the implementations. This platform was developed as a library programmed in the Python3 language (VanRossum and Drake, 2010). With a structure based on object orientation, the library implements the two-dimensional problem with the domain configurations defined in Section 3.1. Therefore, it was named *eispy2d*. The UML class diagram can be seen in Figura 4.5.

The following is a brief explanation of the main classes:

1. **Configuration:** a class that stores the primary information of the problem, such as image size ( $L_X, L_Y$ ), observation radius ( $R_O$ ), number of measurements and incidences ( $N_M, N_S$ );
2. **InputData:** a class that characterizes a problem instance. Its primary information is the data of the scattered field. However, other information can be added, such as the total field (for the linear problem) or the contrast images (for error measurement);
3. **Results:** a class that stores and displays the results of an execution of the nonlinear inverse problem. In addition, it also implements quality indicators;
4. **InverseSolver:** a abstract class for nonlinear inverse solvers implementation. For instance, inversion approaches such as the Born Iterative Method and the Subspace Optimization methods are derived classes which implement the corresponding methods.

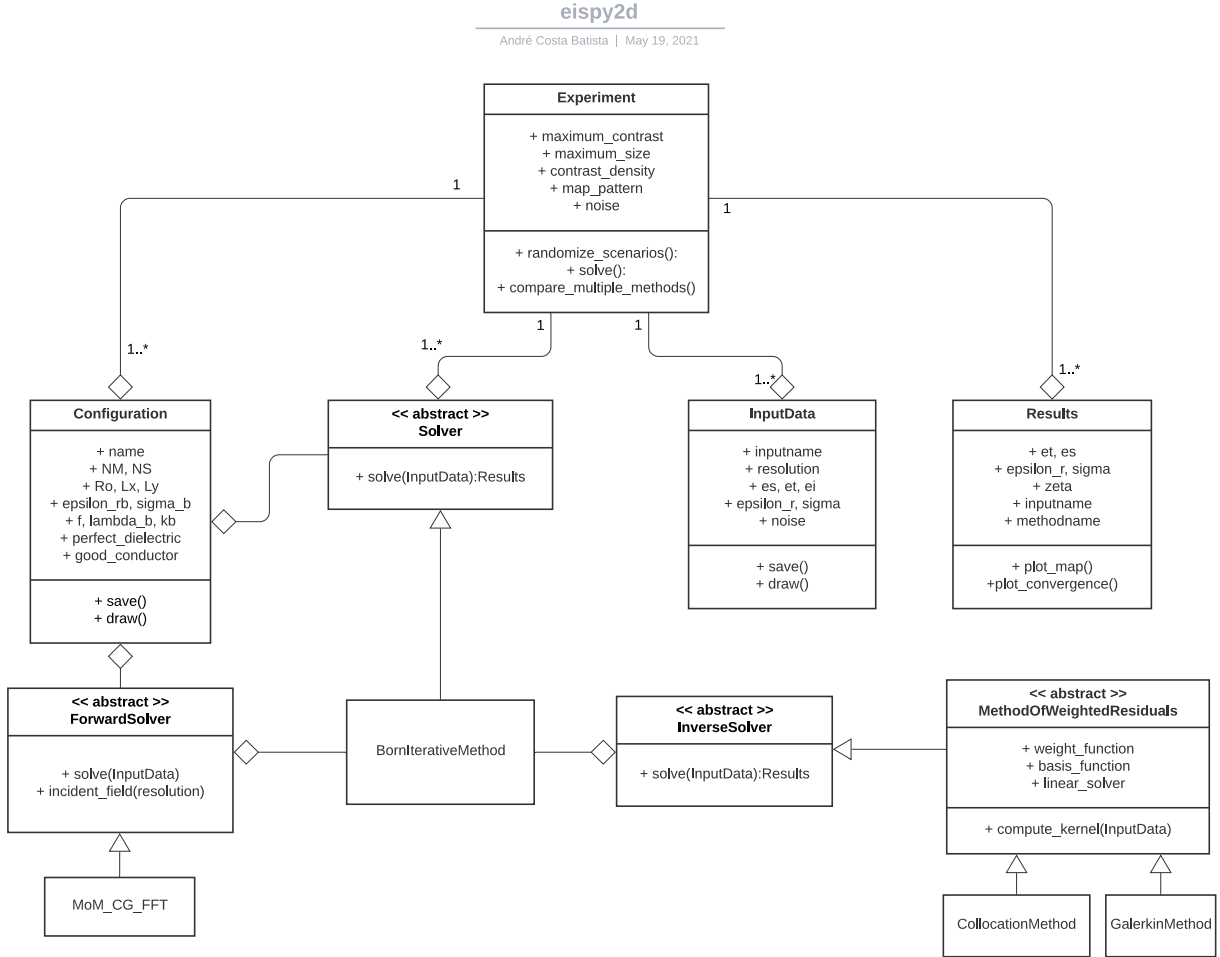


Figura 4.5: UML Class Diagram of *eispy2d* library.

5. **ForwardSolver**: abstract class for implementing forward solvers. One derivation, for example, is the Method of Moments Conjugated Gradient-Fast Fourier Transform (Su, 1987);
6. **Discretization**: abstract class for discretization schemes. Each discretization strategy is a derived class, such as the Collocation Method (Subsection 3.2.2).
7. **Experiment**: an abstract class that represents an experiment. Two schemes are possible: case study and benchmark. For each corresponding class, there are appropriate methods for visualizing and comparing the results.
8. **TestSet**: it is a class that contains a set of problem instances. There are appropriate methods for generating synthetic tests controlling multiple scatterer characteristics.

Three aspects are fundamental to evaluate or compare the performance among the algorithms: the quality indicators, the principles for creating random test sets, and the comparison methodology. The following subsections will provide further explanations of these three aspects. Each of them includes both techniques already known and newly proposed ones; therefore, this investigation's contribution is a more robust structure of synthetic experimentation.

#### 4.4.2 Performance Metrics Proposal

A set of indicators were implemented to assess the quality of the reconstruction done by the algorithms. The indicator were chosen according to their popularity throughout the references in the literature. The intention is also to aggregate indicators with different to enable multiple ways to analyze the performance of a method. Similar to (4.1), the average percentage error of estimation of relative permittivity and the average error of estimation of conductivity will be calculated by:

$$\zeta_{\epsilon PAD} = \frac{1}{N_I N_J} \sum_{i=1}^{N_I} \sum_{j=1}^{N_J} \left| \frac{\epsilon_{r,ij}^* - \epsilon_{r,ij}}{\epsilon_{r,ij}^*} \right| \times 100 [\%/\text{pixel}] \quad (4.17)$$

$$\zeta_{\sigma AD} = \frac{1}{N_I N_J} \sum_{i=1}^{N_I} \sum_{j=1}^{N_J} |\sigma_{ij}^* - \sigma_{ij}| [\text{S}/\text{pixel}] \quad (4.18)$$

In addition, metrics similar to (4.17) and (4.18) were implemented, considering background and object regions only. They are:

$$\zeta_{\epsilon BE} = \frac{1}{N_B} \sum_{\epsilon_{r,ij}^* = \epsilon_{rb}}^{N_I, NJ} \left| \frac{\epsilon_{r,ij}^* - \epsilon_{r,ij}}{\epsilon_{r,ij}^*} \right| \times 100 [\%/\text{pixel}] \quad (4.19)$$

$$\zeta_{\sigma BE} = \frac{1}{N_B} \sum_{\sigma_{ij}^* = \sigma_b}^{N_I, NJ} |\sigma_{ij}^* - \sigma_{ij}| [\text{S}/\text{pixel}] \quad (4.20)$$

$$\zeta_{\epsilon OE} = \frac{1}{N_O} \sum_{\epsilon_{r,ij}^* \neq \epsilon_{rb}}^{N_I, NJ} \left| \frac{\epsilon_{r,ij}^* - \epsilon_{r,ij}}{\epsilon_{r,ij}^*} \right| \times 100 [\%/\text{pixel}] \quad (4.21)$$

$$\zeta_{\sigma OE} = \frac{1}{N_O} \sum_{\sigma_{ij}^* \neq \sigma_b}^{N_I, NJ} |\sigma_{ij}^* - \sigma_{ij}| [\text{S}/\text{pixel}] \quad (4.22)$$

where  $N_B$  e  $N_O$  are the numbers of background and object elements, respectively. The purpose of these metrics is to precisely measure the ability to estimate the contrast of an object and avoid perturbations in the background regions.

Concerning EAs that simultaneously optimize contrast and field, measuring the ability to estimate the total field in the image region is a potential tool. For this reason, the following indicators were implemented:

$$\zeta_{TFMPAD} = \frac{1}{N_P N_Q N_R} \sum_{p=1}^{N_P} \sum_{q=1}^{N_Q} \sum_{r=1}^{N_R} \left| \frac{|E_{pq}^*| - |E_{pq}|}{|E_{pq}^*|} \right| \times 100 [\%/\text{pixel}] \quad (4.23)$$

$$\zeta_{TFPAD} = \frac{1}{N_P N_Q N_R} \sum_{p=1}^{N_P} \sum_{q=1}^{N_Q} \sum_{r=1}^{N_R} |\angle E_{pq}^* - \angle E_{pq}| [\text{rad}/\text{pixel}] \quad (4.24)$$

where the operator “ $\angle$ ” represents the phase of the complex number. Therefore, these two

indicators measure the average magnitude and phase error of the electric field estimate.

When an algorithm fails to locate and detect the shape of objects, metrics (4.17)-(4.22) will be affected. However, it may be that an algorithm estimates the shape and contrast of an object well, but due to errors in position, the evaluation of this solution by the metrics is low. Two metrics are proposed to take specific account of the ability to detect position and shape.

An indicator based on the distance between the “centers of mass” of the objects in the images is proposed to assess the ability to estimate the position of objects:

$$\zeta_P = \sqrt{(x_c^* - x_c)^2 + (y_c^* - y_c)^2} \times 100 [\%] \quad (4.25)$$

where  $(x_c^*, y_c^*)$  is the center of the original figure and  $(x_c, y_c)$  is the center of the reconstructed image. The centers are calculated according to Algorithm 10. After the threshold of the reconstructed image, the contrast values are discarded. This is done to prevent errors in the contrast estimation from influencing the center weighting. In this way, this indicator can be used for images with single or multiple objects.

---

**Algorithm 10:**  $\zeta_P$  measure.

---

**Input:**  $\boldsymbol{\chi}^*, \boldsymbol{\chi}$

**Output:**  $\zeta_P$

- 1  $\chi_{thres} \leftarrow \min\{|\boldsymbol{\chi}|\} + \frac{1}{2}(\max\{|\boldsymbol{\chi}|\} - \min\{|\boldsymbol{\chi}|\})$
  - 2  $\chi_{ij}^* \leftarrow 1 \forall \chi_{ij}^* \neq 0$
  - 3  $\chi_{ij} \leftarrow \begin{cases} 0, & \forall \chi_{ij} < \chi_{thres} \\ 1, & \forall \chi_{ij} \geq \chi_{thres} \end{cases}$
  - 4  $x_i \leftarrow (i-1)/(N_I-1) \forall i = 1, \dots, N_I$
  - 5  $y_j \leftarrow (j-1)/(N_J-1) \forall j = 1, \dots, N_J$
  - 6  $x_c^* \leftarrow \frac{\sum_{i=1}^{N_I} \sum_{j=1}^{N_J} x_i \chi_{ij}^*}{\sum_{i=1}^{N_I} \sum_{j=1}^{N_J} \chi_{ij}^*}$
  - 7  $y_c^* \leftarrow \frac{\sum_{i=1}^{N_I} \sum_{j=1}^{N_J} y_j \chi_{ij}^*}{\sum_{i=1}^{N_I} \sum_{j=1}^{N_J} \chi_{ij}^*}$
  - 8  $x_c \leftarrow \frac{\sum_{i=1}^{N_I} \sum_{j=1}^{N_J} x_i \chi_{ij}}{\sum_{i=1}^{N_I} \sum_{j=1}^{N_J} \chi_{ij}}$
  - 9  $y_c \leftarrow \frac{\sum_{i=1}^{N_I} \sum_{j=1}^{N_J} y_j \chi_{ij}}{\sum_{i=1}^{N_I} \sum_{j=1}^{N_J} \chi_{ij}}$
  - 10  $\zeta_P = \sqrt{(x_c^* - x_c)^2 + (y_c^* - y_c)^2} \times 100 [\%]$
- 

It was necessary to use an algorithm for detecting contours in the images to assess the ability to reconstruct the shape of the objects. The Marching Cubes algorithm (Lorensen and Cline, 1987) is a classic technique for identifying contours in three-dimensional images. The *scikit-image* library efficiently implements the two-dimensional case, which is considered in this work (van der Walt et al., 2014). Then, the shape metric  $\zeta_S$  is defined in terms of the ratio between two areas: (i) the area of the difference between the contours of the two images; and (ii) the area of the original image. The implementation and an example for calculating this

metric can be seen in Appendix E. This approach is not as sophisticated as the one proposed by Kurrant et al. (2021b), since the former is based on a threshold technique while the latter is based on image segmentation through a machine learning technique, which is more robust. In addition, their diverse set of metrics for breast reconstruction can also be adapted to our general scheme and it will be consider in the future. However, up to the date of this thesis, both  $\zeta_S$  and  $\zeta_P$  are indicators that have not been addressed in the literature. Also, indicators such as  $\zeta_{TFMPAD}$  and  $\zeta_{TFPAD}$  were not seen in the literature. Although they are not so relevant since it is not the primary objective to reconstruct the field, they can help understand the performance of some methods, especially the stochastic ones that simultaneously optimize contrast and field.

#### 4.4.3 Randomization of the Test Set

In many studies, synthetic experiments are designed to demonstrate the ability to reconstruct the algorithms in different scenarios. Traditionally, common geometries are used to explore situations such as strong scatterers, different noise levels, separation of objects, heterogeneities, among others. Usually, the images used in the tests are defined arbitrarily, and the performance in the corresponding situation is studied with only one or a few examples of images.

To give some examples, some recent and relevant works in the literature are mentioned: (i) Zhong et al. (2020) used an image type to make comparisons between four noise levels and an image type to compare high contrast situations; (ii) Wei and Chen (2019a) use four images for each of the two levels of contrast and three images to study the reconstruction of conductive objects; and (iii) Salucci et al. (2017) used an image for tests without noise, an image for two levels of noise, an image for inhomogeneity and an image for high contrast. In these works, it is worth mentioning that the images are either composed of only circles or a single square or the traditional Austria profile (composed of a ring and two circles). However, it is also worth noting that, in (Wei and Chen, 2019a), the authors used six images of a base formed by handwriting digits commonly used in Machine Learning; in (Shah and Moghaddam, 2018) and (Batista et al., 2021), the authors use four images with different geometries for experiments with single objects and three for inhomogeneities with different geometries.

In fact, the form of experimentation traditionally used exemplifies the algorithm's ability to deal with different situations, which is relevant for testing the method. A more robust approach to evaluating algorithmic performance would be to utilize synthetic experiments on a sufficiently large dataset of images with randomized geometries. Such a methodology can provide a more comprehensive understanding of the average performance of the algorithms. The utilization of random test sets to assess average performance is more effective than using arbitrary images to make a more efficient comparison. Conducting such studies may be of significant value to the existing literature on optimization algorithms (Beiranvand et al., 2017).

A process of generating a set of random tests was developed to explore this experimen-

tation design. It is embedded within the *TestSet* class in the *eispy2d* library. A set of tests is generated according to the following configuration parameters:

- Geometry pattern: this parameter means what type of geometries will be considered. Three patterns were implemented: regular geometries<sup>2</sup>, random polygons<sup>3</sup>, and random surfaces<sup>4</sup>.
- Maximum contrast: this parameter controls the allowed contrast range for the objects inserted in the image. It is also possible to configure this parameter so that all objects are defined with this contrast. In other words, the set of tests can be created both to study performance with different and unique contrasts.
- Maximum size: this parameter regulates the size of objects. It can also be set to a maximum value or assigned to a fixed value. In regular geometries, all of them are configured so that this parameter defines the radius between the center and the furthest vertex. In other words, it is the largest geometry drawing that fits within a circle defined by this parameter. In the case of random polygons, this parameter regulates the maximum radius that each vertex can have. In exponentials, this parameter controls the maximum radius of the exponential up to three times the standard deviation.
- Maximum contrast density: regulates the maximum value of the average contrast per pixel of the image. This parameter regulates the number of objects in the image.
- Noise: noise level at which the data in the scattered field will be corrupted.
- Sample size: number of test images in the set.

It is important to highlight that each geometry inserted in an image has a randomly defined rotation and position. Therefore, this process aims to create benchmarks that make it possible to study the performance of the methods in isolated configurations and the evolution of effects (e.g., the progression of performance in the growth of the contrast). Moreover, this process allows the study of effect factors on the performance of the algorithms for the problem, isolating the bias present in the arbitrary choice of geometries. This implementation considers only synthetic experiments. However, these principles could be used for a project of a real benchmark, i.e., physical measurements, which are defined following these principles of randomization of geometries and in isolation of effect factors.

#### 4.4.4 Comparison Structure

When a method runs a set of tests, the performance indicator is calculated for the final solution of each instance. The results information can be viewed in different ways. Two of the most traditional ways to visualize the data of a sample are the *boxplot* and the *violinplot* (Chen et al., 2008). The first is essential to visualize the quartiles of a sample, and the last is

---

<sup>2</sup>Square, rectangle, equilateral triangle, cross, circle, ring, ellipse, rhombus, trapezoid, parallelogram, polygons of more than five sides (pentagon, hexagon, etc.) and stars of 4, 5, and 6 points.

<sup>3</sup>Polygons of 3 sides or more with random radius between the center and vertices.

<sup>4</sup>Sum of sines or exponentials.

important to get a sense of the distribution of the data. Routines for visualizing the data of the experiments through these two graphs were implemented from the *matplotlib* library (Hunter, 2007). In addition, the routines also implement the visualization of more than one test set in the same graph, which is relevant to visualize the evolution of the performance of a method when a parameter in the test configuration varies (e.g., maximum contrast). The Quantile-Quantile graph was also used to verify assumptions of normality distribution implemented by the *qqplot* routine of the *pingouin* library (Vallat, 2018).

The test sets represent a sample of a universe of possible cases. The information on the average performance of the method in a particular universe can be relevant to comply with specifications in a given application and for comparison with other methodologies. As this universe of cases is very large, if not infinite, it is common to estimate the confidence interval of this average. The confidence interval can be understood as the range in which, if we repeat the experiment many times, the sampled average will be within that range in a specified percentage of the number of times. This type of study is done using statistical tools that make it possible to estimate the average and compare others, that is, to make comparisons between average performances of algorithms or test sets. It is not in the scope of this dissertation to explain the statistical methods that were used. Reading (Montgomery and Runger, 2010) and the implementations of the *statsmodels* library (Seabold and Perktold, 2010) are recommended for a better understanding. In this text, only the comparison process between two and multiple samples will be presented, representing the results of an indicator for different methods in the same set of tests.

For a comparison between two stochastic methods in a same test instance, the following process was implemented:

1. If the Shapiro-Wilk test does not show a deviation from normality for both samples, then the Two Sample T-Test with a significance of 5% is performed. The effect size<sup>5</sup> is calculated for a power of 80%. If a difference is detected, then there is evidence for the superiority of one of the methods.
2. If the Shapiro-Wilk test shows a deviation from the normal distribution for any of the samples, then the test is repeated using logarithmic and square-root transformations on the data. If a transformation is successful, the same transformation is applied for the other sample, the same procedure as the previous step is repeated, and the same conclusions can be drawn.
3. If none of the transformations are successful, then the Mann–Whitney U test is performed, which allows detecting whether, when randomly selecting an element from each sample, the probability that one element is greater than the other is not the same as otherwise. If the difference is detected at a significance level of 5%, then there is evidence for the superiority of one of the methods.

---

<sup>5</sup>The effect size, in this case, means the minimum difference for which it is possible to identify a false-negative error for the desired power and sample size, i.e., when the hypothesis of equality is not rejected when it is false.

When considering the a stochastic method and a deterministic one, then a similar procedure is employed. When the distribution of the results from the stochastic method is approximately normal, then an One-Sample T-Test is performed. When data transformation is necessary, then the transformation is also applied to the result of the deterministic method. When the distribution of the results obtained by the stochastic method is not normal, approximately, then the Wilcoxon Signed-Rank Test is performed. The test is able to detect whether stochastic data comes from a symmetric population with a specified median which, in this case, is the result obtained by the deterministic method.

The process of comparing the performance of an indicator between two methods in the same test set was implemented according to a paired fashion. Through the results of the methods for the same test set, the estimated average is defined in terms of the difference between indicators of the two methods in each instance. The process can be summarized as follows:

1. If the Shapiro-Wilk test does not show a deviation from normality over the paired difference, then the Paired T-Test with a significance of 5% is performed. The effect size is calculated for a power of 80%. If a difference is detected, then there is evidence for the superiority of one of the methods.
2. If the Shapiro-Wilk test shows a deviation from the normal distribution over the paired difference, then the test is repeated using logarithmic and square-root transformations on the data. If a transformation is successful, then the same procedure as the previous step is repeated, and the same conclusions can be drawn.
3. If none of the transformations are successful, then the Wilcoxon Test is performed, which allows the detection of differences following a symmetrical distribution around zero. If the difference is detected at a significance level of 5%, then there is evidence for the superiority of one of the methods.

The independence assumption between the data is guaranteed because the algorithms' execution is independent. In other words, the pseudo-random variables used in each algorithm are generated with sufficient independence, establishing the independence of samples. When the normality assumption is valid, the routines used are those in the *statsmodels* library, and the non-normal test routine comes from the *scipy* library (Virtanen et al., 2020).

The comparison process between multiple stochastic methods in the same test takes place using the analysis of variances (ANOVA) (Montgomery and Runger, 2010). The comparison process is described as follows:

1. The residues of observations and their corresponding sample means are evaluated.
2. If the Shapiro-Wilk test does not indicate a deviation between residuals and normal distributions, either with or without transformations:
  - (a) If the Fligner Test does not indicate invalidity of the homoscedasticity assumption<sup>6</sup>, then the One Way ANOVA is performed under the 5% significance level. The result will indicate whether there is evidence for at least one performance different from

---

<sup>6</sup>The homoscedasticity assumption means equal sample variances.

the others or not. The effect size is also calculated for a power of 80%.

- (b) If the Fligner test reveals invalidity of the homoscedasticity premise, then the Welch ANOVA test is performed, which may indicate evidence for at least one performance different from the others under a 5% significance level.
  - (c) If any differences are detected and it is necessary to try to identify all possible performance superiorities:
    - i. If the homoscedasticity assumption is valid, the Tukey HSD Multiple Comparison Test will be performed and all differences will be detected with the necessary significance correction.
    - ii. If the homoscedasticity condition is not valid, multiple comparisons will be made from multiple Welch T tests for independent samples with the significance determined by the Bonferroni correction.
  - (d) If a difference is detected and it is necessary to identify if all methods are superior or inferior to a single one (all versus one):
    - i. If the homoscedasticity condition is valid, the Dunnet Test will be performed with the necessary significance correction.
    - ii. If the homoscedasticity premise is not valid, then the comparisons will be made using the Welch test for independent samples with the significance determined by the Bonferroni correction.
3. If it is not possible to assume the normality of the residues, then the Kruskal-Wallis test will be performed with a significance level of 5%. The test allows identifying whether at least one of the samples came from a different distribution from any other.
- (a) If any difference is detected and it is necessary to identify all possible ones, then multiple Mann-Whitney U tests are performed. This test makes it possible to identify whether there is evidence for a probability greater than 50% for the superiority of either method.
  - (b) If any difference is detected and it is necessary to identify only if one method is superior to another, then Mann-Whitney U tests are performed to make the necessary comparisons.

As in the previous process, the hypothesis of independence of observations is guaranteed by the process of executing the algorithms. Test implementations for normal data are those available in the *statsmodels* library and non-normal ones in *scipy*.

When comparing multiple algorithms within the same set of tests, it becomes crucial to employ a pairwise comparison approach. This method involves calculating the differences between each pair of algorithms for each test, thereby generating samples of differences specific to each test. By focusing on the same test set, this approach proves to be more efficient in detecting significant differences. The process for pairwise comparisons bears similarities to comparing multiple algorithms for a single test, but with a few key distinctions. Instead of using ANOVA or the Kruskall-Wallis test, the Randomized Complete Block Design or the Friedman

Rank Sum Test is utilized, respectively, to analyze the data. These tests are specifically tailored for paired comparisons within the same test set. For post hoc analyses following the initial tests, the Paired T-Test and the Wilcoxon Signed-Rank test are employed in place of the standard T Test and Mann-Whitney U test, respectively. These post hoc tests allow for a deeper examination of pairwise differences and help draw more nuanced conclusions regarding algorithm performance.

Finally, the Factor Analysis technique for two and three factors was also implemented, as described in chapter 14 of (Montgomery and Runger, 2010). This technique is used to identify both if an effect factor impacts the performance of an algorithm and the interaction of that factor with more others. For example, through this type of analysis, it is possible to identify whether the increase in the size and number of objects in the image influences its performance as well as to identify whether the variation of these two factors at the same time has any impact. The analysis was standardized to a significance level of 5% and the normality and homoscedasticity assumptions are verified by the Shapiro-Wilk and Fligner tests.

## 4.5 Conclusion

In conclusion, this chapter has presented the proposal of this thesis, which aims to contribute to the advancement of algorithms for the electromagnetic inverse scattering problem. The state-of-the-art in the field has been discussed and the potential gaps in the literature were identified. The chapter also explores the role of surrogate models as a potential technique to address the challenges that have been considered in the literature. The transformation of the inversion problem into a bidimensional optimization one, which enables the use of surrogate models, has been described, and five formulations of surrogate model-assisted algorithms have been proposed, leveraging the Kriging model. Three formulation are based on Evolutionary Algorithms and two are based on Steepest Descent methods.

Furthermore, this chapter has identified a gap in the literature regarding a systematic approach for testing algorithms, which motivated the proposal of a framework for the development and testing of algorithms for the problem. The structure of the framework and the implemented classes have been briefly introduced, and the three key points of contribution, namely the collection of performance metrics and the proposal of two specific metrics, the approach to test set randomization, and the statistical approach for algorithm comparison based on traditional statistical tests, have been highlighted. This framework provides a more robust and systematic approach for testing algorithms for the problem, which is an important step towards the practical application of the proposed algorithms.

# Capítulo 5

## Results

Chapter 5 presents the results of the computational experiments conducted in this thesis, evaluating the proposed methodologies through both case studies and benchmarking. The case studies are detailed in Section 5.1, which encompasses various problem scenarios, including single scatterers (subsection 5.1.1), multiple scatterers (subsection 5.1.2), non-homogeneous scatterers (subsection 5.1.3), and strong scatterers (subsection 5.1.4). In each case study, a comparison is made between the proposed algorithms and traditional deterministic methods.

Following the case studies, Section 5.2 focuses on the benchmarking study, which aims to assess the performance of the proposed methods and identify any potential differences among them. The subsection 5.2.1 introduces the settings of the benchmarking study, providing essential context for the subsequent analysis. Subsequently, the results are presented and discussed, offering insights into the performance of the algorithms.

Some general comments apply to both the case studies and benchmarking stages. Firstly, all designs utilized lossless materials. Additionally, the amplitude of the incident wave was consistently set at 1 [V/m]. To incorporate a level of realism, the scattered field data was subjected to random noise. This noise is a random complex number, with its modulus representing a percentage of the original value and its phase uniformly distributed between 0 and  $2\pi$ .

Regarding runtime results, they were obtained using a specific machine configuration: Ubuntu 20.04.5 LTS, Intel Xeon(R) CPU E5-2640 0 @ 2.50GHz with 8 cores, and 11.7 GB memory. It is important to note that the method implementations may not have been optimized to their fullest extent, potentially impacting runtime analysis fairness. Consequently, a completely fair runtime analysis cannot be guaranteed due to potential variations in implementation optimizations.

### 5.1 Case Studies

Case studies involve a comprehensive analysis of either a single or a set of specific instances of a problem. The aim is to deeply analyze these instances, carefully examining their

unique attributes. These instances are deliberately chosen to explore specific characteristics that hold relevance for the proposal. By examining these selected cases, valuable insights and understanding can be gained.

This section covers four case studies, each focusing on a different scenario. The first case study examines the behavior of the proposed algorithms in situations that can be easily solved using traditional methods. The second case study investigates the performance of the proposed algorithms in a scenario with multiple scatterers and a significant level of contrast. In the third case study, the objective is to analyze the behavior of the proposed algorithms when dealing with a non-homogeneous scatterer that exhibits different levels of contrast. Additionally, this case explores the capability of the qualitative method to provide suitable initial solutions in such scenarios. The fourth and final case study aims to observe the performance of the proposed algorithms in a scenario where traditional methods typically struggle to produce satisfactory solutions.

Throughout all the tests, a noise level of 20 [%/sample] is considered for the scattered field data. Such noise level might affect significantly the performance of some methods and, therefore, the goal is to analyze the performance under a challenging scenario. In addition to the five proposed algorithms discussed in Chapter 4, an evolutionary algorithm that transforms the inverse problem into a two-dimensional optimization problem will also be included. However, this algorithm does not employ surrogate models. Furthermore, four deterministic methods, namely ECSI (Subsection 3.6.6), SOM (Subsection 3.6.8), BIM (Subsection 3.6.1), and DBIM (Subsection 3.6.2), will be employed. The ECSI version van den Berg et al. (1999) of the CSI family of algorithms is chosen due to its slightly better performance and fewer control parameters.

For the algorithms assisted by surrogate models, the threshold variable ranges from 0 to 1. The Method of Moments CG-FFT (MoM-CG-FFT) used in the simulations employs a stopping criterion of a maximum of 20 iterations or an error tolerance level below  $10^{-3}$ . This choice allows for a rougher approximation and helps to save computational time.

The performance of the algorithms will be primarily analyzed based on the error in estimating the object contrast and recovering its shape. Hence, the  $\zeta_{\varepsilon OE}$  and  $\zeta_S$  indicators will be measured, respectively. The decision not to use the  $\zeta_{\varepsilon PAD}$  indicator is motivated by the fact that the thresholding operator employed in the proposed approach ensures a noise-free background. This could heavily favor the proposed approach and make the comparison with traditional methods less meaningful. Lastly, the maximum number of iterations for each algorithm is determined based on the convergence of their objective function or the point just before a divergence behavior is observed.

### 5.1.1 Austria Profile

The present case study considers the Austria profile, which is a widely used instance in the literature (Chen, 2010, 2017), to test the algorithms in a weak scattering scenario ( $DNL = 0.694$ ). The profile has multiple and homogeneous scatterers, one of which is hollow. The Fig. 5.1a shows the ground-truth image and further information regarding the parameters of the scatterers can be found in (Chen, 2010). The Table 5.1 shows the parameters regarding the measurement and imaging domains and the incident field configuration. The resulting background wavelength is 0.749 [m]. Scattered field data was synthesized using MoM-CG-FFT, with a stopping criterion of 15,000 iterations or error tolerance level less than  $10^{-5}$ , and the resolution of the original image was  $64 \times 64$ , while the reconstruction resolution was  $30 \times 30$ .

Tabela 5.1: Parameters for problem specification of Austria profile case study.

$N_M$	$N_S$	$R_O$	$f$	$L_X, L_Y$	$\epsilon_{rb}$
32	16	6 [m]	400 [MHz]	2 [m]	1

The surrogate model-assisted algorithms proposed in this study have many parameters. The parameters for this case study were chosen based on a *prior* analysis. The contrast variable range was set to 0 to 1, and the stopping criterion for each surrogate model-assisted algorithm was defined as the maximum number of evaluations, which was 26 evaluations, with 30 runs due to the stochastic characteristics present in them. Despite being based on deterministic choices, the SADM2 algorithm will be executed multiple times, and the rationale behind this decision will be elucidated in the upcoming case studies. The number of solutions sampled at the beginning was 16, and the local search operation in SAEAs algorithms happened every 5 generations. The mutation factor  $F$  present in the mutation processes of SAEAs algorithms was randomly chosen in the range of 0.6 to 1.5 following a uniform distribution. The population size in the initial solution search process for SADM1 was set at 100 individuals. For the transformation-based algorithms, MoM-CG-FFT forward solver was used to evaluate solutions, with a limited number of iterations of 20 or until reaching an error tolerance level of 0.001. In addition to the surrogate model-assisted evolutionary algorithms, a traditional evolutionary algorithm formulation was also considered in this case study for comparison purposes. The DE/rand/1/bin formulation was chosen, with  $F$  adjusted to 0.5 and the crossing rate to 0.5.

The parameter configuration of the deterministic algorithms is mostly related to the stop criteria, which includes the maximum number of iterations and the error tolerance level. The established stopping criterion for SOM was the maximum number of iterations equal to 50, with a cut-off parameter of eigenvalues set at 15. The initial guess for SOM, ECSI and CGM was defined as the solution of the Backpropagation algorithm (Subsection 3.3.2). The stopping criterion for CGM and ECSI was set to 40 and 50 iterations, respectively. The stopping criterion for DBIM was 3 iterations, with the regularization method as Tikhonov's with a parameter equal to 0.01. Finally, BIM used the same parameters as DBIM, except for the stopping criterion,

which was adjusted to 10 iterations. Both algorithms are considered the Born Approximation (Subsection 3.3.1) as initial guess strategy.

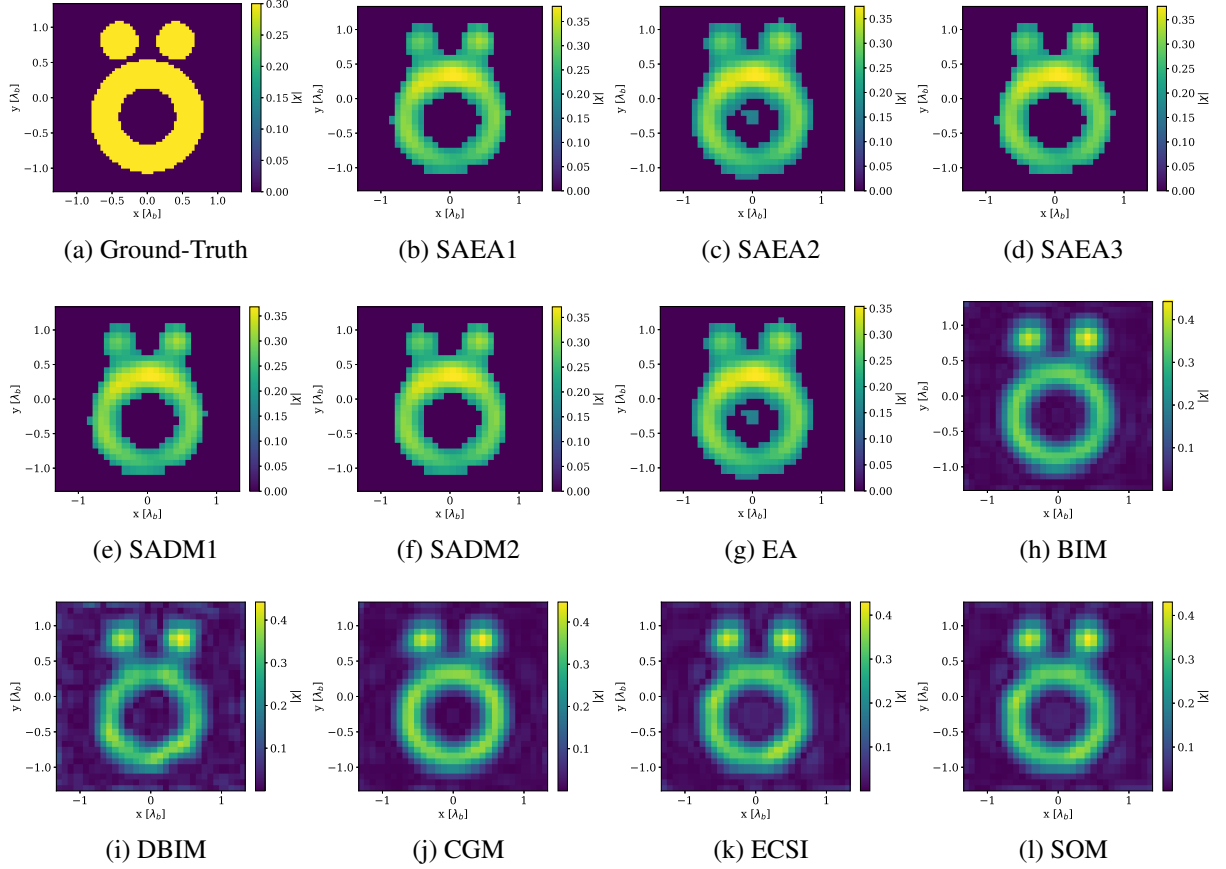


Figura 5.1: Comparison of image reconstructions using surrogate model-assisted algorithms and deterministic methods considering the Austria profile case study: (a) shows the ground-truth image; (b), (c), and (d) depict the best image recovered by SAEA1, SAEA2, and SAEA3, respectively, in 30 execution according to  $\zeta_{\epsilon OE}$  indicator; (e), (f) and (g) show the best image recovered by SADM1, SADM2, and EA, respectively, in 30 execution according to  $\zeta_{\epsilon OE}$  indicator; (g) shows the image recovered by BIM, and (h) shows the image recovered by DBIM; finally, (i), (k), and (l) show the image recovered by CGM, ECSI, and SOM, respectively.

In the results of the case study, Fig. 5.1 displays the best of the reconstructions among the 30 runs of each stochastic algorithm, based on indicator  $\zeta_{\epsilon OE}$  (Figs. 5.1b-5.1g), and also includes the reconstructions of the deterministic algorithms (Figs. 5.1h-5.1l). The figures show that all algorithms overestimated the contrast slightly, which can be seen in the maximum contrast value in each figure. However, algorithms based on the problem transformation proposal tended to have slightly lower overestimation, which compensates for underestimation at the edges of the scatterer. The reconstructions also had some difficulty in detecting the separation between the ring and the two circles, which was related to the proximity between these objects. Additionally, the best SAEA2 and EA reconstructed images showed a small ghost object inside the image ring due to a threshold value adjustment issue. As the  $\zeta_{\epsilon OE}$  indicator only takes into account the estimate within the original region of the scatterer, then errors in the original back-

ground region of the problem do not influence the indicator. Furthermore, algorithms based on transforming the problem into a two-dimensional optimization problem showed a cleaner background region, which was attributed to the thresholding operator. BIM (Fig. 5.2g) presented a slightly cleaner background region than DBIM (Fig. 5.2h), which was associated with the difficulty of DBIM in dealing with significant noise levels.

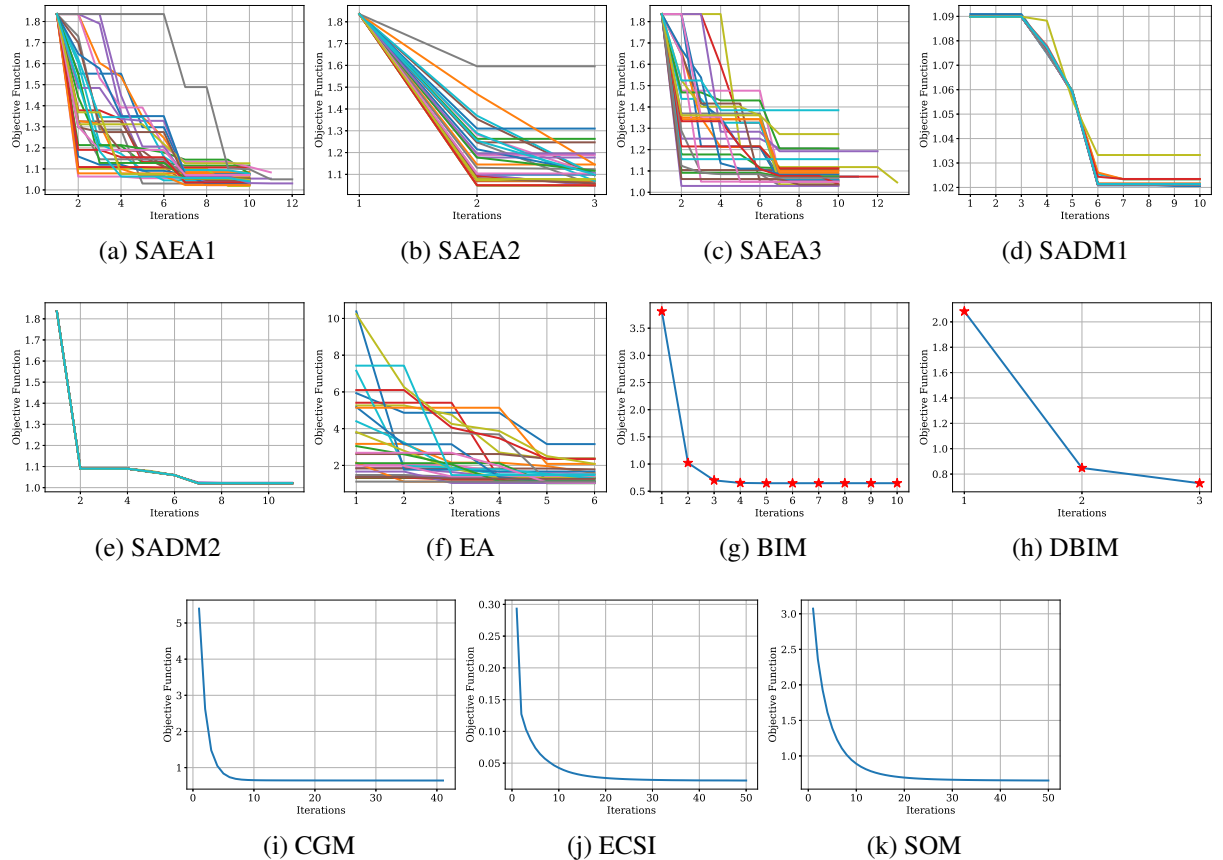


Figura 5.2: Convergence of the objective function for the Austria profile case obtained by the stochastic and deterministic algorithms. (a) to (k) show the curves obtained by SAEA1, SAEA2, SAEA3, SADM1, SADM2, EA, BIM, DBIM, CGM, ECSI, and SOM algorithms, respectively. The x-axis represents the number of iterations, and the y-axis represents the value of the objective function of the correspondent algorithm.

The convergence curve for each algorithm is shown in Fig. 5.2. The y-axis can only be compared between algorithms based on two-dimensional optimization (Figs. 5.2a-5.2f), as each deterministic algorithm has its own objective function that guides its structure. SAEA2 had a few generations but still achieved values close to those achieved by SAEA1 and SAEA3, thanks to the good mapping of the search space done by the initial population. The final values reached by SAEA1 in the 30 runs were more similar than those by SAEA3, which may suggest that SAEA1 convergence is better.

Some SADM1 runs did not converge to the same location as most, which may be an effect of the stochastic search process for the initial solution. The same does not happen for SADM2, as all executions of this algorithm converged equally, indicating a deterministic beha-

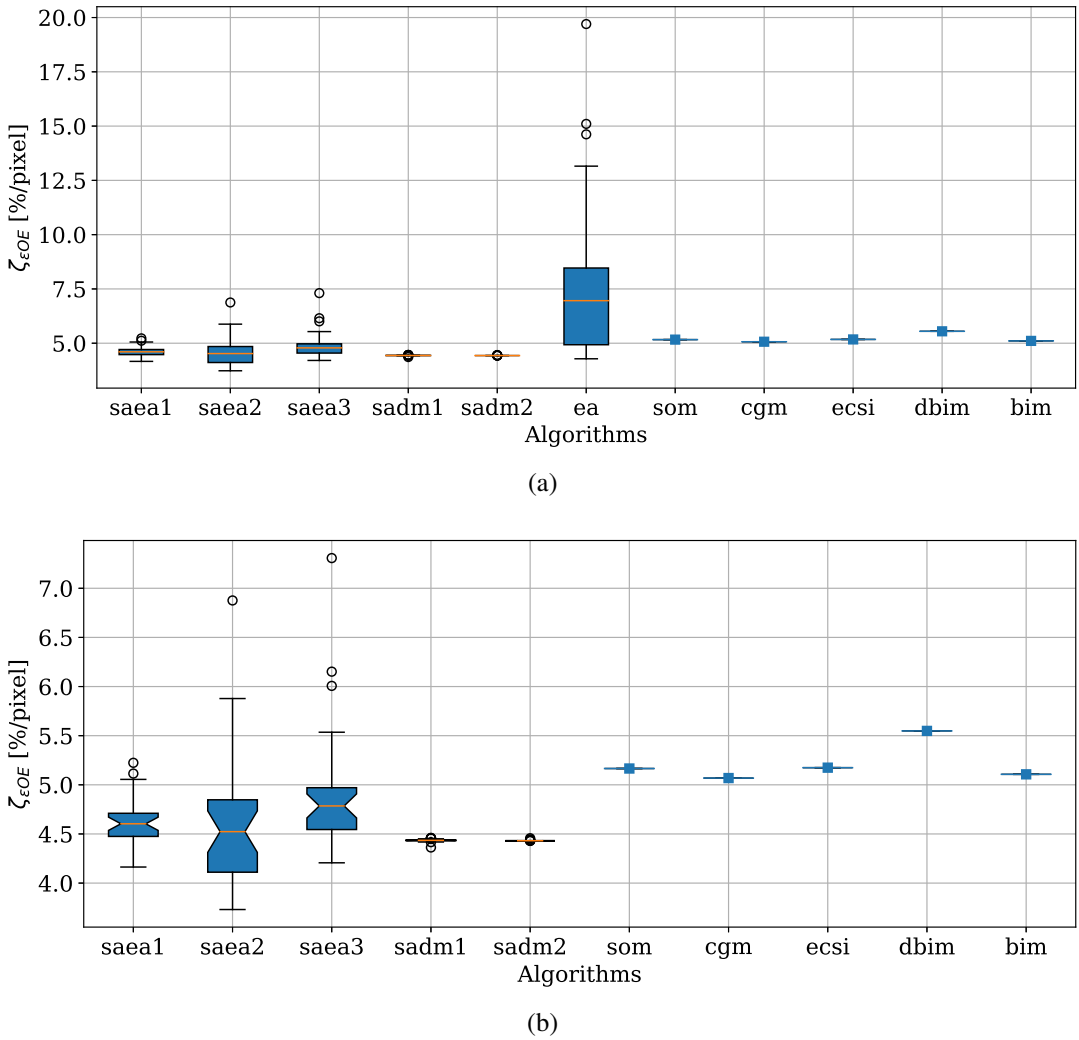


Figura 5.3: Performance of  $\zeta_{\varepsilon OE}$  indicator for various algorithms in the Austria profile. (a) Boxplots show quartiles of 30 executions for stochastic algorithms, and the solid line represents the deterministic ones. (b) Exclusion of the EA algorithm for better visualization of differences among algorithms.

rior. The EA has more generations than the SAEA2, but the greater number of generations did not contribute to reaching the region closer to the minimum more quickly. This is straightforward for SAEA2 because of the solution sampling strategy.

Fig. 5.3a shows the  $\zeta_{\varepsilon OE}$  indicator quartiles for the algorithms in which 30 executions were performed and the value reached by the deterministic ones. The EA quartiles stand out negatively, as the algorithm has difficulty finding a good final estimate of the scatterer contrast. This is attributed to the algorithm's need for more generations to converge closer to the optimum, as in other algorithms assisted by surrogate models.

By removing the EA data (Fig. 5.3b), it is possible to better visualize the differences between the algorithms assisted by surrogate models and the deterministic ones. The median of algorithms assisted by surrogate models was below all deterministic ones. In particular, all SADM1 and SADM2 runs were below the deterministic contrast estimation error. However,

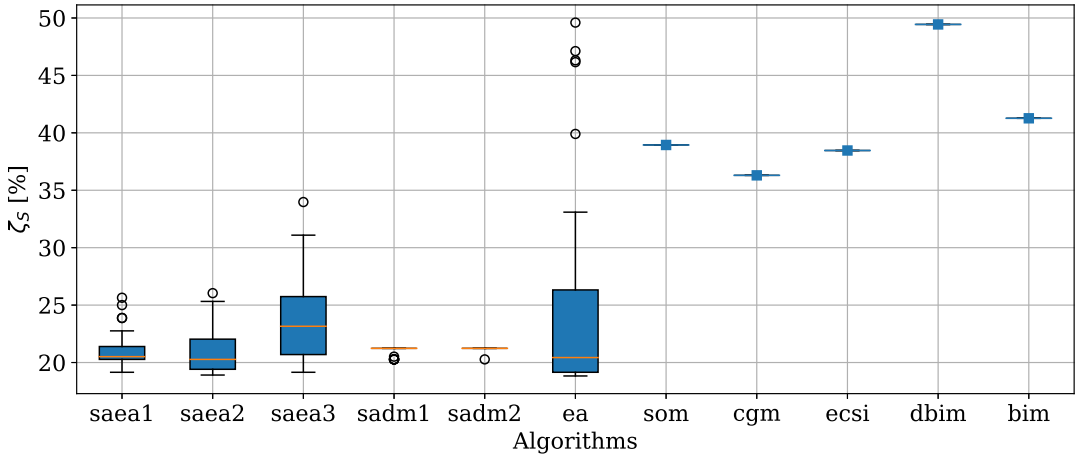


Figura 5.4: Performance of shape error estimation quantified by the  $\zeta_S$  indicator obtained by the set of algorithms considering the Austria profile. The boxes represent the quartiles of the 30 executions of the stochastic algorithms, while the other points indicate the obtained values by the deterministic ones. The shape error is calculated based on the ground-truth image and the reconstructed image obtained by each algorithm.

there have been executions of SAEA's that ended with a minor error. All runs of SADM2 ended with the same error since all runs converged equally (as seen in Fig. 5.2e). Although SADM1 convergence was not as equal between runs, they achieved the same error, indicating that the final solution for each run was very close. The Kruskal-Wallis H-Test confirmed difference among SAEA1, SAEA2, and SAEA3 ( $p\text{-value} = 0.0219$ ), and all-to-all comparison by Mann-Whitney U test confirmed that SAEA1 and SAEA2 overperformed SAEA3 ( $p\text{-values } 0.0199$  and  $0.0191$ , respectively). The Multiple Mann-Whitney U test did not detect difference between SADM1 and SADM2 ( $p\text{-value} = 0.0505$ ).

The contrast estimation error of surrogate model-assisted algorithms has to do with where on the optimization surface they end up. In general, the result indicates that the problem transformation approach can be successful in making a better contrast estimate in the median of cases compared to the traditional approaches. However, in weak scattering scenarios, this difference is not as significant as the graphs show (up to 1.5 [%/pixel]).

The performance of different algorithms for shape recovery error ( $\zeta_S$ ) is shown in Fig. 5.4. The difference in performance between deterministic algorithms and those based on the transformation of the problem is more significant, up to approximately 20% of the area of the original scatterer. The success of the proposed transformation approach in shape recovery results is associated with the quality of the qualitative methods used and the efficiency of the thresholding operation intrinsic to the formulation. The Kruskal-Wallis H-Test confirmed difference among SAEA1, SAEA2, and SAEA3 ( $p\text{-value} < 0.0002$ ), and all-to-all comparison by Multiple Mann-Whitney U test confirmed that SAEA1 and SAEA2 overperformed SAEA3 ( $p\text{-values} < 0.001$  for both cases). The Mann-Whitney U test detected difference suggesting that SADM1 outperforms SADM2 ( $p\text{-value} = 0.013$ ).

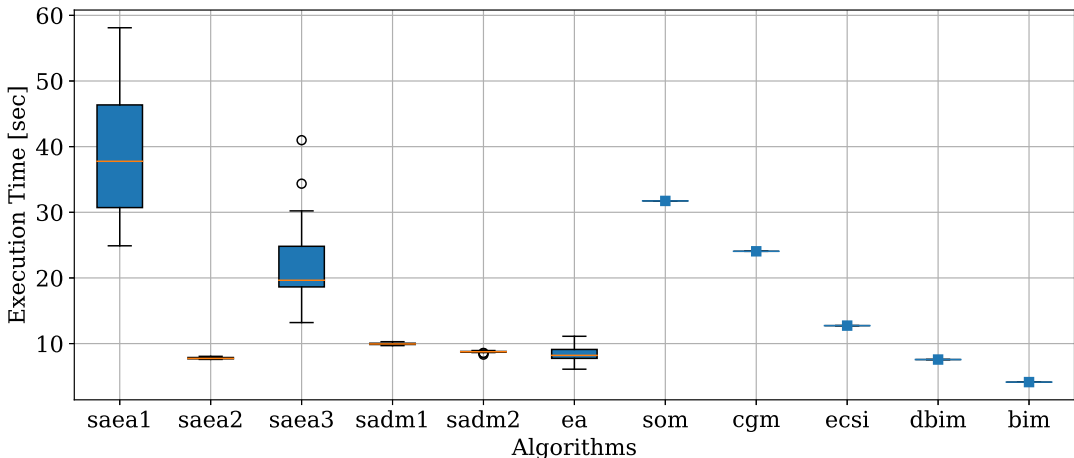


Figura 5.5: Box plot showing the execution time distribution of the set of algorithms considered for the Austria profile case. The boxes represent the quartiles of the 30 executions of the stochastic algorithms, and the whiskers represent the minimum and maximum values. The deterministic algorithms are represented by individual points. The execution time results are presented in seconds.

The running time of the algorithms is shown in Fig. 5.5. The median of SAEA1 was found to be the highest, while SAEA2 was the fastest among SAEA's formulations, even with the same number of evaluations. This suggests the impact of operations within the iterative process of these algorithms, such as the local search process and the number of model training calls that are less triggered in SAEA2 for the same number of evaluations. However, it is important to note that SADMs also need to retrain the model once per iteration, spend one evaluation per iteration, and use the same algorithm applied for the local search process in SAEAs. Other processes that are part of the implementation of these algorithms may also be impacting the runtime. It is also worth highlighting that although BIM takes much less time than SADM2, the latter still manages to deliver good contrast and shape estimation results for a satisfactory time (less than 10 seconds), which is shorter than other algorithms such as SOM, CGM, and ECSI. Therefore, with a little more time, SADM2 can deliver a better result in this instance that is well-treated by traditional algorithms.

Figure 5.6 illustrates the performance of the algorithms, displaying both the objective function surface and the locations of the final solutions obtained by each algorithm after transforming the inverse problem into a two-dimensional optimization problem. The SADMs converged to the same point every time, indicating that they behaved like deterministic algorithms for a reasonably smooth surface in the macro sense. The EA solutions, on the other hand, were widely spread, indicating that the number of evaluations would need to be much higher for the algorithm to converge more often to the optimal location.

The SAEA3 had a similar behavior to EA, which slightly moved away from the point found by the SADMs. However, it is important to note that final solutions that are a little farther from the optimum can sometimes return a smaller error in contrast estimation or shape recovery.

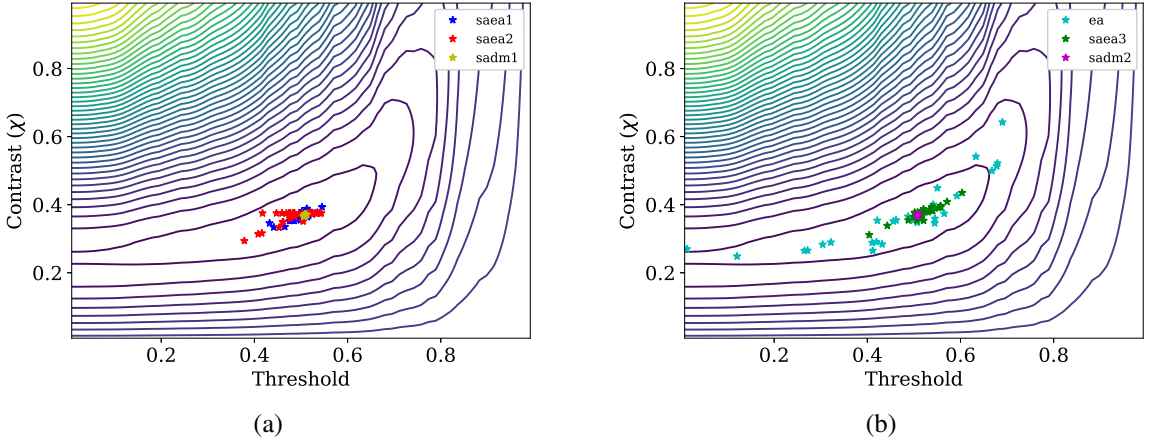


Figura 5.6: Surface of the two-dimensional optimization problem obtained from the transformation of the Austria profile and the final solutions obtained by different algorithms. Subfigure (a) shows the final solutions obtained by SAEA1, SAEA2, and SADM1 algorithms, while sub-figure (b) shows the final solutions obtained by EA, SAEA3, and SADM2 algorithms.

This is because the optimal point of the transformed problem can be slightly displaced from what would be ideal for the thresholding process and the exact contrast value. This displacement is intrinsic to the estimation of the qualitative method. That is, the optimal solution of the transformed problem is not necessarily the exact one, but the best that can be obtained from the qualitative method and minimizing the error of the data equation. Therefore, the performance of the qualitative method influences the position of the optimum.

### 5.1.2 Multiple Scatterers

This subsection presents a case study that examines the ability to separate objects in an image when considering multiple scatterers. This type of scenario is significant and, in order to further explore the application potential of the surrogate models, the contrast of the scatterers will be considerably higher. The study describes three scatterers that have a contrast level equal to 4. The radius of the circle is  $0.1\lambda_b$  and is centered on coordinates  $(L_X/4, 0)$ . The side of the square is  $0.2\lambda_b$  and is centered on coordinates  $(-L_Y/4, -L_X/4)$ , while the side of the triangle is  $0.2\lambda_b$  and is centered on coordinates  $(-L_Y/4, L_X/4)$ . The instance can be seen in Fig. 5.7a and it is inspired in an experiment presented in (Shah and Moghaddam, 2015) and (Batista et al., 2021) where the same geometries were considered and different contrast levels. The DNL of the problem was at 0.915, which is close to threshold 1 for the problem to start to get very non-linear. The parameters that describe the problem domains are present in Table 5.2. All other settings for synthesizing the scattered field data are the same as in the previous case study, except now the original image resolution is  $120 \times 120$ .

In this case study, the configuration of the algorithms was similar to the previous one, but some adjustments were necessary to explore the behavior of the algorithms more effectively.

Tabela 5.2: Parameters for problem specification of the multiple scatterers case study.

$N_M$	$N_S$	$\lambda_b$	$R_O$	$L_X, L_Y$	$\varepsilon_{rb}$
20	20	1 [m]	5 [ $\lambda_b$ ]	0.8 [ $\lambda_b$ ]	1

For the algorithms based on problem transformation, some changes were made, including increasing the maximum limit for the contrast variable to 7 since the true contrast is now 4, setting the stopping criterion to 50 evaluations, and using an initial sample size of 25 solutions. SAEA2 and EA were designed with populations consisting of 20 individuals. As for the deterministic methods, some modifications were made, including 150 iterations for CGM, 200 iterations for ECSI, 4 iterations for DBIM, 20 iterations for BIM, and 200 iterations for SOM, with a cut-off index equal to 5.

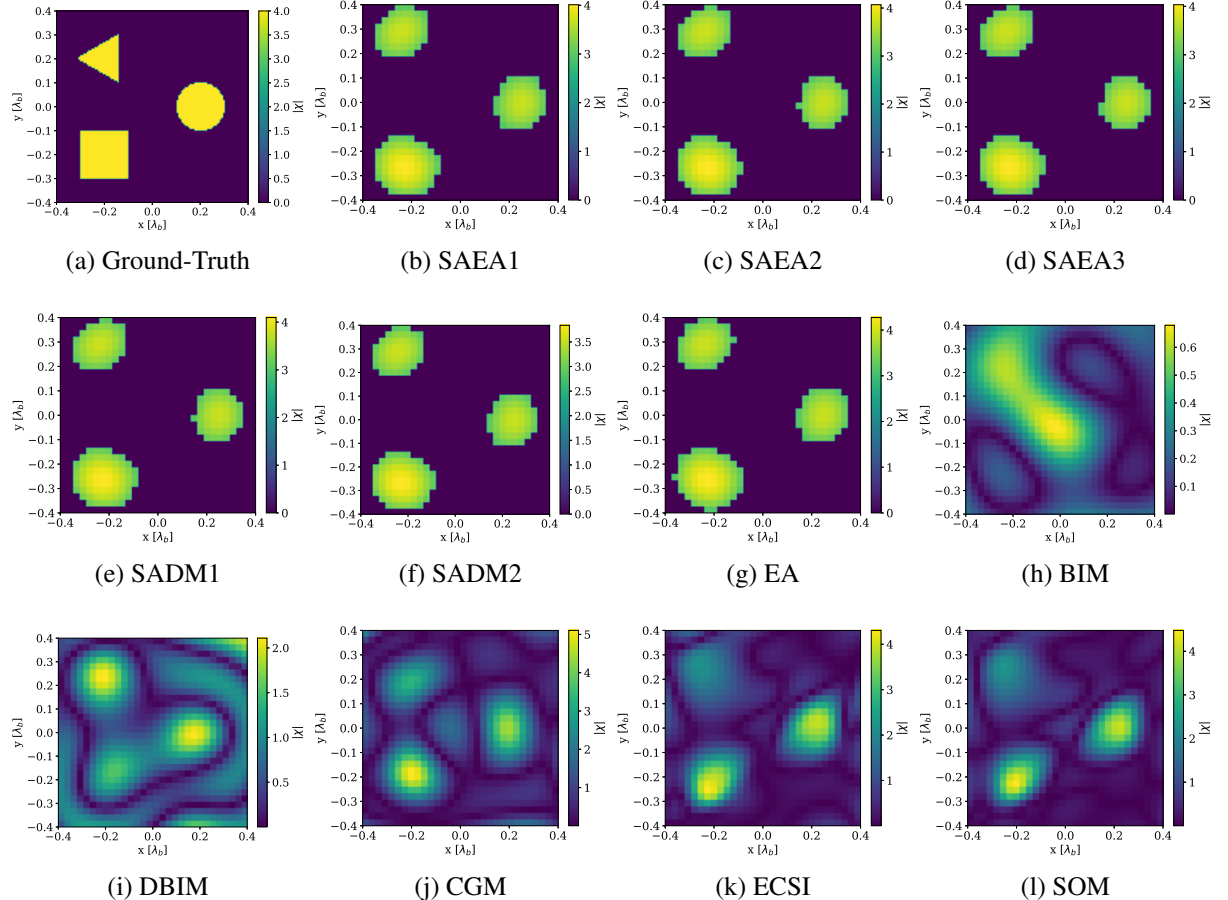


Figura 5.7: Comparison of image reconstructions using surrogate model-assisted algorithms and deterministic methods considering the multiple scatterers case study: (a) shows the ground-truth image; (b), (c), and (d) depict the best image recovered by SAEA1, SAEA2, and SAEA3, respectively, in 30 execution according to  $\zeta_{\varepsilon_{OE}}$  indicator; (e), (f) and (g) show the best image recovered by SADM1, SADM2, and EA, respectively, in 30 execution according to  $\zeta_{\varepsilon_{OE}}$  indicator; (g) shows the image recovered by BIM, and (h) shows the image recovered by DBIM; finally, (i), (k), and (l) show the image recovered by CGM, ECSI, and SOM, respectively.

The results are presented in Fig. 5.7, which displays the best reconstructions of the algorithms that were executed multiple times following the same criteria as the previous case study, along with images of the deterministic methods. In the case of algorithms based on the transformation of the problem (Figs. 5.7b-5.7g), the scatterers appeared a little more displaced from the center of the reconstructed image, and they were very close to the edges of the image. However, the best estimates of the contrast were excellent. BIM (Fig. 5.7h) was not successful in detecting the scatterers, while DBIM (Fig. 5.7i) displayed significant noise in the background region, even though it might look like there are three scatterers in the image. CGM, ECSI, and SOM (Figs. 5.7j-5.7l) were able to detect three scatterers with values less close to the exact one than the proposed algorithms, although CGM had more difficulty with background noise.

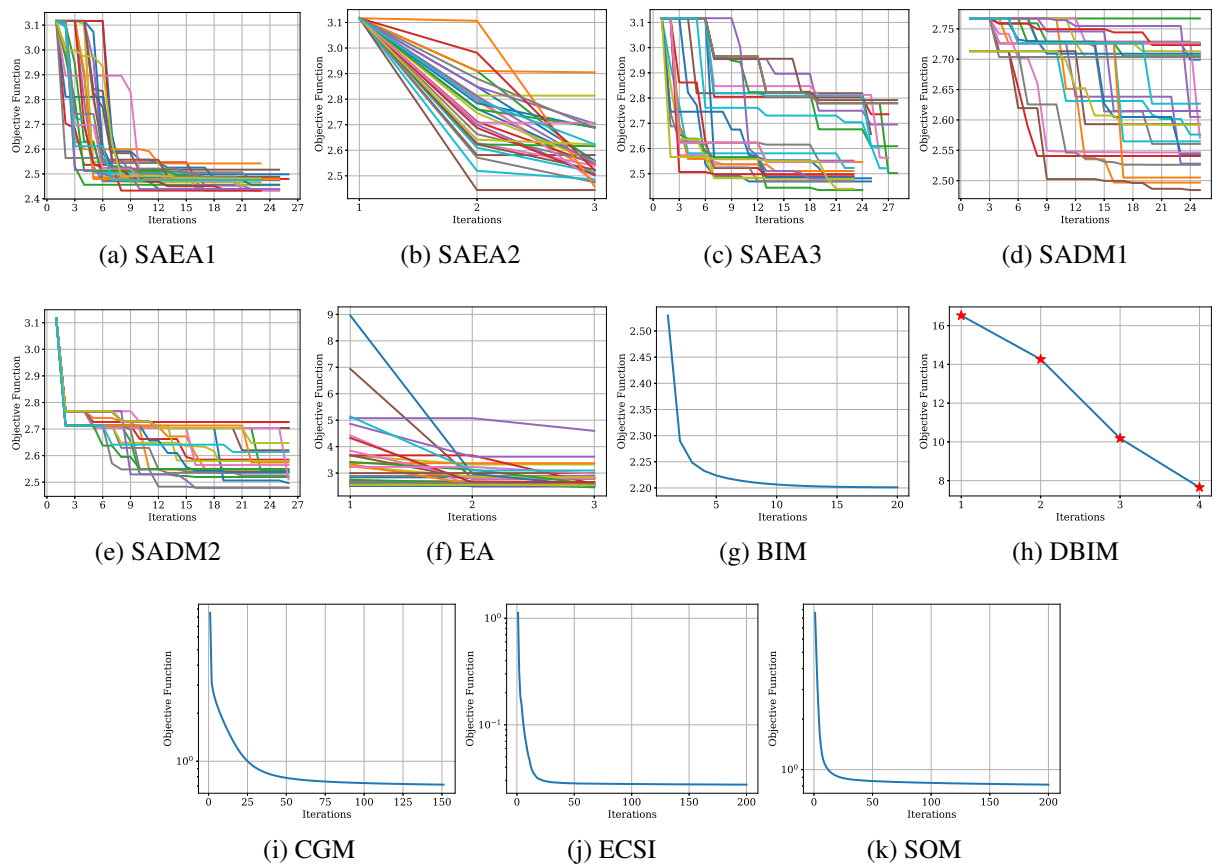


Figura 5.8: Convergence of the objective function for the multiple scatterers case obtained by the stochastic and deterministic algorithms. (a) to (k) show the curves obtained by SAEA1, SAEA2, SAEA3, SADM1, SADM2, EA, BIM, DBIM, CGM, ECSI, and SOM algorithms, respectively. The x-axis represents the number of iterations, and the y-axis represents the value of the objective function of the correspondent algorithm.

Figure 5.8 presents the convergence of the objective function for each algorithm. Interestingly, the convergence of the SADM1 and SADM2 algorithms (Figs. 5.8d-5.8e) was less homogeneous in this case study, behaving more like a stochastic algorithm such as SAEAs. Although the decisions within the iterative process of SADMs are deterministic, the differences in the convergence curves between runs could be due to the processes within the surrogate

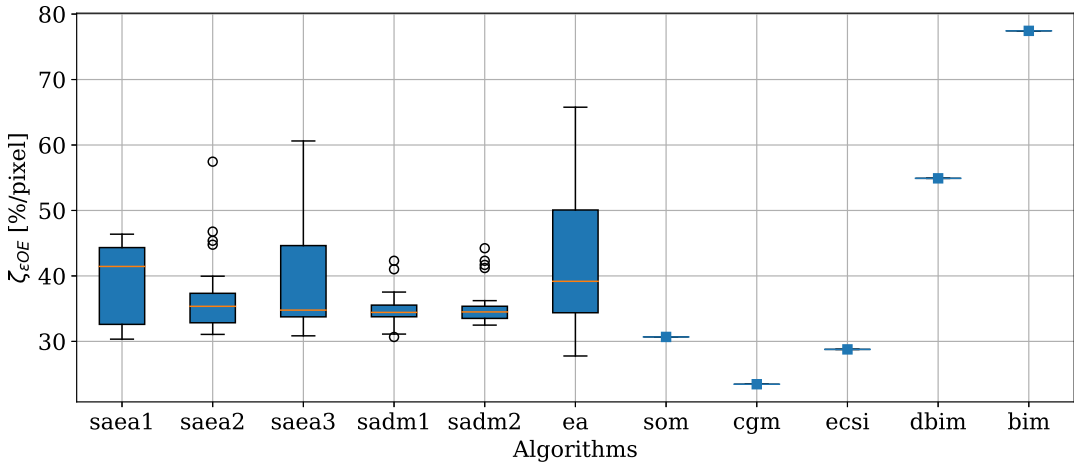


Figura 5.9: Performance of  $\zeta_{\epsilon OE}$  indicator for various algorithms in the multiple scatterers case study. Boxplots show quartiles of 30 executions for stochastic algorithms, and the solid line represents the deterministic algorithms.

model training, which can be more complex in high-contrast scattering scenarios.

On the other hand, the convergence curves of the SAEAs algorithms were similar to those of the previous case study. SAEA1 (Fig. 5.8a) had slightly more homogeneous curves than SAEA3 (Fig. 5.8c), and even though SAEA2 (Fig. 5.8b) had only 3 generations, some of the runs found solutions with the same objective function value as the best solutions found by the other two algorithms.

Finally, the convergence of the CGM, ECSI, and SOM algorithms (Figs. 5.8i-5.8k) indicates that they finished their runs with stable solutions. Therefore, even if more iterations were given, the reconstructed images would not significantly differ from those shown in Figures 5.7j-5.7l. In this scenario, these algorithms would not obtain a better reconstruction.

In Figure 5.9, the results of indicator  $\zeta_{\epsilon OE}$  for each algorithm are presented. The CGM algorithm had the lowest error in estimating the contrast of objects, but its reconstructed image was not as satisfactory as the other algorithms (Fig. 5.7j). However, even with a slight overestimation of the contrast compared to the surrogate model-assisted algorithms, the error may have been smaller due to the lack of distancing behavior observed for the proposed algorithm and that influences the error measure. The Kruskal-Wallis H-Test did not detect any differences in the median performance between the surrogate model-assisted algorithms, despite SAEA1 having a higher median position. The algorithms assisted by surrogate models had higher medians than the SOM, CGM, and ECSI methods, but the difference did not exceed 20 [%/pixel].

The results of the  $\zeta_S$  indicator that evaluates the shape recovery of the scatterers by the algorithms is presented in Fig. 5.10. The CGM algorithm had the lowest shape recovery error, with a significant difference of around 50 [%] compared to the second-best algorithm. However, none of the algorithms were able to reconstruct shapes that resembled the scatterers.

Regarding the surrogate model-assisted algorithms, the medians were very close to each other. When comparing the medians of SAEA2, SAEA3, SADM1, and SADM2 algorithms,

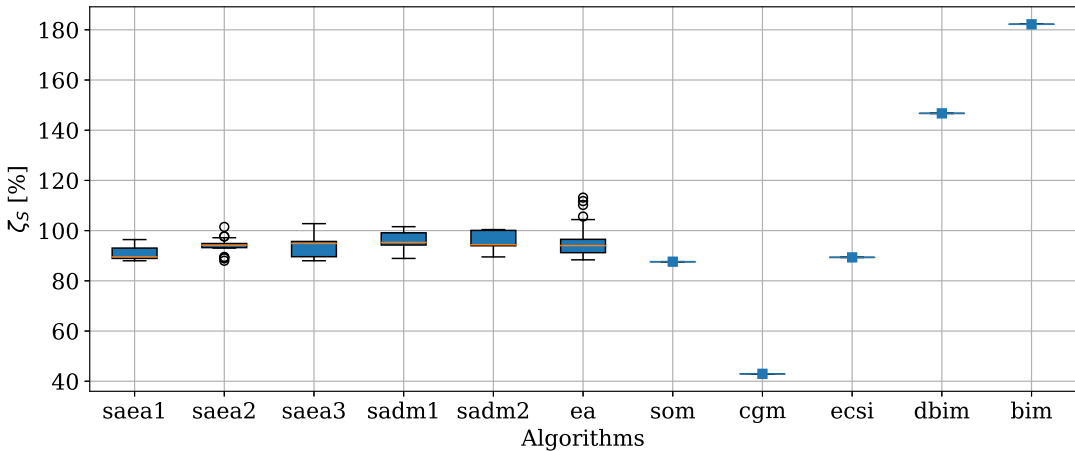


Figura 5.10: Performance of shape error estimation quantified by the  $\zeta_S$  indicator obtained by the set of algorithms considering the multiple scatterers case study. The boxes represent the quartiles of the 30 executions of the stochastic algorithms, while the other points indicate the obtained values by the deterministic ones. The shape error is calculated based on the ground-truth image and the reconstructed image obtained by each algorithm.

the Kruskal-Wallis H-Test did not detect any difference at a significance level of 5% ( $p\text{-value} = 0.065$ ). However, when including SAEA1 in the comparison, it showed a better median performance than the other algorithms ( $p\text{-value} < 0.001$  in all post-hoc comparisons). Nonetheless, the difference is not significant enough from the point of view of the reconstructed image.

Figure 5.11 displays the results of the execution time of the algorithms. BIM and DBIM had shorter execution times since fewer iterations were needed, which means the most expensive calculation was called fewer times during the algorithm execution. The median performances of the SADM2 and EA algorithms were quite similar, and no significant difference was detected based on the Welch Two Sample T-Test ( $p\text{-value} = 0.203$ ). However, the medians of these two algorithms were below that of the other algorithms. By considering this indicator along with the  $\zeta_{\varepsilon OE}$  and  $\zeta_S$  indicators, choosing between SADM2 and CGM in this case could be seen as a trade-off between reconstruction quality and execution time. In other words, while SADM2 may not achieve the same performance as CGM in shape and contrast estimation indicators, it can achieve slightly higher values in a much shorter time.

Figure 5.12 presents the surface of the objective function resulting from the transformation in a two-dimensional optimization problem, along with the location of the final solutions found by the algorithms in multiple runs. As the nonlinearity of the problem increased, the surface became less convex, and there was a certain grouping of solutions around the point  $T$ ,  $(\chi) = (0.75, 4)$  and a smaller one around  $(0.8, 5)$ . It is possible that the latter is a local minimum where some of the runs may have gotten stuck. The occurrence of more difficult to escape local minima may be more common as the problem becomes more non-linear or the contrast of the scatterers increases. The final solutions found for all algorithms were scattered, and only in the case of EA that solutions outside the lowest sublevel region were returned.

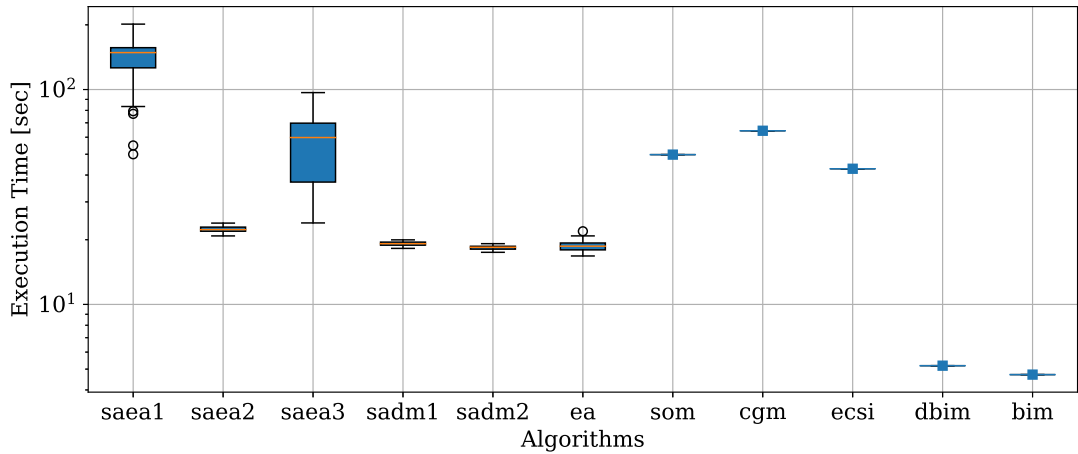


Figura 5.11: Box plot showing the execution time distribution of the set of algorithms considered for the multiple scatterers case study. The boxes represent the quartiles of the 30 executions of the stochastic algorithms, and the whiskers represent the minimum and maximum values. The deterministic algorithms are represented by individual points. The execution time results are presented in seconds.

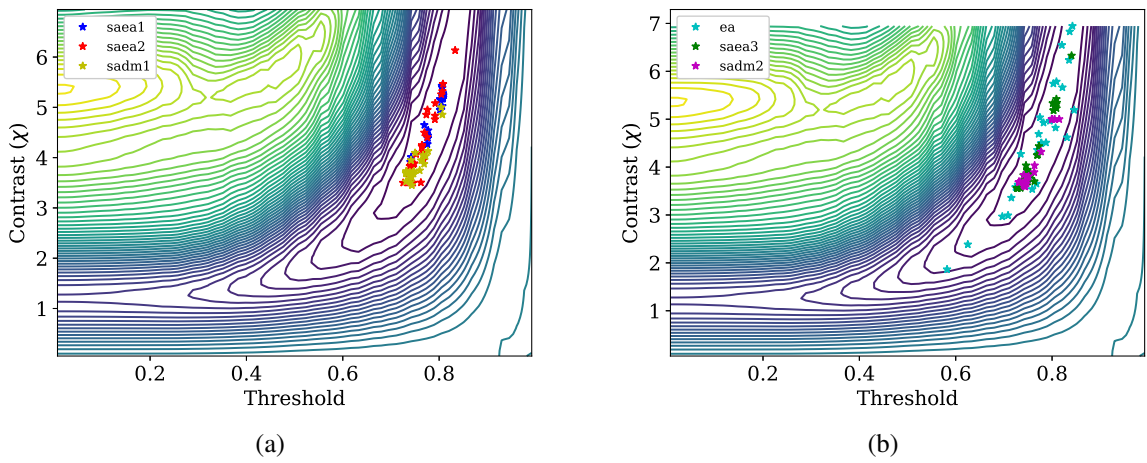


Figura 5.12: Surface of the two-dimensional optimization problem obtained from the transformation of the multiple scatterers case study and the final solutions obtained by different algorithms. Subfigure (a) shows the final solutions obtained by SAEA1, SAEA2, and SADM1 algorithms, while subfigure (b) shows the final solutions obtained by EA, SAEA3, and SADM2 algorithms.

### 5.1.3 Non-Homogeneous Scatterer

The third case study presented in this work focuses on the imaging of a nonhomogeneous scatterer, which is a square of side length equals to  $\lambda_b$  with three different regions of contrast (0.4, 0.9, and 1.25) inside it. This scenario is relevant because it allows the qualitative identification of different levels of contrast using the OSM method. The inspiration for this study comes from a similar experiment presented by Bevacqua et al. (2020). The scatterer's detailed specifications can be found in the reference. Table 5.3 provides the specifications for measurement and imaging domains. Figure 5.13a illustrates the scatterer. The degree of non-linearity for this case is 1.396, which is above the threshold for cases where the Born Approximation can be applied. All settings for synthesizing the scattered field data are the same as in the previous case study.

Tabela 5.3: Parameters for problem specification of the nonhomogeneous scatterer case study.

$N_M$	$N_S$	$\lambda_b$	$R_O$	$L_X, L_Y$	$\epsilon_{rb}$
16	16	1 [m]	3.33 [ $\lambda_b$ ]	1.67 [ $\lambda_b$ ]	1

For this case study, adjustments were made to the algorithm configurations to more effectively explore their behavior. For the problem transformation-based algorithms, the maximum limit for the contrast variable was reduced to 3 since the maximum contrast in the true image is now 1.25. The stopping criterion was set to 60 evaluations. SAEA2 and EA utilized populations of 20 individuals as in the previous case study. Deterministic methods also underwent some modifications, such as CGM and ECSI using 50 iterations, DBIM using 3 iterations, BIM using 15 iterations, and SOM using 500 iterations with a cut-off index of 5.

Figure 5.13 presents the best reconstructions of the algorithms executed multiple times under the same criteria as the previous case study, as well as the images of the deterministic methods. The reconstructed images by the proposed algorithms (Figs. 5.13b-5.13g) were very similar to each other, suggesting that they were reconstructed from the same threshold level and contrast estimation. However, the lowest level of contrast in the scatterer appeared to be proportionately higher than in the original image, resulting in a relatively blurred image with the second level. This may be attributed to the difficulty of the OSM method in estimating differences when they become distant from each other. As a result, the contrast was underestimated in all results since the increment in the contrast multiplication factor would represent an object with a higher average contrast and a higher error in the data equation.

BIM had a satisfactory reconstruction with a notable contour of the scatterer and well-estimated contrast levels. On the other hand, DBIM did not perform well. CGM and ECSI performed reconstructions that resembled the real scatterer, but with some distortions. In CGM, the contrast was overestimated, and in ECSI, the highest contrast region was slightly distorted. Finally, SOM did not perform well, possibly because the noise level greatly affected its performance in this scenario.

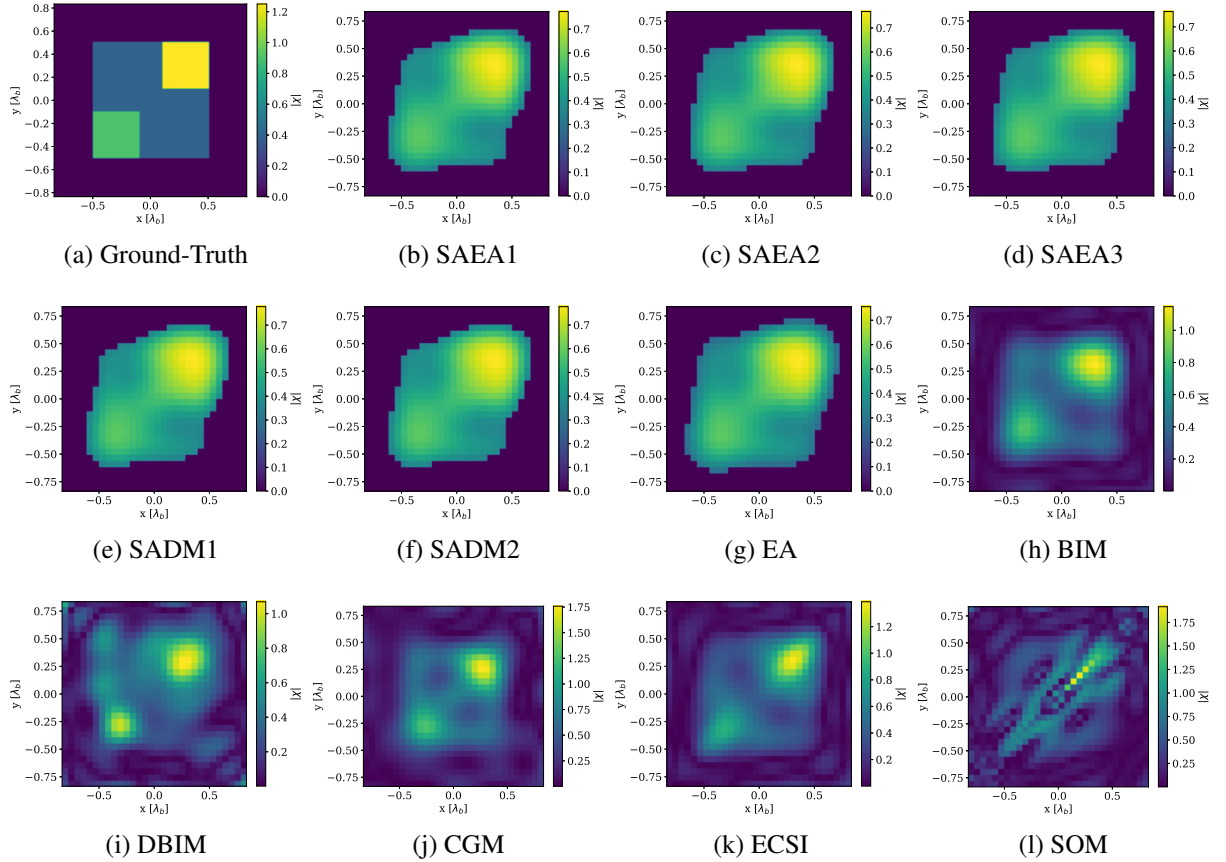


Figura 5.13: Comparison of image reconstructions using surrogate model-assisted algorithms and deterministic methods considering the nonhomogeneous scatterer case study: (a) shows the ground-truth image; (b), (c), and (d) depict the best image recovered by SAEA1, SAEA2, and SAEA3, respectively, in 30 execution according to  $\zeta_{\varepsilon OE}$  indicator; (e), (f) and (g) show the best image recovered by SADM1, SADM2, and EA, respectively, in 30 execution according to  $\zeta_{\varepsilon OE}$  indicator; (g) shows the image recovered by BIM, and (h) shows the image recovered by DBIM; finally, (i), (k), and (l) show the image recovered by CGM, ECSI, and SOM, respectively.

Figure 5.14 presents the convergence curves of the considered algorithms in this study. The figure shows that BIM, CGM, ECSI, and SOM reached a reasonable level of stability in the convergence process and ended their executions, indicating that further iterations would not significantly improve the quality of the reconstructed images. Meanwhile, SADM1 and SADM2 had slight variations between runs, and although SAEA2 had 3 generations, some of the runs were able to arrive at solutions with low objective function values like the final solutions of SAEA1 and SAEA3.

The performance of the algorithms regarding the contrast estimation in the scatterer area was analyzed based on the results of indicator  $\zeta_{\varepsilon OE}$  presented in Figure 5.15. Despite the fact that the image reconstructed by BIM was the most satisfactory, with a well-estimated contrast and reasonably clear scatterer contour, ECSI was the algorithm with the lowest contrast estimation error, although the shape was slightly distorted. Nevertheless, the difference in performance between BIM and ECSI was not significant, with approximately 1 [%/pixel]. The performance

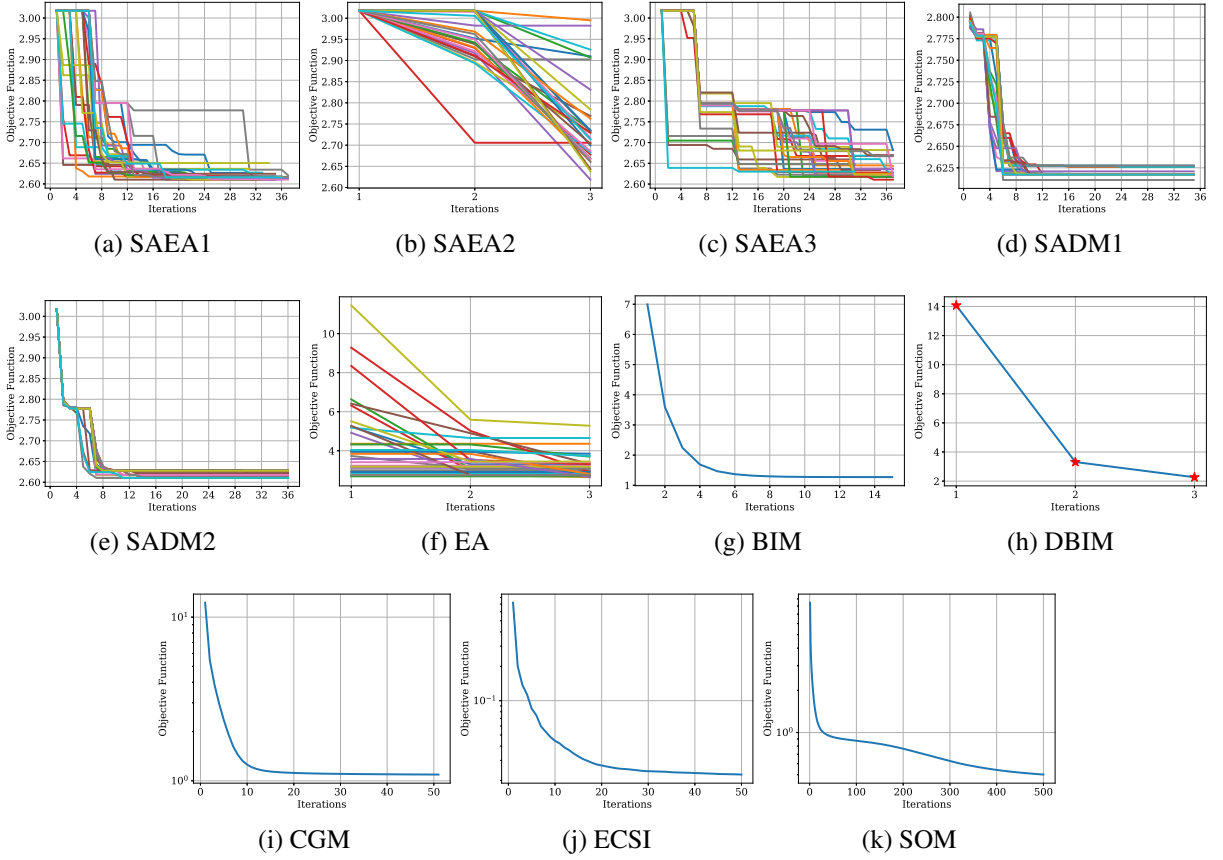


Figura 5.14: Convergence of the objective function for the nonhomogeneous scatterer case obtained by the stochastic and deterministic algorithms. (a) to (k) show the curves obtained by SAEA1, SAEA2, SAEA3, SADM1, SADM2, EA, BIM, DBIM, CGM, ECSI, and SOM algorithms, respectively. The x-axis represents the number of iterations, and the y-axis represents the value of the objective function of the correspondent algorithm.

medians of the proposed algorithms were very similar, and the Kruskal-Wallis H-Test failed to reject the hypothesis of equality between them ( $p$ -value = 0.08). The performance difference between the proposed algorithms and ECSI was not too large, at around 3 [%/pixel].

Figure 5.16 shows the results obtained by the algorithms considering the  $\zeta_S$  indicator. It was observed that the proposed algorithms outperformed the deterministic methods in terms of this indicator. However, it is interesting to note that BIM performed relatively worse than the other proposed algorithms, and this may be related to the difficulty of applying the indicator to significantly heterogeneous images. On the other hand, the proposed algorithms performed better possibly due to the smaller heterogeneity of the scatterer and the difference in respect to the background medium. Among the surrogate model-assisted algorithms, there was no evidence of a significant difference in the median performance of the indicator, as confirmed by the Kruskal-Wallis H-Test ( $p$ -value = 0.088). This suggests that the performance of the proposed algorithms in terms of this indicator is similar, and none of them stands out significantly from the others.

Figure 5.17 displays the running time of the algorithms analyzed in the study. As ex-

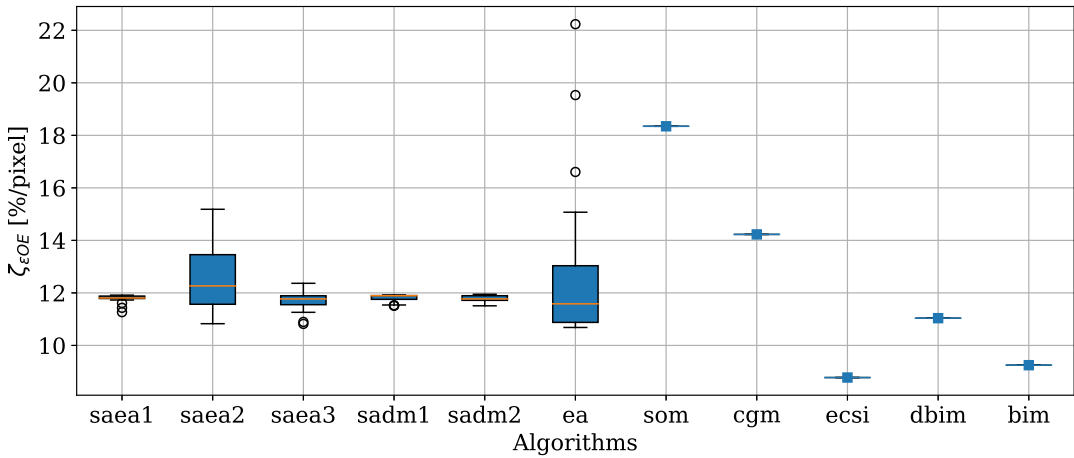


Figura 5.15: Performance of  $\zeta_{\varepsilon OE}$  indicator for various algorithms in the nonhomogeneous scatterer case study. Boxplots show quartiles of 30 executions for stochastic algorithms, and the solid line represents the deterministic algorithms.

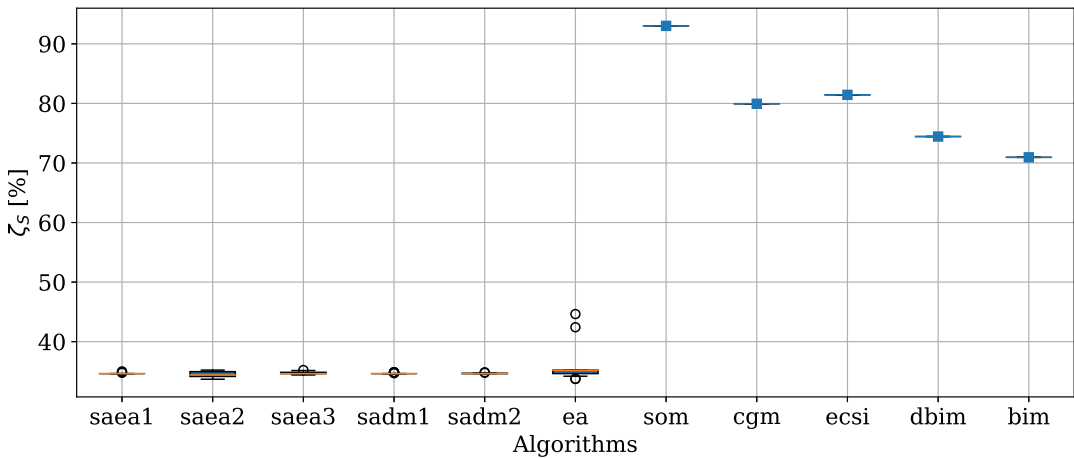


Figura 5.16: Performance of shape error estimation quantified by the  $\zeta_S$  indicator obtained by the set of algorithms considering the nonhomogeneous scatterer study. The boxes represent the quartiles of the 30 executions of the stochastic algorithms, while the other points indicate the obtained values by the deterministic ones. The shape error is calculated based on the ground-truth image and the reconstructed image obtained by each algorithm.

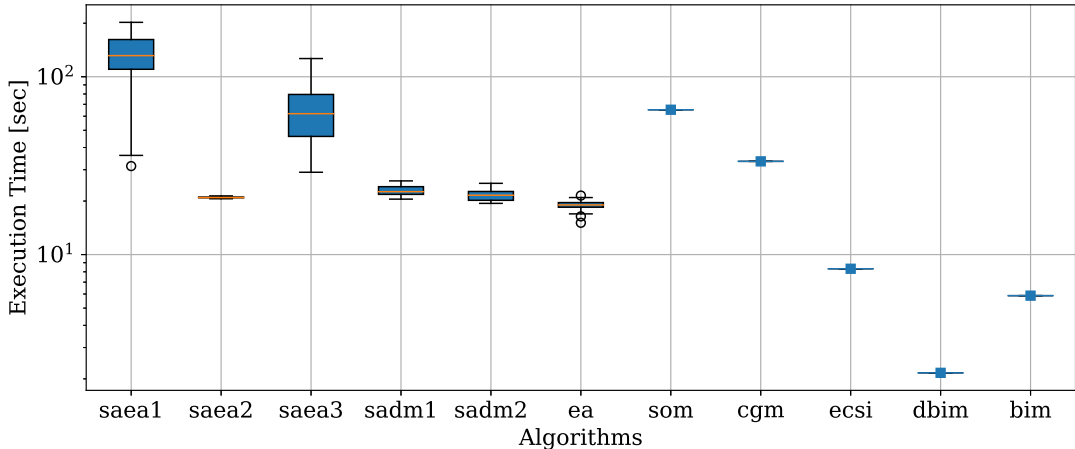


Figura 5.17: Box plot showing the execution time distribution of the set of algorithms considered for the nonhomogeneous scatterer case study. The boxes represent the quartiles of the 30 executions of the stochastic algorithms, and the whiskers represent the minimum and maximum values. The deterministic algorithms are represented by individual points. The execution time results are presented in seconds.

pected, some of the deterministic methods required less computational time than the proposed algorithms that use surrogate models. Among them, DBIM had the shortest time, thanks to the low number of iterations in which it can run without diverging. The second shortest time was taken by BIM, which was able to reconstruct the image adequately in a reasonably short time. Among the proposed algorithms, some executions had shorter times than others. Specifically, SAEA2, SADM1, SADM2, and EA required less time than SOM and CGM.

Figure 5.18 shows the surface of the objective function along with the location of the final solutions found by the algorithms in multiple runs. The surface of the objective function is similar to that obtained in the Austria profile case study (Fig. 5.6). The figure shows that only EA did not have all the final solutions within the sublevel region with the lowest value in the graph. This suggests that the EA algorithm may not be as efficient as the other algorithms in finding the optimal solutions. In contrast, the final solutions of the SADMs were more concentrated, as expected because of their respective convergence graphs.

#### 5.1.4 Strong Scatterer

In the final case study, we explore the reconstruction of a strong scatterer, aiming to showcase the applicability of the proposed methodology in a more challenging scenario where traditional methods often struggle. The scatterer in focus is a 5-pointed star with a radius from the center to the farthest vertex approximately  $0.4\lambda_b$  (see Fig. 5.19a). To emphasize the difficulty, the object contrast has been set to 4, making it even more challenging to accurately reconstruct. Detailed information about the measurement and imaging domains can be found in Table 5.4, providing essential specifications for the experimental setup.

To ensure higher precision in data synthesis, we increased the image resolution to  $120 \times 120$ .

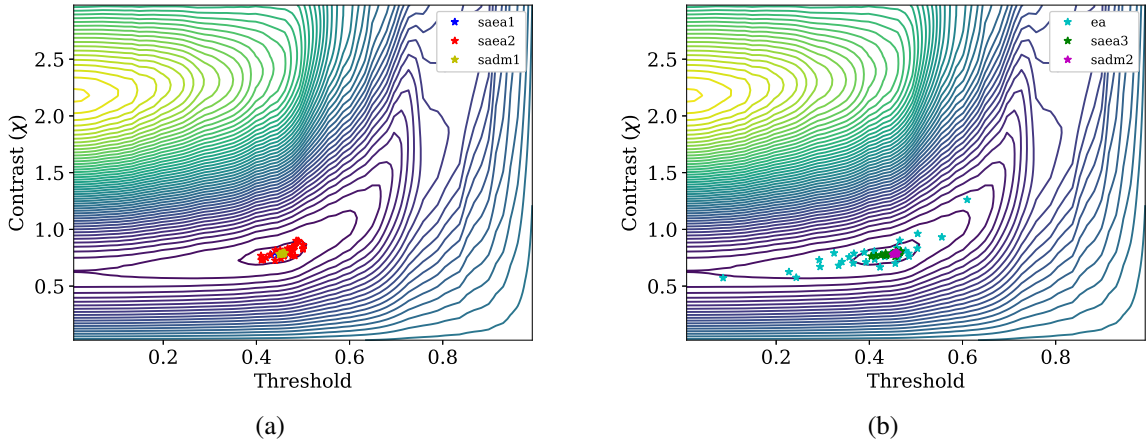


Figura 5.18: Surface of the two-dimensional optimization problem obtained from the transformation of the nonhomogeneous scatterer case study and the final solutions obtained by different algorithms. Subfigure (a) shows the final solutions obtained by SAEA1, SAEA2, and SADM1 algorithms, while subfigure (b) shows the final solutions obtained by EA, SAEA3, and SADM2 algorithms.

This resolution enhancement was chosen to minimize errors during the synthesis of the scattered field, considering the complexity of the problem at hand. Other parameters for data synthesis remained consistent with those used in the previous case studies.

The DNL for this particular problem is notably high, measuring 7.39. Such a high DNL value indicates the significant nonlinearity of the problem, further accentuating the challenge in accurately reconstructing the strong scatterer. The combination of the intricate scatterer shape and the high object contrast poses a substantial test for the proposed methodology.

Tabela 5.4: Parameters for problem specification of the strong scatterer case study.

$N_M$	$N_S$	$\lambda_b$	$R_O$	$L_X, L_Y$	$\epsilon_{rb}$
50	50	1 [m]	5 [ $\lambda_b$ ]	1 [ $\lambda_b$ ]	1

In order to tackle the increased complexity of the problem, several adjustments were made to the operating parameters of both the surrogate model-assisted algorithms and the deterministic methods. These modifications aimed to enhance the performance and adaptability of the algorithms to the more nonlinear nature of the scenario.

For the surrogate model-assisted algorithms, the upper bound of the contrast variable was set to 7, reflecting the higher contrast range present in the problem. Additionally, the maximum number of iterations for the MoM-CG-FFT in the evaluation of solutions remained at 20, despite this representing a greater error in the field approximation. This choice was deliberate to showcase the methodology's robustness even in challenging scenarios, where highly precise field calculations are not necessary. Furthermore, the maximum number of evaluations, serving as a stopping criterion, was increased to 80. To provide a more comprehensive initial sample, the number of solutions was increased to 36. These adjustments, while increasing the

computational cost, were essential to address the growing complexity of the problem and obtain accurate results.

The remaining parameters for the surrogate model-assisted algorithms remained consistent with the previous study, ensuring continuity and comparability. Similarly, adjustments were made to the deterministic methods. For SOM and CGM, the maximum number of iterations was extended to 1000, allowing for more comprehensive convergence. ECSI iterations were adjusted to 50. BIM iterations were set to 4, while DBIM iterations were limited to 2, considering the nature of the problem and the desired accuracy of the reconstructions. The number of iterations of the last three algorithms were chosen according to their own limitation in this scenario.

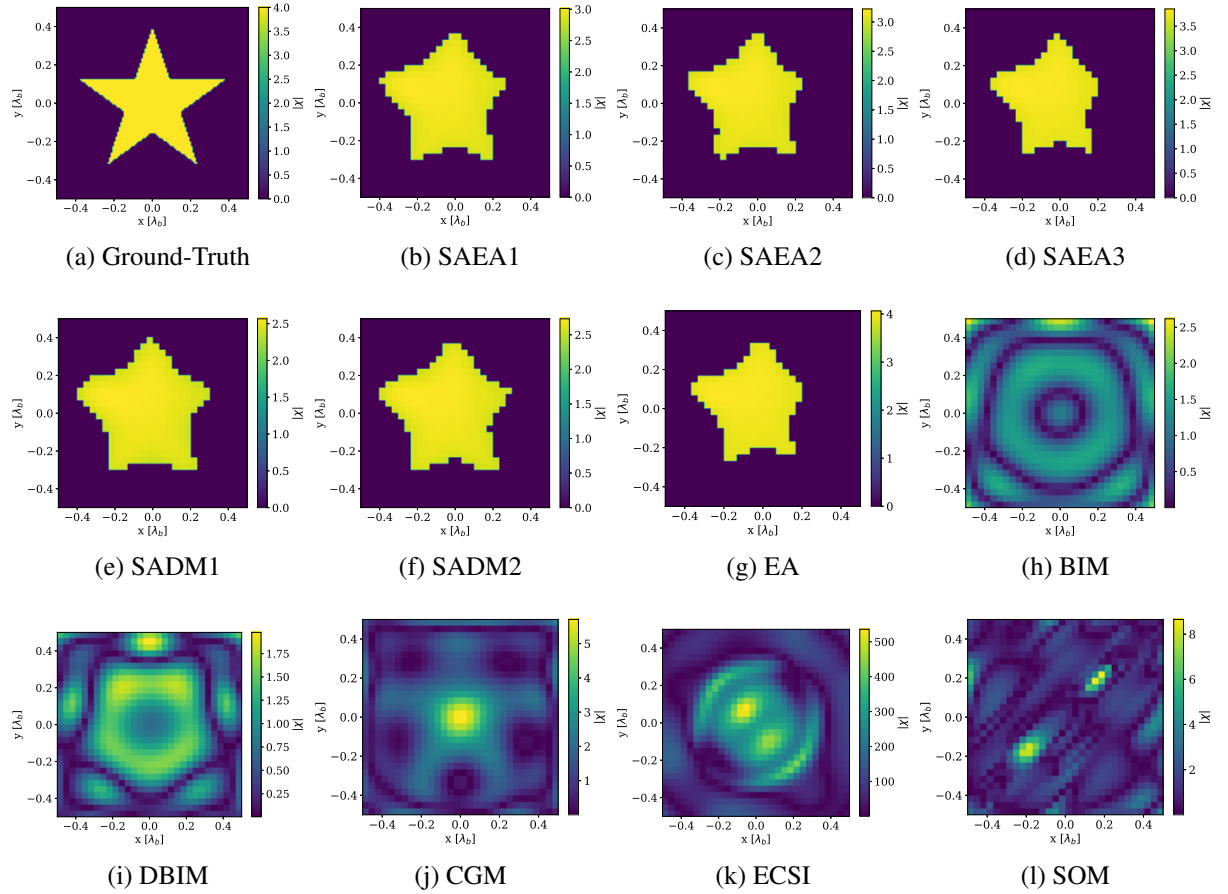


Figura 5.19: Comparison of image reconstructions using surrogate model-assisted algorithms and deterministic methods considering the strong scatterer case study: (a) shows the ground-truth image; (b), (c), and (d) depict the best image recovered by SAEA1, SAEA2, and SAEA3, respectively, in 30 execution according to  $\zeta_{\varepsilon OE}$  indicator; (e), (f) and (g) show the best image recovered by SADM1, SADM2, and EA, respectively, in 30 execution according to  $\zeta_{\varepsilon OE}$  indicator; (g) shows the image recovered by BIM, and (h) shows the image recovered by DBIM; finally, (i), (k), and (l) show the image recovered by CGM, ECSI, and SOM, respectively.

The Fig. 5.19 provides a visual representation of the best reconstructions obtained from the stochastic algorithms, as evaluated by the  $\zeta_{\varepsilon OE}$  indicator, alongside the reconstructions pro-

duced by the deterministic algorithms. It is noteworthy that the best images generated by the algorithms based on problem transformation exhibited variations in both contrast estimation and the application of the thresholding operator. Despite these variations, the reconstructed images still bear some resemblance to the geometry of the original image. This suggests that the qualitative method was able to capture certain structural characteristics despite the challenges posed by the problem. However, the contrast was underestimated in some cases. On the other hand, the deterministic algorithms failed to achieve satisfactory image reconstructions, although CGM was able to detect a region similar to a star with reasonable contrast estimation close to the boundaries and considerable overestimation at the center.

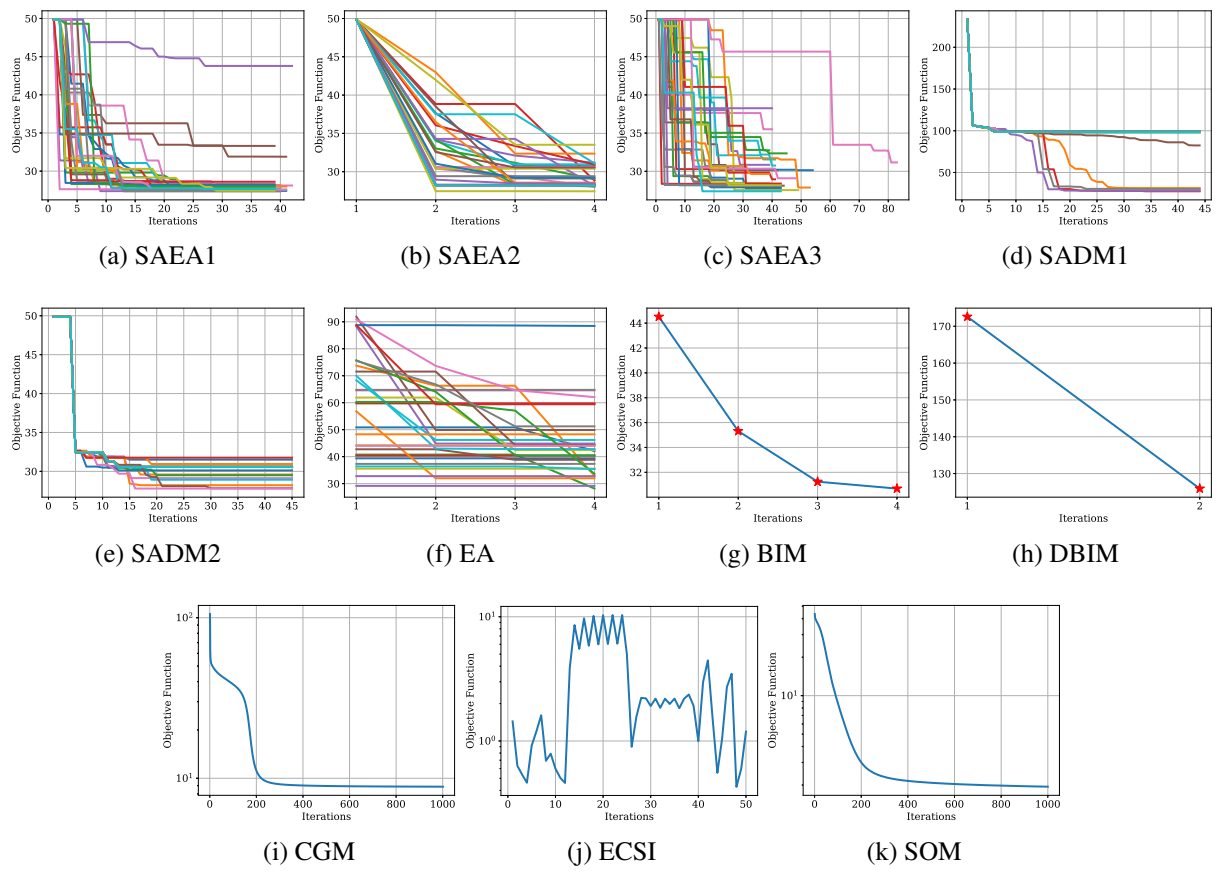


Figura 5.20: Convergence of the objective function for the strong scatterer case obtained by the stochastic and deterministic algorithms. (a) to (k) show the curves obtained by SAEA1, SAEA2, SAEA3, SADM1, SADM2, EA, BIM, DBIM, CGM, ECSI, and SOM algorithms, respectively. The x-axis represents the number of iterations, and the y-axis represents the value of the objective function of the correspondent algorithm.

Figure 5.20 provides a visual representation of the convergence behavior of the objective function for all algorithms employed in the study. Similar to the observations made in the case study involving multiple scatterers, this analysis reveals notable differences in the convergence patterns of the SADMs algorithms across multiple executions. This finding suggests that as the problem becomes more non-linear, the behavior of these algorithms tends to exhibit stochastic characteristics.

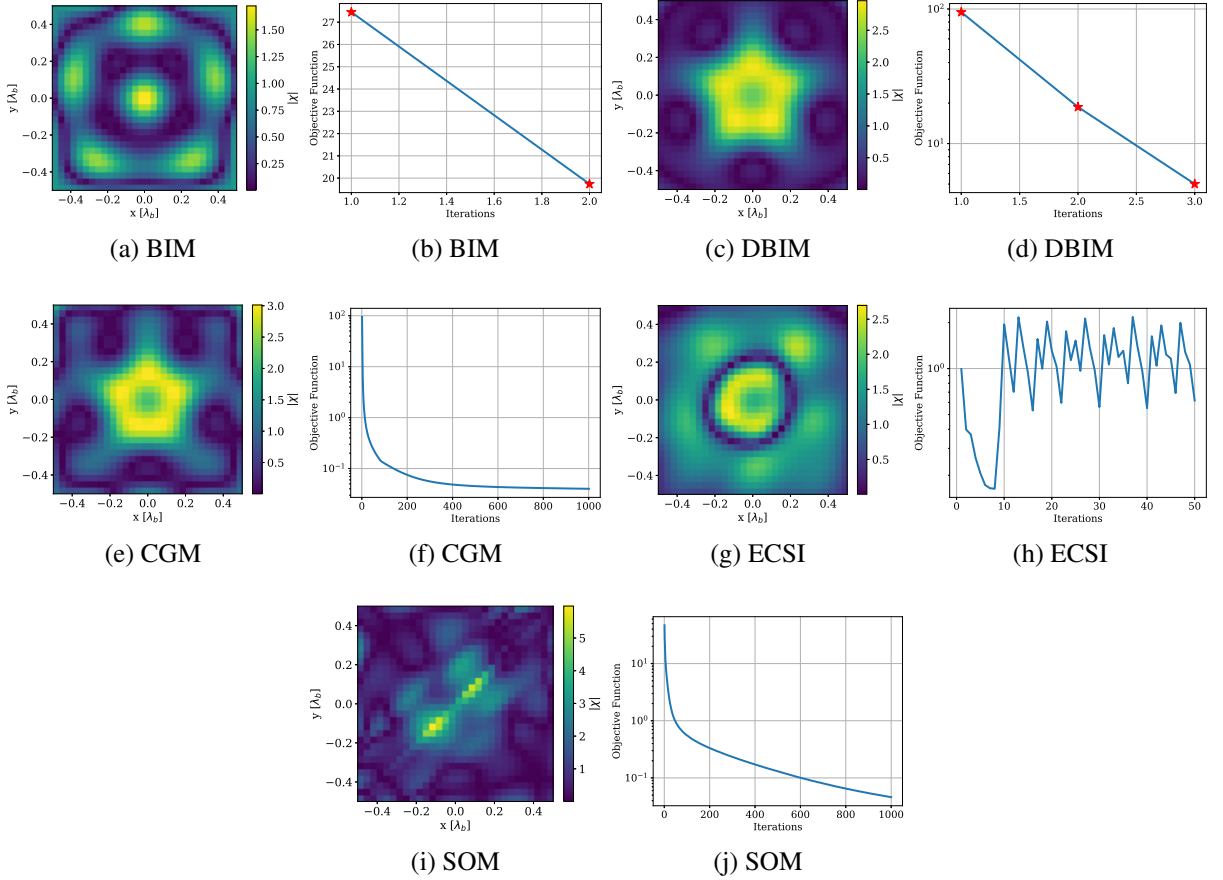


Figura 5.21: Reconstruction and convergence of the objective function for BIM (a)-(b), DBIM (c)-(d), CGM (e)-(f), ECSI (g)-(h), and SOM (i)-(j) algorithms with initial guess from the qualitative method.

Notably, ECSI exhibits an atypical behavior characterized by oscillations in its convergence curve. This observation highlights the algorithm's limitation when confronted with highly non-linear scenarios. The oscillatory nature of the convergence indicates the algorithm's struggle to converge to a stable and accurate solution, impairing its performance in such challenging scenarios.

On the other hand, the convergence curves of the CGM and SOM algorithms exhibit a different pattern. These algorithms demonstrate a stabilized behavior towards the end of the run, suggesting that further iterations would have minimal impact on the reconstructed images depicted in Figs. 5.19j and 5.20k. This stabilization indicates that the algorithms have reached a reasonably stable state, and additional iterations would not significantly enhance the quality of the reconstructions.

Initialization by the Backpropagation algorithm and the Born Approximation can be very bad in strong scattering scenarios, which can compromise all convergence of the deterministic algorithms. Therefore, one of the questions that may arise from the results is the impact of starting with the OSM qualitative method solution, i.e., how the deterministic algorithms would perform if they also received the image obtained by OSM as initial guess.

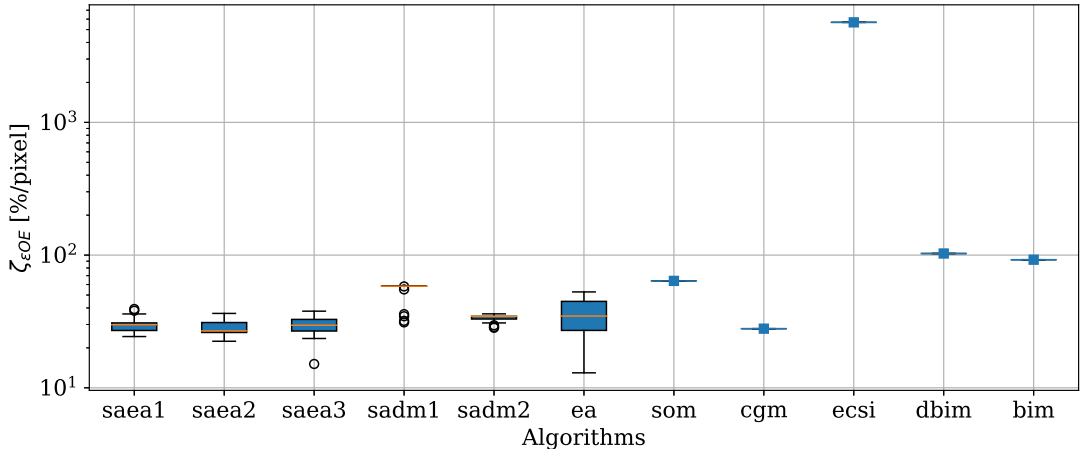


Figura 5.22: Performance of  $\zeta_{\varepsilon OE}$  indicator for various algorithms in the strong scatterer case study. Boxplots show quartiles of 30 executions for stochastic algorithms, and the solid line represents the deterministic algorithms.

Figure 5.21 showcases the reconstructions and convergence behavior of the deterministic algorithms when initialized with the normalized image from the qualitative method. Interestingly, the initialization strategy does not yield improvements for BIM, ECSI, and SOM algorithms. This indicates that relying solely on the qualitative method's image is insufficient to ensure better performance of these methods in such challenging scenarios. However, the DBIM and CGM algorithms demonstrate similar images resembling a smaller star, with a contrast estimate comparable to the surrogate model-assisted methods.

Analyzing the respective convergence graphs, it can be observed that the CGM image would not undergo significant changes beyond 1000 iterations, suggesting limited improvement in eliminating middle background noises. On the other hand, DBIM exhibits divergence with additional iterations. These findings highlight the importance of transforming the problem into a two-variable optimization framework, which proves to be the most effective approach for leveraging the reconstructed image provided by the qualitative method.

In Fig. 5.22, we can observe the results of the  $\zeta_{\varepsilon OE}$  indicator obtained by the different algorithms. Although the CGM algorithm did not produce reconstructions as visually clear as the proposed algorithms, its performance in terms of the contrast error indicator was comparable to the median value of most surrogate model-assisted algorithms. Despite the slightly blurred nature of its reconstructions, CGM was able to provide a reasonable estimation of the contrast value in the object region.

To further analyze the performance of the algorithms, a statistical comparison was conducted through Kruskal-Wallis H-Test. Comparing the median performance of the SAEAs and SADM2, evidence of a difference in performance was found ( $p\text{-value} < 10^{-6}$ ). Post-hoc comparisons revealed that the difference in performance is found when each SAEA is compared against SADM2 ( $p\text{-value} < 0.001$  in each case). In each case, the performance of the corresponding SAEA formulation overcame SADM2's performance.

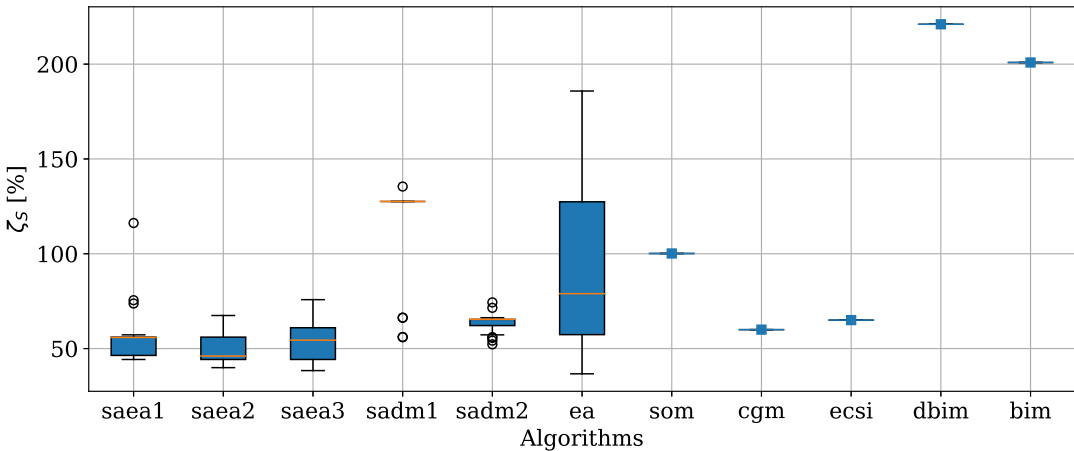


Figura 5.23: Performance of shape error estimation quantified by the  $\zeta_S$  indicator obtained by the set of algorithms considering the strong scatterer study. The boxes represent the quartiles of the 30 executions of the stochastic algorithms, while the other points indicate the obtained values by the deterministic ones. The shape error is calculated based on the ground-truth image and the reconstructed image obtained by each algorithm.

In Fig. 5.23, it is observed the results of the  $\zeta_S$  indicator obtained by the algorithms. The median values of the SAEAs were now found to be lower than the median value achieved by the CGM algorithm. No evidence for differences in the median performance among the SAEAs formulation was found according to the Kruskal-Wallis H-Test ( $p\text{-value} = 0.1983$ ). Furthermore, the Wilcoxon signed-rank test detected evidence for a worst median performance of SADM2 when compared against CGM.

Figure 5.24 displays the running time results of the algorithms used in the study. Among the algorithms, ECSI, DBIM, and BIM exhibited the lowest running times. This can be attributed to their poor convergence, which led to a lower number of iterations required for completion.

Notably, there is a significant difference in running time between the SAEA2 and SADM2 algorithms when compared against CGM. It is important to note that although CGM achieved a better value for the  $\zeta_{\epsilon OE}$  indicator, the other two algorithms, SAEA2 and SADM2, demonstrated the ability to produce satisfactory reconstructions within a significantly shorter time frame.

Figure 5.25 showcases the surface of the objective function resulting from the transformation in a two-dimensional optimization problem, providing insights into the behavior of the algorithms and the location of their final solutions in multiple runs. Upon observing the surface, it becomes apparent that the objective function exhibits two macro basins of attraction.

The distribution of the final solutions found by the algorithms reveals a scattering pattern, suggesting the location of the global optimum and the presence of small basins of attraction associated with local minima. Notably, such region appears to be very narrow, indicating a challenging optimization scenario. Therefore, the algorithms encountered greater difficulty converging to a single point in this particular instance. Furthermore, it is important to consider that the contrast value in the region of the global optimum is significantly underestimated.

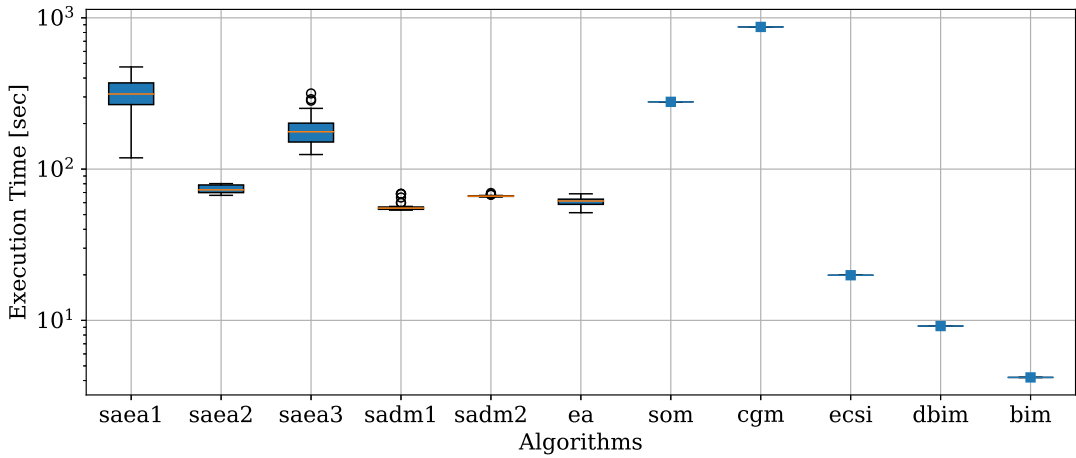


Figura 5.24: Box plot showing the execution time distribution of the set of algorithms considered for the strong scatterer case study. The boxes represent the quartiles of the 30 executions of the stochastic algorithms, and the whiskers represent the minimum and maximum values. The deterministic algorithms are represented by individual points. The execution time results are presented in seconds.

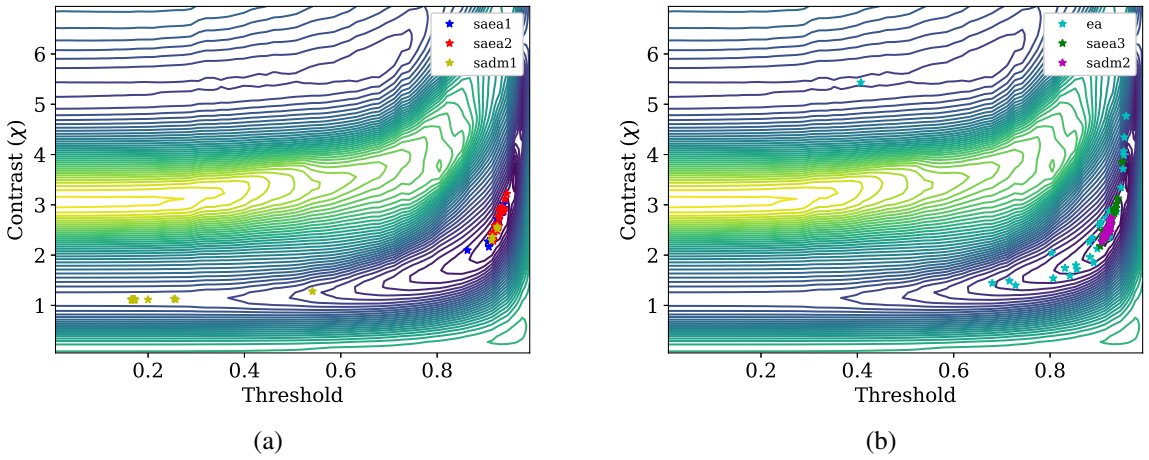


Figura 5.25: Surface of the two-dimensional optimization problem obtained from the transformation of the strong scatterer case study and the final solutions obtained by different algorithms. Subfigure (a) shows the final solutions obtained by SAEA1, SAEA2, and SADM1 algorithms, while subfigure (b) shows the final solutions obtained by EA, SAEA3, and SADM2 algorithms.

This outcome aligns with the expected behavior of qualitative methods when reconstructing the shape of strong scatterers, as demonstrated in this case study.

## 5.2 Benchmarking

This section presents a benchmarking experiment designed to evaluate the performance of the algorithms proposed in this thesis. While studying specific instances can provide valuable insights into experimental effects, a broader study with a larger number of instances enables a more comprehensive evaluation. To ensure a thorough analysis of the methods' performance, it is crucial to identify and consider influential factors when designing the experiment.

The experiment aims to isolate certain factors while varying others of interest, creating a diverse range of test scenarios represented by the selected problem samples. By employing a set of quality indicators, the performance of the techniques can be objectively measured and rigorously compared. The study focuses on evaluating the quality of contrast estimation and shape recovery while varying the contrast level of objects. Additionally, the number of evaluations required by each algorithm will be investigated to identify the most efficient approaches.

Unlike the case studies that examine specific instances, this benchmarking experiment encompasses multiple test sets. Within each set, scatterers possess a fixed contrast value, while their position and geometry vary. As a result, each set represents a collection of scatterers with the same contrast value but different configurations and positions within the images.

By analyzing the median behavior through statistical analysis, valuable insights into performance can be derived. This approach enables the identification of the strengths and weaknesses of the proposed techniques in a more robust and comparative manner, facilitating informed conclusions about their efficacy.

### 5.2.1 Test Sets and Algorithms Parameters Considerations

The overview of the general settings and parameters used in the generation of the test sets is presented as follows. The formulation and generation process followed the *TestSet* class structure implemented in the *eispy2d* library. Five test sets have been created where each set consisted of instances with a single scatterer, all sharing the same contrast value.

The selected contrast levels for the test sets were 0.5, 1, 2, 3, and 4, representing a range of different scattering strengths. The scatterers are random polygons that varied in geometry and position within the image, ensuring diversity in the test scenarios. Additionally, the size of the scatterers was controlled, with the size parameter defined as the distance from the center of the scatterer to its farthest vertex. For each contrast level, a specific size value was assigned. The size values for each contrast level, in increasing order of contrast, were 1.06, 0.8, 0.41, 0.33, and 0.27 [ $\lambda_b$ ].

The choice of object size values was based on an extensive preliminary study that exa-

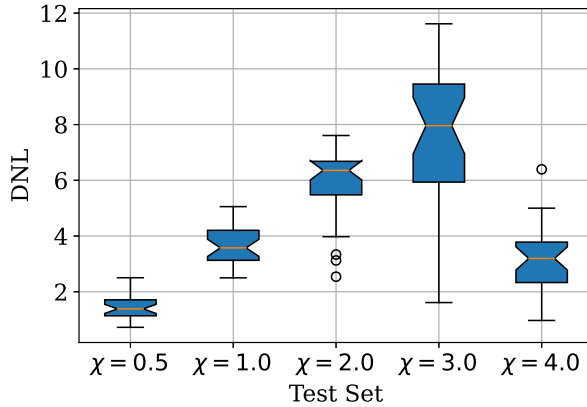


Figura 5.26: Box plot depicting the DNL across test sets: Test Set 1 (Contrast: 0.5), Test Set 2 (Contrast: 1), Test Set 3 (Contrast: 2), Test Set 4 (Contrast: 3), and Test Set 5 (Contrast: 4). The box plots showcase the distribution of non-linearity values, with the notches roughly indicating differences between medians. Non-overlapping notches mean significant differences between the medians.

mined the accuracy of the shape reconstruction by the qualitative method for different scatterer sizes at a given contrast value. The selected sizes represent the optimal scenarios for applying OSM in terms of shape quality.

Tabela 5.5: Parameters for measurement and imaging domains specification of benchmark study.

$N_M$	$N_S$	$R_O$	$\lambda_b$	$\epsilon_{rb}$
20	20	5 [ $\lambda_b$ ]	1 [m]	1

Table 5.5 presents specifications of the measurement and imaging domains used in the test sets. The size of the imaging domain ( $L_X, L_Y$ ) varied depending on the contrast value, with smaller domain size corresponding to higher contrast levels. The specific imaging domain sizes for each set, in ascending order of contrast values, were  $4 \times 4$ ,  $4 \times 4$ ,  $2 \times 2$ ,  $2 \times 2$ , and  $1 \times 1$  [ $\lambda_b^2$ ].

Each test set consisted of 30 individual tests. To generate the scattered field data, we employed the MoM-CG-FFT forward solver with 5000 iterations and a tolerance level of 0.001. Additionally, a noise level of 20 [%/sample] was added to all synthesized data to simulate realistic measurement conditions. Finally, the original images of each test had a resolution of  $120 \times 120$  pixels, ensuring sufficient detail for accurate analysis and evaluation.

Fig. 5.26 presents the distribution of the DNL for each test set, showcasing the variability in DNL despite the same contrast level across tests. The confidence interval for the median in each case is also displayed. The diversity in scatterer geometry within each set contributes to the observed variability in DNL. Notably, the median DNL increases with contrast level up to  $\chi = 3$ , after which a significant decrease in scatterer size for the  $\chi = 4$  contrast set leads to a smaller median DNL. However, it is important to note that even in this case, the DNL remains above 1, indicating the challenging nature of the problem. To further explore the range of DNL

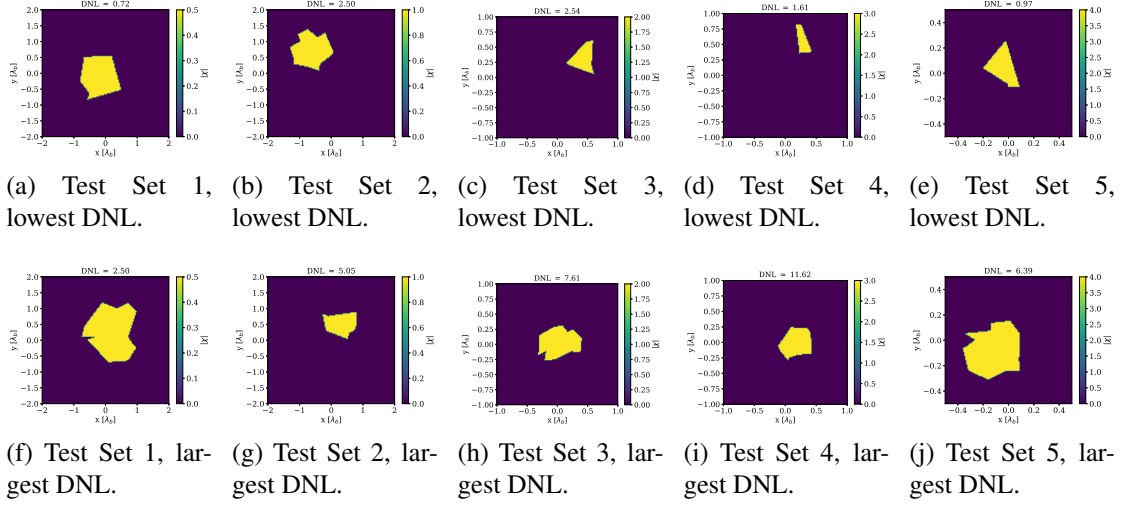


Figura 5.27: Instances with the lowest and largest DNL for each test set. Figures (a) to (e) display the instances with the lowest DNL for Test Sets 1 to 5, respectively. Conversely, figures (f) to (j) showcase the instances with the largest DNL for the corresponding test sets.

values, Fig. 5.27 showcases the instances with the smallest and largest DNL within each test set.

For this comparative evaluation, only algorithms assisted by surrogate models will be considered. By narrowing down the scope to these specific methods, we can delve deeper into understanding their unique characteristics and distinguishing features. This selection allows us to explore the differences between the proposed algorithms and observe their effectiveness and suitability.

To ensure a fair evaluation, the algorithms will be configured with identical parameters across all test sets. The maximum value of the contrast variable has been set to 7 in all cases, providing a wide range of contrast levels that covers each test set adequately. Additionally, the stopping criterion for the algorithms will be based on either a lack of improvement for 10 iterations or a maximum of 1000 evaluations. This criterion ensures that the algorithms have a reasonable time frame to converge or identify a lack of progress.

In all test sets, the number of initial samples used for model generation will be fixed at 36. This choice ensures a reasonable number of samples to train the surrogate models accurately in the hardest scenario. Furthermore, for SAEAs, a population size of 20 individuals has been determined. This population size was chosen aiming a balance between exploration and exploitation within the evolutionary search process.

### 5.2.2 Discussion

In this subsection, the results of the benchmarking study will be presented and discussed. The study aimed to evaluate the performance of different algorithms based on diverse performance indicator data. These indicators were obtained at the end of the algorithm executions and

will be organized in a boxplot format.

For each algorithm, it is showcased the performance evolution based on the contrast value that defines each test set. To better understand the performance evolution, a straight line obtained through linear regression will be displayed. This line represents an estimate of the expectation of the average performance as the contrast value increases. By considering the averages in the test sets of an algorithm, we can approximate the average performance along the growth of the contrast.

It's important to note that each algorithm was executed 30 times for each test in each set. This approach was taken to ensure reliable and consistent results. To determine the final performance of an algorithm in a specific test, we will consider the average of the respective indicator based on these 30 executions. This averaging process helps mitigate the impact of any outliers or random variations that might occur during individual executions. In the same fashion, 30 executions will return 30 recovered images for each test and the final one will be chosen as the one which has the median value according to  $\zeta_{\varepsilon OE}$  indicator.

Figure 5.28 displays the contrast estimation error indicator in the object region for each algorithm. The y-axis range is consistent among all algorithms, except for SADM1. Due to significantly larger errors obtained by SADM1, the range had to be increased for this particular algorithm.

The distinctive performance of SADM1, specially on the test set  $\chi = 1$ , raises curiosity. To investigate this occurrence, the reconstructed images generated by SADM1 for each test in the set were analyzed. Figure 5.29 provides visual evidence, presenting the true image from the first test set alongside the corresponding reconstruction by the method. It is apparent that the contrast estimate in SADM1's reconstruction is much higher than the true value, nearing the maximum limit of the contrast variable. This effect persists across all reconstructions of the algorithm in the same test set. Thus, these results suggest that the algorithm had a tendency to become trapped in a local minimum region, unlike the other algorithms. This behavior may be associated with the performance of the Differential Evolution (DE) as a solution initialization strategy.

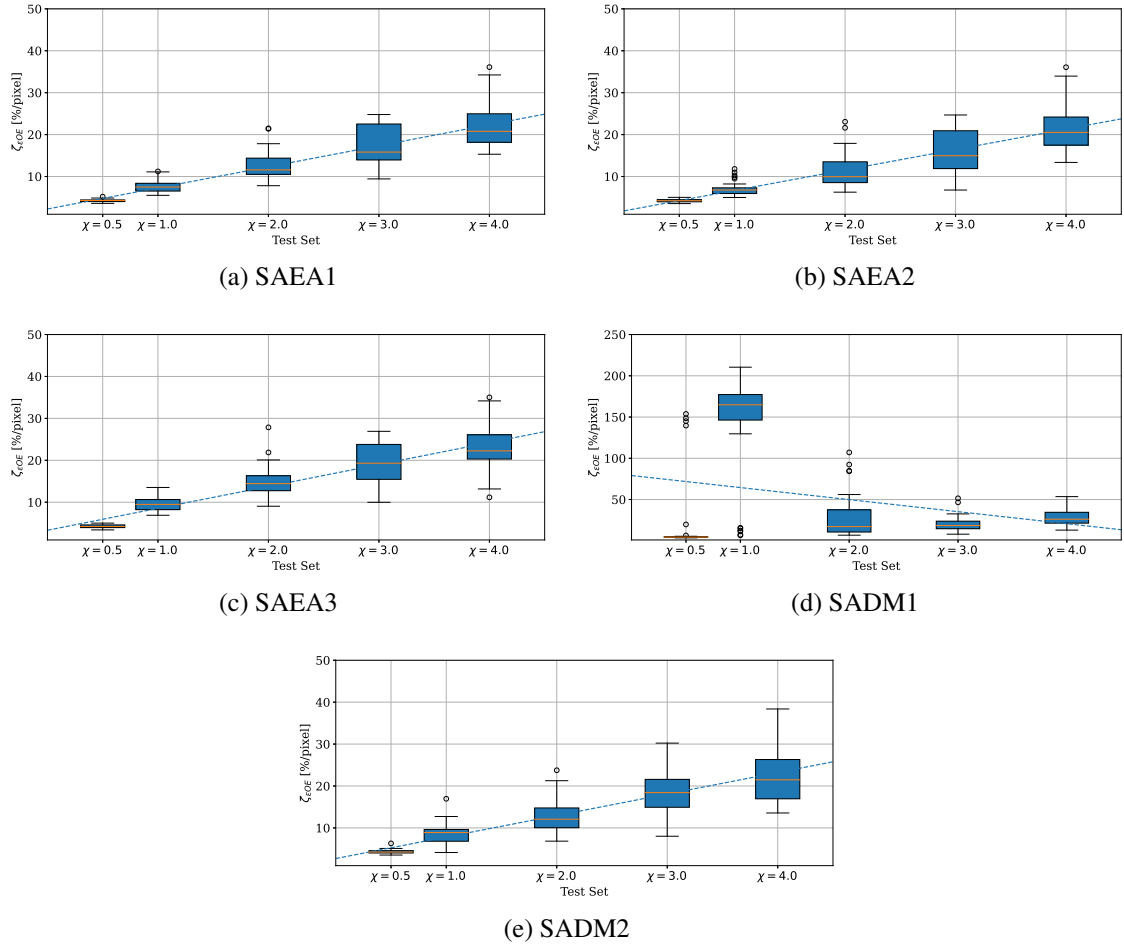


Figura 5.28: Evolution of the contrast estimation error ( $\zeta_{\varepsilon OE}$ ) in the object region for the proposed algorithms (a)-(e): SAEA1, SAEA2, SAEA3, SADM1, and SADM2, respectively. Additionally, a straight line obtained through linear regression is overlaid on each subfigure. This line represents the estimated evolution of the average performance, based on the means of each test set.

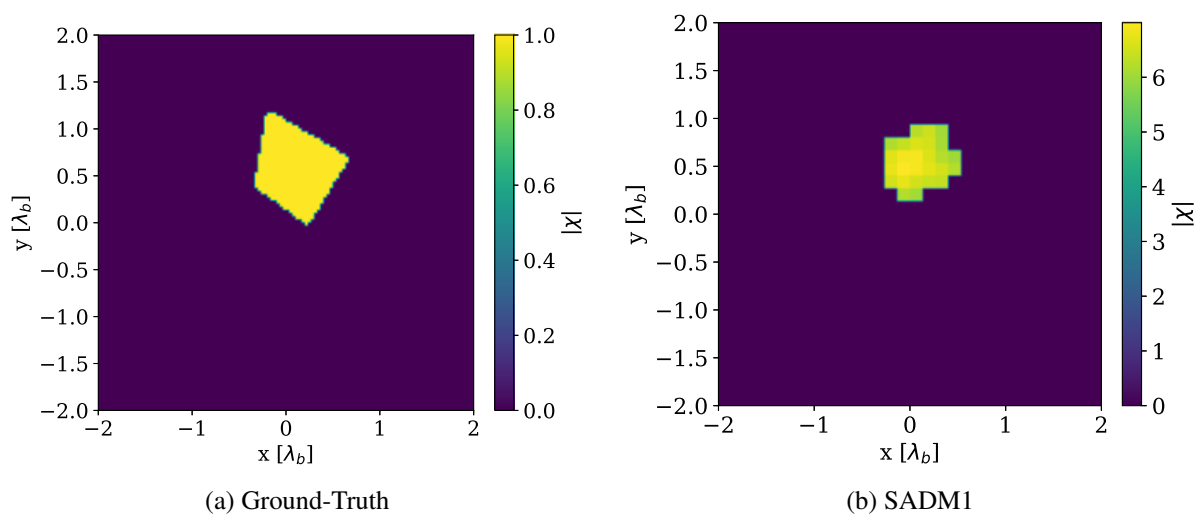


Figura 5.29: (a) Ground-truth and (b) recovered images by SADM1 in test 1 for Test Set  $\chi = 1$ . It is evident from the figure that SADM1 has overestimated the contrast of the object in its reconstruction.

Tabela 5.6: P-values for posthoc multiple pairwise comparisons considering the  $\zeta_{EOE}$  indicator, with the compatible statistical test for each test set. The significance level has been corrected using the Bonferroni method, resulting in 0.0083. Detected differences are indicated in bold format. Confidence intervals are compute for means when Paired T-Test are evaluated and for medians when the Wilcoxon Signed-Rank Test is evaluated.

Pairs	$\chi = 0.5$						$\chi = 3$					
	$\chi = 1$			$\chi = 2$			$\chi = 1$			$\chi = 2$		
	Wilcoxon		Signed-Rank test	Paired T-Test		Signed-Rank test	Wilcoxon		Signed-Rank test	Wilcoxon		Signed-Rank test
p-value	Conf. In.	p-value	Conf. In.	p-value	Conf. In.	p-value	Conf. In.	p-value	Conf. In.	p-value	Conf. In.	p-value
SAEA1-SAEA2	0.2988	(-0.031, 0.034)	<b>&lt;0.0001</b>	(0.322, 0.895)	<b>&lt;0.0001</b>	(0.675, 1.576)	<b>&lt;0.0001</b>	(0.4, 1.484)				
SAEA1-SAEA3	0.1706	(0.012, 0.124)	<b>&lt;0.0001</b>	(-2.5, -1.33)	<b>&lt;0.0001</b>	(-2.165, -0.916)	<b>&lt;0.0001</b>	(-2.574, -1.019)				
SAEA1-SADM2	0.0577	(-0.089, 0.002)	<b>0.003</b>	(-1.99, -0.132)	0.6702	(-0.804, 0.842)	0.2054	(-1.35, 0.862)				
SAEA2-SAEA3	0.2988	(-0.017, 0.148)	<b>&lt;0.0001</b>	(-3.18, -1.87)	<b>&lt;0.0001</b>	(-4.152, -2.3)	<b>&lt;0.0001</b>	(-4.301, -2.237)				
SAEA2-SADM2	0.0164	(-0.109, -0.009)	<b>&lt;0.0001</b>	(-2.71, -0.634)	<b>0.0008</b>	(-1.542, -0.063)	<b>0.0015</b>	(-2.494, 0.137)				
SAEA3-SADM2	0.1347	(-0.21, -0.023)	0.023	(-0.153, 1.86)	0.0113	(0.912, 3.128)	0.1642	(-0.886, 2.103)				

Tabela 5.7: P-values for posthoc multiple pairwise comparisons obtained by Wilcoxon Signed-Rank tests considering the  $\zeta_S$  indicator. The significance level has been corrected using the Bonferroni method, resulting in 0.0083. Detected differences are indicated in bold format. The confidence interval for medians is also presented.

Pairs	$\chi = 0.5$						$\chi = 3$					
	p-value	Conf. In.	p-value	Conf. In.	p-value	Conf. In.						
SAEA1-SAEA2	<b>&lt;0.0001</b>	(0.34, 0.92)	<b>&lt;0.0001</b>	(0.49, 1.09)	<b>&lt;0.0001</b>	(1.02, 2.04)	<b>0.0002</b>	(0.67, 2.01)	0.0145	(0.2, 2)		
SAEA1-SAEA3	<b>0.0002</b>	(-1.32, -0.49)	<b>&lt;0.0001</b>	(-5.38, -3.52)	<b>&lt;0.0001</b>	(-2.46, -1.34)	<b>&lt;0.0001</b>	(-3.16, -1.28)	<b>0.0066</b>	(-3.08, -0.92)		
SAEA1-SADM2	<b>0.0012</b>	(0.02, 0.69)	<b>0.0081</b>	(-2.38, 0.37)	0.3931	(-0.85, 0.59)	0.1706	(-1.72, 1.16)	0.9515	(-1.70, 1.58)		
SAEA2-SAEA3	<b>&lt;0.0001</b>	(-2.15, -0.97)	<b>&lt;0.0001</b>	(-5.80, -3.40)	<b>&lt;0.0001</b>	(-4.69, -1.97)	<b>&lt;0.0001</b>	(-5.73, -2.71)	<b>0.0028</b>	(-4.79, -1.37)		
SAEA2-SADM2	0.1996	(-0.20, 0.15)	<b>&lt;0.0001</b>	(-2.64, -0.17)	<b>&lt;0.0001</b>	(-2.70, -0.66)	<b>0.0007</b>	(-3.61, 0.08)	0.1059	(-2.17, 0.72)		
SAEA3-SADM2	<b>&lt;0.0001</b>	(0.51, 1.82)	<b>0.0081</b>	(0.91, 3.32)	0.0087	(0.83, 2.88)	0.2801	(-0.62, 1.93)	0.1094	(0.67, 4.32)		

On the other hand, the remaining algorithms exhibit similar average performances when analyzing the regression curves based on the averages of each set. As expected, the error increases with higher contrasts. The average error ranges from approximately 5 to 25 [%/pixel] within the considered contrast range.

However, statistical pairwise comparison tests have revealed some differences. Only in the highest contrast test set ( $\chi = 4$ ) there was no evidence of a significant difference (Friedman Rank Sum Test p-value = 0.0693).

Table 5.30 provides the p-values for all post-hoc comparisons, along with their respective tests. Considering the significance level corrected by the Bonferroni method (= 0.0083), no difference was detected in the first test set. Therefore, it is possible that a Type I error occurred during the test with multiple samples. The confidence intervals for means (in case of Paired T-Test) and for medians (in case of Wilcoxon Signed-Rank Test) are also shown in Table 5.30. It is worth noting that SAEA2 exhibits superior performance compared to other SAEAs. However, SAEA2 did not outperform SADM2 in the third and fourth test sets. Summarizing, when considering indicator  $\zeta_{\varepsilon OE}$ , SAEA2 tends to perform at an equivalent or superior level compared to the other algorithms in all cases.

Figure 5.30 showcases the results of the shape recovery indicator ( $\zeta_S$ ). Anomalous behavior in the test set  $\chi = 1$ , similar to what was observed previously, is once again apparent in the SADM1 method. However, this behavior is significantly attenuated compared to previous indicator. It is notable that all algorithms exhibit an increase in error as the contrast level rises. This outcome is expected since the qualitative method employed to generate the initial image tends to loose performance with higher contrast levels. In terms of indicator samples, test sets  $\chi = 1$  and  $\chi = 2$  demonstrate considerable similarity across all algorithms, with the exception of SADM1.

Regarding the lines obtained through regression analysis for the means in each test set, they demonstrate high similarity between the algorithms, with the exception of SADM1. However, when applying pairwise statistical comparisons using the Friedman Rank Sum Test, differences are found between the SAEA1, SAEA2, SAEA3, and SADM2 algorithms in each test set. In the first four test sets, the hypothesis of equal performance was rejected with a p-value less than 0.0001 at a 95% confidence level. Even in the fifth test set, where the p-value was slightly higher (0.0015), the null hypothesis was still rejected.

Table 5.7 displays the results of the post-hoc analysis, presenting the p-values for multiple pairwise comparisons obtained by Wilcoxon Signed-Rank Test in all cases. The table reveals that differences in performance are more frequently detected in the first four test sets. As for the latter test set, the difference is detected in only two of the six cases. An examination of the confidence interval of the medians for each pairwise comparison was accomplished and showed that SAEA2 demonstrates better performance in the first four test sets compared to the other SAEAs. Furthermore, in the second, third, and fourth test sets, SAEA2 outperforms SADM2 as well.

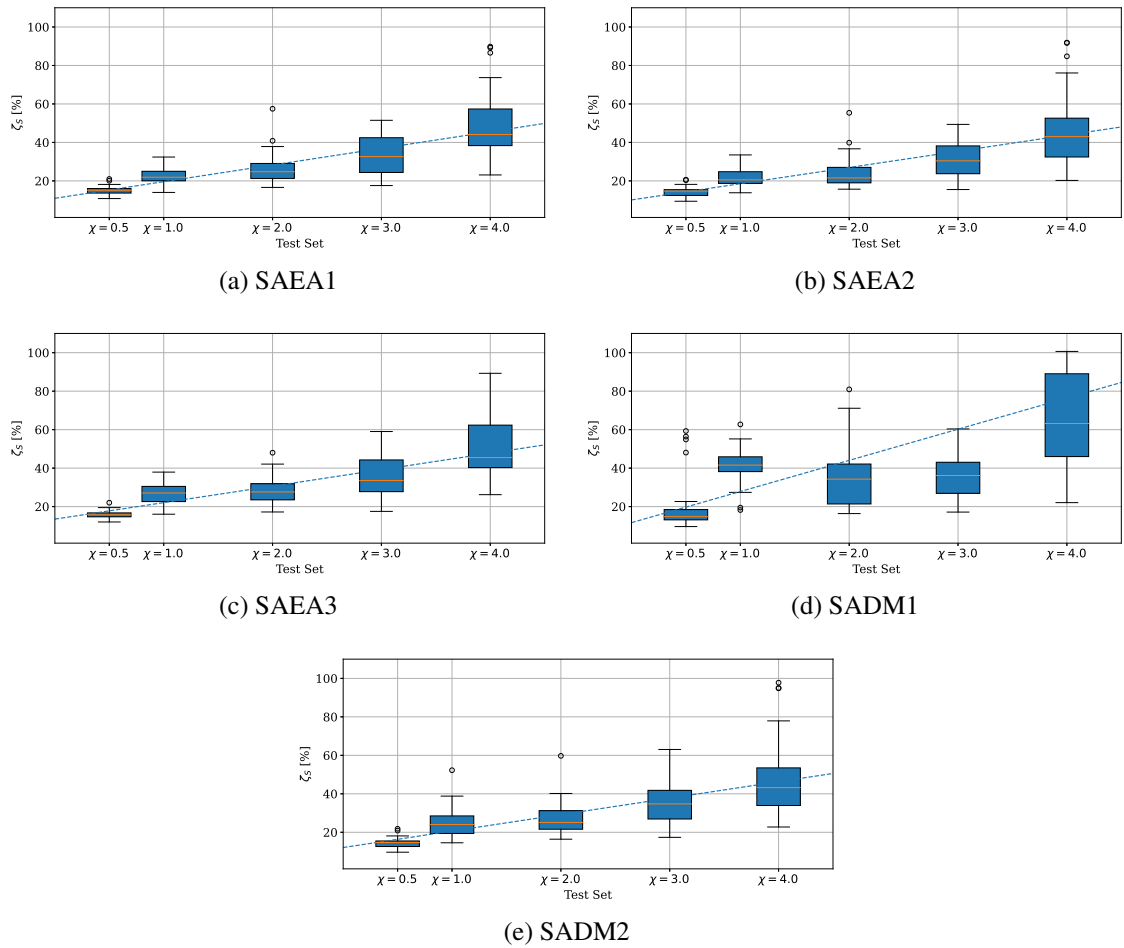


Figura 5.30: Evolution of the shape recovering error ( $\zeta_S$ ) for the proposed algorithms (a)-(e): SAEA1, SAEA2, SAEA3, SADM1, and SADM2, respectively. Additionally, a straight line obtained through linear regression is overlaid on each subfigure. This line represents the estimated evolution of the average performance, based on the means of each test set.

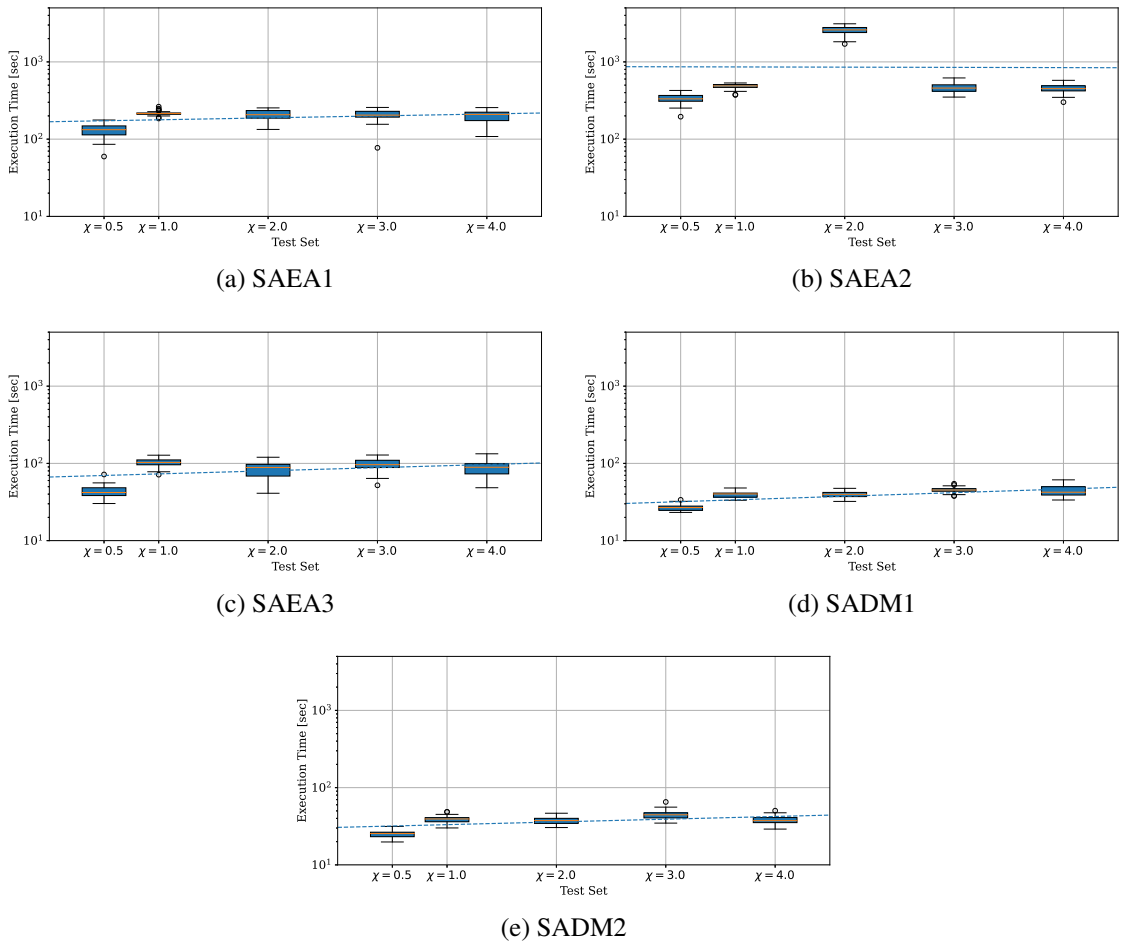


Figura 5.31: Evolution of execution time for the proposed algorithms (a)-(e): SAEA1, SAEA2, SAEA3, SADM1, and SADM2, respectively. Additionally, a straight line obtained through linear regression is overlaid on each subfigure. This line represents the estimated evolution of the average performance, based on the means of each test set.

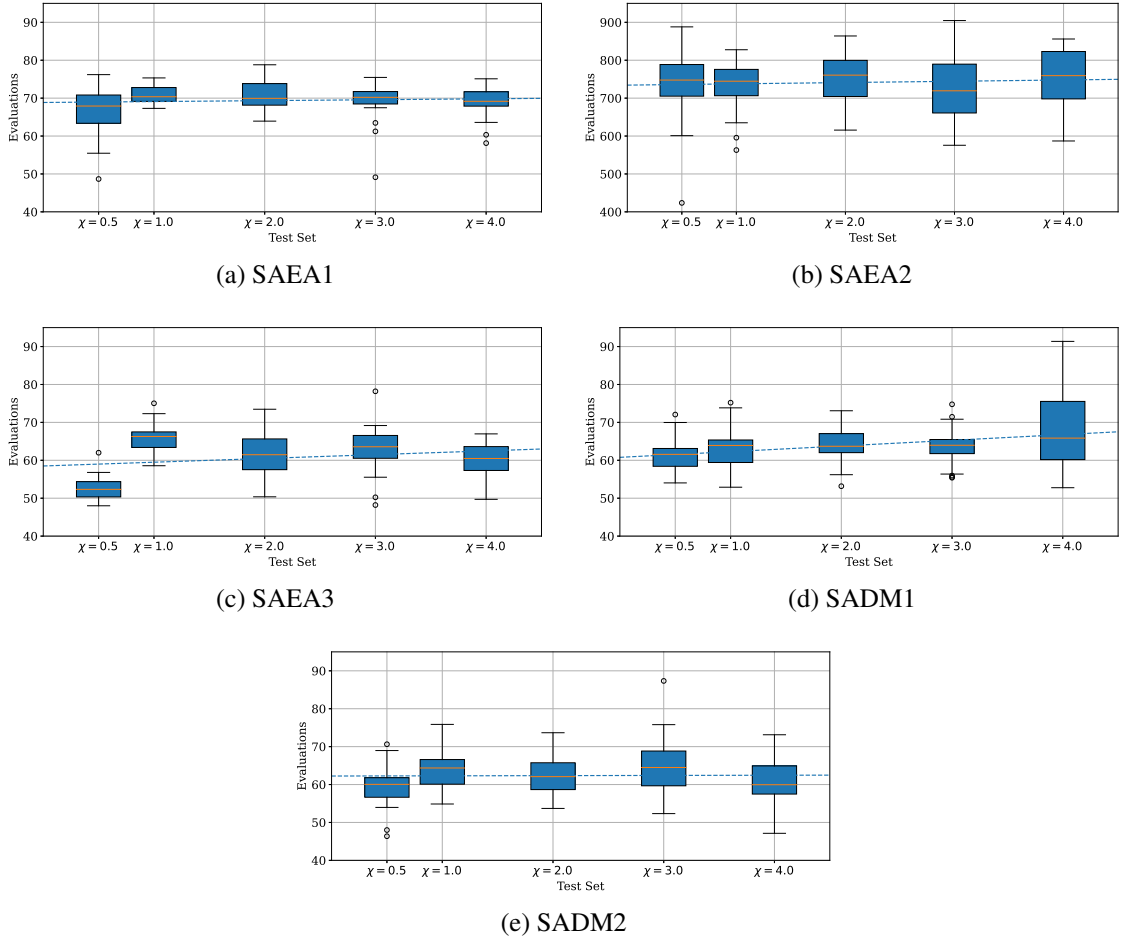


Figura 5.32: Evolution of the number of evaluations for the proposed algorithms (a)-(e): SAEA1, SAEA2, SAEA3, SADM1, and SADM2, respectively. Additionally, a straight line obtained through linear regression is overlaid on each subfigure. This line represents the estimated evolution of the average performance, based on the means of each test set.

Figure 5.31 displays the running time of the algorithms for each test set. The curve obtained through linear regression of the means reveals that the execution time of the algorithms exhibits minimal variation as the contrast increases. This finding suggests that the growth of contrast does not have a significant impact on the running time of the algorithms. A notable exception is observed in the results of the third test set for the SAEA2 algorithm. In this case, the running time differs significantly from the other test sets. There is no clear reason for this anomalous behavior and an unexpected process in the used computer might be a hypothesis. Comparatively, the execution time of the SADM1 and SADM2 algorithms tends to be shorter than that of the other algorithms. On the other hand, the SAEA2 algorithm generally exhibits the longest execution time among the tested algorithms.

Figure 5.32 illustrates the number of evaluations performed by each algorithm in each test set. Similar to the runtime results, the number of evaluations shows minimal variation as the contrast increases. This indicates that the algorithms' ability to converge is largely unaffected by increasing contrast levels.

Tabela 5.8: P-values for post-hoc multiple pairwise comparisons considering the number of evaluations, with the compatible statistical test for each test set. The significance level has been corrected using the Bonferroni method, resulting in a significance threshold of 0.0167. Detected differences are indicated in bold format. Confidence intervals for means are also available.

Pairs	$\chi = 0.5$		$\chi = 4$	
	p-value	Confi. In.	p-value	Confi. In.
SAEA3-SADM1	<b>&lt;0.0001</b>	(-11.1, -6.27)	<b>0.0004</b>	(-12.7, -2.84)
SAEA3-SADM2	<b>&lt;0.0001</b>	(-10.3, -4.62)	0.6238	(-3.75, 2.53)
SADM1-SADM2	0.2693	(-1.52, 3.95)	<b>0.0005</b>	(2.48, 11.8)

Among the algorithms, SAEA2 exhibits the highest number of evaluations, approximately 10 times more than the other algorithms. This outcome was expected since SAEA2 requires more iterations to converge. Interestingly, in contrast to the runtime results, the number of evaluations for SAEA2 in the third test set aligns with the other sets. This suggests that the unexpected increase in execution time observed in the third set was unrelated to the number of evaluations. This finding can support the hypothesis that an external factor, such as an unexpected process on the computer running the experiments, might have influenced the execution time.

In terms of the algorithms with the lowest number of evaluations, SAEA3, SADM1, and SADM2 stand out. Statistical tests rejected the hypothesis of equal performance among these three algorithms under the 95% confidence level only in the test sets  $\chi = 0.5$  and  $\chi = 4$ , with p-values smaller than 0.0001 obtained by the Randomized Complete Block Design. Subsequent post hoc analysis through multiple pairwise comparisons (Table 5.8) reveals that, for  $\chi = 0.5$ , SAEA3 had from 4 to 11 fewer evaluations than SADM1 or SADM2, in average. For  $\chi = 4.0$ , SAEA3 had from 3 to 13 fewer evaluations than SADM1, in average, and SADM1 had from 2 to 12 more evaluations than SADM2, in average. Therefore, there is no clear tendency of superiority among these three algorithms.

# Capítulo 6

## Conclusion

This chapter concludes the thesis. Firstly, a recapitulation of the main topics explored in the thesis is presented in Section 6.1. This serves as a concise summary, highlighting the main ideas, proposals, key findings, and their significance within the research context. By revisiting the main research questions and objectives, the recapitulation provides a holistic view of the thesis's scope and accomplishments.

Following the recapitulation, a critical analysis of the research methodology, limitations, and potential biases is presented in Section 6.2. Self-criticism plays a crucial role in research as it allows for a reflective assessment of the strengths and weaknesses of the study. By acknowledging any limitations or areas for improvement, this section contributes to the overall integrity and maturity of the research project.

Next, the chapter discusses the proposal continuity in Section 6.3. In the continuity proposals, different ideas are described that can be addressed after this project. The topics are developments of subjects that were part of the work, which could receive more attention and could contribute to the literature. Lastly, the chapter concludes with a list of the bibliographic production generated during the project (Section 6.4).

### 6.1 Recapitulation

Microwave imaging is a significant inverse problem with applications in various fields such as defect identification in structures, through-wall imaging, cancer detection, among others. It involves reconstructing the interior of inaccessible regions based on field measurements at microwave frequencies and images derived from the electrical properties of the materials within the investigated space.

This thesis aimed to comprehensively review the mathematical aspects of the problem, recognizing that microwave imaging is an electromagnetic inverse scattering problem. The objective is to determine the cause, i.e., one or more scatterers, of the observed effect, i.e., the scattered field. Maxwell's Equations provide integral equations that relate the observed

scattered field outside the region of interest with the unknown electromagnetic field and the mapping of electrical properties inside the region. However, this relationship is nonlinear due to the unknown nature of the electromagnetic field and the mapping of electrical properties, requiring simultaneous resolution of both variables.

The inverse problem is known to be ill-posed, lacking a unique solution or continuity in the relationship between the scattered field and the imaged medium. To address this, various formulas, including traditional integral formulas, have been developed to mitigate the inherent challenges of the problem. The degree of nonlinearity increases with the number of scatterers or their contrast, further complicating the solution process.

The thesis also presented an extensive overview of numerical methodologies to solve the problem, covering topics such as discretization, linear approximations, and regularization methods for ill-posed systems of equations. In the literature, numerical methods for the inverse electromagnetic scattering problem are classified into qualitative and quantitative methods. Qualitative methods focus on reconstructing the shape of scatterers, while quantitative methods aim to estimate the electrical properties in addition to recovering their geometries.

Noteworthy within qualitative methods is the Orthogonality Sampling Method (OSM), capable of recovering scatterer geometry and detecting different contrast levels. On the other hand, quantitative methods can be further categorized as deterministic or stochastic, depending on whether they rely on well-defined sequences of steps or stochastic processes. Deep Learning techniques have gained attention for their potential in enabling real-time imaging. Additionally, the application of Surrogate Models to assist algorithms for the problem, particularly those dependent on forward problem simulations, is an emerging area that holds promise in reducing computational costs while requiring effective representation methods.

The thesis also identified others shortcomings in the field, such as the lack of an integrated platform for algorithm development and testing, the need for standardized performance indicators, and limited generalization capacity in experimental designs. To address these issues, the thesis proposed two main propositions in the two-dimensional case of the electromagnetic inverse problem.

The first proposal involved applying Surrogate Models to assist Evolutionary Algorithms and Descent Methods, utilizing images generated by the OSM qualitative method for representing solutions. Such approach implies in transforming the inverse problem into a two-dimensional optimization problem, allowing for efficient treatment by Surrogate Models and achieving greater precision than similar proposals in the literature (Salucci et al., 2022b). Five formulations for surrogate model-assisted algorithms were proposed, utilizing both evolutionary and descent algorithms.

The second proposal focused on implementing a comprehensive algorithm development and testing structure that supports experimental design, quantification, and performance comparison of algorithms for the problem. This structure included software with object-oriented features capable of conducting case studies and benchmarking, a less explored area in the lite-

ature. The software facilitated exploring different problem characteristics, measuring various aspects of obtained images, and performing statistical comparisons to evaluate results more robustly.

The computational experiments conducted in the thesis included both case studies and benchmarking. The case studies covered four problem scenarios: simple, multiple, nonhomogeneous, and strong scatterers. In these studies, the proposed methods were compared against traditional deterministic methods. The benchmarking study focused on evaluating the performance of the proposed algorithms, specifically considering increasing object contrast levels.

The computational experiments conducted in this thesis provided valuable insights into the performance of algorithms assisted by surrogate models for microwave imaging. In general, the results indicated that these proposed algorithms have the capability to obtain images with comparable or slightly better qualities than traditional methods in the simplest cases. However, this improvement comes at a slightly higher computational cost in some instances.

One of the notable findings was that in high-contrast scenarios, the methodology assisted by surrogate models was able to reconstruct objects that traditional methods struggled with, all while maintaining a reasonable computational cost. This suggests that the surrogate models have the potential to address the limitations of traditional techniques and enable the imaging of challenging objects. It was also observed that the limitations of OSM posed restrictions on the application of the proposed methodology, particularly when dealing with numerous scatterers and varying levels of contrast. This highlights the need to consider the limitations of the qualitative method when applying the proposed approach.

In terms of the performance comparison between different algorithm versions, one of the evolutionary versions (SAEA2) demonstrated better image quality indicators but at a higher computational cost. On the other hand, a version based on the descent method (SADM2) showed comparable results in terms of image quality indicators while requiring significantly fewer computational resources. This finding suggests that a descent-based approach may offer a good balance between performance and computational efficiency.

Based on these results, it is evident that the application of surrogate models in the transformation of the inverse problem into a two-dimensional optimization problem is highly feasible. The objective function becomes much easier to predict using surrogate models, enabling the solution of scenarios where traditional techniques struggle to reconstruct images. The advantage of the approach lies in the reduced number of variables, which can be effectively handled by surrogate models. However, it is important to acknowledge that the limitations of OSM in certain scenarios prevent a more general application of the proposed methodology, unlike what is achievable with existing techniques in the literature (Salucci et al., 2022b).

These promising results encourage further development of the technique of applying surrogate models to strike a better balance between the number of variables that the surrogate model must handle and the ability to generalize to more complex scattering scenarios. By refining the application of surrogate models, it may be possible to overcome current limitations

and expand the scope of microwave imaging, opening new avenues for improved imaging performance in challenging environments.

## 6.2 Self-Criticism

Some critical points in conducting this research are commented below:

- In this work, a case study based on real measurements from the Fresnel Institute (Geffrin et al., 2005), which is commonly used in the literature, was not considered. Although including this case study could provide additional support for the real-world applicability of the proposed methodology, it was not feasible due to the slight differences in the electromagnetic propagation model used in the data. Adapting the model would require substantial time and effort, which was not available during the completion of this work.
- Regarding the benchmark study, the option was made to be more succinct and focus on the proposed methods. Therefore, the traditional deterministic methods were not included in the analysis. While including these methods would have allowed for a more comprehensive comparison, it would have increased the number of graphs and data to analyze, which was not the primary objective of this study.
- Salucci et al. (2022b) presented the only methodology available in the literature that applied surrogate models to the problem, and this work frequently cites their contribution to contextualize its own. However, the methodology proposed by them was not implemented in this study. It would have been interesting to include their methodology in the comparison to evaluate the efficiency of the transformation into a two-dimensional optimization problem and identify scenarios where their approach may outperform the one proposed in this work.
- In the obtained results, it was observed that the formulations based on the SAEAs took longer to run, even when the number of evaluations had the same limit than SADMs. This suggests that the evolutionary operations employed in the algorithm may have a significant impact on the overall computational cost. Further investigation would be necessary to implement optimizations and improve the performance of these algorithms in terms of computational efficiency.

## 6.3 Continuity Proposals

There are some topics that can be further explored in a future work:

- **Improvements to the initial image approach:** In this work, one of the evident needs is to expand the scope of application of OSM to address more challenging scenarios effectively. This requires modifying equations (3.114)-(3.117) to enhance the method's robustness against highly nonlinear problems. One approach could be exploring new integral

equations (Bevacqua and Isernia, 2021c) or investigating efficient domain decomposition techniques (Zhang et al., 2022). Another alternative could be developing more efficient ways to obtain an initial image while controlling the computational cost.

- **A better elaborated comparative study addressing traditional deterministic methods:** The implementation of a benchmark tool opens up possibilities for a more elaborate experimental design to quantitatively describe the average performance of traditional deterministic methods using the proposed indicators. This type of study is currently lacking in the literature and could provide valuable insights into the differences between these algorithms when subjected to a comprehensive comparison.
- **Creation of standard test sets:** Creating a standard test suite would be beneficial to the field, as it would enable researchers to compare their algorithms using well-defined and meaningful scenarios. This standardized approach would facilitate future studies by multiple authors, ensuring consistency and facilitating comparisons.
- **Creation of test sets based on DNL value:** Furthermore, it would be advantageous to design a problem generation mechanism based on a DNL target value. This mechanism would enable studies analyzing the variation of performance indicators of algorithms with varying DNL. Machine learning techniques could be employed to predict the DNL using only the characteristics of the desired problem, further enhancing the efficiency of these investigations.
- **Limits of application of the methods:** During the experiments in this work, it was observed that DNL alone is not always sufficient to quantify the difficulty of solving a particular problem for an algorithm. In some cases, algorithms may struggle to solve problems with lower DNL while being able to solve higher DNL problems. It would be valuable to develop a way to quantify the application limits of an algorithm, taking into account the problem's specific characteristics. This approach would provide a more comprehensive description of the operating limits of each method.
- **Implementation of the 3D model:** To continue this work, formulating a standard definition for the three-dimensional problem and implementing a library capable of supporting and adapting the development and testing of algorithms in this context would be valuable. Additionally, implementing the methodology proposed in this work in its three-dimensional version would further extend its applicability and provide insights into its performance in more complex scenarios.

## 6.4 Bibliographic Production

### Journals:

- Batista, A. C., Batista, L. S., & Adriano, R. (2021). A quadratic programming approach for microwave imaging. *IEEE Transactions on Antennas and Propagation*, 69(8), 4923-

4934.

- Vargas, J. O., Batista, A. C., Batista, L. S., & Adriano, R. (2021). On the computational complexity of the conjugate-gradient method for solving inverse scattering problems. *Journal of Electromagnetic Waves and Applications*, 35(17), 2323-2334.
- Batista, A. C., Adriano, R., & Batista, L. S. (2021). EISPY2D: An Open-Source Python Library for the Development and Comparison of Algorithms in Two-Dimensional Electromagnetic Inverse Scattering Problems. *arXiv preprint arXiv:2111.02185*. **Under review**.

#### Conferences:

- Vargas, J. O., Batista, A. C. ; Batista, L. S., Adriano, R. A Fast Conjugate Gradient Method for Solving Two-Dimensional Electromagnetic Inverse Scattering Problems. *XX Simpósio Brasileiro de Micro-Ondas e Optoeletrônica, 2022, Natal, RN*. Anais do XX Simpósio Brasileiro de Micro-Ondas e Optoeletrônica, 2022.

# Referências Bibliográficas

- Abubakar, A., Hu, W., van den Berg, P. M., and Habashy, T. M. (2008). A finite-difference contrast source inversion method. *Inverse Problems*, 24(6):065004.
- Abubakar, A., van den Berg, P., and Mallorqui, J. (2002). Imaging of biomedical data using a multiplicative regularized contrast source inversion method. *IEEE Transactions on Microwave Theory and Techniques*, 50(7):1761–1771.
- Afkham, B. M., Chung, J., and Chung, M. (2021). Learning regularization parameters of inverse problems via deep neural networks. *Inverse Problems*, 37(10):105017.
- Akinci, M. N., Cayoren, M., and Akduman, I. (2016). Near-field orthogonality sampling method for microwave imaging: Theory and experimental verification. *IEEE Transactions on Microwave Theory and Techniques*, 64(8):2489–2501.
- Ashtari, A., Noghalian, S., Sabouni, A., Aronsson, J., Thomas, G., and Pistorius, S. (2010). Using a priori information for regularization in breast microwave image reconstruction. *IEEE Transactions on Biomedical Engineering*, 57(9):2197–2208.
- Asok, A. O., S. J., G. N., and Dey, S. (2022). Concealed object detection with microwave imaging using vivaldi antennas utilizing novel time-domain beamforming algorithm. *IEEE Access*, 10:116987–117000.
- Azimi-Sadjadi, M., Poole, D., Sheedvash, S., Sherbondy, K., and Stricker, S. (1992). Detection and classification of buried dielectric anomalies using a separated aperture sensor and a neural network discriminator. *IEEE Transactions on Instrumentation and Measurement*, 41(1):137–143.
- Bach, F., Jenatton, R., Mairal, J., Obozinski, G., et al. (2011). Convex optimization with sparsity-inducing norms. *Optimization for Machine Learning*, 5:19–53.
- Balanis, C. A. (2012). *Advanced engineering electromagnetics*. John Wiley & Sons.
- Bao, G., Hou, S., and Li, P. (2007). Inverse scattering by a continuation method with initial guesses from a direct imaging algorithm. *Journal of Computational Physics*, 227(1):755–762.

- Bao, G., Li, P., Lin, J., and Triki, F. (2015). Inverse scattering problems with multi-frequencies. *Inverse Problems*, 31(9):093001.
- Bartle, R. G. (1995). *The elements of integration and Lebesgue measure*, volume 27. John Wiley & Sons, Ltd.
- Batista, A. C., Batista, L. S., and Adriano, R. (2021). A quadratic programming approach for microwave imaging. *IEEE Transactions on Antennas and Propagation*.
- Beiranvand, V., Hare, W., and Lucet, Y. (2017). Best practices for comparing optimization algorithms. *Optimization and Engineering*, 18(4):815–848.
- Benedetti, M., Donelli, M., and Massa, A. (2007). Multicrack detection in two-dimensional structures by means of ga-based strategies. *IEEE Transactions on Antennas and Propagation*, 55(1):205–215.
- Benedetti, M., Lesselier, D., Lambert, M., and Massa, A. (2010). Multiple-shape reconstruction by means of multiregion level sets. *IEEE Transactions on Geoscience and Remote Sensing*, 48(5):2330–2342.
- Bertero, M. and Boccacci, P. (2020). *Introduction to inverse problems in imaging*. CRC press.
- Bevacqua, M. T., Crocco, L., Di Donato, L., and Isernia, T. (2015). An algebraic solution method for nonlinear inverse scattering. *IEEE Transactions on Antennas and Propagation*, 63(2):601–610.
- Bevacqua, M. T. and Isernia, T. (2021a). An effective rewriting of the inverse scattering equations via green's function decomposition. *IEEE Transactions on Antennas and Propagation*, pages 1–1.
- Bevacqua, M. T. and Isernia, T. (2021b). A new hybrid yo-nie model for nonlinear inverse scattering problems. In *2021 IEEE 19th International Symposium on Antenna Technology and Applied Electromagnetics (ANTEM)*, pages 1–2.
- Bevacqua, M. T. and Isernia, T. (2021c). Quantitative non-linear inverse scattering: A wealth of possibilities through smart rewritings of the basic equations. *IEEE Open Journal of Antennas and Propagation*, 2:335–348.
- Bevacqua, M. T., Isernia, T., Palmeri, R., Akıncı, M. N., and Crocco, L. (2020). Physical insight unveils new imaging capabilities of orthogonality sampling method. *IEEE Transactions on Antennas and Propagation*, 68(5):4014–4021.
- Bevacqua, M. T., Palmeri, R., Isernia, T., and Crocco, L. (2021). A simple procedure to design virtual experiments for microwave inverse scattering. *IEEE Transactions on Antennas and Propagation*, 69(12):8652–8663.

- Bisio, I., Estatico, C., Fedeli, A., Lavagetto, F., Pastorino, M., Randazzo, A., and Sciarrone, A. (2018). Brain stroke microwave imaging by means of a newton-conjugate-gradient method in  $l^p$  banach spaces. *IEEE Transactions on Microwave Theory and Techniques*, 66(8):3668–3682.
- Bisio, I., Estatico, C., Fedeli, A., Lavagetto, F., Pastorino, M., Randazzo, A., and Sciarrone, A. (2020). Variable-exponent lebesgue-space inversion for brain stroke microwave imaging. *IEEE Transactions on Microwave Theory and Techniques*, 68(5):1882–1895.
- Bisio, I., Fedeli, A., Lavagetto, F., Pastorino, M., Randazzo, A., Sciarrone, A., and Estatico, C. (2017). Microwave data inversion in hemorrhagic brain stroke imaging: A newton-conjugate-gradient based approach in  $l^p$  banach spaces (invited paper). In *2017 IEEE Conference on Antenna Measurements Applications (CAMA)*, pages 275–278.
- Böttcher, A. and Grudsky, S. M. (2000). *Toeplitz Matrices, Asymptotic Linear Algebra and Functional Analysis*. Texts and Readings in Mathematics. Hindustan Book Agency, India, 1 edition.
- Breard, A., Perrusson, G., and Lesselier, D. (2008). Hybrid differential evolution and retrieval of buried spheres in subsoil. *IEEE Geoscience and Remote Sensing Letters*, 5(4):788–792.
- Brignone, M., Bozza, G., Randazzo, A., Piana, M., and Pastorino, M. (2008). A hybrid approach to 3d microwave imaging by using linear sampling and aco. *IEEE Transactions on Antennas and Propagation*, 56(10):3224–3232.
- Brown, K. G., Gedert, N., Asefi, M., LoVetri, J., and Jeffrey, I. (2019). Hybridizable discontinuous galerkin method contrast source inversion of 2-d and 3-d dielectric and magnetic targets. *IEEE Transactions on Microwave Theory and Techniques*, 67(5):1766–1777.
- Bucci, O. M., Cardace, N., Crocco, L., and Isernia, T. (2001). Degree of nonlinearity and a new solution procedure in scalar two-dimensional inverse scattering problems. *J. Opt. Soc. Am. A*, 18(8):1832–1843.
- Bucci, O. M. and Franceschetti, G. (1989). On the degrees of freedom of scattered fields. *IEEE Transactions on Antennas and Propagation*, 37(7):918–926.
- Bucci, O. M. and Isernia, T. (1997). Electromagnetic inverse scattering: Retrievable information and measurement strategies. *Radio Science*, 32(6):2123–2137.
- Buche, D., Schraudolph, N. N., and Koumoutsakos, P. (2005). Accelerating evolutionary algorithms with gaussian process fitness function models. *IEEE Transactions on Systems, Man, and Cybernetics, Part C (Applications and Reviews)*, 35(2):183–194.
- Burfeindt, M. J., Colgan, T. J., Mays, R. O., Shea, J. D., Behdad, N., Van Veen, B. D., and

- Hagness, S. C. (2012). Mri-derived 3-d-printed breast phantom for microwave breast imaging validation. *IEEE Antennas and Wireless Propagation Letters*, 11:1610–1613.
- Byrd, R. H., Lu, P., Nocedal, J., and Zhu, C. (1995). A limited memory algorithm for bound constrained optimization. *SIAM Journal on Scientific Computing*, 16(5):1190–1208.
- Cakoni, F. and Colton, D. (2016). *A Qualitative Approach to Inverse Scattering Theory*. Springer, New York, NY, 1 edition.
- Calvetti, D., Hansen, P. C., and Reichel, L. (2002). L-curve curvature bounds via lanczos didiagonalization. *ETNA. Electronic Transactions on Numerical Analysis [electronic only]*, 14:20–35.
- Calvetti, D., Morigi, S., Reichel, L., and Sgallari, F. (2000). Tikhonov regularization and the l-curve for large discrete ill-posed problems. *Journal of Computational and Applied Mathematics*, 123(1):423–446. Numerical Analysis 2000. Vol. III: Linear Algebra.
- Campbell, S. D., Jenkins, R. P., O'Connor, P. J., and Werner, D. (2021). The explosion of artificial intelligence in antennas and propagation: How deep learning is advancing our state of the art. *IEEE Antennas and Propagation Magazine*, 63(3):16–27.
- Campelo, F. and Aranha, C. (2018). EC Bestiary: A bestiary of evolutionary, swarm and other metaphor-based algorithms.
- Candès, E. and Romberg, J. (2007). Sparsity and incoherence in compressive sampling. *Inverse Problems*, 23(3):969–985.
- Caorsi, S., Costa, A., and Pastorino, M. (2001). Microwave imaging within the second-order born approximation: stochastic optimization by a genetic algorithm. *IEEE Transactions on Antennas and Propagation*, 49(1):22–31.
- Caorsi, S., Donelli, M., Franceschini, D., and Massa, A. (2002). An iterative multiresolution approach for microwave imaging applications. *Microwave and Optical Technology Letters*, 32(5):352–356.
- Caorsi, S., Donelli, M., Franceschini, D., and Massa, A. (2003a). A new methodology based on an iterative multiscaling for microwave imaging. *IEEE Transactions on Microwave Theory and Techniques*, 51(4):1162–1173.
- Caorsi, S., Donelli, M., Lommi, A., and Massa, A. (2004a). Location and imaging of two-dimensional scatterers by using a particle swarm algorithm. *Journal of Electromagnetic Waves and Applications*, 18(4):481–494.
- Caorsi, S., Donelli, M., and Massa, A. (2004b). Detection, location, and imaging of multiple scatterers by means of the iterative multiscaling method. *IEEE Transactions on Microwave Theory and Techniques*, 52(4):1217–1228.

- Caorsi, S., Gragnani, G., Medicina, S., Pastorino, M., and Zunino, G. (1991). Microwave imaging method using a simulated annealing approach. *IEEE Microwave and Guided Wave Letters*, 1(11):331–333.
- Caorsi, S., Gragnani, G., Medicina, S., Pastorino, M., and Zunino, G. (1994). Microwave imaging based on a markov random field model. *IEEE Transactions on Antennas and Propagation*, 42(3):293–303.
- Caorsi, S., Massa, A., and Pastorino, M. (1996). Iterative numerical computation of the electromagnetic fields inside weakly nonlinear infinite dielectric cylinders of arbitrary cross sections using the distorted-wave born approximation. *IEEE Transactions on Microwave Theory and Techniques*, 44(3):400–412.
- Caorsi, S., Massa, A., Pastorino, M., Raffetto, M., and Randazzo, A. (2003b). Detection of buried inhomogeneous elliptic cylinders by a memetic algorithm. *IEEE Transactions on Antennas and Propagation*, 51(10):2878–2884.
- Caorsi, S., Massa, A., Pastorino, M., and Randazzo, A. (2003c). Electromagnetic detection of dielectric scatterers using phaseless synthetic and real data and the memetic algorithm. *IEEE Transactions on Geoscience and Remote Sensing*, 41(12):2745–2753.
- Caorsi, S., Massa, A., Pastorino, M., and Rosani, A. (2004c). Microwave medical imaging: potentialities and limitations of a stochastic optimization technique. *IEEE Transactions on Microwave Theory and Techniques*, 52(8):1909–1916.
- Caorsi, S. and Pastorino, M. (2000). Two-dimensional microwave imaging approach based on a genetic algorithm. *IEEE Transactions on Antennas and Propagation*, 48(3):370–373.
- Caro, P. (2010). Stable determination of the electromagnetic coefficients by boundary measurements. *Inverse Problems*, 26(10).
- Catapano, I., Crocco, L., D’Urso, M., and Isernia, T. (2007a). On the effect of support estimation and of a new model in 2-d inverse scattering problems. *IEEE Transactions on Antennas and Propagation*, 55(6):1895–1899.
- Catapano, I., Crocco, L., and Isernia, T. (2007b). On simple methods for shape reconstruction of unknown scatterers. *IEEE Transactions on Antennas and Propagation*, 55(5):1431–1436.
- Chankong, V. and Haimes, Y. Y. (2008). *Multiobjective decision making: theory and methodology*. Courier Dover Publications.
- Chen, C.-h., Härdle, W. K., and Unwin, A. (2008). *Handbook of Data Visualization*. Springer Handbooks of Computational Statistics. Springer-Verlag Berlin Heidelberg, first edition.
- Chen, G., Shah, P., Stang, J., and Moghaddam, M. (2020a). Learning-assisted multimodality dielectric imaging. *IEEE Transactions on Antennas and Propagation*, 68(3):2356–2369.

- Chen, X. (2009). Application of signal-subspace and optimization methods in reconstructing extended scatterers. *J. Opt. Soc. Am. A*, 26(4):1022–1026.
- Chen, X. (2010). Subspace-based optimization method for solving inverse-scattering problems. *IEEE Transactions on Geoscience and Remote Sensing*, 48(1):42–49.
- Chen, X. (2017). *Computational Methods for Electromagnetic Inverse Scattering*. Wiley-IEEE Press.
- Chen, X., Wei, Z., Li, M., and Rocca, P. (2020b). A review of deep learning approaches for inverse scattering problems (invited review). *Progress In Electromagnetics Research*, 167:67–81.
- Chen, X. and Zhong, Y. (2008). MUSIC electromagnetic imaging with enhanced resolution for small inclusions. *Inverse Problems*, 25(1):015008.
- Chen, Y., Xiao, L.-Y., Zhuo, J., Han, F., and Liu, Q. H. (2021). Quantitative electromagnetic inversion of irregular scatterers based on a threefold hybrid method. *IEEE Transactions on Antennas and Propagation*, 69(12):8664–8674.
- Chen, Y., Zhang, H., Cui, T. J., Teixeira, F. L., and Li, L. (2023). A mesh-free 3-d deep learning electromagnetic inversion method based on point clouds. *IEEE Transactions on Microwave Theory and Techniques*, pages 1–10.
- Chen, Y., Zhong, M., Guan, Z., and Han, F. (2022). A tailored semiphysics-driven artificial neural network for electromagnetic full-wave inversion. *IEEE Transactions on Antennas and Propagation*, 70(8):6207–6217.
- Chew, W. (2009). *Integral equation methods for electromagnetic and elastic waves*. Morgan & Claypool Publishers, San Rafael, Calif.
- Chew, W. and Lin, J. (1995). A frequency-hopping approach for microwave imaging of large inhomogeneous bodies. *IEEE Microwave and Guided Wave Letters*, 5(12):439–441.
- Chew, W. and Liu, Q.-H. (1994). Inversion of induction tool measurements using the distorted born iterative method and cg-ffht. *IEEE Transactions on Geoscience and Remote Sensing*, 32(4):878–884.
- Chew, W. and Wang, Y. (1990). Reconstruction of two-dimensional permittivity distribution using the distorted born iterative method. *IEEE Transactions on Medical Imaging*, 9(2):218–225.
- Chew, W. C. (1995). *Waves and Fields in Inhomogeneous Media*. IEEE Press.
- Chew, W. C., Wang, Y. M., Otto, G., Lesselier, D., and Bolomey, J. C. (1994). On the inverse source method of solving inverse scattering problems. *Inverse Problems*, 10(3):547–553.

- Chiu, C. C. and Liu, P. (1996). Image reconstruction of a perfectly conducting cylinder by the genetic algorithm. *IEE Proceedings - Microwaves, Antennas and Propagation*, 143:249–253(4).
- Colgan, T. J., Hagness, S. C., and Van Veen, B. D. (2015). A 3-d level set method for microwave breast imaging. *IEEE Transactions on Biomedical Engineering*, 62(10):2526–2534.
- Colton, D. and Kirsch, A. (1996). A simple method for solving inverse scattering problems in the resonance region. *Inverse problems*, 12(4):383.
- Colton, D. and Kress, R. (2019). *Inverse Acoustic and Electromagnetic Scattering Theory*. Number 93 in Applied Mathematical Science. Springer, 4 edition.
- Colton, D. and Päivärinta, L. (1992). The uniqueness of a solution to an inverse scattering problem for electromagnetic waves. *Archive for rational mechanics and analysis*, 119(1):59–70.
- Crocco, L., Catapano, I., Di Donato, L., and Isernia, T. (2012). The linear sampling method as a way to quantitative inverse scattering. *IEEE Transactions on Antennas and Propagation*, 60(4):1844–1853.
- Dachena, C., Fedeli, A., Fanti, A., Lodi, M. B., Pastorino, M., and Randazzo, A. (2021). A microwave imaging technique for neck diseases monitoring. In *2021 15th European Conference on Antennas and Propagation (EuCAP)*, pages 1–5.
- Deb, K., Pratap, A., Agarwal, S., and Meyarivan, T. (2002). A fast and elitist multiobjective genetic algorithm: Nsga-ii. *IEEE transactions on evolutionary computation*, 6(2):182–197.
- Deputat, V., Oja, P., and Saveljeva, D. (2005). Quadratic spline subdomain method for volterra integral equations. *Mathematical Modelling and Analysis*, 10(4):335–344.
- Di Donato, L., Bevacqua, M. T., Crocco, L., and Isernia, T. (2015). Inverse scattering via virtual experiments and contrast source regularization. *IEEE Transactions on Antennas and Propagation*, 63(4):1669–1677.
- Di Donato, L., Palmeri, R., Sorbello, G., Isernia, T., and Crocco, L. (2016). A new linear distorted-wave inversion method for microwave imaging via virtual experiments. *IEEE Transactions on Microwave Theory and Techniques*, 64(8):2478–2488.
- Donelli, M., Franceschini, D., Rocca, P., and Massa, A. (2009). Three-dimensional microwave imaging problems solved through an efficient multiscaling particle swarm optimization. *IEEE Transactions on Geoscience and Remote Sensing*, 47(5):1467–1481.
- Donelli, M., Franceschini, G., Martini, A., and Massa, A. (2006). An integrated multiscaling strategy based on a particle swarm algorithm for inverse scattering problems. *IEEE Transactions on Geoscience and Remote Sensing*, 44(2):298–312.

- Donelli, M. and Massa, A. (2005). Computational approach based on a particle swarm optimizer for microwave imaging of two-dimensional dielectric scatterers. *IEEE Transactions on Microwave Theory and Techniques*, 53(5):1761–1776.
- Donelli, M., Massa, A., Oliveri, G., Pastorino, M., and Randazzo, A. (2010). A differential evolution-based iterative multi-scaling algorithm for microwave imaging of dielectric structures. In *2010 IEEE International Conference on Imaging Systems and Techniques*, pages 90–95.
- Donoho, D. (2006). Compressed sensing. *IEEE Transactions on Information Theory*, 52(4):1289–1306.
- Dorn, O. and Lesselier, D. (2006). Level set methods for inverse scattering. *Inverse Problems*, 22(4):R67–R131.
- D’Urso, M., Isernia, T., and Morabito, A. F. (2010). On the solution of 2-d inverse scattering problems via source-type integral equations. *IEEE Transactions on Geoscience and Remote Sensing*, 48(3):1186–1198.
- Eiben, A. E. and Smith, J. E. (2015). *Introduction to Evolutionary Computing*. Natural Computing Series. Springer Berlin Heidelberg, Berlin, Heidelberg, 2 edition.
- El-Shenawee, M., Dorn, O., and Moscoso, M. (2009). An adjoint-field technique for shape reconstruction of 3-d penetrable object immersed in lossy medium. *IEEE Transactions on Antennas and Propagation*, 57(2):520–534.
- Elad, M. (2010). *Sparse and Redundant Representations: From Theory to Applications in Signal and Image Processing*. Springer-Verlag New York, first edition.
- Emmerich, M., Giannakoglou, K., and Naujoks, B. (2006). Single- and multiobjective evolutionary optimization assisted by gaussian random field metamodels. *IEEE Transactions on Evolutionary Computation*, 10(4):421–439.
- Engl, H. W. and Neubauer, A. (1988). Convergence rates for tikhonov regularization in finite-dimensional subspaces of hilbert scales. *Proceedings of the American Mathematical Society*, 102(3):587–592.
- Estatico, C., Fedeli, A., Pastorino, M., and Randazzo, A. (2014). A numerical analysis concerning microwave imaging in  $L^p$  banach spaces by using an inexact newton method. In *2014 IEEE International Conference on Imaging Systems and Techniques (IST) Proceedings*, pages 11–16.
- Estatico, C., Fedeli, A., Pastorino, M., and Randazzo, A. (2015a). A multifrequency inexact-newton method in  $L^p$  banach spaces for buried objects detection. *IEEE Transactions on Antennas and Propagation*, 63(9):4198–4204.

- Estatico, C., Fedeli, A., Pastorino, M., and Randazzo, A. (2017). Feasibility assessment of a banach-space inversion procedure for biomedical applications. In *2017 11th European Conference on Antennas and Propagation (EUCAP)*, pages 677–681.
- Estatico, C., Fedeli, A., Pastorino, M., and Randazzo, A. (2018a). Quantitative microwave imaging method in lebesgue spaces with nonconstant exponents. *IEEE Transactions on Antennas and Propagation*, 66(12):7282–7294.
- Estatico, C., Fedeli, A., Pastorino, M., Randazzo, A., and Tavanti, E. (2015b). A banach-space multifrequency imaging approach for electromagnetic subsurface sensing. In *2015 IEEE 15th Mediterranean Microwave Symposium (MMS)*, pages 1–4.
- Estatico, C., Fedeli, A., Pastorino, M., Randazzo, A., and Tavanti, E. (2018b). A newton-conjugate-gradient method in  $l^p$  banach spaces for three-dimensional microwave imaging. In *2018 IEEE International Conference on Imaging Systems and Techniques (IST)*, pages 1–5.
- Estatico, C., Fedeli, A., Pastorino, M., Randazzo, A., and Tavanti, E. (2020). A phaseless microwave imaging approach based on a lebesgue-space inversion algorithm. *IEEE Transactions on Antennas and Propagation*, 68(12):8091–8103.
- Estatico, C., Pastorino, M., and Randazzo, A. (2012a). A banach-space regularization approach for microwave imaging. In *2012 6th European Conference on Antennas and Propagation (EUCAP)*, pages 1382–1386.
- Estatico, C., Pastorino, M., and Randazzo, A. (2012b). A novel microwave imaging approach based on regularization in  $l^p$  banach spaces. *IEEE Transactions on Antennas and Propagation*, 60(7):3373–3381.
- Estatico, C., Pastorino, M., and Randazzo, A. (2013). Buried object detection by means of a  $l^p$  banach-space inversion procedure. In *2013 International Symposium on Electromagnetic Theory*, pages 131–134.
- Estatico, C., Pastorino, M., Randazzo, A., and Tavanti, E. (2016). A three-dimensional microwave imaging approach based on a  $l^p$  banach space inversion procedure. In *2016 URSI International Symposium on Electromagnetic Theory (EMTS)*, pages 148–151.
- Estatico, C., Pastorino, M., Randazzo, A., and Tavanti, E. (2018c). Three-dimensional microwave imaging in  $l^p$  banach spaces: Numerical and experimental results. *IEEE Transactions on Computational Imaging*, 4(4):609–623.
- Etminan, A. and Moghaddam, M. (2018). Electromagnetic imaging of dielectric objects using a multidirectional-search-based simulated annealing. *IEEE Journal on Multiscale and Multiphysics Computational Techniques*, 3:167–175.
- Fajardo, J. E., Galván, J., Vericat, F., Carlevaro, C. M., and Irastorza, R. M. (2019). Phaseless

- microwave imaging of dielectric cylinders: An artificial neural networks-based approach. *Progress In Electromagnetics Research*, 166:95–105.
- Fedeli, A., Pastorino, M., and Randazzo, A. (2015a). Quantitative microwave imaging in  $l^p$  banach spaces: A numerical assessment. In *2015 IEEE International Instrumentation and Measurement Technology Conference (I2MTC) Proceedings*, pages 2055–2060.
- Fedeli, A., Pastorino, M., and Randazzo, A. (2017a). Electromagnetic biomedical imaging in banach spaces: A numerical case study. In *2017 XXXIIInd General Assembly and Scientific Symposium of the International Union of Radio Science (URSI GASS)*, pages 1–3.
- Fedeli, A., Pastorino, M., Randazzo, A., and Estatico, C. (2015b). A multifrequency banach-space inversion method for ground penetrating radar imaging. In *2015 European Radar Conference (EuRAD)*, pages 225–228.
- Fedeli, A., Pastorino, M., Randazzo, A., and Todella, S. (2017b). Preliminary assessment of an  $l^p$  banach-space inversion approach for through-the-wall imaging. In *2017 IEEE Conference on Antenna Measurements Applications (CAMA)*, pages 167–169.
- Fedeli, A., Schenone, V., Estatico, C., Pastorino, M., and Randazzo, A. (2021). Nonlinear inverse-scattering in variable-exponent spaces for multifrequency subsurface imaging. In *2021 15th European Conference on Antennas and Propagation (EuCAP)*, pages 1–5.
- Fletcher, C. A. J. (1984). *Computational Galerkin Methods*. Scientific Computation. Springer, Verlag Berlin Heidelberg, 1 edition.
- Fogel, D. B. (1998). *Evolutionary Computation: The Fossil Record*. Wiley-IEEE Press, Piscataway, NJ.
- Fogel, L. J., Owens, A. J., and Walsh, M. J. (1966). Artificial intelligence through simulated evolution.
- Fouda, A. E. and Teixeira, F. L. (2014a). Bayesian compressive sensing for ultrawideband inverse scattering in random media. *Inverse Problems*, 30(11):114017.
- Fouda, A. E. and Teixeira, F. L. (2014b). Ultra-wideband microwave imaging of breast cancer tumors via bayesian inverse scattering. *Journal of Applied Physics*, 115(6):064701.
- Franchois, A. and Pichot, C. (1997). Microwave imaging-complex permittivity reconstruction with a levenberg-marquardt method. *IEEE Transactions on Antennas and Propagation*, 45(2):203–215.
- Gabbasov, N. and Zamaliev, R. (2014). A special variant of the subdomain method for integral equations of the third kind with singularities in the kernel. *Russian Mathematics*, 58:15–21.
- Garnero, L., Franchois, A., Hugonin, J.-P., Pichot, C., and Joachimowicz, N. (1991). Microwave

- imaging-complex permittivity reconstruction-by simulated annealing. *IEEE Transactions on Microwave Theory and Techniques*, 39(11):1801–1807.
- Gaspar-Cunha, A., Takahashi, R., and Antunes, C. H. (2013). *Manual de computação evolutiva e metaheurística*. Editora UFMG, 1 edition.
- Geffrin, J.-M., Sabouroux, P., and Eyraud, C. (2005). Free space experimental scattering database continuation: experimental set-up and measurement precision. *Inverse Problems*, 21(6):S117–S130.
- Gerth, D. (2021). A new interpretation of (tikhonov) regularization. *Inverse Problems*, 37(6):064002.
- Gilmore, C., Mojabi, P., and LoVetri, J. (2009). Comparison of an enhanced distorted born iterative method and the multiplicative-regularized contrast source inversion method. *IEEE Transactions on Antennas and Propagation*, 57(8):2341–2351.
- Golub, G. H., Heath, M., and Wahba, G. (1979). Generalized cross-validation as a method for choosing a good ridge parameter. *Technometrics*, 21(2):215–223.
- Guo, L., Song, G., and Wu, H. (2021). Complex-valued pix2pix—deep neural network for nonlinear electromagnetic inverse scattering. *Electronics*, 10(6).
- Guo, R., Shan, T., Song, X., Li, M., Yang, F., Xu, S., and Abubakar, A. (2022). Physics embedded deep neural network for solving volume integral equation: 2-d case. *IEEE Transactions on Antennas and Propagation*, 70(8):6135–6147.
- Guo, R., Song, X., Li, M., Yang, F., Xu, S., and Abubakar, A. (2019). Supervised descent learning technique for 2-d microwave imaging. *IEEE Transactions on Antennas and Propagation*, 67(5):3550–3554.
- Hadamard, J. (1923). *Lectures on Cauchy's Problem in Linear Partial Differential Equations*. Yale University Press, New Haven.
- Hajebi, M. and Hoofifar, A. (2022). Multiple buried target reconstruction using a multiscale hybrid of diffraction tomography and cma-es optimization. *IEEE Transactions on Geoscience and Remote Sensing*, 60:1–13.
- Han, F., Zhong, M., and Fei, J. (2022). Hybrid microwave imaging of 3-d objects using lsm and bim aided by a cnn u-net. *IEEE Transactions on Geoscience and Remote Sensing*, 60:1–9.
- Hansen, P. C. and O'Leary, D. P. (1993). The use of the l-curve in the regularization of discrete ill-posed problems. *SIAM Journal on Scientific Computing*, 14(6):1487–1503.
- Harrington (2001). *Time-Harmonic Electromagnetic*. John Wiley & Sons.

- He, C., Zhang, Y., Gong, D., and Ji, X. (2023). A review of surrogate-assisted evolutionary algorithms for expensive optimization problems. *Expert Systems with Applications*, 217:119495.
- Holland, J. H. (1973). Genetic algorithms and the optimal allocation of trials. *SIAM Journal on Computing*, 2(2):88–105.
- Hu, Y., Jin, Y., Wu, X., and Chen, J. (2022). A theory-guided deep neural network for time domain electromagnetic simulation and inversion using a differentiable programming platform. *IEEE Transactions on Antennas and Propagation*, 70(1):767–772.
- Huang, C.-H., Chiu, C.-C., Li, C.-L., and Chen, K.-C. (2008). Time domain inverse scattering of a two-dimensional homogenous dielectric object with arbitrary shape by particle swarm optimization. *Progress In Electromagnetics Research*, 82:381–400.
- Huang, T. and Sanagavarapu Mohan, A. (2007). A microparticle swarm optimizer for the reconstruction of microwave images. *IEEE Transactions on Antennas and Propagation*, 55(3):568–576.
- Hunter, J. D. (2007). Matplotlib: A 2d graphics environment. *Computing in Science & Engineering*, 9(3):90–95.
- Hursán, G. and Zhdanov, M. S. (2002). Contraction integral equation method in three-dimensional electromagnetic modeling. *Radio Science*, 37(6):1–13.
- Iman, R. L., Helton, J. C., and Campbell, J. E. (1981). An approach to sensitivity analysis of computer models: Part i—introduction, input variable selection and preliminary variable assessment. *Journal of Quality Technology*, 13(3):174–183.
- Isakov, V., Lai, R.-Y., and Wang, J.-N. (2016). Increasing stability for the conductivity and attenuation coefficients. *SIAM Journal on Mathematical Analysis*, 48(1):569–594.
- Isernia, T., Crocco, L., and D’Urso, M. (2004). New tools and series for forward and inverse scattering problems in lossy media. *IEEE Geoscience and Remote Sensing Letters*, 1(4):327–331.
- Ji, S., Dunson, D., and Carin, L. (2009). Multitask compressive sensing. *IEEE Transactions on Signal Processing*, 57(1):92–106.
- Ji, S., Xue, Y., and Carin, L. (2008). Bayesian compressive sensing. *IEEE Transactions on Signal Processing*, 56(6):2346–2356.
- Jin, Y. (2005). A comprehensive survey of fitness approximation in evolutionary computation. *Soft computing*, 9(1):3–12.
- Joachimowicz, N., Pichot, C., and Hugonin, J. (1991). Inverse scattering: an iterative numerical method for electromagnetic imaging. *IEEE Transactions on Antennas and Propagation*, 39(12):1742–1753.

- Jones, D. R., Schonlau, M., and Welch, W. J. (1998). Efficient global optimization of expensive black-box functions. *Journal of Global optimization*, 13(4):455.
- Keller, J. B. (1976). Inverse problems. *The American Mathematical Monthly*, 83(2):107–118.
- Kellogg, O. D. (1953). *Foundations of potential theory*, volume 31. Courier Corporation.
- Kent, S. and Günel, T. (1997). Dielectric permittivity estimation of cylindrical objects using genetic algorithm. *Journal of Microwave Power and Electromagnetic Energy*, 32(2):109–113.
- Khoshdel, V., Asefi, M., Ashraf, A., and LoVetri, J. (2021). A multi-branch deep convolutional fusion architecture for 3d microwave inverse scattering: Stored grain application. *Neural Computing and Applications*, 33:13467–13479.
- Khoshdel, V., Ashraf, A., and LoVetri, J. (2019). Enhancement of multimodal microwave-ultrasound breast imaging using a deep-learning technique. *Sensors*, 19(18):4050.
- Kirsch, A. (2002). The MUSIC-algorithm and the factorization method in inverse scattering theory for inhomogeneous media. *Inverse Problems*, 18(4):1025–1040.
- Kirsch, A. (2011). *An Introduction to the Mathematical Theory of Inverse Problems*. Number 120 in Applied Mathematical Science. Springer, Verlag, NY, 2 edition.
- Kleinman, R. and den Berg, P. (1992). A modified gradient method for two-dimensional problems in tomography. *Journal of Computational and Applied Mathematics*, 42(1):17–35.
- Kleinman, R. E. and van den Berg, P. M. (1993). An extended range-modified gradient technique for profile inversion. *Radio Science*, 28(5):877–884.
- Kleinman, R. E. and van den Berg, P. M. (1994). Two-dimensional location and shape reconstruction. *Radio Science*, 29(4):1157–1169.
- Koziel, S. and Leifsson, L. (2008). *Engineering Design via Surrogate Modelling*. John Wiley & Sons, Ltd.
- Kurrant, D., Abdollahi, N., Omer, M., Mojabi, P., Fear, E., and LoVetri, J. (2021a). Mwsegerval—an image analysis toolbox for microwave breast images. *SoftwareX*, 15:100728.
- Kurrant, D., Omer, M., Abdollahi, N., Mojabi, P., Fear, E., and LoVetri, J. (2021b). Evaluating performance of microwave image reconstruction algorithms: Extracting tissue types with segmentation using machine learning. *Journal of Imaging*, 7(1).
- Lanczos, C. (1961). *Linear Differential Operators*. Society for Industrial and Applied Mathematics, Van Nostrand, NY.
- Lavarello, R. and Oelze, M. (2008). A study on the reconstruction of moderate contrast targets

using the distorted born iterative method. *IEEE Transactions on Ultrasonics, Ferroelectrics, and Frequency Control*, 55(1):112–124.

- Lazebnik, M., Popovic, D., McCartney, L., Watkins, C. B., Lindstrom, M. J., Harter, J., Sewall, S., Ogilvie, T., Magliocco, A., Breslin, T. M., et al. (2007). A large-scale study of the ultrawideband microwave dielectric properties of normal, benign and malignant breast tissues obtained from cancer surgeries. *Physics in medicine & biology*, 52(20):6093.
- Lebedev, L. P., Vorovich, I. I., and Gladwell, G. (1996). *Functional Analysis - Applications in Mechanics and Inverse Problems*. Number 41 in Solid Mechanics and Its Applications. Springer, Netherlands, 1 edition.
- LeCun, Y., Bengio, Y., and Hinton, G. (2015). Deep learning. *Nature*, 521(7553):436–444.
- Li, C., Xu, C., Gui, C., and Fox, M. D. (2010). Distance regularized level set evolution and its application to image segmentation. *IEEE Transactions on Image Processing*, 19(12):3243–3254.
- Li, F., Liu, H., and Song, L.-P. (2004). Three-dimensional reconstruction of objects buried in layered media using born and distorted born iterative methods. *IEEE Geoscience and Remote Sensing Letters*, 1(2):107–111.
- Li, J., Hu, H.-J., Wang, J., Zhuang, M., Xiao, L.-Y., and Liu, Q. H. (2023). A transceiver-configuration-independent 2-d electromagnetic full-wave inversion scheme based on end-to-end artificial neural networks. *IEEE Transactions on Antennas and Propagation*, pages 1–1.
- Li, L., Wang, L. G., and Teixeira, F. L. (2019a). Performance analysis and dynamic evolution of deep convolutional neural network for electromagnetic inverse scattering. *IEEE Antennas and Wireless Propagation Letters*, 18(11):2259–2263.
- Li, L., Wang, L. G., Teixeira, F. L., Liu, C., Nehorai, A., and Cui, T. J. (2019b). Deepnis: Deep neural network for nonlinear electromagnetic inverse scattering. *IEEE Transactions on Antennas and Propagation*, 67(3):1819–1825.
- Li, M., Guo, R., Zhang, K., Lin, Z., Yang, F., Xu, S., Chen, X., Massa, A., and Abubakar, A. (2021). Machine learning in electromagnetics with applications to biomedical imaging: A review. *IEEE Antennas and Propagation Magazine*, 63(3):39–51.
- Lin, Z., Guo, R., Li, M., Yang, F., Xu, S., and Abubakar, A. (2021). Study on the degrees of freedom of scattered fields in nonlinear inverse scattering problems. In *2021 IEEE International Symposium on Antennas and Propagation and USNC-URSI Radio Science Meeting (APS/URSI)*, pages 1845–1846.
- Lippmann, B. A. and Schwinger, J. (1950). Variational principles for scattering processes. i. *Phys. Rev.*, 79:469–480.

- Liu, B., Zhang, Q., and Gielen, G. G. E. (2014). A gaussian process surrogate model assisted evolutionary algorithm for medium scale expensive optimization problems. *IEEE Transactions on Evolutionary Computation*, 18(2):180–192.
- Liu, G.-R. (2009). *Meshfree Methods: Moving Beyond the Finite Element Method*. CRC Press, Boca Raton, US, 2 edition.
- Liu, J., Zhou, H., Ouyang, T., Liu, Q., and Wang, Y. (2022a). Physical model-inspired deep unrolling network for solving nonlinear inverse scattering problems. *IEEE Transactions on Antennas and Propagation*, 70(2):1236–1249.
- Liu, Y., Soldovieri, F., and Erricolo, D. (2020). A combination of deterministic regularizations and genetic algorithms in two-dimentional inverse scattering problems. In *2020 43rd International Conference on Telecommunications and Signal Processing (TSP)*, pages 466–469.
- Liu, Y., Zhao, H., Song, R., Chen, X., Li, C., and Chen, X. (2022b). Som-net: Unrolling the subspace-based optimization for solving full-wave inverse scattering problems. *IEEE Transactions on Geoscience and Remote Sensing*, 60:1–15.
- Liu, Z. and Nie, Z. (2019). Subspace-based variational born iterative method for solving inverse scattering problems. *IEEE Geoscience and Remote Sensing Letters*, 16(7):1017–1020.
- Lobel, P., Blanc-Féraud, L., Pichot, C., and Barlaud, M. (1997). A new regularization scheme for inverse scattering. *Inverse Problems*, 13(2):403.
- Lobel, P., Kleinman, R., Pichot, C., Blanc-Feraud, L., and Barlaud, M. (1996). Conjugate-gradient method for soliving inverse scattering with experimental data. *IEEE Antennas and Propagation Magazine*, 38(3):48–.
- Lorensen, W. E. and Cline, H. E. (1987). Marching cubes: A high resolution 3d surface construction algorithm. *SIGGRAPH Comput. Graph.*, 21(4):163–169.
- Low, T. and Chao, B. (1992). The use of finite elements and neural networks for the solution of inverse electromagnetic problems. *IEEE Transactions on Magnetics*, 28(5):2811–2813.
- Luo, F., Wang, J., Zeng, J., Zhang, L., Zhang, B., Xu, K., and Luo, X. (2022). Cascaded complex u-net model to solve inverse scattering problems with phaseless-data in the complex domain. *IEEE Transactions on Antennas and Propagation*, 70(8):6160–6170.
- Ma, Z., Xu, K., Song, R., Wang, C.-F., and Chen, X. (2021). Learning-based fast electromagnetic scattering solver through generative adversarial network. *IEEE Transactions on Antennas and Propagation*, 69(4):2194–2208.
- MacKay, D. J. et al. (1998). Introduction to gaussian processes. *NATO ASI series F computer and systems sciences*, 168:133–166.

- Massa, A., Franceschini, D., Franceschini, G., Pastorino, M., Raffetto, M., and Donelli, M. (2005). Parallel ga-based approach for microwave imaging applications. *IEEE Transactions on Antennas and Propagation*, 53(10):3118–3127.
- Massa, A., Oliveri, G., Salucci, M., Anselmi, N., and Rocca, P. (2018). Learning-by-examples techniques as applied to electromagnetics. *Journal of Electromagnetic Waves and Applications*, 32(4):516–541.
- Massa, A., Rocca, P., and Oliveri, G. (2015). Compressive sensing in electromagnetics - a review. *IEEE Antennas and Propagation Magazine*, 57(1):224–238.
- Maxwell, J. C. (1865). Viii. a dynamical theory of the electromagnetic field. *Philosophical transactions of the Royal Society of London*, (155):459–512.
- Mendes, M. H. S., Soares, G. L., Coulomb, J.-L., and Vasconcelos, J. a. A. (2013). A surrogate genetic programming based model to facilitate robust multi-objective optimization: A case study in magnetostatics. *IEEE Transactions on Magnetics*, 49(5):2065–2068.
- Michalski, K. A. (2000). Electromagnetic imaging of circular–cylindrical conductors and tunnels using a differential evolution algorithm. *Microwave and Optical Technology Letters*, 27(5):330–334.
- Michalski, K. A. (2001). Electromagnetic imaging of elliptical–cylindrical conductors and tunnels using a differential evolution algorithm. *Microwave and Optical Technology Letters*, 28(3):164–169.
- Milgram, S., Bickman, L., and Berkowitz, L. (1969). Note on the drawing power of crowds of different size. *Journal of personality and social psychology*, 13(2):79.
- Miller, E. and Willsky, A. (1996a). A multiscale, statistically based inversion scheme for linearized inverse scattering problems. *IEEE Transactions on Geoscience and Remote Sensing*, 34(2):346–357.
- Miller, E. L. and Willsky, A. S. (1996b). Wavelet-based methods for the nonlinear inverse scattering problem using the extended born approximation. *Radio Science*, 31(1):51–65.
- Modiri, A. and Kiasaleh, K. (2012). A novel discrete particle swarm optimization algorithm for estimating dielectric constants of tissue. In *2012 Annual International Conference of the IEEE Engineering in Medicine and Biology Society*, pages 5490–5493. IEEE.
- Moghaddam, M. and Chew, W. (1992). Nonlinear two-dimensional velocity profile inversion using time domain data. *IEEE Transactions on Geoscience and Remote Sensing*, 30(1):147–156.
- Moghaddam, M. and Chew, W. (1993). Study of some practical issues in inversion with the born

- iterative method using time-domain data. *IEEE Transactions on Antennas and Propagation*, 41(2):177–184.
- Moghaddam, M., Chew, W. C., and Oristaglio, M. (1991). Comparison of the born iterative method and tarantola's method for an electromagnetic time-domain inverse problem. *International Journal of Imaging Systems and Technology*, 3(4):318–333.
- Montgomery, D. C. and Runger, G. C. (2010). *Applied Statistics and Probability for Engineers*. John Wiley & Sons.
- Morozov, V. (1984). *Methods for Solving Incorrectly Posed Problems*. Springer-Verlag New York, 1 edition.
- Nagayasu, S., Uhlmann, G., and Wang, J.-N. (2013). Increasing stability in an inverse problem for the acoustic equation. *Inverse Problems*, 29(2):025012.
- Ney, M. M., Smith, A. M., and Stuchly, S. S. (1984). A solution of electromagnetic imaging using pseudoinverse transformation. *IEEE Transactions on Medical Imaging*, 3(4):155–162.
- Noghanian, S., Sabouni, A., Desell, T., and Ashtari, A. (2014). *Microwave Tomography - Global Optimization, Parallelization and Performance Evaluation*. Microwaves, RF and Optical Engineering. Springer-Verlag New York, first edition.
- Oliveri, G., Lizzi, L., Pastorino, M., and Massa, A. (2012). A nested multi-scaling inexact-newton iterative approach for microwave imaging. *IEEE Transactions on Antennas and Propagation*, 60(2):971–983.
- Oliveri, G., Poli, L., Anselmi, N., Salucci, M., and Massa, A. (2019). Compressive sensing-based born iterative method for tomographic imaging. *IEEE Transactions on Microwave Theory and Techniques*, 67(5):1753–1765.
- Oliveri, G., Salucci, M., Anselmi, N., and Massa, A. (2017). Compressive sensing as applied to inverse problems for imaging: Theory, applications, current trends, and open challenges. *IEEE Antennas and Propagation Magazine*, 59(5):34–46.
- Oliveri, G., Zhong, Y., Chen, X., and Massa, A. (2011). Multiresolution subspace-based optimization method for inverse scattering problems. *J. Opt. Soc. Am. A*, 28(10):2057–2069.
- Osher, S. and Fedkiw, R. (2003). *Level Set Methods and Dynamic Implicit Surfaces*. Applied Mathematical Sciences. Springer, New York, US, 1 edition.
- Palmeri, R., Bevacqua, M. T., Crocco, L., Isernia, T., and Di Donato, L. (2017). Microwave imaging via distorted iterated virtual experiments. *IEEE Transactions on Antennas and Propagation*, 65(2):829–838.
- Pan, L., Chen, X., Zhong, Y., and Yeo, S. P. (2010). Comparison among the variants of

- subspace-based optimization method for addressing inverse scattering problems: transverse electric case. *JOSA A*, 27(10):2208–2215.
- Pan, X.-M., Song, B.-Y., Wu, D., Wei, G., and Sheng, X.-Q. (2021). On phase information for deep neural networks to solve full-wave nonlinear inverse scattering problems. *IEEE Antennas and Wireless Propagation Letters*, 20(10):1903–1907.
- Pankratov, O. V., Avdeyev, D. B., and Kuvshinov, A. V. (1995). Electromagnetic field scattering in a heterogeneous earth: A solution to the forward problem, phys. *Solid Earth*.
- Pastorino, M. (2007). Stochastic optimization methods applied to microwave imaging: A review. *IEEE Transactions on Antennas and Propagation*, 55(3):538–548.
- Pastorino, M. (2010a). *Microwave Imaging*. WILEY.
- Pastorino, M. (2010b). *Quantitative Stochastic Reconstruction Methods*, chapter Seven, pages 153–192. John Wiley & Sons, Ltd.
- Pastorino, M., Caorsi, S., Massa, A., and Randazzo, A. (2004). Reconstruction algorithms for electromagnetic imaging. *IEEE Transactions on Instrumentation and Measurement*, 53(3):692–699.
- Pastorino, M., Massa, A., and Caorsi, S. (2000). A microwave inverse scattering technique for image reconstruction based on a genetic algorithm. *IEEE Transactions on Instrumentation and Measurement*, 49(3):573–578.
- Polyanin, A. D. and Manzhirov, A. V. (2008). *Handbook of integral equations*. CRC press.
- Potthast, R. (2006). A survey on sampling and probe methods for inverse problems. *Inverse Problems*, 22(2):R1.
- Potthast, R. (2010). A study on orthogonality sampling. *Inverse Problems*, 26(7):074015.
- Qin, Y., Ran, P., Rodet, T., and Lesselier, D. (2022). Breast imaging by convolutional neural networks from joint microwave and ultrasonic data. *IEEE Transactions on Antennas and Propagation*, 70(8):6265–6276.
- Qing, A. (2003). Electromagnetic inverse scattering of multiple perfectly conducting cylinders by differential evolution strategy with individuals in groups (geds) [geds read gdes]. In *IEEE Antennas and Propagation Society International Symposium. Digest. Held in conjunction with: USNC/CNC/URSI North American Radio Sci. Meeting (Cat. No.03CH37450)*, volume 1, pages 519–522 vol.1.
- Qing, A. (2006). Dynamic differential evolution strategy and applications in electromagnetic inverse scattering problems. *IEEE Transactions on Geoscience and Remote Sensing*, 44(1):116–125.

- Qing, A., Lee, C. K., and Jen, L. (2001). Electromagnetic inverse scattering of two-dimensional perfectly conducting objects by real-coded genetic algorithm. *IEEE Transactions on Geoscience and Remote Sensing*, 39(3):665–676.
- Ran, P., Qin, Y., and Lesselier, D. (2019). Electromagnetic imaging of a dielectric microstructure via convolutional neural networks. In *2019 27th European Signal Processing Conference (EUSIPCO)*, pages 1–5.
- Randazzo, A., Estatico, C., Fedeli, A., Rosatti, P., Salucci, M., Zardi, F., and Pastorino, M. (2021a). Assessment of an  $l_p$ -space multi-focusing inversion method for subsoil mapping with multi-frequency data. *Microwave and Optical Technology Letters*, n/a(n/a).
- Randazzo, A., Tavanti, E., Mikulenas, M., Boero, F., Fedeli, A., Sansalone, A., Allasia, G., and Pastorino, M. (2021b). An electrical impedance tomography system for brain stroke imaging based on a lebesgue-space inversion procedure. *IEEE Journal of Electromagnetics, RF and Microwaves in Medicine and Biology*, 5(1):54–61.
- Rao, S. S. (2019). *Engineering Optimization Theory and Practice*. John Wiley & Sons, Ltd.
- Remis, R. F. and van den Berg, P. M. (2000). On the equivalence of the newton-kantorovich and distorted born methods. *Inverse Problems*, 16(1):L1–L4.
- Richmond, J. (1965). Scattering by a dielectric cylinder of arbitrary cross section shape. *IEEE Transactions on Antennas and Propagation*, 13(3):334–341.
- Rocca, P., Benedetti, M., Donelli, M., Franceschini, D., and Massa, A. (2009). Evolutionary optimization as applied to inverse scattering problems. *Inverse Problems*, 25(12):123003.
- Rocca, P., Oliveri, G., and Massa, A. (2011). Differential evolution as applied to electromagnetics. *IEEE Antennas and Propagation Magazine*, 53(1):38–49.
- Sacks, J., Welch, W. J., Mitchell, T. J., and Wynn, H. P. (1989). Design and Analysis of Computer Experiments. *Statistical Science*, 4(4):409 – 423.
- Salucci, M., Arrebolá, M., Shan, T., and Li, M. (2022a). Artificial intelligence: New frontiers in real-time inverse scattering and electromagnetic imaging. *IEEE Transactions on Antennas and Propagation*, 70(8):6349–6364.
- Salucci, M., Poli, L., Anselmi, N., and Massa, A. (2017). Multifrequency particle swarm optimization for enhanced multiresolution gpr microwave imaging. *IEEE Transactions on Geoscience and Remote Sensing*, 55(3):1305–1317.
- Salucci, M., Poli, L., Rocca, P., and Massa, A. (2022b). Learned global optimization for inverse scattering problems: Matching global search with computational efficiency. *IEEE Transactions on Antennas and Propagation*, 70(8):6240–6255.

- Sanghvi, Y., Kalepu, Y., and Khankhoje, U. K. (2020). Embedding deep learning in inverse scattering problems. *IEEE Transactions on Computational Imaging*, 6:46–56.
- Schonlau, M. (1997). *Computer Experiments and Global Optimization*. PhD thesis, University of Waterloo.
- Schöpfer, F., Louis, A. K., and Schuster, T. (2006). Nonlinear iterative methods for linear ill-posed problems in banach spaces. *Inverse Problems*, 22(1):311–329.
- Seabold, S. and Perktold, J. (2010). statsmodels: Econometric and statistical modeling with python. In *9th Python in Science Conference*.
- Seretis, A. and Sarris, C. D. (2022a). An overview of machine learning techniques for radiowave propagation modeling. *IEEE Transactions on Antennas and Propagation*, 70(6):3970–3985.
- Seretis, A. and Sarris, C. D. (2022b). Toward physics-based generalizable convolutional neural network models for indoor propagation. *IEEE Transactions on Antennas and Propagation*, 70(6):4112–4126.
- Shah, P., Chen, G., Stang, J., and Moghaddam, M. (2019). 3-d level set method for joint contrast and shape recovery in microwave imaging. *IEEE Transactions on Computational Imaging*, 5(1):97–108.
- Shah, P., Khankhoje, U. K., and Moghaddam, M. (2016). Inverse scattering using a joint  $l_1 - l_2$  norm-based regularization. *IEEE Transactions on Antennas and Propagation*, 64(4):1373–1384.
- Shah, P. and Moghaddam, M. (2015). Fast level set based method for high contrast microwave imaging. In *Proc. PIERS*, pages 253–257.
- Shah, P. and Moghaddam, M. (2018). A fast level set method for multimaterial recovery in microwave imaging. *IEEE Transactions on Antennas and Propagation*, 66(6):3017–3026.
- Shan, T., Lin, Z., Song, X., Li, M., Yang, F., and Xu, S. (2023). Neural born iterative method for solving inverse scattering problems: 2d cases. *IEEE Transactions on Antennas and Propagation*, 71(1):818–829.
- Shao, W. and Zhou, B. (2022). Dielectric breast phantoms by generative adversarial network. *IEEE Transactions on Antennas and Propagation*, 70(8):6256–6264.
- Shung-Wu Lee, Boersma, J., Chak-Lam Law, and Deschamps, G. (1980). Singularity in green's function and its numerical evaluation. *IEEE Transactions on Antennas and Propagation*, 28(3):311–317.
- Sobester, A., Forrester, A., and Keane, A. (2008). *Engineering design via surrogate modelling: a practical guide*. John Wiley & Sons.

- Song, R., Huang, Y., Xu, K., Ye, X., Li, C., and Chen, X. (2021). Electromagnetic inverse scattering with perceptual generative adversarial networks. *IEEE Transactions on Computational Imaging*, 7:689–699.
- Song, R., Huang, Y., Ye, X., Xu, K., Li, C., and Chen, X. (2022). Learning-based inversion method for solving electromagnetic inverse scattering with mixed boundary conditions. *IEEE Transactions on Antennas and Propagation*, 70(8):6218–6228.
- Stefanov, P. (1990). Stability of the inverse problem in potential scattering at fixed energy. In *Annales de l'institut Fourier*, volume 40, pages 867–884.
- Su, C.-C. (1987). Calculation of electromagnetic scattering from a dielectric cylinder using the conjugate gradient method and fft. *IEEE Transactions on Antennas and Propagation*, 35(12):1418–1425.
- Sun, C., Jin, Y., Cheng, R., Ding, J., and Zeng, J. (2017). Surrogate-assisted cooperative swarm optimization of high-dimensional expensive problems. *IEEE Transactions on Evolutionary Computation*, 21(4):644–660.
- Sun, Y., Xia, Z., and Kamilov, U. S. (2018). Efficient and accurate inversion of multiple scattering with deep learning. *Opt. Express*, 26(11):14678–14688.
- Taflove, A. and Hagness, S. C. (2005). *Computational Electrodynamics: the Finite-Difference Time-Domain Method*. Artech House.
- Tikhonov, A. N. (1963). Regularization of incorrectly posed problems. volume 4, pages 1624–1627. Soviet Mathematics Doklady.
- Vallat, R. (2018). Pingouin: statistics in python. *Journal of Open Source Software*, 3(31):1026.
- Van Bladel, J. (1961). Some remarks on green's dyadic for infinite space. *IRE Transactions on Antennas and Propagation*, 9(6):563–566.
- van den Berg, P. M., Abubakar, A., and Fokkema, J. T. (2003). Multiplicative regularization for contrast profile inversion. *Radio Science*, 38(2).
- van den Berg, P. M. and Kleinman, R. E. (1995). A total variation enhanced modified gradient algorithm for profile reconstruction. *Inverse Problems*, 11(3):L5–L10.
- van den Berg, P. M. and Kleinman, R. E. (1997). A contrast source inversion method. *Inverse Problems*, 13(6):1607–1620.
- van den Berg, P. M., van Broekhoven, A. L., and Abubakar, A. (1999). Extended contrast source inversion. *Inverse Problems*, 15(5):1325–1344.
- van der Walt, S., Schönberger, J. L., Nunez-Iglesias, J., Boulogne, F., Warner, J. D., Yager, N.,

- Gouillart, E., Yu, T., and the scikit-image contributors (2014). scikit-image: image processing in Python. *PeerJ*, 2:e453.
- Van Dyke, M. C. C., Teixeira, M. M., and Barker, B. M. (2019). Fantastic yeasts and where to find them: the hidden diversity of dimorphic fungal pathogens. *Current opinion in microbiology*, 52:55–63.
- VanRossum, G. and Drake, F. L. (2010). *The python language reference*. Python Software Foundation Amsterdam, Netherlands.
- Varah, J. M. (1983). Pitfalls in the numerical solution of linear ill-posed problems. *SIAM Journal on Scientific and Statistical Computing*, 4(2):164–176.
- Vargas, J. O. and Adriano, R. (2022). Subspace-based conjugate-gradient method for solving inverse scattering problems. *IEEE Transactions on Antennas and Propagation*, 70(12):12139–12146.
- Vargas, J. O., Batista, A. C., Batista, L. S., and Adriano, R. (2021). On the computational complexity of the conjugate-gradient method for solving inverse scattering problems. *Journal of Electromagnetic Waves and Applications*, 35(17):2323–2334.
- Vent, W. (1975). Rechenberg, ingo, evolutionsstrategie — optimierung technischer systeme nach prinzipien der biologischen evolution. *Feddes Repertorium*, 86(5):337–337.
- Virtanen, P., Gommers, R., Oliphant, T. E., Haberland, M., Reddy, T., Cournapeau, D., Burovski, E., Peterson, P., Weckesser, W., Bright, J., van der Walt, S. J., Brett, M., Wilson, J., Millman, K. J., Mayorov, N., Nelson, A. R. J., Jones, E., Kern, R., Larson, E., Carey, C. J., Polat, İ., Feng, Y., Moore, E. W., VanderPlas, J., Laxalde, D., Perktold, J., Cimrman, R., Henriksen, I., Quintero, E. A., Harris, C. R., Archibald, A. M., Ribeiro, A. H., Pedregosa, F., van Mulbregt, P., and SciPy 1.0 Contributors (2020). SciPy 1.0: Fundamental Algorithms for Scientific Computing in Python. *Nature Methods*, 17:261–272.
- Wang, Y. M. and Chew, W. C. (1989). An iterative solution of the two-dimensional electromagnetic inverse scattering problem. *International Journal of Imaging Systems and Technology*, 1(1):100–108.
- Wei, Z. (2022). Exploring multiple-incidence information in deep learning schemes for inverse scattering problems. *IEEE Transactions on Antennas and Propagation*, 70(11):10876–10884.
- Wei, Z. and Chen, X. (2019a). Deep-learning schemes for full-wave nonlinear inverse scattering problems. *IEEE Transactions on Geoscience and Remote Sensing*, 57(4):1849–1860.
- Wei, Z. and Chen, X. (2019b). Physics-inspired convolutional neural network for solving full-wave inverse scattering problems. *IEEE Transactions on Antennas and Propagation*, 67(9):6138–6148.

- Wirgin, A. (2004). The inverse crime. *arXiv preprint math-ph/0401050*.
- Woten, D. A., Hajishemmi, M. R., Hassan, A. M., and El-Shenawee, M. (2010). Experimental microwave validation of level set reconstruction algorithm. *IEEE Transactions on Antennas and Propagation*, 58(1):230–233.
- Wu, X., Peng, X., Chen, W., and Zhang, W. (2019). A developed surrogate-based optimization framework combining hdmr-based modeling technique and tlbo algorithm for high-dimensional engineering problems. *Structural and Multidisciplinary Optimization*, 60:663–680.
- Xiao, J., Li, J., Chen, Y., Han, F., and Liu, Q. H. (2020). Fast electromagnetic inversion of inhomogeneous scatterers embedded in layered media by born approximation and 3-d u-net. *IEEE Geoscience and Remote Sensing Letters*, 17(10):1677–1681.
- Xiao, L.-Y., Hong, R., Zhao, L.-Y., Hu, H.-J., and Liu, Q. H. (2022). A hybrid neural network electromagnetic inversion scheme (hnnemis) for super-resolution 3-d microwave human brain imaging. *IEEE Transactions on Antennas and Propagation*, 70(8):6277–6286.
- Xiong, K., Zhao, G., Shi, G., and Wang, Y. (2019). A convex optimization algorithm for compressed sensing in a complex domain: The complex-valued split bregman method. *Sensors*, 19(20):4540.
- Xu, K., Qian, Z., Zhong, Y., Su, J., Gao, H., and Li, W. (2022). Learning-assisted inversion for solving nonlinear inverse scattering problem. *IEEE Transactions on Microwave Theory and Techniques*, pages 1–12.
- Xu, K., Zhang, L., and Wei, Z. (2020). Fourier bases-expansion contraction integral equation for inversion highly nonlinear inverse scattering problem. *IEEE Transactions on Microwave Theory and Techniques*, 68(6):2206–2214.
- Xu, K., Zhong, Y., and Chen, X. (2018a). A fast algorithm for microwave biomedical imaging with inhomogeneous background. In *2018 IEEE International Microwave Biomedical Conference (IMBioC)*, pages 34–36.
- Xu, K., Zhong, Y., Chen, X., and Lesselier, D. (2018b). A fast integral equation-based method for solving electromagnetic inverse scattering problems with inhomogeneous background. *IEEE Transactions on Antennas and Propagation*, 66(8):4228–4239.
- Xu, K., Zhong, Y., and Wang, G. (2016). Multiplicative-regularized subspace technique to solve high contrast inverse scattering problems. In *2016 Progress in Electromagnetic Research Symposium (PIERS)*, pages 156–157.
- Xu, K., Zhong, Y., and Wang, G. (2018c). A hybrid regularization technique for solving highly

- nonlinear inverse scattering problems. *IEEE Transactions on Microwave Theory and Techniques*, 66(1):11–21.
- Yaghjian, A. D. (1980). Electric dyadic green's functions in the source region. *Proceedings of the IEEE*, 68(2):248–263.
- Yago Ruiz, A., Cavagnaro, M., and Crocco, L. (2022). A physics-assisted deep learning microwave imaging framework for real-time shape reconstruction of unknown targets. *IEEE Transactions on Antennas and Propagation*, 70(8):6184–6194.
- Yang, C., Zhang, J., and Tong, M. S. (2021a). An fft-accelerated particle swarm optimization method for solving far-field inverse scattering problems. *IEEE Transactions on Antennas and Propagation*, 69(2):1078–1093.
- Yang, C., Zhang, J., and Tong, M. S. (2021b). A hybrid inversion method based on the bat algorithm for microwave imaging of two-dimensional dielectric scatterers. *Progress In Electromagnetics Research M*, 102:91–104.
- Yang, C. X., Zhang, J., and Tong, M. S. (2021c). A hybrid quantum-behaved particle swarm optimization algorithm for solving inverse scattering problems. *IEEE Transactions on Antennas and Propagation*, pages 1–1.
- Yang, Z., Qiu, H., Gao, L., Jiang, C., and Zhang, J. (2019). Two-layer adaptive surrogate-assisted evolutionary algorithm for high-dimensional computationally expensive problems. *Journal of Global Optimization*, 74:327–359.
- Yao, H. M., Guo, R., Li, M., Jiang, L., and Ng, M. K. P. (2022). Enhanced supervised descent learning technique for electromagnetic inverse scattering problems by the deep convolutional neural networks. *IEEE Transactions on Antennas and Propagation*, 70(8):6195–6206.
- Yao, H. M., Jiang, L., and Ng, M. (2023). Implementing the fast full-wave electromagnetic forward solver using the deep convolutional encoder-decoder architecture. *IEEE Transactions on Antennas and Propagation*, 71(1):1152–1157.
- Yao, H. M., Sha, W. E. I., and Jiang, L. (2019). Two-step enhanced deep learning approach for electromagnetic inverse scattering problems. *IEEE Antennas and Wireless Propagation Letters*, 18(11):2254–2258.
- Yao, Y., Wang, Y., Pei, Y., Zhu, W., and Barbour, R. L. (1997). Frequency-domain optical imaging of absorption and scattering distributions by a born iterative method. *J. Opt. Soc. Am. A*, 14(1):325–342.
- Ye, X. and Chen, X. (2017). Subspace-based distorted-born iterative method for solving inverse scattering problems. *IEEE Transactions on Antennas and Propagation*, 65(12):7224–7232.
- Yee, K. (1966). Numerical solution of initial boundary value problems involving maxwell's

- equations in isotropic media. *IEEE Transactions on Antennas and Propagation*, 14(3):302–307.
- Yin, T., Wang, C.-F., Xu, K., Zhou, Y., Zhong, Y., and Chen, X. (2022). Electric flux density learning method for solving 3-d electromagnetic scattering problems. *IEEE Transactions on Antennas and Propagation*, 70(7):5144–5155.
- Yin, T., Wei, Z., and Chen, X. (2020). Non-iterative methods based on singular value decomposition for inverse scattering problems. *IEEE Transactions on Antennas and Propagation*, 68(6):4764–4773.
- Zaiping, N., Feng, Y., Yanwen, Z., and Yerong, Z. (2000). Variational born iteration method and its applications to hybrid inversion. *IEEE Transactions on Geoscience and Remote Sensing*, 38(4):1709–1715.
- Zaiping, N. and Yerong, Z. (1998). Hybrid born iterative method in low-frequency inverse scattering problem. *IEEE Transactions on Geoscience and Remote Sensing*, 36(3):749–753.
- Zakaria, A., Gilmore, C., and LoVetri, J. (2010). Finite-element contrast source inversion method for microwave imaging. *Inverse Problems*, 26(11):115010.
- Zhang, H. H., Yao, H. M., Jiang, L., and Ng, M. (2023a). Enhanced two-step deep-learning approach for electromagnetic-inverse-scattering problems: Frequency extrapolation and scatterer reconstruction. *IEEE Transactions on Antennas and Propagation*, 71(2):1662–1672.
- Zhang, H. H., Yao, H. M., Jiang, L., and Ng, M. (2023b). Solving electromagnetic inverse scattering problems in inhomogeneous media by deep convolutional encoder–decoder structure. *IEEE Transactions on Antennas and Propagation*, 71(3):2867–2872.
- Zhang, L., Ma, Z., Xu, K., and Zhong, Y. (2020a). Wavelet-based subspace regularization for solving highly nonlinear inverse scattering problems with contraction integral equation. *Electronics*, 9(11):1760.
- Zhang, L., Xu, K., Song, R., Ye, X., Wang, G., and Chen, X. (2020b). Learning-based quantitative microwave imaging with a hybrid input scheme. *IEEE Sensors Journal*, 20(24):15007–15013.
- Zhang, L., Xu, K., Zhong, Y., and Agarwal, K. (2020c). Solving phaseless highly nonlinear inverse scattering problems with contraction integral equation for inversion. *IEEE Transactions on Computational Imaging*, 6:1106–1116.
- Zhang, Y., Lambert, M., Fraysse, A., and Lesselier, D. (2023c). Unrolled convolutional neural network for full-wave inverse scattering. *IEEE Transactions on Antennas and Propagation*, 71(1):947–956.
- Zhang, Y., Yin, T., Zhao, Z., Nie, Z., and Chen, X. (2022). An iterative domain decomposition

- technique based on subspace-based optimization method for solving highly nonlinear inverse problem. *IEEE Transactions on Geoscience and Remote Sensing*, 60:1–13.
- Zhao, L., Choi, K. K., and Lee, I. (2011). Metamodeling method using dynamic kriging for design optimization. *AIAA Journal*, 49(9):2034–2046.
- Zhao, L.-Y., Xiao, L.-Y., Cheng, Y., Hong, R., and Liu, Q. H. (2022). Machine-learning-based inversion scheme for super-resolution three-dimensional microwave human brain imaging. *IEEE Antennas and Wireless Propagation Letters*, 21(12):2437–2441.
- Zhong, Y. (2010). *Subspace-based inversion methods for solving electromag-netic inverse scattering problems*. PhD thesis, National University of Singapore, Singapore.
- Zhong, Y. and Chen, X. (2009). Twofold subspace-based optimization method for solving inverse scattering problems. *Inverse Problems*, 25(8):085003.
- Zhong, Y. and Chen, X. (2011). An fft twofold subspace-based optimization method for solving electromagnetic inverse scattering problems. *IEEE Transactions on Antennas and Propagation*, 59(3):914–927.
- Zhong, Y., Chen, X., and Agarwal, K. (2010). An improved subspace-based optimization method and its implementation in solving three-dimensional inverse problems. *IEEE Transactions on Geoscience and Remote Sensing*, 48(10):3763–3768.
- Zhong, Y., Lambert, M., Lesselier, D., and Chen, X. (2016). A new integral equation method to solve highly nonlinear inverse scattering problems. *IEEE Transactions on Antennas and Propagation*, 64(5):1788–1799.
- Zhong, Y., Salucci, M., Xu, K., Polo, A., and Massa, A. (2020). A multiresolution contraction integral equation method for solving highly nonlinear inverse scattering problems. *IEEE Transactions on Microwave Theory and Techniques*, 68(4):1234–1247.
- Zhou, H., Cheng, Y., Zheng, H., Liu, Q., and Wang, Y. (2022). Deep unfolding contrast source inversion for strong scatterers via generative adversarial mechanism. *IEEE Transactions on Microwave Theory and Techniques*, 70(11):4966–4979.
- Zhou, Y., Leng, N., Wei, Z., Yin, T., Bai, M., and Chen, X. (2023). Physics-assisted learning scheme for quantitative imaging via near-field scanning microwave microscopy. *IEEE Transactions on Microwave Theory and Techniques*, pages 1–11.
- Zhou, Y., Zhong, Y., Wei, Z., Yin, T., and Chen, X. (2021). An improved deep learning scheme for solving 2-d and 3-d inverse scattering problems. *IEEE Transactions on Antennas and Propagation*, 69(5):2853–2863.
- Zhou, Z., Ong, Y. S., Nair, P. B., Keane, A. J., and Lum, K. Y. (2007). Combining global

- and local surrogate models to accelerate evolutionary optimization. *IEEE Transactions on Systems, Man, and Cybernetics, Part C (Applications and Reviews)*, 37(1):66–76.
- Zhu, C., Byrd, R. H., Lu, P., and Nocedal, J. (1997). Algorithm 778: L-bfgs-b: Fortran subroutines for large-scale bound-constrained optimization. *ACM Trans. Math. Softw.*, 23(4):550–560.
- Zong, Z., Wang, Y., and Wei, Z. (2022). A wavelet-based compressive deep learning scheme for inverse scattering problems. *IEEE Transactions on Geoscience and Remote Sensing*, 60:1–11.

## Apêndice A

### Como fazer citações

Você pode fazer uma citação de diversas formas. Se você quiser fazer uma citação entre parênteses, você pode fazer assim: (Milgram et al., 1969). Se você quiser mencionar o número da página, você pode fazer assim: (Deb et al., 2002, p. 10). Agora, se você quiser fazer uma citação onde o autor é parte da sentença, você pode fazer assim: Maxwell (1865) afirma que... Se você quiser fazer uma citação com mais de um autor, você pode fazer assim: (Van Dyke et al., 2019; ?).

# Apêndice B

## Dyadic Green's Function

The dyadic Green's function is an important tool for solving electromagnetic problems that include the radiation phenomenon. For this reason, this appendix aims to briefly discuss its definition and singularity. This text is based on chapter 7 of the book written by Chew (1995), which deepens the discussion and provides a better bibliographical reference on the topic.

### B.1 Dyadic Green's Function for Homogeneous Medium

A very general and essential problem for electromagnetic theory is that of radiation from a point source. This problem is fundamental for integral equations since the radiation of a current distribution is based on the contribution of all points at which the current is defined. That is, considering a generic scalar problem such as:

$$(\nabla^2 + k^2)\phi(\mathbf{r}) = s(\mathbf{r}) \quad (\text{B.1})$$

defined in a homogeneous region  $V$ , the solution can be obtained through:

$$\psi(\mathbf{r}) = - \int_V d\mathbf{r}' g(\mathbf{r}, \mathbf{r}') s(\mathbf{r}') \quad (\text{B.2})$$

where  $g(\mathbf{r}, \mathbf{r}')$  is the Green's function which is the solution to the equation:

$$(\nabla^2 + k^2)g(\mathbf{r}, \mathbf{r}') = -\delta(\mathbf{r} - \mathbf{r}') \quad (\text{B.3})$$

Particularly, this solution follows from the interpretation that  $s(\mathbf{r})$  is a linear superposition of point sources.

To obtain Green's function for a homogeneous and infinite medium, we will change the source position in the problem of eq.(B.3) to the origin of spherical coordinates:

$$(\nabla^2 + k^2)g(\mathbf{r}) = -\delta(\mathbf{r}) = -\delta(x)\delta(y)\delta(z) \quad (\text{B.4})$$

For  $\mathbf{r} \neq 0$ , the solution of (B.4) is given by:

$$g(\mathbf{r}) = C \frac{e^{jkr}}{r} + D \frac{e^{-jkr}}{r} \quad (\text{B.5})$$

where  $r = |\mathbf{r}|$ . Assuming that there are no sources at infinity, only the first term on the right-hand side of (B.5) is a solution:

$$g(\mathbf{r}) = C \frac{e^{jkr}}{r} \quad (\text{B.6})$$

The constant  $C$  is determined by calculating both sides of (B.4) in the singularity. To do this, we combine (B.6) into (B.4) and integrated into a small volume around the origin:

$$\int_{\Delta V} dV \nabla \cdot \nabla \frac{Ce^{jkr}}{r} + \int_{\Delta V} dV k^2 \frac{Ce^{jkr}}{r} = -1 \quad (\text{B.7})$$

The second integral of (B.7) tends to zero if  $\Delta V \rightarrow 0$ , since  $dV = 4\pi r^2 dr$ . Besides, Gauss' theorem can be used to transform the first integral into a surface one, and with that, we obtain:

$$\lim_{r \rightarrow 0} 4\pi r^2 \frac{d}{dr} C \frac{e^{jkr}}{r} = -1 \quad (\text{B.8})$$

or  $C = 1/4\pi$ . Also, the solution (B.6) can be generalized for the case in which the source is shifted to a point  $\mathbf{r}'$ . In this case, eq.(B.6) can be rewritten as:

$$g(\mathbf{r}, \mathbf{r}') = g(\mathbf{r} - \mathbf{r}') = \frac{e^{jk|\mathbf{r}-\mathbf{r}'|}}{4\pi|\mathbf{r}-\mathbf{r}'|} \quad (\text{B.9})$$

Solution (32) can be used to obtain Green's dyadic<sup>1</sup> function for the vector wave equation in a homogeneous and isotropic medium:

$$\nabla \times \nabla \times \mathbf{E}(\mathbf{r}) - k^2 \mathbf{E}(\mathbf{r}) = -j\omega\mu \mathbf{J}(\mathbf{r}) \quad (\text{B.10})$$

Since  $\nabla \times \nabla \times \mathbf{E} = -\nabla^2 \mathbf{E} + \nabla \nabla \cdot \mathbf{E}$  and that, according to the continuity equation,  $\nabla \cdot \mathbf{E} = \rho/\epsilon = \nabla \cdot \mathbf{J}/j\omega\epsilon$ , eq.(B.10) can be rewritten as:

$$\nabla^2 \mathbf{E}(\mathbf{r}) + k^2 \mathbf{E}(\mathbf{r}) = j\omega\mu \left[ \bar{\mathbf{I}} + \frac{\nabla \nabla}{k^2} \right] \cdot \mathbf{J}(\mathbf{r}) \quad (\text{B.11})$$

where  $\bar{\mathbf{I}}$  is the identity operator. In Cartesian coordinates, eq.(B.11) is actually three equations that can be solved just as it was done for the scalar equation. Thus, the solution for (B.11) is:

$$\mathbf{E}(\mathbf{r}) = -j\omega\mu \int_V d\mathbf{r}' g(\mathbf{r}' - \mathbf{r}) \left[ \bar{\mathbf{I}} + \frac{\nabla' \nabla'}{k^2} \right] \cdot \mathbf{J}(\mathbf{r}') \quad (\text{B.12})$$

---

<sup>1</sup>Dyad is an example of a second rank tensor, formed from two vectors and maps one vector field to another. Besides, they have the property of having nullspace of rank two. For a deeper discussion of tensors and their mathematical properties, we recommend reading Appendix B of (Chew, 1995).

Taking into account the vector identities  $\nabla g f = f \nabla g + g \nabla f$  and  $\nabla \cdot g \mathbf{F} = g \nabla \cdot \mathbf{F} + (\nabla g) \cdot \mathbf{F}$ , the following integrals can be rewritten as:

$$\int_V d\mathbf{r}' g(\mathbf{r}' - \mathbf{r}) \nabla' f(\mathbf{r}') = - \int_V [\nabla' g(\mathbf{r}' - \mathbf{r})] f(\mathbf{r}') \quad (\text{B.13})$$

$$\int_V d\mathbf{r}' [\nabla' g(\mathbf{r}' - \mathbf{r})] \nabla' \cdot \mathbf{J}(\mathbf{r}') = - \int_V d\mathbf{r}' \mathbf{J}(\mathbf{r}') \cdot \nabla' \nabla' g(\mathbf{r}' - \mathbf{r}) \quad (\text{B.14})$$

which allows us to rewrite (B.12) as:

$$\mathbf{E}(\mathbf{r}) = -j\omega\mu \int_V d\mathbf{r}' \mathbf{J}(\mathbf{r}') \cdot \left[ \bar{\mathbf{I}} + \frac{\nabla' \nabla'}{k^2} \right] g(\mathbf{r}', \mathbf{r}) \quad (\text{B.15})$$

However, as demonstrated in chapter 7 of (Chew, 1995), it is also possible to write eq.(B.15) as follows:

$$\mathbf{E}(\mathbf{r}) = j\omega\mu \int_V d\mathbf{r}' \mathbf{J}(\mathbf{r}') \cdot \bar{\mathbf{G}}(\mathbf{r}, \mathbf{r}') \quad (\text{B.16})$$

where:

$$\bar{\mathbf{G}}(\mathbf{r}, \mathbf{r}') = - \left[ \bar{\mathbf{I}} + \frac{\nabla \nabla}{k^2} \right] \frac{e^{jk|\mathbf{r}-\mathbf{r}'|}}{4\pi|\mathbf{r}-\mathbf{r}'|} \quad (\text{B.17})$$

## B.2 The Singularity of the Dyadic Green's Function

As can be seen in equation (B.13), Green's dyadic function has singularity for  $\mathbf{r} = \mathbf{r}'$ . That is, to calculate the field at a point within the region of the source  $\mathbf{J}$ , it is necessary to rewrite the integral equation (B.16) with the support of the exclusion volume  $V_\delta$  around the singularity point:

$$\mathbf{E}(\mathbf{r}) = \lim_{V_\delta \rightarrow 0} j\omega\mu \int_{V-V_\delta} d\mathbf{r}' \mathbf{J}(\mathbf{r}') \cdot \bar{\mathbf{G}}(\mathbf{r}', \mathbf{r}) \quad (\text{B.18})$$

In this way, the equation is defined in terms of an improper integral. Generally, improper integrals converge if there is a fixed limit regardless the shape of  $V_\delta$ . However, in the case of (B.18), a necessary condition for convergence is that  $\mathbf{J}$  must satisfy Holder's condition (Kellogg, 1953) in  $\mathbf{r} = \mathbf{r}'$ , in which there must be constants  $c$ ,  $A$ , and  $\alpha$  such that  $|\mathbf{J}(\mathbf{r}) - \mathbf{J}(\mathbf{r}')| \leq A|\mathbf{r}' - \mathbf{r}|^\alpha$  for  $|\mathbf{r}' - \mathbf{r}| < c$ . This condition is slightly stronger than general continuity. In addition, the derivatives of (B.17) do not allow the integral to converge in a traditional fashion, i.e., the principal value of the integral exists but depends on the chosen shape for  $V_\delta$ .

To calculate the limit of the term that includes those derived in eq.(B.18), we need to take into account both the integral over the region without the singularity and the region with

the singularity:

$$\nabla \nabla \cdot \int_V d\mathbf{r}' g(\mathbf{r}, \mathbf{r}') \mathbf{J}(\mathbf{r}') = \lim_{V_\delta \rightarrow 0} \left[ \nabla \nabla \cdot \int_{V-V_\delta} d\mathbf{r}' g(\mathbf{r}, \mathbf{r}') \mathbf{J}(\mathbf{r}') + \nabla \nabla \cdot \int_{V_\delta} d\mathbf{r}' g(\mathbf{r}, \mathbf{r}') \mathbf{J}(\mathbf{r}') \right] \quad (\text{B.19})$$

where  $\mathbf{r} \in V_\delta$ . The first integral on the right-hand side of the equation does not contain  $\mathbf{r}$ , so the operator  $\nabla \nabla \cdot$  might enter into the integral. The second integral converges only if an operator  $\nabla$  is introduced in the integral. In this way, eq.(B.19) can be rewritten as:

$$\nabla \nabla \cdot \int_V d\mathbf{r}' g(\mathbf{r}, \mathbf{r}') \mathbf{J}(\mathbf{r}') = \lim_{V_\delta \rightarrow 0} \left[ \int_{V-V_\delta} d\mathbf{r}' \nabla \nabla \cdot g(\mathbf{r}, \mathbf{r}') \mathbf{J}(\mathbf{r}') - \nabla \int_{V_\delta} d\mathbf{r}' \nabla' g(\mathbf{r}, \mathbf{r}') \cdot \mathbf{J}(\mathbf{r}') \right] \quad (\text{B.20})$$

Therefore, the two integrals on the right-hand side of (B.20) converge to a value that depends on the shape of  $V_\delta$ . However, the sum of the two integrals must be equal to the left-hand side, which does not depend on the shape chosen for  $V_\delta$ .

If we use the integration by parts and the relation  $\nabla \cdot \mathbf{J} = j\omega\rho$ , the second integral of (46) can be rewritten as:

$$\nabla \int_{V_\delta} d\mathbf{r}' \nabla' g(\mathbf{r}, \mathbf{r}') \cdot \mathbf{J}(\mathbf{r}') = \int_{S_\delta} dS' \mathbf{n} \cdot \mathbf{J}(\mathbf{r}') g(\mathbf{r}, \mathbf{r}') - j\omega \int_{V_\delta} g(\mathbf{r}, \mathbf{r}') \rho(\mathbf{r}') \quad (\text{B.21})$$

The second integral of (B.21) will tend to zero when  $V_\delta \rightarrow 0$  assuming that, for a volumetric current,  $\rho(\mathbf{r})$  is continuous. The first integral, on the other hand, has the term  $\mathbf{n} \cdot \mathbf{J}(\mathbf{r}')$  which is the surface charge on  $S_\delta$ , the surface of  $V_\delta$ . Because of this surface charge, the first integral is proportional to the field in  $\mathbf{r}$  and does not vary depending on the scale. In other words, it does not disappear when  $V_\delta \rightarrow 0$ , but depends on the shape of  $V_\delta$ . At the limit, eq.(B.21) is linearly proportional to  $\mathbf{J}(\mathbf{r})$ . Therefore, with the aid of  $\bar{\mathbf{L}}$ , a dyad which depends on the shape of  $V_\delta$ , we can rewrite (B.20) as:

$$\nabla \nabla \cdot \int_V d\mathbf{r}' g(\mathbf{r}, \mathbf{r}') \mathbf{J}(\mathbf{r}') = \lim_{V_\delta \rightarrow 0} \int_{V-V_\delta} d\mathbf{r}' \nabla \nabla(\mathbf{r}, \mathbf{r}') \cdot \mathbf{J}(\mathbf{r}') - \bar{\mathbf{L}} \cdot \mathbf{J}(\mathbf{r}) \quad (\text{B.22})$$

Using this result in (B.16), we will obtain:

$$\mathbf{E}(\mathbf{r}) = j\omega\mu \lim_{V_\delta \rightarrow 0} \int_{V-V_\delta} d\mathbf{r}' \bar{\mathbf{G}}(\mathbf{r}, \mathbf{r}') \cdot \mathbf{J}(\mathbf{r}') + \frac{\bar{\mathbf{L}} \cdot \mathbf{J}(\mathbf{r})}{j\omega\epsilon} \quad (\text{B.23})$$

The integral of (B.23) is equivalent to the principal value integral operator whose notation is expressed by  $P.V. \int_V$ , that is:

$$\mathbf{E}(\mathbf{r}) = j\omega\mu P.V. \int_V d\mathbf{r}' \bar{\mathbf{G}}(\mathbf{r}, \mathbf{r}') \cdot \mathbf{J}(\mathbf{r}') + \frac{\bar{\mathbf{L}} \cdot \mathbf{J}(\mathbf{r})}{j\omega\epsilon}, \quad \forall \mathbf{r} \in V \quad (\text{B.24})$$

Therefore, although the two terms on the right-hand side of (B.24) are dependent on the choice of  $V_\delta$ , the  $\mathbf{E}$  field is unique. This method for determining the field value in the region of singularity is known as the Principal Volume Method (Van Bladel, 1961).

Physically, this method of solution corresponds to opening a space around the observation point within the current region. Since this current is discontinuous on the surface of that space, the surface accumulates charges which, when decreasing the space to an infinitesimal volume, have an electrostatic nature. This electrostatic field satisfies the Laplace equation and depends on the shape of that space, no matter how small it is. Therefore, the second term in eq.(B.24) aims to remove the contribution from this electrostatic field, since it is not part of the problem but has been added as a mathematical resource.

Finally, some values for  $\bar{\mathbf{L}}$  for certain types of exclusion volumes have already been determined in the literature (Shung-Wu Lee et al., 1980; Yaghjian, 1980). In addition, generally, the trace  $[\bar{\mathbf{L}}] = 1$  (Yaghjian, 1980). Board B.1 shows some values for  $\bar{\mathbf{L}}$  considering some geometric shapes:

Tabela B.1: Dyad  $\bar{\mathbf{L}}$  values for different shapes of exclusion volume applied to the singularity of dyadic Green's function. Sources: (Shung-Wu Lee et al., 1980; Yaghjian, 1980).

Geometric shape	$\bar{\mathbf{L}}$
Spheres or cubes	$\frac{\mathbf{I}}{3}$
Disks	$\mathbf{zz}$
Needles	$\frac{\mathbf{xx}+\mathbf{yy}}{2}$

### B.3 Dyadic Green's Function for Inhomogeneous Medium

To determine the dyadic Green function for a non-homogeneous medium, we will assume a region  $V_1$  and another  $V_2 \subset V_1$ . The contrasts of these media in relation to the vacuum

will be denominated  $\chi_1$  and  $\chi_2$ , respectively. We can write  $\chi_2$  as:

$$\chi_2(\mathbf{r}) = \chi_1(\mathbf{r}) + \Delta\chi(\mathbf{r}) \quad (\text{B.25})$$

Consequently, the integral equation for the electric field at any point in space can be written as:

$$\mathbf{E}(\mathbf{r}) = \mathbf{E}_i(\mathbf{r}) + k_0^2 \int_{V_1} d\mathbf{r}' \bar{\mathbf{G}}(\mathbf{r}, \mathbf{r}') \cdot \chi_1(\mathbf{r}') \mathbf{E}(\mathbf{r}') + k_0^2 \int_{V_1} d\mathbf{r}' \bar{\mathbf{G}}(\mathbf{r}, \mathbf{r}') \cdot \chi_2(\mathbf{r}') \mathbf{E}(\mathbf{r}') \quad (\text{B.26})$$

However,  $\mathbf{E}$  can be interpreted as the sum of the scattered field and by  $\chi_1$  for  $\mathbf{r} \in V_1$ . The former is due to the *excess* of contrast in  $V_2$  when the incident field is the field that propagates in an inhomogeneous medium characterized by  $\epsilon_0$  for  $\mathbf{r} \notin V_1$ . Mathematically, this is equivalent to:

$$\mathbf{E}(\mathbf{r}) = \mathbf{E}_1(\mathbf{r}) + k_0^2 \int_{V_2} d\mathbf{r}' \bar{\mathbf{G}}_{\text{in}}(\mathbf{r}, \mathbf{r}') \cdot \chi_2(\mathbf{r}') \mathbf{E}(\mathbf{r}') \quad (\text{B.27})$$

where  $\mathbf{E}_1$  is given by:

$$\mathbf{E}_1(\mathbf{r}) = \mathbf{E}_i(\mathbf{r}) + k_0^2 \int_{V_1} d\mathbf{r}' \bar{\mathbf{G}}(\mathbf{r}, \mathbf{r}') \cdot \chi_1(\mathbf{r}') \mathbf{E}(\mathbf{r}') \quad (\text{B.28})$$

and the Green's function for the inhomogeneous medium satisfies:

$$\bar{\mathbf{G}}_{\text{in}}(\mathbf{r}, \mathbf{r}') = \bar{\mathbf{G}}(\mathbf{r}, \mathbf{r}') + k_0^2 \int_{V_1} d\mathbf{r}'' \bar{\mathbf{G}}(\mathbf{r}, \mathbf{r}'') \cdot \chi_1(\mathbf{r}'') \bar{\mathbf{G}}_{\text{in}}(\mathbf{r}'', \mathbf{r}') \quad (\text{B.29})$$

Analytical solutions for (B.29) are rarely available. Frequently, when inhomogeneous modeling for Green's function is necessary, numerical methods are employed to estimate this function.

# Apêndice C

## Integral Equation Formulation

Integral equations are an important method for electromagnetic theory. In this appendix, the derivation of the Electric Field Integral Equation from wave equation and dyadic Green's function will be discussed. The text is based on section 3.4 of (Chew, 2009).

Let us suppose a volume  $V_{inf}$  whose surface is  $S_{inf}$  in which there is a source  $J_2$  within a region  $V_2$  and another source  $J_1$  for a region  $V_1$  separate from  $V_2$  for a closed surface  $S$  (see Figure C.1). Assuming that the medium in  $V_1$  is homogeneous with properties  $\epsilon_1$  and  $\mu_1$ , the relationship between electric field  $\mathbf{E}(\mathbf{r})$  and a current distribution  $\mathbf{J}(\mathbf{r})$  representing currents  $J_1$  and  $J_2$  is given by the wave equation:

$$\nabla \times \nabla \times \mathbf{E}(\mathbf{r}) - \omega^2 \epsilon_1 \mu_1 \mathbf{E}(\mathbf{r}) = -j\omega \mu_1 \mathbf{J}(\mathbf{r}) \quad (\text{C.1})$$

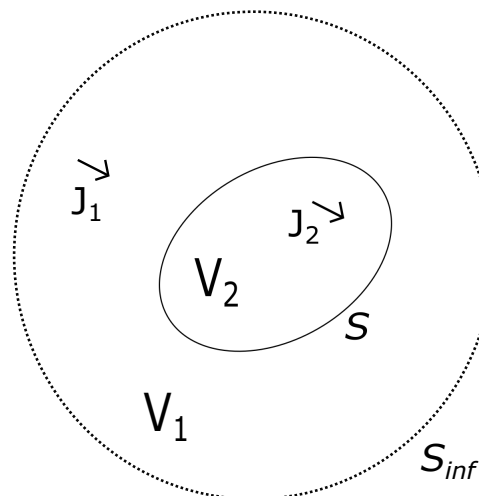


Figura C.1: Derivation of integral equation.

The solution to this equation is obtained with the support of the dyadic Green's function  $\bar{\mathbf{G}}(\mathbf{r}, \mathbf{r}')$  for a homogeneous and isotropic medium, where  $\mathbf{r}'$  is an observation point in the source

region. Under these conditions, the Green's function is a solution to the following equation:

$$\nabla \times \nabla \times \bar{\mathbf{G}}(\mathbf{r}, \mathbf{r}') - \omega^2 \epsilon_1 \mu_1 \bar{\mathbf{G}}(\mathbf{r}, \mathbf{r}') = -\bar{\mathbf{I}} \delta(\mathbf{r} - \mathbf{r}') \quad (\text{C.2})$$

Postmultiplying (C.1) by  $\bar{\mathbf{G}}(\mathbf{r}, \mathbf{r}')$ , premultiplying (C.2) by  $\mathbf{E}(\mathbf{r})$ , and then subtracting the resultant equations, we will obtain:

$$\begin{aligned} \mathbf{E}(\mathbf{r}) \cdot \nabla \times \nabla \times \bar{\mathbf{G}}(\mathbf{r}, \mathbf{r}') - \nabla \times \nabla \times \mathbf{E}(\mathbf{r}) \cdot \bar{\mathbf{G}}(\mathbf{r}, \mathbf{r}') \\ = j\omega \mu_1 \mathbf{J}(\mathbf{r}) \cdot \bar{\mathbf{G}}(\mathbf{r}, \mathbf{r}') - \mathbf{E}(\mathbf{r}) \delta(\mathbf{r} - \mathbf{r}') \end{aligned} \quad (\text{C.3})$$

If we integrate both sides of the equation (C.3) in the volume  $V_1$ , we get:

$$\int_{V_1} dV [\mathbf{E}(\mathbf{r}) \cdot \nabla \times \nabla \times \bar{\mathbf{G}}(\mathbf{r}, \mathbf{r}') - \nabla \times \nabla \times \mathbf{E}(\mathbf{r}) \cdot \bar{\mathbf{G}}(\mathbf{r}, \mathbf{r}')] = \mathbf{E}_1(\mathbf{r}') - \mathbf{E}(\mathbf{r}')$$

in which:

$$\mathbf{E}(\mathbf{r}') = \int_{V_1} d\mathbf{r} \delta(\mathbf{r} - \mathbf{r}') \mathbf{E}(\mathbf{r}) \quad (\text{C.4})$$

$$\mathbf{E}_1(\mathbf{r}') = j\omega \mu_1 \int_{V_1} d\mathbf{r} \mathbf{J}_1(\mathbf{r}) \cdot \bar{\mathbf{G}}(\mathbf{r}, \mathbf{r}') \quad (\text{C.5})$$

The field  $\mathbf{E}_1$  is produced by the source  $\mathbf{J}_1$  in  $V_1$ . Since  $\mathbf{J}_2$  is not in  $V_1$ , it does not contribute to the integral.

Through the identity:

$$\begin{aligned} -\nabla \cdot [\mathbf{E}(\mathbf{r}) \times \nabla \times \bar{\mathbf{G}}(\mathbf{r}, \mathbf{r}') + \nabla \times \mathbf{E}(\mathbf{r}) \times \bar{\mathbf{G}}(\mathbf{r}, \mathbf{r}')] \\ = \mathbf{E}(\mathbf{r}) \cdot \nabla \times \nabla \times \bar{\mathbf{G}}(\mathbf{r}, \mathbf{r}') - \nabla \times \nabla \times \mathbf{E}(\mathbf{r}) \cdot \bar{\mathbf{G}}(\mathbf{r}, \mathbf{r}') \end{aligned} \quad (\text{C.6})$$

we can apply Gauss' theorem and rewrite eq. (C.4) as:

$$\mathbf{E}_1(\mathbf{r}') - \mathbf{E}(\mathbf{r}') = \oint_{S+S_{inf}} dS \mathbf{n} \cdot [\mathbf{E}(\mathbf{r}) \times \nabla \times \bar{\mathbf{G}}(\mathbf{r}, \mathbf{r}') + \nabla \times \mathbf{E}(\mathbf{r}) \times \bar{\mathbf{G}}(\mathbf{r}, \mathbf{r}')] \quad (\text{C.7})$$

$$\begin{aligned} &= \oint_{S+S_{inf}} dS \cdot [\mathbf{n} \times \mathbf{E}(\mathbf{r}) \cdot \nabla \times \bar{\mathbf{G}}(\mathbf{r}, \mathbf{r}') \\ &\quad - j\omega \mu_1 \mathbf{n} \times \mathbf{H}(\mathbf{r}) \cdot \bar{\mathbf{G}}(\mathbf{r}, \mathbf{r}')] \end{aligned} \quad (\text{C.8})$$

where  $\mathbf{n}$  is the normal vector on the surface  $S$  which points outwards. Depending on the position of  $\mathbf{r}'$ , we have different results for eq.(C.8):

$$\mathbf{E}_1(\mathbf{r}') - \oint_{S+S_{inf}} dS [\mathbf{n} \times \mathbf{E}(\mathbf{r}) \cdot \nabla \times \bar{\mathbf{G}}(\mathbf{r}, \mathbf{r}') - j\omega \mu_1 \mathbf{n} \times \mathbf{H}(\mathbf{r}) \cdot \bar{\mathbf{G}}(\mathbf{r}, \mathbf{r}')] = \begin{cases} \mathbf{E}(\mathbf{r}'), & \mathbf{r}' \in V_1 \\ 0, & \mathbf{r}' \notin V_1 \end{cases} \quad (\text{C.9})$$

As the distance between the field observation point and the source point increases, the integral over  $S_{inf}$  vanishes. Although the surface of  $S_{inf}$  increases with this distance, the two terms on the left-hand side of the eq.(C.9) will cancel each other out so that the integrator decays.

Swapping the observations points  $\mathbf{r}$  and  $\mathbf{r}'$ , we get:

$$\mathbf{E}_1(\mathbf{r}) - \oint_S dS' [\mathbf{n}' \times \mathbf{E}(\mathbf{r}') \cdot \nabla' \times \bar{\mathbf{G}}(\mathbf{r}', \mathbf{r}) - j\omega\mu_1 \mathbf{n}' \times \mathbf{H}(\mathbf{r}') \cdot \bar{\mathbf{G}}(\mathbf{r}', \mathbf{r})] = \begin{cases} \mathbf{E}(\mathbf{r}), & \mathbf{r} \in V_1 \\ 0, & \mathbf{r} \in V_2 \end{cases} \quad (\text{C.10})$$

From the following transposition properties:

$$\nabla \times \bar{\mathbf{G}}(\mathbf{r}, \mathbf{r}') = [\nabla' \times \bar{\mathbf{G}}(\mathbf{r}', \mathbf{r})]^t \quad (\text{C.11})$$

$$\bar{\mathbf{G}}(\mathbf{r}, \mathbf{r}') = [\bar{\mathbf{G}}(\mathbf{r}', \mathbf{r})]^t \quad (\text{C.12})$$

we can calculate the transpose of eq.(C.10) by:

$$\mathbf{E}_1(\mathbf{r}) - \oint_S dS' [\nabla \times \bar{\mathbf{G}}(\mathbf{r}', \mathbf{r}) \cdot \mathbf{n}' \times \mathbf{E}(\mathbf{r}') - j\omega\mu_1 \bar{\mathbf{G}}(\mathbf{r}', \mathbf{r}) \cdot \mathbf{n}' \times \mathbf{H}(\mathbf{r}')] = \begin{cases} \mathbf{E}(\mathbf{r}), & \mathbf{r} \in V_1 \\ 0, & \mathbf{r} \in V_2 \end{cases} \quad (\text{C.13})$$

Letting  $\mathbf{M}_s(\mathbf{r}') = -\mathbf{n}' \times \mathbf{E}(\mathbf{r}')$  and  $\mathbf{J}_s(\mathbf{r}') = \mathbf{n}' \times \mathbf{H}(\mathbf{r}')$ , we may write the eq.(C.13) in terms of equivalent surface electric and magnetic currents imposed on the  $S$  surface. Thus, the equation becomes:

$$\mathbf{E}_1(\mathbf{r}) + \oint_S dS' [\bar{\mathbf{G}}(\mathbf{r}', \mathbf{r}) \cdot \mathbf{M}_s(\mathbf{r}') + j\omega\mu_1 \bar{\mathbf{G}}(\mathbf{r}', \mathbf{r}) \cdot \mathbf{J}_s(\mathbf{r}')] = \begin{cases} \mathbf{E}(\mathbf{r}), & \mathbf{r} \in V_1 \\ 0, & \mathbf{r} \in V_2 \end{cases} \quad (\text{C.14})$$

In other words, the field observed at a point in the region  $V_1$  is due to the source  $\mathbf{J}_1$  in  $V_1$  and the equivalent currents  $\mathbf{M}_s$  and  $\mathbf{J}_s$  on the surface of  $S$  which has the same effect as  $\mathbf{J}_2$ . It is also worth noting that (C.14) also applies to other types of equivalent currents, such as induction currents due to the penetration of an incident field in a dielectric material. In these cases, eq.(C.14) can simply be written as:

$$\mathbf{E}(\mathbf{r}) = \mathbf{E}^i(\mathbf{r}) + j\omega\mu \oint_S dS' \bar{\mathbf{G}}(\mathbf{r}', \mathbf{r}) \cdot \mathbf{J}(\mathbf{r}') \quad (\text{C.15})$$

# Apêndice D

## Functional Analysis

An important issue within the scope of integral equations is functional analysis since it is a problem composed of an operator applied to functions of a vector space. Therefore, this chapter is a brief approach to the concepts of normed spaces and operators which will be a reference for discussions found in the dissertation. This text was written based on Appendix A of (Kirsch, 2011). Therefore, more information can be found in this reference and a more in-depth study can also be found in (Lebedev et al., 1996).

### D.1 Normed and Hilbert Spaces

Let us start with some basic definitions:

**Definição 2.** *Inner Product*

*Let  $X$  be a vector space defined on  $\mathbb{K} = \mathbb{R}$  or  $\mathbb{K} = \mathbb{C}$ . The scalar product is a mapping*

$$\langle \cdot, \cdot \rangle : X \times X \rightarrow \mathbb{K}$$

*with the following properties:*

1.  $\langle x+y, z \rangle = \langle x, z \rangle + \langle y, z \rangle$ ,  $\forall x, y, z \in X$ ;
2.  $\langle x, y+z \rangle = \langle x, y \rangle + \langle x, z \rangle$ ,  $\forall x, y, z \in X$ ;
3.  $\langle \alpha x, y \rangle = \alpha \langle x, y \rangle$ ,  $\forall x, y \in X$  and  $\alpha \in \mathbb{K}$ ;
4.  $\langle x, y \rangle = \overline{\langle y, x \rangle}$ ,  $\forall x, y \in X$ ;
5.  $\langle x, x \rangle \in \mathbb{R}$  and  $\langle x, x \rangle \geq 0$ ,  $\forall x \in X$ ;
6.  $\langle x, x \rangle > 0$  if  $x \neq 0$ ;
7.  $\langle x, \alpha y \rangle = \bar{\alpha} \langle x, y \rangle$ ,  $\forall x, y \in X$  and  $\alpha \in \mathbb{K}$ .

**Definição 3.** *Pre-Hilbert space*

*A vector space  $X$  over  $\mathbb{K}$  with inner product  $\langle \cdot, \cdot \rangle$  is called a pre-Hilbert space over  $\mathbb{K}$ .*

**Definição 4.** *Norm*

Let  $X$  be a vector space over the field  $\mathbb{K} = \mathbb{R}$  or  $\mathbb{K} = \mathbb{C}$ . A norm on  $X$  is a mapping

$$\|\cdot\| : X \rightarrow \mathbb{R}$$

with the following properties:

1.  $\|x\| > 0, \forall x \in X$  with  $x \neq 0$ ;
2.  $\|\alpha x\| = |\alpha| \|x\|, \forall x \in X$  and  $\alpha \in \mathbb{K}$ ;
3.  $\|x+y\| \leq \|x\| + \|y\|$  and  $\|x-y\| \geq \left| \|x\| - \|y\| \right|, \forall x, y \in X$  (Triangle Inequality).

A vector space  $X$  over  $\mathbb{K}$  with norm  $\|\cdot\|$  is called normed space over  $\mathbb{K}$

Now, the following theorem is introduced:

**Teorema 5.** Let  $X$  be a pre-Hilbert space. The mapping  $\|\cdot\| : X \rightarrow \mathbb{R}$  defined by

$$\|x\| := \sqrt{\langle x, x \rangle}, x \in X$$

is a norm. Furthermore:

1.  $|(x,y)| \leq \|x\| \|y\|, \forall x, y \in X$  (Cauchy-Schwarz inequality);
2.  $\|x \pm y\|^2 = \|x\|^2 + \|y\|^2 \pm 2\Re\{\langle x, y \rangle\} \forall x, y \in X$  (binomial formula);
3.  $\|x+y\|^2 + \|x-y\|^2 = 2\|x\|^2 + 2\|y\|^2 \forall x, y \in X$ .

An example of a pre-Hilbert space over  $\mathbb{R}$  is the space of real or complex continuous functions over the interval  $[a,b]$ , denoted by  $C[a,b]$ , whose internal product is:

$$(x, y)_{L^2} := \int_a^b x(t) \overline{y(t)} dt, \quad x, y \in C[a, b] \quad (\text{D.1})$$

and whose norm is Euclidean, i.e.:

$$\|x\|_{L^2} := \sqrt{\langle x, x \rangle} = \sqrt{\int_a^b |x(t)|^2 dt}, \quad x \in C[a, b] \quad (\text{D.2})$$

When a norm is defined for a vector space, it introduces as well a topology. Based on the norm definition, it is also possible to define open, closed, compact sets, and others features. Firstly, we will introduce the definition of a ball with radius  $r$  and center  $x \in X$  which will be useful for the next definitions:

$$K(x, r) := \{y \in X : \|y - x\| < r\}, \quad K[x, r] := \{y \in X : \|y - x\| \leq r\}$$

**Definição 6.** Let  $X$  be a normed space over the field  $\mathbb{K} = \mathbb{R}$  or  $\mathbb{C}$ .

1. A subset  $M \subset X$  is called bounded if there exists  $r > 0$  with  $M \subset K(x, r)$ . The set  $M \subset X$  is called open if for every  $x \in M$  there exists  $\epsilon > 0$  such that  $K(x, \epsilon) \subset M$ . The set  $M \subset X$  is called closed if the complement  $X \setminus M$  is open.
2. A sequence  $(x_k)_k \subset X$  is called bounded if there exists  $c > 0$  such that  $\|x_k\| < c$  for all  $k$ . The sequence  $(x_k)_k \subset X$  is called convergent if there exist  $x \in X$  such that  $\|x - x_k\|$

converges to zero in  $\mathbb{R}$ . We denote the limit by  $x = \lim_{k \rightarrow \infty} x_k$ , or we write  $x_k \rightarrow x$  as  $k \rightarrow \infty$ . The sequence  $(x_k)_k \subset X$  is called a Cauchy sequence if for every  $\varepsilon > 0$  there exists  $N \in \mathbb{N}$  with  $\|x_m - x_k\| < \varepsilon$  for all  $m, k \geq N$ .

3. Let  $(x_k)_k \subset X$  be a sequence.  $x \in X$  is called an accumulation point if there exists a subsequence  $(a_{k_n})_n$  that converges to  $x$ .
4. A set  $M \subset X$  is called compact if every sequence in  $M$  has an accumulation point in  $M$ .

A property derived from these concepts is that a set  $M$  is closed if and only if the limit of each convergent sequence  $(x_k)_k \subset M$  also belongs to  $M$ . Furthermore, we call the sets  $M^o := \{x \in M : \text{there exists } \varepsilon > 0 \text{ with } K(x, \varepsilon) \subset M\}$  and  $\overline{M} := \{x \in X : \text{there exists } (x_k)_k \subset M \text{ with } x = \lim_{k \rightarrow \infty} x_k\}$  interior and closure of  $M$ , respectively. In addition, the set  $M \subset X$  is said to be dense in  $X$  if  $\overline{M} = X$ .

We can exemplify some of these concepts defined through the set  $X = C[0,1]$  on  $\mathbb{R}$  and  $x_k(t) = t^k$ ,  $t \in [0,1]$ ,  $k \in \mathbb{N}$  with norm  $\|\cdot\|_{L^2}$ . In this case, the sequence  $(x_k)$  converges to zero. The dependence between topological properties and the definition of the norm of a set is usual; however, this is not the case with finite-dimensional spaces in which the properties are independent.

**Teorema 7.** Let  $X$  be a finite-dimensional space with norms  $\|\cdot\|_1$  and  $\|\cdot\|_2$ . Then both norms are equivalent, i.e., there exist constants  $c_2 \geq c_1 > 0$  with

$$c_1\|x\|_1 \leq \|x\|_2 \leq c_2\|x\|_1, \quad \forall x \in X.$$

Therefore, each ball defined on  $\|\cdot\|_1$  contains a ball defined on  $\|\cdot\|_2$  and vice versa.

**Teorema 8.** Let  $X$  be a normed space over  $\mathbb{K}$  and  $M \subset X$  be a subset.

1.  $M$  is closed if and only if  $M = \overline{M}$ , and  $M$  is open if and only if  $M = M^o$ .
2. If  $M \neq X$  is a linear subspace, then  $M^o = \emptyset$ , and  $\overline{M}$  is also a linear subspace.
3. In finite-dimensional spaces, every subspace is closed.
4. Every compact set is closed and bounded. In finite-dimensional spaces, the reverse is also true (Theorem of Bolzano-Weierstrass): In a finite-dimensional normed space, every closed and bounded set is compact.

From now on, we can introduce an important concept in functional analysis, which is completeness. This concept is a crucial feature of the set of real numbers, for example.

**Definição 9. Banach Space, Hilbert Space**

A normed space  $X$  over  $\mathbb{K}$  is called complete or a Banach Space if every Cauchy sequence converges in  $X$ . A complete pre-Hilbert space is called a Hilbert space.

The spaces  $\mathbb{C}^n$  and  $\mathbb{R}^n$  with their canonical inner products are examples of Hilbert spaces. The space  $C[a,b]$  with inner product  $\langle \cdot, \cdot \rangle_{L^2}$  is not an example. However, any normed or pre-Hilbert space can be “completed”, i.e., a smaller Banach or Hilbert space that extends  $X$  can be defined. Let us see in the next theorem:

**Teorema 10.** Let  $X$  be a normed space with norm  $\|\cdot\|_X$ . There exist a Banach space  $(\tilde{X}, \|\cdot\|_{\tilde{X}})$

and a injective linear operator  $\mathcal{J} : X \rightarrow \tilde{X}$  such that

1. The range  $J(X) \subset \tilde{X}$  is dense in  $\tilde{X}$ , and
2.  $\|\mathcal{J}\{x\}\|_{\tilde{X}} = \|x\|_X, \forall x \in X$ , i.e.,  $\mathcal{J}$  preserves the norm.

Furthermore,  $\tilde{X}$  is uniquely determined in the sense that if  $\tilde{X}$  is a second space with properties 1 and 2 with respect to a linear injective operator  $\hat{\mathcal{J}}$ , then the operator  $\hat{\mathcal{J}} \mathcal{J}^{-1} : \mathcal{J}(X) \rightarrow \hat{\mathcal{J}}(X)$  has an extension to a norm-preserving isomorphism from  $\tilde{X}$  onto  $\hat{X}$ . In other words,  $\tilde{X}$  and  $\hat{X}$  can be identified.

For the pre-Hilbert space  $(C[a,b], \langle \cdot, \cdot \rangle_{L^2})$  to be complete, it is necessary to make use of Lebesgue's integration theory (Bartle, 1995). From the Lebesgue measure and its definitions of measurability and integrability, the complete space of  $(C[a,b], \langle \cdot, \cdot \rangle_{L^2})$  will be denoted as  $L^2(a,b)$ . For this, we first define the vector space  $\mathcal{L}^2(a,b) := \{x : (a,b) \rightarrow \mathbb{C} : x \text{ is measurable and } |x|^2 \text{ integrable}\}$ , in which scalar addition and multiplication are defined pointwise in almost everywhere. From this,  $\mathcal{L}^2(a,b)$  is a vector space since for  $x, y \in \mathcal{L}^2(a,b)$  and  $\alpha \in \mathbb{C}$ ,  $x+y$  and  $\alpha x$  are also measurable and  $\alpha x, x+y \in \mathcal{L}^2(a,b)$ . We define a sesquilinear form on  $\mathcal{L}^2(a,b)$  by:

$$\langle x, y \rangle := \int_a^b x(t) \overline{y(t)} dt, \quad x, y \in \mathcal{L}^2(a,b) \quad (\text{D.3})$$

However, (D.3) is not an inner product on  $\mathcal{L}^2(a,b)$  since  $\langle x, y \rangle = 0$  only implies that  $x$  vanishes almost everywhere, i.e., that  $x \in \mathcal{N}$ , where  $\mathcal{N} := \{x \in \mathcal{L}^2(a,b) : x(t) = 0 \text{ almost everywhere on } (a,b)\}$ . Now, we define  $L^2(a,b)$  as the factor space

$$L^2(a,b) := \mathcal{L}^2(a,b) \setminus \mathcal{N} \quad (\text{D.4})$$

and equip  $L^2(a,b)$  with the inner product

$$\langle [x], [y] \rangle_{L^2} := \int_a^b x(t) \overline{y(t)} dt, \quad x \in [x], y \in [y]$$

where  $[x], [y] \in L^2(a,b)$  are equivalence classes of functions in  $\mathcal{L}^2(a,b)$ . From now on, we will write  $x \in L^2(a,b)$  instead of  $x \in [x] \in L^2(a,b)$ . Finally,  $L^2(a,b)$  is a Hilbert space and contains  $C[a,b]$  as a dense subspace.

## D.2 Linear Bounded and Compact Operators

In this section, for all definitions and theorems, we will assume that  $X$  and  $Y$  are normed spaces and  $\mathcal{A} : X \rightarrow Y$  is a linear operator.

**Definição 11. Boundedness, Norm of  $\mathcal{A}$**

The linear operator  $\mathcal{A}$  is called bounded if there exists  $c > 0$  such that

$$\|\mathcal{A}\{x\}\| \leq c\|x\|, \quad \forall x \in X.$$

The smallest of these constants is called the norm of  $\mathcal{A}$ , i.e.,

$$\|\mathcal{A}\| := \sup_{x \neq 0} \frac{\|\mathcal{A}\{x\}\|}{\|x\|}.$$

**Teorema 12.** The following assertions are equivalent:

1.  $\mathcal{A}$  is bounded.
2.  $\mathcal{A}$  is continuous at  $x = 0$ , i.e.,  $x_j \rightarrow 0$  implies that  $\mathcal{A}\{x_j\} \rightarrow 0$ .
3.  $\mathcal{A}$  is continuous for every  $x \in X$ .

Hence,  $\mathcal{L}(X, Y)$  can be understood as all bounded linear mappings from  $X$  to  $Y$  in which the operator norm is a normed space.

**Teorema 13.** 1. Let  $k \in L^2((c,d) \times (a,b))$ . The operator

$$\mathcal{A}\{x(t)\} := \int_a^b k(t,s)x(s)ds, \quad t \in (c,d), \quad x \in L^2(a,b) \quad (\text{D.5})$$

is well-defined, linear, and bounded from  $L^2(a,b)$  into  $L^2(c,d)$ . Furthermore,

$$\|\mathcal{A}\|_{L^2} \leq \int_c^d \int_a^b |k(t,s)| ds dt.$$

2. Let  $k$  be continuous on  $[c,d] \times [a,b]$ . Then  $\mathcal{A}$  is also well-defined, linear, and bounded from  $C[a,b]$  into  $C[c,d]$  and

$$\|\mathcal{A}\|_\infty = \max_{t \in [c,d]} \int_a^b |k(t,s)| ds.$$

Within the context of integral operators, those whose kernel is weakly singular are also of interest. Mathematically, a kernel  $k$  is weakly singular in  $[a,b] \times [a,b]$  if  $k$  is defined and continuous for every  $t,s \in [a,b]$ ,  $t \neq s$ , and there is a  $c > 0$  and  $\alpha \in [0,1)$  such that

$$|k(t,s)| \leq c|t-s|^{-\alpha}, \quad \forall t,s \in [a,b], t \neq s.$$

**Teorema 14.** Let  $k$  be weakly singular on  $[a,b]$ . Then the integral operator  $\mathcal{A}$  defined by (D.5) for  $[c,d] = [a,b]$ , is well-defined and bounded as an operator in  $L^2(a,b)$  as well as in  $C[a,b]$ .

Another important definition for the study is the adjoint operator:

**Teorema 15. Adjoint Operator**

Let  $\mathcal{A} : X \rightarrow Y$  be a linear and bounded operator between Hilbert spaces. Then there exists one and only linear bounded operator  $\mathcal{A}^* : Y \rightarrow X$  with the property

$$\langle \mathcal{A}\{x\}, y \rangle = \langle x, \mathcal{A}^*\{y\} \rangle \quad \forall x \in X, y \in Y.$$

This operator  $\mathcal{A}^* : Y \rightarrow X$  is called the adjoint operator to  $\mathcal{A}$ . For  $X = Y$ , the operator  $\mathcal{A}$  is

called self-adjoint if  $\mathcal{A}^* = \mathcal{A}$ .

To exemplify the adjunct operators, let  $X = L^2(a,b)$ ,  $Y = L^2(c,d)$ , and  $k \in L^2((c,d) \times (a,b))$ . The adjoint operator  $\mathcal{A}^*$  of the integral operator

$$\mathcal{A}\{x(t)\} = \int_a^b k(t,s)x(s)ds, \quad t \in (c,d), x \in L^2(a,b)$$

which is given by

$$\mathcal{A}^*\{y(t)\} = \int_c^d \overline{k(s,t)}y(s)ds, \quad t \in (a,b), y \in L^2(c,d).$$

Finally, a final important definition is the compact operators:

**Definição 16.** *Compact Operator*

The operator  $\mathcal{K} : X \rightarrow Y$  is called compact if it maps every bounded set  $S$  into a relatively compact set  $\mathcal{K}(S)$ .

A set  $M \subset Y$  is called relatively compact if every bounded sequence  $(y_j) \subset M$  has an accumulation point in  $\overline{M}$ , i.e., if the closure  $\overline{M}$  is compact. The set of all compact operators from  $X$  to  $Y$  is a closed subspace of  $\mathcal{L}(X,Y)$ . In respect to integral operators:

**Teorema 17.** *Compactness of integral operators*

1. Let  $k \in L^1((c,d) \times (a,b))$ . The operator  $\mathcal{K} : L^2(a,b) \rightarrow L^2(c,d)$ , defined by

$$\mathcal{K}\{x(t)\} := \int_a^b k(t,s)x(s)ds, \quad t \in (c,d), x \in L^2(a,b) \quad (\text{D.6})$$

is compact from  $L^2(a,b)$  into  $L^2(c,d)$ .

2. Let  $k$  be continuous on  $[c,d] \times [a,b]$  or weakly singular on  $[a,b] \times [a,b]$  (in this case  $[c,d] = [a,b]$ ). Then  $\mathcal{K}$  defined by (D.6) is also compact as an operator from  $C[a,b]$  into  $C[c,d]$ .

# Apêndice E

## Shape metrics

In an Electromagnetic Inverse Scattering (EISP) problem, we are interested in detecting objects in an image. These objects have three characteristics: position, shape and contrast value. In the literature of this problem, there are measures to evaluate the error of a method when estimating the contrast of an object. However, up to the date of this thesis, there is no reference for measuring position and shape. This appendix aims to investigate and develop ways to measure the quality of an algorithm in recovering shapes. In addition, this annex is dedicated to analyzing the case of reconstructing a single object within the image.

The identification of objects in an image is a classic problem in the area of Image Processing. Traditionally, the goal is to recognize patterns in figures and to identify those patterns. In EISP, identifying the object is not the purpose, in the sense of comparing it with a database, but only to retrieve shapes. This kind of problem can be addressed with methods known as Marching Squares, which generate contours from a threshold process.

Suppose an algorithm designed to recover an image. The original and the recovered images are show in Figure E.1. If we apply the Marching Squares algorithm do obtain the contours using the same threshold for the recovered image as in Algorithm 10, we will obtain the results which are in E.2.

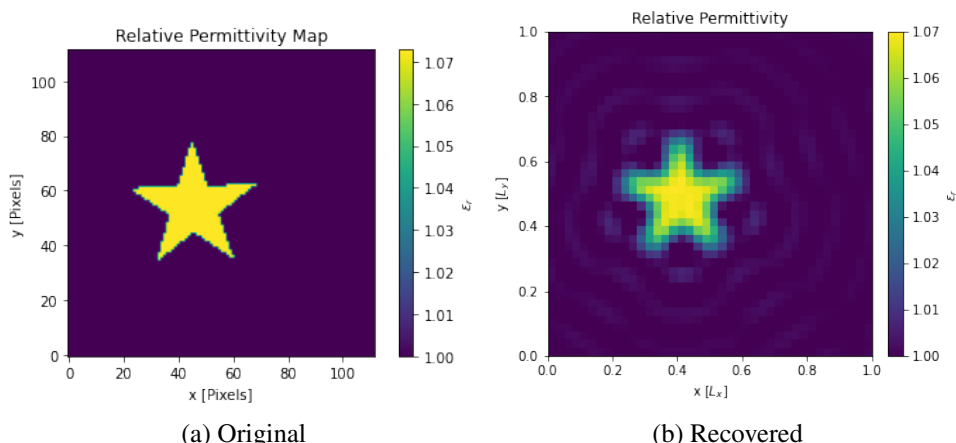


Figura E.1: Example images for shape metrics.

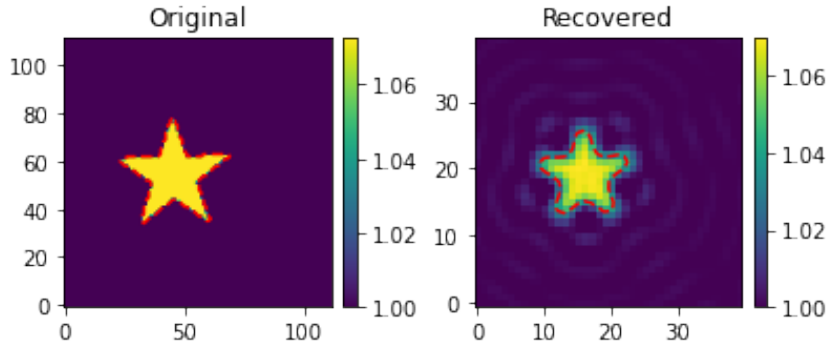


Figura E.2: Contours of original and recovered images.

The main idea is to calculate the difference area of the two contours. Of course, the area of one minus the area of the other would not work because the two forms might have equal areas but completely different forms. The following algorithm calculates the area of the difference:

1. Calculate the contours;
2. Correct the scale of the recovered contour to be equivalent to the size of the original image;
3. Center the image to isolate the object's position effect;
4. Check which pixels of the image are on each of the objects;
5. Separate those pixels that are in one of the objects and not in the other;
6. Calculate the quantity and multiply by an area element considering the limits equal to 0 and 1.

This algorithm is implemented in the following Python3 code:

```
# Evaluate contours
co = measure.findContours(original, 1.0, fully_connected='high')
cr = measure.findContours(recovered, threshold)

# Converting scale of recovered contour
for i in range(len(cr)):
    cr[i][:, 1] = original.shape[1]*cr[i][:, 1]/recovered.shape[1]
    cr[i][:, 0] = original.shape[0]*cr[i][:, 0]/recovered.shape[0]

# Thresholding
masko = np.zeros(original.shape, dtype=bool)
maskr = np.zeros(recovered.shape, dtype=bool)
masko[original > 1] = True
maskr[recovered >= threshold] = True

# Evaluate centers
xo, yo = np.meshgrid(np.arange(0, original.shape[1]),
                     np.arange(0, original.shape[0]))
xr, yr = np.meshgrid(np.linspace(0, original.shape[1]-1, recovered.shape[1]),
                     np.linspace(0, original.shape[0]-1, recovered.shape[0]))
xco = np.sum(masko*xo)/np.sum(masko)
```

```

yco = np.sum(masko*yo)/np.sum(masko)
xcr = np.sum(maskr*xr)/np.sum(maskr)
ycr = np.sum(maskr*yr)/np.sum(maskr)

# Centralization
for i in range(len(co)):
    co[i][:, 0] = co[i][:, 0]-yco+original.shape[0]/2
    co[i][:, 1] = co[i][:, 1]-xco+original.shape[1]/2

# Centralization
for i in range(len(cr)):
    cr[i][:, 0] = cr[i][:, 0]-ycr+original.shape[0]/2
    cr[i][:, 1] = cr[i][:, 1]-xcr+original.shape[1]/2

# Verify points
masko = np.zeros(original.shape, dtype=bool)
counter = np.zeros(original.shape)
for i in range(len(co)):
    maskt = measure.grid_points_in_poly(original.shape, co[i])
    counter[maskt] += 1
masko[np.mod(counter, 2) == 1] = True

# Verify points
maskr = np.zeros(original.shape, dtype=bool)
counter = np.zeros(original.shape)
for i in range(len(cr)):
    maskt = measure.grid_points_in_poly(original.shape, cr[i])
    counter[maskt] += 1
maskr[np.mod(counter, 2) == 1] = True

# Xor operation
diff = np.logical_xor(masko, maskr)

# Area of the difference
zeta_s = np.sum(diff)/np.sum(masko)*100

# Figure
fig, axis = plt.subplots(ncols=3, figsize=[3*6.4,4.8])
fig.subplots_adjust(wspace=.5)
axis[0].imshow(masko, origin='lower')
axis[0].set_title('Original')
axis[1].imshow(maskr, origin='lower')
axis[1].set_title('Recovered')
axis[2].imshow(diff, origin='lower')
axis[2].set_title('Difference')

plt.show()

```

This code yields results in Figura E.3. The  $\zeta_S$  measure in this case was 20.68%.

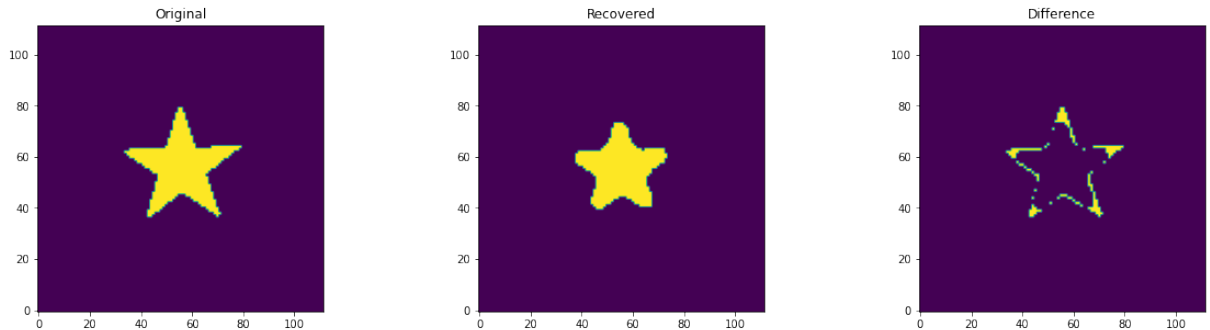


Figura E.3: Original, recovered and difference area.